Summer 2005

Modeling the Effects of Physical and Biogeochemical Processes on Phytoplankton Species and Carbon Production in the Equatorial Pacific Ocean

Baris Salihoglu
Old Dominion University

MODELING THE EFFECTS OF PHYSICAL AND BIOGEOCHEMICAL PROCESSES ON PHYTOPLANKTON SPECIES AND CARBON PRODUCTION IN THE EQUATORIAL PACIFIC OCEAN

by

Barış Salihoğlu
B.S. June 1996, Middle East Technical University
M.S. June 1998, Middle East Technical University

A Dissertation Submitted to the Faculty of
Old Dominion University in Partial Fulfillment of the
Requirement for the Degree of

DOCTOR OF PHILOSOPHY

OCEANOGRAPHY

OLD DOMINION UNIVERSITY
August 2005

Approved by:

Eileen E. Hofmann (Director)

Larry P. Atkinson

Antonio J. Busalacchi

Mariorie A. M. Friedrichs

John M. Klinck

Raghu Murtugudde

ABSTRACT

MODELING THE EFFECTS OF PHYSICAL AND BIOGEOCHEMICAL PROCESSES ON PHYTOPLANKTON SPECIES AND CARBON PRODUCTION IN THE EQUATORIAL PACIFIC OCEAN

Barış Salihoğlu
Old Dominion University, 2005
Director: Dr. Eileen E. Hofmann

The primary objective of this research is to investigate phytoplankton community response to variations in physical forcing and biological processes in the Cold Tongue region of the equatorial Pacific Ocean at 0°N, 140°W. This research objective was addressed using a one-dimensional multi-component lower trophic level ecosystem model that includes detailed algal physiology, such as spectrally-dependent photosynthetic processes and iron limitation on algal growth. The ecosystem model is forced by a one-year (1992) time series of spectrally-dependent light, temperature, and water column mixing obtained from a Tropical Atmosphere-Ocean (TAO) Array mooring. Autotrophic growth is represented by five algal groups, which have light and nutrient utilization characteristics of low-light adapted *Prochlorococcus*, high-light adapted *Prochlorococcus*, *Synechococcus*, autotrophic eukaryotes, and large diatoms. The simulated distributions and rates are validated using observations from the 1992 U.S. Joint Global Ocean Flux Study Equatorial Pacific cruises. The model-data comparisons show that the simulations successfully reproduce the temporal distribution of each algal group and that multiple algal groups are needed to fully resolve the variations observed for phytoplankton communities in the equatorial Pacific.

The 1992 simulations show seasonal variations in algal species composition superimposed on which are shorter time scale variations (e.g., 8-20 days) that arise from changes in the upwelling/downwelling environmental structure. The simulated time

evolution of the algal groups shows that eukaryotes are the most abundant group, being responsible for half of the annual biomass and 69% of the primary production and export. Filtering out low frequency physical forcing results in a 30% increase in primary production and dominance of high-light adapted *Prochlorococcus* and autotrophic eukaryotes. Sensitivity studies show that iron availability is the primary control on carbon export and production; whereas, algal biomass concentration is largely regulated by zooplankton grazing. Recycled iron is an important component of the ecosystem dynamics because sustained growth of algal groups depends on remineralized iron which accounts for 40% of the annual primary production in the Cold Tongue region.

Sensitivity studies show that although all algal groups have a considerable effect on simulated phytoplankton carbon biomass, not all have a strong effect on primary production and carbon export. Thus, these sensitivity studies indicate that it may not be necessary to represent a broad spectrum of algal groups in carbon cycle models, because a few key groups appear to have a large influence on primary production and export variability. Combining the low-light adapted *Prochlorococcus*, high-light adapted *Prochlorococcus* and *Synechococcus* groups as a single group and using a three algal group model may be sufficient to simulate primary production and export variability in the tropical Pacific waters.

The effects of El Niño-Southern Oscillation (ENSO) processes on the lower trophic levels of Cold Tongue region were examined with eight-year simulations for a time, 1991-1999, that included three ENSO cycles. As a comparison, simulations were done for a region in the western Pacific at 165°E at the equator, which is known as the Warm Pool. The simulated response of the lower trophic levels in the two regions of the equatorial Pacific to ENSO cycles differs in community structure and level of production. For the Cold Tongue region, the ENSO warm phase results in a shift to small algal forms (e.g., *Prochlorococcus* spp. and *Synechecoccus*) and low primary productivity (25 mmol C m^{-2} d^{-1} versus an annual average of 75 mmol C m^{-2} d^{-1}). For the Warm Pool region, the phytoplankton community is dominated by larger algal forms (e.g., autotrophic eukaryotes) and primary production increases

(150 mmol C m^{-2} d^{-1} versus an annual average of 59 mmol C m^{-2} d^{-1}). Also, during ENSO events carbon production and export in the Cold Tongue are limited by iron, whereas the relative abundance of iron and macronutrients (i.e. nitrate, silicate) limits production and export in the Warm Pool.

The results from this modeling study suggest that for conditions of increased stratification and temperature, carbon export in the Cold Tongue region would decrease and the phytoplankton community would shift towards smaller algal forms (e.g., *Prochlorococcus* spp. and *Synechecoccus*). Increased stratification can result in decreased iron concentration and reduced vertical velocities, both of which contribute to decreased carbon export. Also, stratified conditions enhances the remineralization rate of nutrients (e.g., iron), which enhances carbon production and export. Thus, inclusion of iron dynamics in climate models may be needed to fully represent the effect of climate variability on equatorial Pacific ecosystems.

To my mother and father, for their unconditional love and support.

ACKNOWLEDGMENTS

First and foremost I would like to thank my advisor, Eileen Hofmann, who has shown plenty of encouragement, patience, and support as she guided me through this endeavour, fostering my development as an independent scientist. Eileen was also very generous in providing opportunities for travel to national and international meetings and cruises, which is gratefully acknowledged. I am also thankful for the contributions and comments of my committee members, Larry Atkinson, Antonio Busalacchi, Marjy Friedrichs, John Klinck, and Raghu Murtugudde.

I am especially grateful to Drs. Raghu Murtugudde, Jim Christian, and Marjy Friedrichs for being great mentors. Raghu, has been a constant source of encouragement and helped me gain the self-confidence I needed. Jim Christian has always been very generous in sharing his expertise in ocean biochemistry. Raghu and Jim always made time for scientific discussions during meetings and they kindly provided unpublished data and model output. Marjy Friedrichs, my main collaborator in the department, was very generous in providing the model details that I needed. She helped me navigate through the often difficult life as a student, always having an open ear and lots of helpful advise. Without their support I would not have been able to achieve this.

Drs. Sergio Signorini, Chuck McClain, Pete Strutton, Robert Le Borgne, Marie-Helene Radenac, John Dunne, Keith Moore, Paul Bissett, Mike Behrenfeld, Ajit Subramaniam, Raleigh Hood, Yvette Spitz, Temel Oğuz, Chet Grosch, and Jerry Wiggert were generous in sharing their expertise and providing model details.

I am grateful to many people here at CCPO without whom this endeavour would have been much harder to accomplish. Julie Morgan handled all administrative matters very professionally and at the same time provided lots of much needed moral support. Joe Ruettgers helped overcome all computer related, as well as many other problems, no matter what time of day or night. Special thanks go out to all my fellow graduate students who have made this experience much more pleasant. I am especially indebted to my friend Sinan Hüsrevoğlu, for his friendship and continuous

support. Without him this work would have been much less fulfilling. Special thanks to my friend Gamze Karayaz for being the "PhD cop" and a great study companion.

I am very grateful to my parents for their unconditional love and support over the past years. They have always believed in me and have gone out of their way to help me realize my dream. And finally to Dr. Bettina Fach: I cannot adequately express my heartfelt gratitude for her unwavering support and encouragement through this experience.

This work would not have been possible without the hard work of the many scientists involved in the collection of the JGOFS EqPac data sets used in this study. I would also like to thank the TAO Project Office, Dr. Michael McPhaden, Director, for the use of the extensive data available from their mooring array, as well as the SeaWiFS Project and the Distributed Active Archive Center at the Goddard Space Flight Center, for the production and distribution of these data. I wish to thank the programme leaders, Drs. Robert Le Borgne and Marie-Helene Radenac for the FLUPAC data, Drs. Martine Rodier for nutrients, Jacques Neveux for photosynthetic pigments, Dr. Aubert Le Bouteiller for ^{14}C uptake measurements. Thanks to the program leader Dr. James Murray for Zonal Flux data, Dr. Martine Rodier for nutrients, Dr. Aubert Le Bouteiller for pigments and primary productivity. Thanks to Dr. Paul Ginoux for his atmospheric dust model output.

This research was generously supported by the National Aeronautics and Space Administration contract NCC-5-258. The computer facilities and resources were provided by the Commonwealth Center for Coastal Physical Oceanography at Old Dominion University.

TABLE OF CONTENTS

LIST OF TABLES

LIST OF FIGURES

CHAPTER I

INTRODUCTION

The equatorial Pacific Ocean is the largest contiguous region of oceanic upwelling and as such provides waters rich in nutrients and inorganic carbon to a large part of the ocean above 100 m. The high macronutrient concentration (e.g., typical nitrate concentrations of $\sim$5 μM, Chavez et al. (1996)) enhances photosynthesis, new production of organic carbon, and therefore sedimentation of particulate carbon. The high carbon content of the upwelled waters maintains a high partial pressure of carbon dioxide (CO_2) at the sea surface, and the large area of the equatorial Pacific makes this region the largest natural oceanic source of CO_2, annually supplying 0.7 to 1.5 Pg (10^{15} g) of carbon as CO_2 to the atmosphere (Chavez et al., 1999). The magnitude of this carbon flux is regulated by the interactions of physical and biological processes. The flux of CO_2 from the ocean into the atmosphere, and also from the atmosphere into surface waters and into the deep ocean as a result of biological processes, contribute to the processes affecting climate variations. Thus, the interactions between physical and biological processes and the relative effects of these on the lower trophic levels of the equatorial Pacific Ocean are integral to understanding and quantifying the ocean-atmosphere carbon flux.

In spite of upwelling which provides nutrients to the upper water column, the equatorial Pacific is characterized by modest chlorophyll concentrations and low rates of primary production of about 0.2 to 0.3 μg l^{-1} and 75 mmol C m^{-2} d^{-1}, respectively (Chavez et al., 1999). This high-nutrient, low-chlorophyll (HNLC) environment has been attributed to low iron concentration (Martin et al., 1994; Coale et al., 1996a,b; Barber et al., 1996) and high zooplankton grazing rates (Walsh, 1976; Cullen et al., 1992). The deficiency in iron keeps phytoplankton growth rates below their physical potentials (Landry et al., 1997) and affects the composition of the phytoplankton community by selecting for smaller cells (Morel et al., 1991; Sunda and Huntsman, 1995). The grazer community, particularly microzooplankton, remove most of the

This dissertation follows the style of *Deep-Sea Research I.*

daily production of phytoplankton biomass (Landry et al., 1997), thereby contributing to low chlorophyll conditions. The low iron concentrations contribute to maintenance of high nitrate conditions because in iron-stressed regions phytoplankton preferentially remove ammonium over nitrate (Wheeler and Kokkinakis, 1990; Price et al., 1994; Armstrong, 1999).

The high carbon fluxes to the atmosphere and to the deep ocean, and the HNLC conditions of the equatorial Pacific are found in other tropical upwelling regions, the subarctic Pacific, and the Antarctic. The property that is unique to the equatorial Pacific Ocean is that it is the principal site of the El Niño-Southern Oscillation (ENSO), which is the primary cause of interannual climate variability in the tropical oceans (Philander, 1990). The equatorial Pacific marine ecosystem is also affected by Kelvin waves (Kessler et al., 1995; Chavez et al., 1998), advection of oligotrophic waters (Chavez et al., 1998; Le Borgne et al., 2002), tropical instability waves (TIWs, Qiao and Weisberg, 1995; Yu et al., 1995), equatorially trapped internal gravity waves (IGWs, Wunsch and Gill, 1976; Friedrichs and Hofmann, 2001), and variations in the strength and depth of the Equatorial Undercurrent (EUC, Barber et al., 1996). The available studies consider the response of the equatorial Pacific phytoplankton communities to these physical forcings, which occur at a range of space and time scales (Bidigare and Ondrusek, 1996; Chavez et al., 1998; Friedrichs and Hofmann, 2001) and are variable so that individual events can significantly alter local primary production, species composition, and carbon export. These studies provide the basis for the **first research objective of this study which is directed at identifying and quantifying the response of equatorial Pacific phytoplankton communities to different physical forcings and the implication of these responses for carbon production and export.**

Pigment and size fractional studies of equatorial Pacific phytoplankton communities indicate that *Prochlorococcus*, *Synechococcus*, autotrophic eukaryotes, and large (~20 μm cell size) diatoms represent the dominant autotrophic biomass (Lindley et al., 1995; Bidigare and Ondrusek, 1996; Chavez et al., 1996; Coale et al., 1996b; Landry et al., 1996; Latasa et al., 1997; Higgins and Mackey, 2000; Landry

et al., 2000a). The carbon biomass, chlorophyll *a* and primary production of each of these phytoplankton algal groups can be regulated by biological interactions as well as by physical forcing. For example, production by *Prochlorococcus* spp. is sensitive to the light field (Partensky et al., 1999; Rippka et al., 2000; Moore et al., 2002b; Rocap et al., 2002) and ambient nutrient concentrations (Moore et al., 2002b), and autotrophic eukaryotes and large diatoms can avoid grazing by microzooplankton relative to the smaller phytoplankton species (Landry et al., 1995; Verity et al., 1996; Dam et al., 1995; Roman and Gauzens, 1997). Thus, **the second research objective for this study is directed at understanding the role of biological processes and interactions in regulating carbon biomass, chlorophyll *a* concentration, and primary production of the dominant algal groups composing equatorial Pacific phytoplankton communities.**

Micronutrient (e.g., iron) limitation is now recognized as an important control on the biomass and production of equatorial Pacific phytoplankton communities (Morel et al., 1991; Martin et al., 1994; Sunda and Huntsman, 1995; Coale et al., 1996a,b; Barber et al., 1996). Also iron affects the composition of the phytoplankton community by selecting for smaller dominant forms (Morel et al., 1991; Sunda and Huntsman, 1995). The abundance and distribution of dissolved iron, the ambient and cellular iron to nitrogen and iron to carbon ratios, the remineralization and scavenging of iron, and the magnitude, distribution and solubility of the aeolian iron flux are recognized as important contributers to the regulation of phytoplankton community by iron. These observations underline **the third research objective which is focused on understanding the role of iron limitation in regulating the production and composition of the equatorial Pacific phytoplankton community.**

The three primary research objectives of this study are addressed using a one-dimensional, multi-component marine ecosystem model that is designed to include the physical and biological dynamics that control the biomass and production of the lower trophic levels in the equatorial Pacific Ocean. The primary implementation of the ecosystem model is for a site at 140°W on the equator, which is referred to as

the Cold Tongue (Murray et al., 1992). The Cold Tongue is represented as an area where upwelling is persistent, which is reflected in generally high phytoplankton production. Additional simulations consider the applicability of the ecosystem model to other regions of the equatorial Pacific, such as the Warm Pool in the western Pacific at 165°E at the equator. This second region is characterized by warm (annual mean of 28°C to 30°C) surface water temperatures and a shallow mixed layer (30-40 m) which is separated from the thermocline (deeper than 65 m) by a high-salinity barrier layer (Lukas and Lindstorm, 1991). Comparisons of the simulations from the two regions provide insight into variability in phytoplankton biomass, community composition, primary production, and export production for regions of the Pacific that have different environmental structure, physical forcing, and biological interactions. Additional simulations provide insight into the effect of El Niño/La Niña events, which are part of the ENSO cycle, on biological production in the two regions.

The next chapter presents background information on the physical and biological controls on the equatorial Pacific ecosystem that is directly related to the results ofthis study and gives a description of issues related to the use of ecosystem models that include one or two size fractions of phytoplankton. Chapter 3 gives a summary of the data used in this study. Chapter 4 describes the lower trophic level model used in this study and the data sets input to the model. The results of the simulations done for the Cold Tongue and Warm Pool are given in Chapter 5. This chapter also presents results of sensitivity studies done with the lower trophic level model that are designed to highlight important physical and biological processes that affect carbon production and export. Chapter 6 provides a discussion of the results that places them within the context of other studies and current understanding of the factors controlling lower trophic level production in the equatorial Pacific. The final chapter gives the conclusions derived from this study.

CHAPTER II

BACKGROUND

II.1 THE RESPONSE OF THE CENTRAL EQUATORIAL PACIFIC ECOSYSTEM TO PHYSICAL FORCING EFFECTS

In the central equatorial Pacific Ocean meridional velocities can show variability in amplitude and direction that change from positive (north) to negative (south) with a period of 20 d. These features are the TIWs. Particle motions of these waves are described by eccentric ellipses oriented toward the north (Qiao and Weisberg, 1995). Zonal wavelengths of these waves range from 800 to 2000 km, and westward propagation occurs with phase velocities of roughly 0.6 m s^{-1} (Halpern et al., 1988; Qiao and Weisberg, 1995; Yu et al., 1995).

The effect of the variability in meridional velocities is in association with the sea surface temperature (SST) structure and satellite chlorophyll observations in the central equatorial Pacific. Satellite chlorophyll observations exhibit north-south undulations at scales similar to the SSTs, however, although the cool tongue of SST covers a broad area, the chlorophyll rich region is just a narrow band centered at the equator, which is advected north and south of the equator. North of the equator, the undulations are associated with anticyclonic eddies (Flament et al., 1996).

These anticyclonic vortices not only play an important role in the meridional transport of heat, salt and momentum, but are also associated with regions of intense horizontal convergence along the equator, where high concentrations of primary and secondary production occurs (Flament et al., 1996). These instabilities in the equatorial Pacific Ocean can affect dynamically the spatial distribution of phytoplankton (Chavez et al., 1999; Strutton et al., 2001) and in addition to dynamical controls, biological consequences of these physical processes contribute significantly to the regulation of phytoplankton growth and distribution (Foley et al., 1997; Strutton et al., 2001). For example, high chlorophyll concentrations are likely responses to enhanced fluxes of nutrients, such as iron, to the euphotic zone in the upwelling

centers associated with TIWs (Friedrichs and Hofmann, 2001; Strutton et al., 2001).

In the central equatorial Pacific, high frequency physical variability also exists in the form of IGWs. Internal gravity waves are indicated by temperature oscillations of 2-4°C at 100 m, with periods of 6-8 d (Wunsch and Gill, 1976). These temperature oscillations result from high-frequency variability in the vertical velocity field. Friedrichs and Hofmann (2001) suggested that the effect of IGWs may dominate the variability in the primary production and biomass fields. The variability in the vertical velocity can advect nutrient rich waters into the euphotic zone resulting in *in situ* growth in the upper water column (Friedrichs and Hofmann, 2001)

The equatorial Pacific system is also affected by perturbations at lower frequencies. The physical and biological dynamics of the region are perturbed on average every 3-4 years by El Niño (Quinn et al., 1987). During El Niño the trade winds weaken and may reverse, thus removing the driving force for upwelling. This weakening of the trades is usually first observed as westerly wind bursts in the western equatorial Pacific, giving rise to equatorially trapped, downwelling Kelvin waves which propagate from west to east at speeds in excess of 200 km d^{-1} (Strutton and Chavez, 2000). The Kelvin waves initiate the relaxation of the zonal sea level and thermocline gradients, followed by advection of the western equatorial Warm Pool into the central Pacific. The warmer waters (> 28°C, Picaut et al. (1996)) are low in nutrients (Mackey et al., 1995). Their advection over the central equatorial Pacific, combined with the weakening of the upwelling leads to reduced phytoplankton productivity in the region (Chavez et al., 1999; Strutton and Chavez, 2000).

The onset of the 1997-1998 El Niño was indicated by two westerly wind bursts centered at 150°E. These wind bursts each gave rise to a downwelling Kelvin wave which propagated from west to east from December 1996 to January 1997 and from March to April 1998 (Chavez et al., 1999; Strutton and Chavez, 2000). During these periods, surface nitrate was depleted almost to zero across the equatorial Pacific. West of 140°W this nitrate depletion extended over the entire euphotic zone and Strutton and Chavez (2000) argued that it was correlated with iron depletion.

Other than the biological effects, the dynamical effects of the 1997-1998 ENSO

also affected the spatial distribution of phytoplankton. Murtugudde et al. (1999) and Picaut et al. (2002) showed that the northerly wind anomalies dominated the central Pacific from November 1997 through April 1998. The associated shift in the Ekman divergence shifted the equatorial upwelling Kelvin wave to the north by almost 2° of latitude (Murtugudde et al., 1999). After the 1997 El Niño, during February 1998 a phytoplankton bloom appeared several degrees north of the equator with chlorophyll concentrations of $\sim$0.3 mg m^{-3}. This was a signature of the Kelvin wave that ended the El Niño. Between March and June 1998 the cold waters associated with the upwelling Kelvin wave slowly propagated towards the equator (Picaut et al., 2002). The bloom also moved towards the equator with chlorophyll concentrations reaching $\sim$1 mg m^{-3} in June 1998 (Murtugudde et al., 1999).

II.2 BIOLOGICAL INTERACTIONS

In the equatorial Pacific measurements of phytoplankton community composition show that *Prochlorococcus*, *Synechococcus*, autotrophic eukaryotes, and large ($\sim$20 μm cell size) diatoms represent the dominant autotrophic biomass (Lindley et al., 1995; Bidigare and Ondrusek, 1996; Coale et al., 1996b; Chavez et al., 1996; Landry et al., 1996; Latasa et al., 1997; Higgins and Mackey, 2000; Landry et al., 2000a). The carbon biomass, chlorophyll *a* and primary production of each of these phytoplankton algal groups can be regulated by biological interactions as well as by physical forcing.

The central equatorial Pacific is an HNLC region, which is characterized by consistently high near-surface concentrations of macronutrients, low phytoplankton biomass, and the dominance of small species of primary and secondary producers. The growing consensus is that the properties of HNLC regions are explained by the complementary interactions of micronutrient limitation and grazing (Chavez et al., 1991; Frost, 1991; Price et al., 1994). However, little is known about the dynamics of different components of the phytoplankton and zooplankton populations and specifically how they are affected by micronutrients, grazers, and natural environmental variability. Experimental results (Lindley et al., 1995; Bidigare and Ondrusek, 1996)

and recent mesoscale iron enrichment experiments (Martin et al., 1994; Coale et al., 1996b; Landry et al., 2000a) provide some guidance as to some of these interactions. During the two open-ocean *in situ* iron-fertilization experiments (IronEx I and II, Martin et al., 1994; Coale et al., 1996b; Landry et al., 2000a) that were done at about 4°S, 105°W, limited taxa specific measurements that distinguish between different pigment types were made. Size fractional studies during iron-fertilization experiments show that the chlorophyll bloom in response to iron fertilization was due to initially rare diatoms, with the increase in phytoplankton biomass attributed almost completely to cells > 5 μm (Coale et al., 1996b). There is also evidence that the smaller, initially dominant phytoplankton were stimulated by the iron addition (Coale et al., 1996b), and the taxon-specific pigment data indicated that all groups were iron limited at the start of the iron-fertilization experiments (Cavender-Bares et al., 1999). The relative constancy of smaller algal forms under iron fertilization is attributed to the efficient cropping by micrograzers (Walsh, 1976; Cullen et al., 1992).

Advances in the understanding of grazing and iron controls on phytoplankton in HNLC regions have been made, but much about these regions remain to be studied. For example different phytoplankton species do not have identical iron requirements (Sunda and Huntsman, 1995, 1997), larger species may be held below their physiological growth potential to a greater degree than others. Further, high rates of phytoplankton growth and steady-state microbial communities (Cullen, 1991; Cullen et al., 1992; Frost and Franzen, 1992) in the HNLC region of equatorial Pacific imply strong links to rapid grazer removal of phytoplankton and efficient nutrient recycling.

Grazers can contribute directly to the maintenance of phytoplankton steady state by cropping daily production. Microzooplankton grazing generally balances the daily production by prymnesiophytes, and consumes much of the daily production of picoplankton (Verity et al., 1996). However, microzooplankton consumes only about half the production by diatoms, implying that other loss processes (e.g., macroozooplankton grazing, sinking) regulate diatom abundance in these waters (Verity et al., 1996). For example, during the two U.S. Joint Global Ocean Flux Study (JGOFS)

cruises (cruise details are explained in section 3.3), herbivory by microzooplankton, averaged 133% (15 m)-123% (60 m) and 70% (15 m)-105% (60 m) of phytoplankton growth, respectively (Verity et al., 1996). Thus, this suggests that the grazing of phytoplankton by microzooplankton represents a major pathway of organic carbon transformation at the equatorial Pacific during both El Niño and non-El Niño conditions.

In addition to the direct impact of grazers on phytoplankton biomass, they return remineralised elements to phytoplankton, including iron (Hutchins et al., 1993), which is essential for a high growth rate in the equatorial Pacific. The combination of direct cropping and remineralization processes provides a potentially powerful feedback mechanism by which grazers influence both the biomass and rate of phytoplankton production. Moreover, ammonium suppresses nitrate uptake (Wheeler and Kokkinakis, 1990) and *Prochlorococcus* spp. cannot use nitrate (Moore et al., 2002b). Thus remineralization of nitrogen as ammonium by grazers can be important in maintaining high levels of nitrate in the HNLC region of the equatorial Pacific.

Inter-species competition for nutrients and light can affect the transfer routes of carbon to higher trophic levels and eventually to the deep ocean. Because smaller species have an intrinsic competitive advantage for nutrient uptake over larger species, they can grow more efficiently compared to the larger algal forms under nutrient deplete conditions (Price et al., 1994; Sunda and Huntsman, 1995). Also algal forms which can better adapt to low-light conditions can take advantage of the nutrient replete deeper waters (Partensky et al., 1999; Rippka et al., 2000; Moore et al., 2002b; Rocap et al., 2002). Although small algal forms grow better under HNLC conditions, the high grazing pressure on them controls their biomass. Autotrophic eukaryotes and large diatoms are less efficiently grazed by microzooplankton (Dam et al., 1995; Landry et al., 1995; Verity et al., 1996; Roman and Gauzens, 1997). Thus, the relative contribution of small algal forms to carbon production and export can be higher than their relative biomass.

II.3 A COMPARISON OF THE COLD TONGUE AND THE WARM POOL CHARACTERISTICS

The equatorial Pacific is subject to physical forcings that differ markedly from west to east. The Warm Pool in the west is characterized by some of the warmest SSTs (annual mean of 28°C to 30°C) in the global ocean and has a shallow mixed layer (30-40 m) separated from the thermocline (deeper than 65 m) by a high-salinity barrier layer (Lukas and Lindstorm, 1991). Mackey et al. (1995) and Radenac and Rodier (1996) both emphasize that the suppression of nutrient fluxes by the salinity barrier layer is the primary factor controlling surface phytoplankton concentrations in the Warm Pool.

In contrast, the Cold Tongue region east of the Warm Pool is subject to the divergence of the South Equatorial Current (SEC). Such a divergence generates upwelling of the waters from the EUC, which brings waters with higher salinity, dissolved inorganic carbon and nutrient concentrations to the surface (Le Borgne et al., 2002). Despite the differences in physical and chemical forcings between the Warm Pool and the Cold Tongue, the depth-integrated chlorophyll concentrations in the Cold Tongue (25-36 mg m^{-2}) region are only slightly higher than those observed in the Warm Pool (20-30 mg m^{-2}, Mackey et al. (1997)) under normal or El Niño conditions.

The manifestation of the ENSO is also different in two regions. Under non-El Niño conditions, the trade winds pile up water in the western equatorial Pacific, resulting in an increase in sea level and deepening of the thermocline (Wyrtki, 1975, 1985). When the trade winds weaken, these perturbations of the thermocline and the sea surface can propagate eastward as downwelling Kelvin waves. Kelvin waves carry energy and heat across the basin rapidly, resulting in a depression of the thermocline and a warming of the sea surface in the east, which in turn reduces atmospheric subsidence driven by oceanic upwelling and weakens the trade winds (Hansen, 1990; Philander, 1990). The equatorial Pacific then takes on a self-sustaining state characterized by warm surface temperatures, weak trade winds, a weak or reversed SEC, and a significantly reduced east-west slope of the sea surface, which results

in the attenuation and occasional disappearance of the EUC (Firing et al., 1983). The depth of the thermocline, the main reservoir of nutrients for phytoplankton, is deeper than usual in the east and shallower in the west. In the western equatorial Pacific the shoaling of the thermocline during El Niño that brings the nutrients into the euphotic zone, causes an increase in the chlorophyll concentration in the deep chlorophyll maxima layer (Blanchot et al., 1992; Radenac and Rodier, 1996).

II.4 ISSUES RELATED TO AVAILABLE ECOSYSTEM MODELS FOR THE EQUATORIAL PACIFIC REGION

The available ecosystem models developed for the equatorial Pacific Ocean (e.g., Chai et al., 1996; Loukos et al., 1997; Leonard et al., 1999; Friedrichs and Hofmann, 2001; Christian et al., 2002a) included either one or two size classes of phytoplankton. Chai et al. (1996), Loukos et al. (1997), Leonard et al. (1999) and Friedrichs and Hofmann (2001) are one-dimensional (depth-time) models developed for the central equatorial Pacific Ocean. Iron is not included in the Chai et al. (1996) and Loukos et al. (1997) models, however uniformly low values of the photosynthetic parameters are used as a proxy for iron limitation by Chai et al. (1996). This limits the Chai et al. (1996) model's ability to simulate spatial and temporal variability of plankton communities. Loukos et al. (1997) and Friedrichs and Hofmann (2001) included only a single phytoplankton and zooplankton compartment and Leonard et al. (1999) included two size classes (e.g., nanoplankton and netplankton) of phytoplankton and two size classes of zooplankton. The model described in Christian et al. (2002a) is the first basin-scale model developed for the equatorial Pacific region which includes simultaneous iron and nitrogen limitation. The ecosystem structure of this model is identical to the Leonard et al. (1999) model and it consists of nine components, two phytoplankton size classes, two zooplankton size classes, dissolved iron, nitrate, ammonium, and two detrital size fractions. In this model all biological model components (phytoplankton, zooplankton, detritus) except netphytoplankton (> 10 μm)

are assigned the same constant iron to carbon ratio. A variable chlorophyll to nitrogen ratio is formulated according to Geider et al. (1996) which neglects nutrient effects.

The models that include one box for phytoplankton and zooplankton (e.g., Loukos et al., 1997; Friedrichs and Hofmann, 2001) used the assumption that species composition of the phytoplankton and zooplankton is invariant. This precludes the ability to investigate species composition change in response to environmental and biological variables. With a single phytoplankton component it is also not possible to simulate the changes in primary production that arise from differential responses of the phytoplankton species to different environmental factors. The equatorial Pacific models that include two phytoplankton size classes and iron (e.g., Leonard et al., 1999; Christian et al., 2002a), assume that large phytoplankton growth rates are much more strongly limited by iron and experience reduced rates of grazing mortality relative to the smaller phytoplankton component. Netphytoplankton therefore escape grazing control under strong upwelling conditions and become dominant because the smaller forms remain under strong grazer control. However, in the equatorial Pacific the netplankton (e.g., diatoms) generally do not exceed 20% of the total biomass even under nutrient replete conditions (Chavez, 1989; Bidigare and Ondrusek, 1996). In addition, in these models export rates increase excessively when biomass increases. Results from the iron enrichment experiments suggest that even when netphytoplankton growth rates increase due to iron fertilization, the food web is tightly coupled with little export (Landry et al., 2000a). Thus, iron enrichment experiments suggest that a tightly coupled phytoplankton-grazer system exist even under nutrient replete conditions and simple food web models exaggerate the extent of carbon removal by netphytoplankton.

In the available models (e.g., Chai et al., 1996; Loukos et al., 1997; Leonard et al., 1999; Friedrichs and Hofmann, 2001; Christian et al., 2002a) cellular iron to nitrogen ratios are assumed to be constant. However, field and culture studies show that iron to carbon and nitrogen to carbon ratios in algal cells can vary independently, depending on environmental conditions (Laws and Bannister, 1980; Kana et al., 1992;

Moore et al., 1995; Sunda and Huntsman, 1995; Kudo and Harrison, 1997). Furthermore, these ratios show very different characteristics between different species (Laws and Bannister, 1980; Kana et al., 1992; Moore et al., 1995; Sunda and Huntsman, 1995; Kudo and Harrison, 1997; Sunda and Huntsman, 1997) and experimental studies suggest that iron to nitrogen ratios for small phytoplankton (especially for cyanobacteria) are greater than those for netplankton. However, models that use constant cellular nutrient ratios require iron to nitrogen ratios for netplankton that are greater than those for small phytoplankton (e.g., Christian et al., 2002a). In the constant ratio models nitrate tends to accumulate in the surface waters because of retention of iron concentrations in the cells. To prevent accumulation of nitrate in the surface waters of the equatorial Pacific in the simulations significant inputs of iron are needed (Christian et al., 2002a). It is possible that a more realistic food web structure would reduce the sensitivity of these models to the availability of iron.

Another important issue related to the early models developed for the equatorial Pacific (e.g., Leonard et al., 1999; Friedrichs and Hofmann, 2001), is that iron is included in a similar manner as nutrients (e.g., nitrate). However, recent studies show that although iron has a nutrient-type profile (Martin et al., 1989; Bruland et al., 1994; Johnson et al., 1997), sometimes enrichment characteristics are observed in the euphotic zone that are characteristics of scavenged-type elements (Bruland et al., 1994). More recently it has been demonstrated that iron is rapidly recycled in pelagic microbial communities (DiTullio et al., 1993; Hutchins et al., 1993; Barbeau et al., 1996), and this recycling may be a critical source of iron for phytoplankton in iron-limited regions.

CHAPTER III

DATA SOURCES AND PROCEDURES

III.1 VERTICAL VELOCITY, DIFFUSION, AND MIXING

The one-dimensional lower trophic level ecosystem model, described in Chapter 4, includes explicit effects of vertical advection. One approach for specifying a time-varying vertical velocity field is to estimate it using a numerical circulation model, such as the one developed for the equatorial Pacific by Murtugudde et al. (1996). However, simulated fields do not contain much of the high-frequency variability, such as TIWs and IGWs, that are of interest for this study. Therefore, the approach taken here is to use direct observations of the horizontal velocities (u and v) and temperature obtained from the Tropical Ocean-Global Atmosphere (TOGA) program and the Tropical Atmosphere-Ocean (TAO) Array, which were obtained from moorings/buoys at fixed locations in the equatorial Pacific Ocean. Details of the TAO Array are given in McPhaden et al. (1998) and data from the mooring are available via the TAO web-site (http://www.pmel.noaa.gov/toga-tao).

The TAO mooring array provides time series of current meter-measured horizontal velocity and temperature at locations along the equator at 155°W, 140°W, and 125°W, and along 140°W at 2°N, and 2°S. The vertical distribution of the velocity and temperature measurements (Table 1) was sufficient to resolve variations in the upper water column environmental structure due to high-frequency events, such as TIWs and IGWs, and low frequency events such as ENSO.

Throughout 1991-1999, the data availability was 90% or more for horizontal velocity and temperature at 0°N, 140°W, respectively and was 90% or more for horizontal velocity and 80% or more for temperature at 0°N, 165°E (Table 1). The periods of missing data were filled in by averaging the equivalent measurements from TAO moorings at 2°N and 2°S at 140°W and 165°E. For times when no measurements were available from any of the sites, the data were linearly interpolated in time using the available points on either side of the data gaps. The resultant daily time series

Table 1
Tropical Atmosphere-Ocean (TAO) mooring data at 140°W and 165°E at the equator for 1991-1999 time period (McPhaden et al., 1998)

Data Type	Location	Sample depth (m)	Availability (%)	Missing dates (month/year)
Horizontal velocity	0°N, 140°W	3, 25, 45, 80, 120	>90%	—
Temperature	0°N, 140°W	1, 3, 10, 25, 35, 45, 60, 80, 100, 120	>90%	—
Shortwave radiation	0°N, 140°W	3 m above sea surface	>85%	08/1991-12/1991 01/1994-03/1994 03/1994-06/1995
Horizontal velocity	0°N, 165°E	3, 25, 45, 80, 120	>85%	02/1994-01/1995
Temperature	0°N, 165°E	1, 3, 10, 25, 35, 45, 60, 80, 100, 120	>80%	01/1992-03/1992 02/1994-01/1995
Shortwave radiation	0°N, 165°E	3 m above sea surface	>75%	08/1991-07/1992 12/1993-02/1994 06/1998-02/1999

Type, location, sampling depth, percent (%) availability, and major missing periods of the data are listed. Continuous measurements are indicated by —.

was then linearly interpolated to 1-hour intervals to be consistent with the time step used for the lower trophic level ecosystem model (see section 4.10).

The temperature and horizontal velocity time series from the TAO Array for 1991-1999 were used with the procedure given in Friedrichs and Hofmann (2001) to estimate vertical velocities. This approach is based on scaling vertical velocity relative to local upward movement of an isotherm and advection along a stationary, sloping isotherm. Daily estimates of local upward movement of the isotherms are obtained by evaluating the change in the depths of the isotherms measured by the TAO temperature sensors. The advection along a stationary, sloping isotherm is computed by multiplying zonal velocity data, measured by the TAO current meters, by estimates of zonal isotherm slopes.

Mixed layer depth is set to the depth where water temperature is 1°C lower than the SST. The comparisons between the mixed layer depths observed during the U.S.

JGOFS cruises and the mixed layer depths estimated using 1°C difference from the observed SSTs gives very satisfactory results at 0°N, 140°W (not shown). These comparisons provide the justification for not explicitly using a mixed layer model (e.g., Price et al., 1986).

The mixed layer depth at 0°N, 140°W is estimated using the hourly temperature measurements to incorporate the diurnal variability in the mixed layer depth, whereas daily temperature values are used at 0°N, 165°E. The vertical diffusion (K_z) effects are simulated with a theoretical model (Pacanowski and Philander, 1981) using the TAO mooring (u, v, T) observations. All of the components (e.g., state variables) of the lower trophic level model (Chapter 4) are homogeneously distributed in the mixed layer at each time step.

III.2 SHORTWAVE RADIATION

The TAO mooring at 0°N, 140°W and 0°N, 165°E provides time series of integrated incoming short wave radiation (Table 1). For 1991-1999, this record was about 85% complete at 0°N, 140°W and was about 75% complete at 0°N, 165°E. The missing portions of the shortwave radiation time series were estimated from either adjacent moorings or linear interpolation between available data points, similar to what was done for the horizontal velocities. When there were no data available from all the three sites, the effect of cloud cover is neglected. The resultant shortwave radiation time series was used with a clear sky radiation model to estimate the spectrally-resolved underwater light field, as described in section 4.2.1.

III.3 COLD TONGUE *IN SITU* OBSERVATIONS

The data sets used for calibration and verification (section 5.1.7) of the simulations obtained from the lower trophic level ecosystem model for the Cold Tongue were obtained from the U.S. JGOFS Equatorial Pacific process study (EqPac) (Murray et al., 1994, 1995). The primary data sets are from two process-oriented survey cruises that took place in February (S1) and August (S2) 1992 and two 20-day time

series cruises that took place in March (TS1) and October (TS2) 1992. The time series cruises occupied a site at 0°N, 140°W and the survey cruises covered the area around this site (Murray et al., 1992, 1995). Data collected on these cruises followed U.S. JGOFS data protocol (http://usjgofs.whoi.edu/protocols.html) and were obtained for this study via the U.S. JGOFS Data Management System, which is available at http://www1.whoi.edu/jgofs.html.

The largest suite of data available from the JGOFS EqPac cruises consists of measurements of algal biomass from direct cell counts (Table 2) and algal pigment concentration obtained from high-pressure liquid chromatography (Table 2). These data sets provide the basis for the algal groups included in the lower trophic level model as well as providing a means for verifying the realism of the simulations. The phytoplankton cell counts were converted to microplankton carbon biomass using a factor of 53, 250, and 2,100 fg C per cell for *Prochlorococcus* spp., *Synechecoccus*, and autotrophic eukaryotes (Campbell et al., 1994; Binder et al., 1996; Landry et al., 1996), respectively.

Primary production measurements for natural *in situ* phytoplankton assemblages (Table 2) were obtained during the EqPac cruises using standard radioactive carbon (^{14}C) uptake approaches (Barber et al., 1996). These measurements provide verification for the primary production rates obtained from the lower trophic level ecosystem model.

The EqPac data sets provide vertical distributions of macronutrients, such as nitrate and silicate (Table 2). In addition, measurements of dissolved trace metals, such as iron are available (Table 2). These data sets provide verification of the simulated macronutrient and iron distributions. The availability of the iron measurements makes the inclusion of iron dynamics in the model feasible.

Limited observations for trophic levels higher than phytoplankton are available as part of the EqPac data sets (Table 2). Micro- and mesozooplankton data consist mainly of distribution and biomass estimates. However, these are adequate for the level of detail included for this trophic level in the ecosystem model.

An important diagnostic from the ecosystem model is the flux of carbon from

Table 2
The data available for the Cold Tongue from the U.S. Joint Global Ocean Flux Study (JGOFS) Equatorial Pacific process study (EqPac) (Murray et al., 1994, 1995)

Data type	Sample depth	Cruise	Reference
Pico- and nano-phytoplankton counts	10-m intervals from the surface to 120 m	S1, S2, TS1, TS2	1
Microphytoplankton counts (>15 μm)	10-m intervals from the surface to 120 m	S1, S2, TS1, TS2	2
Primary production	1, 15, 25, 40, 50, 60, 90, 120	S1, S2, TS1, TS2	3
Pigment concentrations	1, 15, 30, 60, 75, 90, 100, 120	S1, S2, TS1, TS2	4
Nutrient concentration (NO_3^-, NH_4^+, $Si(OH)_4$)	20, 40, 60, 80, 100, 125	S1, S2, TS1, TS2	5
Dissolved trace metals (iron)	20, 40, 60, 80, 100, 125	TS1, TS2	6
Microzooplankton carbon biomass	1, 15, 30, 45, 60, 90, 120	S1, S2, TS1, TS2	7
Mesozooplankton carbon biomass	5, 15, 30, 50, 70, 90, 120	S1, S2, TS1, TS2	8
Carbon flux	50, 120	S1, S2	9

The primary data sets are from two process-oriented survey cruises that took place in February (S1) and August (S2) 1992 and two 20-day time series cruises that took place in March (TS1) and October (TS2) 1992. The time series cruises occupied a site at 0°N, 140°W and the survey cruises covered the area around this site (Murray et al., 1992, 1995). Type and sampling depth of the data and the cruises during which sampling was made are listed. The reference citations are as follows: 1. Landry et al. (1996); 2. Kaczmarska and Fryxell (1995); 3. Barber et al. (1996); 4. Bidigare and Ondrusek (1996); 5. Archer et al. (1996); 6. Martin et al. (1994); 7. Roman et al. (1995); 8. Zhang et al. (1995); 9. Dunne et al. (2000).

the surface ocean. Limited measurements that can be used to constrain and verify the simulated carbon flux estimates were made during the two JGOFS EqPac survey cruises (Table 2).

Data collected during the 1992 JGOFS EqPac cruises are used for the model-data comparisons at 0°N, 140°W (section 5.1.7). The samples that were collected at the nominal depths given in Table 2 are linearly interpolated to 1-m depth intervals for comparison with the corresponding simulated distributions.

III.4 WARM POOL *IN SITU* OBSERVATIONS

Observations that can be used to describe the distributions and rates of the lower trophic levels in the Warm Pool are considerably limited relative to those available for the Cold Tongue (Table 3 versus Table 2). As part of the French JGOFS study of the equatorial Pacific, two stations were occupied at 0°N, 165°E as part of the FLUPAC and Zonal Flux cruises (Rodier and Le Borgne, 1997; Le Borgne et al., 2002), which occurred in September-October 1994 and April 1996, respectively. Observations made during the FLUPAC cruise provide measurements of macronutrients (nitrate, ammonium, silicate), chlorophyll *a* concentration and primary production (Table 3). The measurements from the Zonal Flux cruise consists of macronutrients and rates of primary production (Table 3).

Data collected during the FLUPAC and Zonal Flux cruises are used for the model-data comparisons in the Warm Pool region at 0°N, 165°E (section 5.8.4). The samples that were collected at the nominal depths given in Table 3 are linearly interpolated to 1-m depth intervals to for comparison with the corresponding simulated distributions.

III.5 SATELLITE-DERIVED OCEAN COLOR MEASUREMENTS

The Sea-viewing Wide Field of view Sensor (SeaWiFS) data used in this analysis are daily composites, averaged over a 2° longitude by 2° latitude rectangle centered on 0°N, 140°W and 0°N, 165°E. The time-series begins with the first reliable retrieval on September 1997 and continues through February 1999. Strong ENSO conditions

Table 3
Data collected during the French JGOFS FLUPAC and Zonal Flux cruises in the Warm Pool region

Data type	Sample depth (m)	Cruise
Nutrient concentration (NO_3^-, NH_4^+, $Si(OH)_4$)	3, 19, 39, 59, 80, 90, 99, 110, 120	FLUPAC
Primary production	5, 20, 40, 60, 80, 120	FLUPAC
Chlorophylly *a*	3, 19, 39, 59, 80, 90, 99, 110, 120	FLUPAC
Nutrient concentration (NO_3^-, NH_4^+, $Si(OH)_4$)	10-m intervals from the surface to 120	Zonal Flux
Primary production	5, 10, 20, 30, 40, 50, 60, 70, 80, 100, 120	Zonal Flux

The data are primarily from two stations at 0°N, 165°E. Nutrient and chlorophyll *a* samples are collected on 29 September 1994 and primary production on 3 October 1994 during the FLUPAC cruise. Nutrient and primary production samples are collected on 22 April 1996 during the Zonal Flux cruise (Rodier and Le Borgne, 1997; Le Borgne et al., 2002). Type and sampling depth of the data and the cruises during which sampling was made are listed.

were present throughout the 1997-1998 portion of the data. The SeaWiFS surface chlorophyll *a* data are used for the model-data comparison in the Cold Tongue (section 5.6.2) and the Warm Pool (section 5.8.2) regions.

CHAPTER IV

LOWER TROPHIC LEVEL MODEL

IV.1 MODEL STRUCTURE

In this study a one-dimensional, algal group-based phytoplankton model (e.g., Bissett et al., 1999a) is used to simulate phytoplankton dynamics in the upper 120 m of equatorial Pacific Ocean. The phytoplankton model is part of a lower trophic level ecosystem model that is coupled to a larger model structure (Fig. 1) that provides a simulated spectrally-dependent underwater light field that drives phytoplankton primary production via a bio-optical model.

The simulated surface light field, which provides input to the underwater light field is obtained from a clear sky spectral irradiance model (Gregg and Carder, 1990) that is corrected for cloud cover effects using the shortwave radiation measurements from the TOGA TAO observations described in section 3.2. The spectral attenuation of light energy with increased water depth is estimated as a function of the spectral absorption and backscattering of the water and particulate materials and used to force the full-spectral, algal group-based phytoplankton model. The pigment concentrations estimated for each algal group in the phytoplankton model are used to estimate particulate material concentration as a feedback into the bio-optical model (section 4.2.3).

The effects of the physical environment are included in the ecosystem model using the advective velocity and temperature time series from the TAO mooring as described in Chapter 3. Similarly the time varying mixed layer depth obtained from the TAO mooring measurements and the theoretically derived vertical diffusion coefficients are input into the ecosystem model.

Atmospheric (aeolian) deposition of iron provides another input for the lower trophic level ecosystem model (Fig. 1) because iron is believed to limit phytoplankton growth in equatorial Pacific waters. Aeolian iron deposition is estimated using the monthly atmospheric dust flux, which is obtained from Ginoux et al. (2001).

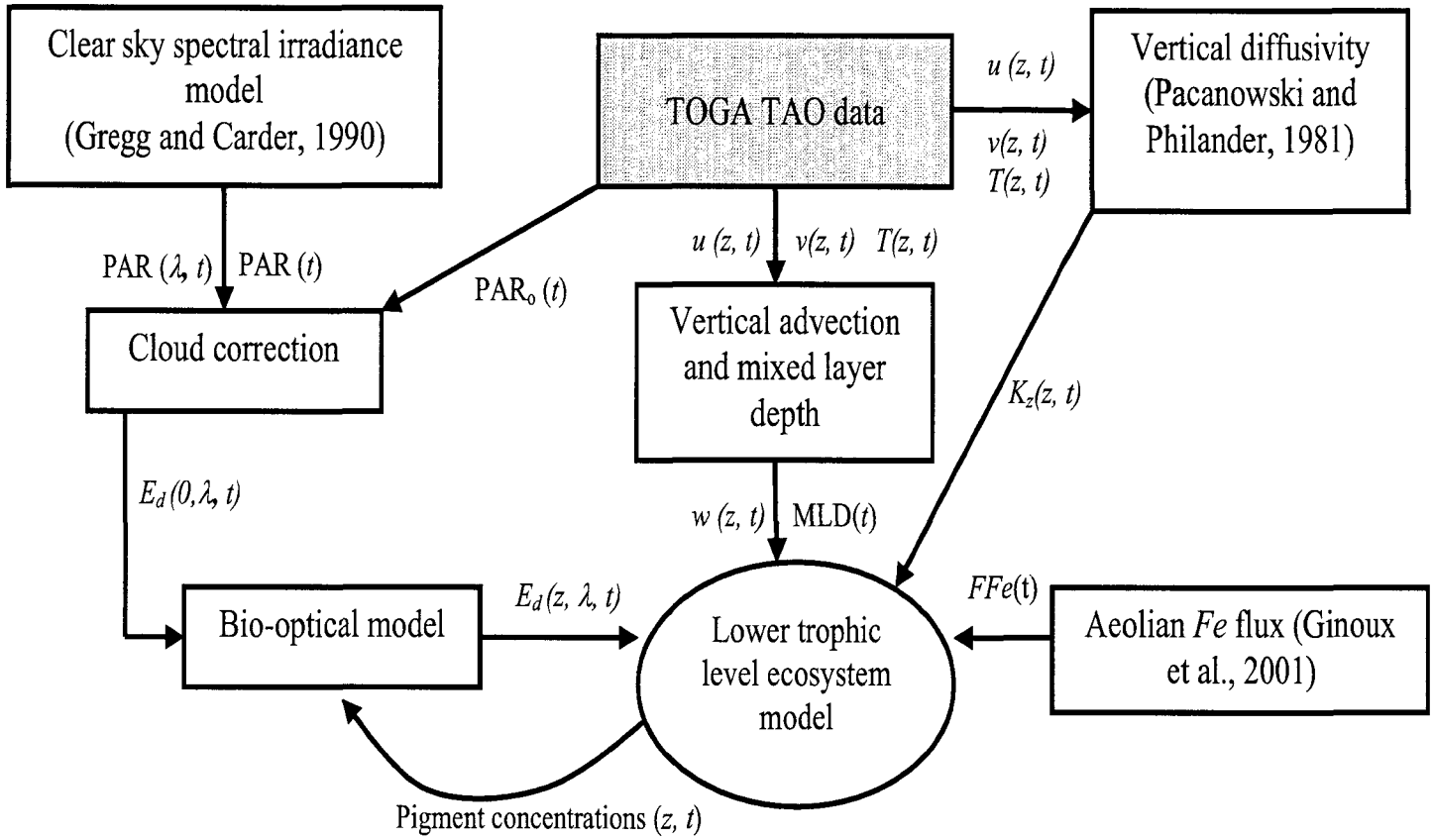

Fig. 1. Schematic of the principal components of the one-dimensional lower trophic level model developed for the equatorial Pacific Ocean. The arrows indicate the direction of the transfer between the model compartments and the model process that provides the transfer. Outputs of the shaded box are the data products, outputs of other boxes are simulated products. Relevant references for the various model compartments are given. Abbreviations used on the schematic are: PAR(λ, t)-spectral (λ) and time (t) dependent photosynthetically active radiation; PAR(t)-scalar photosynthetically active radiation; PAR$_o(t)$-observed, scalar photosynthetically active radiation, estimated from the observed shortwave radiation; E$_d(0, \lambda, t)$-spectrally and time dependent surface downwelling irradiance; $u(z,t)$, $v(z,t)$-horizontal velocity fields; $w(z,t)$-vertical velocity field; $T(z,t)$-temperature; MLD(t)-mixed layer depth; $K_z(z,t)$-vertical diffusivity coefficient; Fe-iron; FFe-aeolian iron flux.

Table 4
Listing of the size and accessory pigments for the five phytoplankton algal groups (AG) used in the phytoplankton model

Phytoplankton group	Size (μm)	Accessory pigments
$AG1$ LL *Prochlorococcus*	~0.7	chl *a*, chl *b*, PPC
$AG2$ HL *Prochlorococcus*	~0.7	chl *a*, chl *b*, PPC
$AG3$ *Synechococcus*	~1	chl *a*, PE, PPC
$AG4$ Autotrophic eukaryotes	~2.5	chl *a*, chl c, PSC, PPC
$AG5$ Large diatoms	~20	chl *a*, chl *c*, PSC, PPC

The pigments include chlorophyll *a* (chl *a*), chlorophyll *b* (chl *b*), chlorophyll *c* (chl *c*), photosynthetic carotenoids (PSC), photoprotective carotenoids (PPC), and phycoerythrin (PE). Other abbreviations used are: LL- low light-adapted and HL-high light-adapted.

The phytoplankton algal groups (AG) included as state variables in the ecosystem model (Fig. 2) represent the dominant autotrophic biomass in the equatorial Pacific as determined from pigment and size fractional studies (Chavez, 1989; Iriarte and Fryxell, 1995; Lindley et al., 1995; Bidigare and Ondrusek, 1996; Chavez et al., 1996; Coale et al., 1996b; Landry et al., 1996; Latasa et al., 1997; Higgins and Mackey, 2000; Landry et al., 2000a) and are sufficient to represent over 90% of the equatorial Pacific phytoplankton biomass. The accessory pigments included in the model are categorized as chlorophyll *a*, chlorophyll *b*, chlorophyll *c*, photosynthetic carotenoids, photoprotective carotenoids, and phycoerythrin. The five algal groups with their pigment suites are defined in Table 4.

The first two algal groups which represent *Prochlorococcus* spp. account for a significant fraction of carbon biomass (i.e. photosynthetic carbon standing stock, 27%-41%) in the equatorial Pacific waters (Vaulot et al., 1995; Binder et al., 1996; Landry et al., 1996). The division of *Prochlorococcus* into two groups represents species that grow in high-light surface waters and those that occur in the low-light, subsurface chlorophyll *a* maximum (Moore et al., 1995; Partensky et al., 1999; Rippka

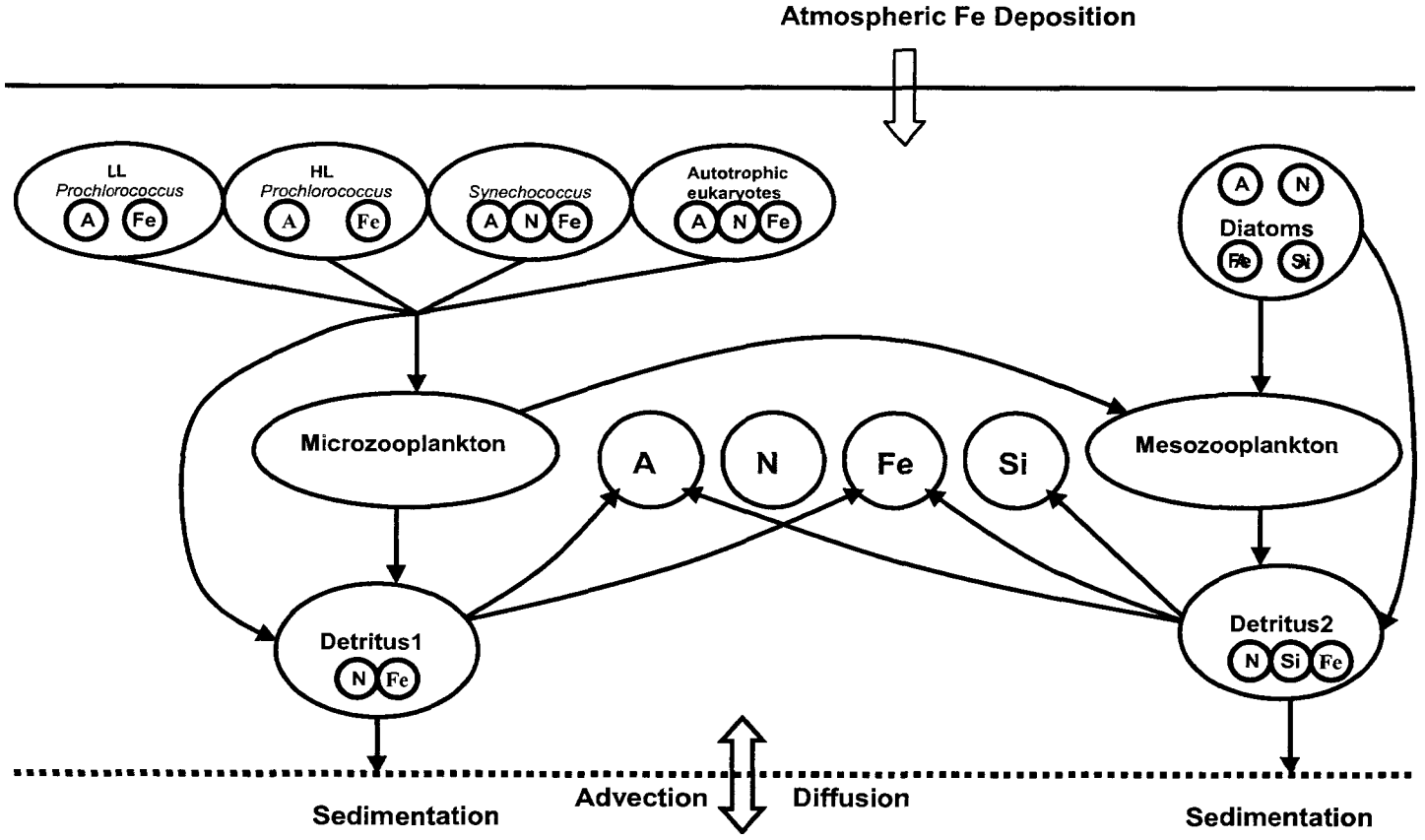

Fig. 2. Schematic of the lower trophic level ecosystem model components. Small circles inside the big circles indicate the internal nutrient compartments of each algal and detrital group. Interactions between nutrient, phytoplankton, zooplankton, and detritus compartments are shown by solid lines and arrows. Small arrows indicate the direction of transfer between model compartments; whereas, open arrows indicate the direction of transfer at the boundaries. Upper model boundary is indicated by a solid line, and it is only open to aeolian iron deposition. The bottom boundary is an open boundary which is indicated by a dotted line. Abbreviations used are: LL- low light-adapted; HL-high light-adapted; A-ammonium; N-nitrate; Fe-iron; Si-silicate.

et al., 2000; Moore et al., 2002b; Rocap et al., 2002). These two *Prochlorococcus* groups also show distinct nutrient utilization characteristics in that they are not able to use nitrate but they grow well on ammonium (Moore et al., 2002b). Differential nutrient use by *Prochlorococcus* groups is included in the model.

Algal group 3, *Synechecoccus*, is slightly larger than *Prochlorococcus* (Table 4) (Chisholm et al., 1988) and represents 7-8% of the carbon biomass in the equatorial Pacific waters (Binder et al., 1996). Autotrophic eukaryotes are represented by algal group 4 and have been referred to as picoeukaryotes (Campbell and Vaulot, 1993), nanoeukaryotes (Landry et al., 1995), and eukaryotic ultraplankton (Li et al., 1993). Autotrophic eukaryotes account for the largest fraction of the carbon biomass (52%-65%) in the equatorial Pacific (Landry et al., 1996; Binder et al., 1996). The fifth algal group includes large ($\sim$20 μm cell size) diatoms. Large diatoms are the only microphytoplankton group included in the ecosystem model because this group consistently comprises $>$ 80% of the total microphytoplankton autotrophic biomass (Iriarte and Fryxell, 1995) in the equatorial Pacific.

The current consensus is that nitrogen and iron both limit primary production in the eastern and central equatorial Pacific Ocean (Martin et al., 1990, 1991; Price et al., 1994; Behrenfeld et al., 1996; Coale et al., 1996a; Landry et al., 1997, 2000a) and that silicate limits diatom growth (Dugdale and Wilkerson, 1998). This understanding is included in the formulations used for growth of the five algal groups, which incorporates uptake of ammonium, nitrate, iron, and silicate. All of the algal groups use ammonium and iron; whereas, nitrate is only used by algal group 3, algal group 4, and algal group 5 (Fig. 2). Silicate is only used by algal group 5.

Each algal group has cellular carbon, nitrogen (ammonium + nitrate), and iron compartments and algal group 5 has a cellular silicate compartment. The phytoplankton cellular nitrogen, iron, and silicate are needed to calculate uptake of nitrogen, iron and silicate by phytoplankton and to estimate nitrogen, iron and silicate limited growth rates. The chlorophyll a equations are linked to cellular carbon, nitrogen, and iron state equations by variable cellular carbon to chlorophyll a, nitrogen to chlorophyll a, and iron to chlorophyll a ratios (section 4.6).

Two groups of zooplankton are included in the ecosystem model. The first group represents microzooplankton, which includes phagotrophic protists, and small animals that pass through a 200 μm mesh net (Landry et al., 1995). The second group, the mesozooplankton, include 200 μm to 2000 μm size animals (mostly copepods) (Dam et al., 1995). In this model, microzooplankton graze on *Prochlorococcus* spp., *Synechecoccus*, and autotrophic eukaryotes (Fig. 2). The mesozooplankton graze on large diatoms and microzooplankton (Dam et al., 1995; Landry et al., 1995; Zhang et al., 1995; Verity et al., 1996).

The detrital component of the ecosystem model is divided into small (Detritus1, Fig. 2) and large detritus groups (Detritus2, Fig. 2). Detrital components are split into two groups because each group has unique sinking and remineralization rates (Nelson et al., 1995; Laws et al., 2000). The small detrital pool receives inputs from algal groups 1-4 that results from losses due to non-grazing mortality. Additional inputs to this detrital pool are from microzooplankton excretion and fecal pellet production (unassimilated ingestion). Losses by algal group 5 from non-grazing mortality and mesozooplankton excretion and fecal pellet production provide the inputs to the large detrital pool. Remineralization of small and large detritus provide sources of ammonium and iron (Laws et al., 2000). Dissolution of silicate in the large detritus compartment provides a source for this nutrient (Nelson et al., 1995).

Forcing by the physical environment is provided by vertical advection, vertical diffusion, and mixing. This forcing acts on all model state variables. The detritus compartments are also allowed to sink at a fixed rate. Details of the irradiance model (Fig. 1) and the equations used to describe the dynamics of the model state variables (Fig. 2) are given in the sections that follow.

IV.2 IRRADIANCE MODEL

IV.2.1 Irradiance at the sea surface

The clear-sky irradiance just above the sea surface, and just below the sea surface at wavelengths from 350-700 nm (photosynthetically active radiation, PAR) was

simulated using a clear-sky irradiance model (Gregg and Carder, 1990).

The shortwave radiation time series measured at 0°N, 140°W by optical sensors on the TAO mooring (see section 3.2) was converted to PAR by multiplying by 0.5 (Baker and Frounin, 1987). The ratio between the observed and simulated PAR values was used to obtain an estimate for the reduction in sea surface irradiance due to cloud cover. This ratio was then applied to the simulated direct and diffuse components of irradiance, for wavelengths of 350-700 nm, just below the sea surface. The resulting cloud-corrected spectral irradiance just below the sea surface was used with an underwater irradiance model to estimate the total downwelling spectral irradiance in the water column. Details of the model used to simulate the underwater light field are given in the following sections, and definitions and units of the variables used in the light model are given in Table 5.

IV.2.2 Total downwelling spectral irradiance

The total downwelling spectral irradiance, $E_d(\lambda, z)$, at a given wavelength (λ) and depth (z), is expressed as the sum of the direct, $E_{dir}(\lambda, z)$, and diffuse, $E_{dif}(\lambda, z)$, irradiance components:

$$E_d(\lambda, z) = E_{dir}(\lambda, z) + E_{dif}(\lambda, z). \tag{1}$$

The direct light component over a given depth interval (Δz) is computed as

$$E_{dir}(\lambda, z) = E_{dir}(\lambda, z - \Delta z)e^{-K_{dir}(\lambda)\Delta z}, \tag{2}$$

and, the diffuse light component is given by

$$E_{dif}(\lambda, z) = E_{dif}(\lambda, z - \Delta z)e^{-K_{dif}(\lambda)\Delta z}. \tag{3}$$

The vertical attenuation coefficients for the direct and diffuse components are given by K_{dir} and K_{dif}, respectively, and are of the form

$$K_{dir}(\lambda, z) = [a'(\lambda, z) + b'(\lambda, z)]/cos\theta', \tag{4}$$

Table 5
Definitions and units of the variables or parameters used in the underwater irradiance model

Symbol	Definition	Units
$E_d(\lambda, z)$	The total downwelling spectral irradiance	(μmol quanta m^{-2} s^{-1})
$E_{dir}(\lambda, z)$	Direct component of $E_d(\lambda, z)$	(μmol quanta m^{-2} s^{-1})
$E_{dif}(\lambda, z)$	Diffuse component of $E_d(\lambda, z)$	(μmol quanta m^{-2} s^{-1})
$K_{dir}(\lambda, z)$	Vertical attenuation coefficient for $E_{dir}(\lambda, z)$	m^{-1}
$K_{dif}(\lambda, z)$	Vertical attenuation coefficient for $E_{dif}(\lambda, z)$	m^{-1}
$a'(\lambda, z)$	Total absorption coefficient	m^{-1}
$b'(\lambda, z)$	Total backscattering coefficient	m^{-1}
θ'	The sun zenith angle in water	degrees
$\overline{\mu}^*$	The mean cosine for perfectly diffuse skylight after refraction	unitless
$a'_w(\lambda, z)$	The absorption coefficient of pure sea water	m^{-1}
$a'_p(\lambda, z)$	The absorption coefficient of particulate materials	m^{-1}
$a_{ph}(\lambda, z)$	The absorption of each algal group	m^{-1}
$pig(z)$	The concentration of each pigment	mg m^{-3}
$a^*_{pig}(\lambda)$	Specific absorption of the particular pigment	m^2 mg^{-1}
b_{bw}	Relative proportion of photons that are backscattered by water	unitless
$b_w(\lambda, z)$	Total scattering coefficient of water	m^{-1}
b_{bp}	Relative proportion of photons that are backscattered by particulate materials	unitless
$b_p(\lambda, z)$	Total scattering coefficient particulate materials	m^{-1}

and

$$K_{dif}(\lambda, z) = [a'(\lambda, z) + b'(\lambda, z)]/\overline{\mu}^*, \tag{5}$$

where $a'(\lambda, z)$, is the total absorption coefficient of light, $b'(\lambda, z)$ is the total backscattering coefficient, θ' is the sun zenith angle and $\overline{\mu}^*$ (0.83) is the mean cosine for perfectly diffuse skylight after refraction at a flat sea surface (Kyewalyanga et al., 1992).

IV.2.3 Total spectral absorption of light

The total absorption coefficient of light is the sum of absorption by pure sea water ($a'_w(\lambda, z)$) and absorption by particulate materials ($a'_p(\lambda, z)$). The spectral absorption of light by sea water was obtained using the observations given in Smith and Baker (1981), and the data were interpolated to a 1-nm resolution.

The absorption coefficient of particulate materials, $a'_p(\lambda, z)$, was obtained from the sum of absorption coefficients of five algal groups which are functions of the algal pigment concentrations:

$$a'_p(\lambda, z) = \sum_{i=1}^{5} a_{ph_i}(\lambda, z), \tag{6}$$

where $a_{ph_i}(\lambda, z)$ is the light absorption by $AG(i)$ at each wavelength, λ, at depth, z, and is calculated as

$$a_{ph_i}(\lambda, z) = \sum (pig(z)\, a^*_{pig}(\lambda)), \tag{7}$$

where $pig(z)$ is the concentration of each photosynthetically-active pigment within each algal group at a given depth, and $a^*_{pig}(\lambda)$ is the weight-specific absorption of the particular pigment at a given wavelength.

The specific absorption values for the specific pigments found in each algal group (cf. Table 4), $a^*_{pig}(\lambda)$, are taken from Bidigare et al. (1990). The resulting maximal and minimal chlorophyll a-specific absorption spectra for each algal group (Fig. 3) show maximum absorption between 440 and 500 nm and a second absorption peak

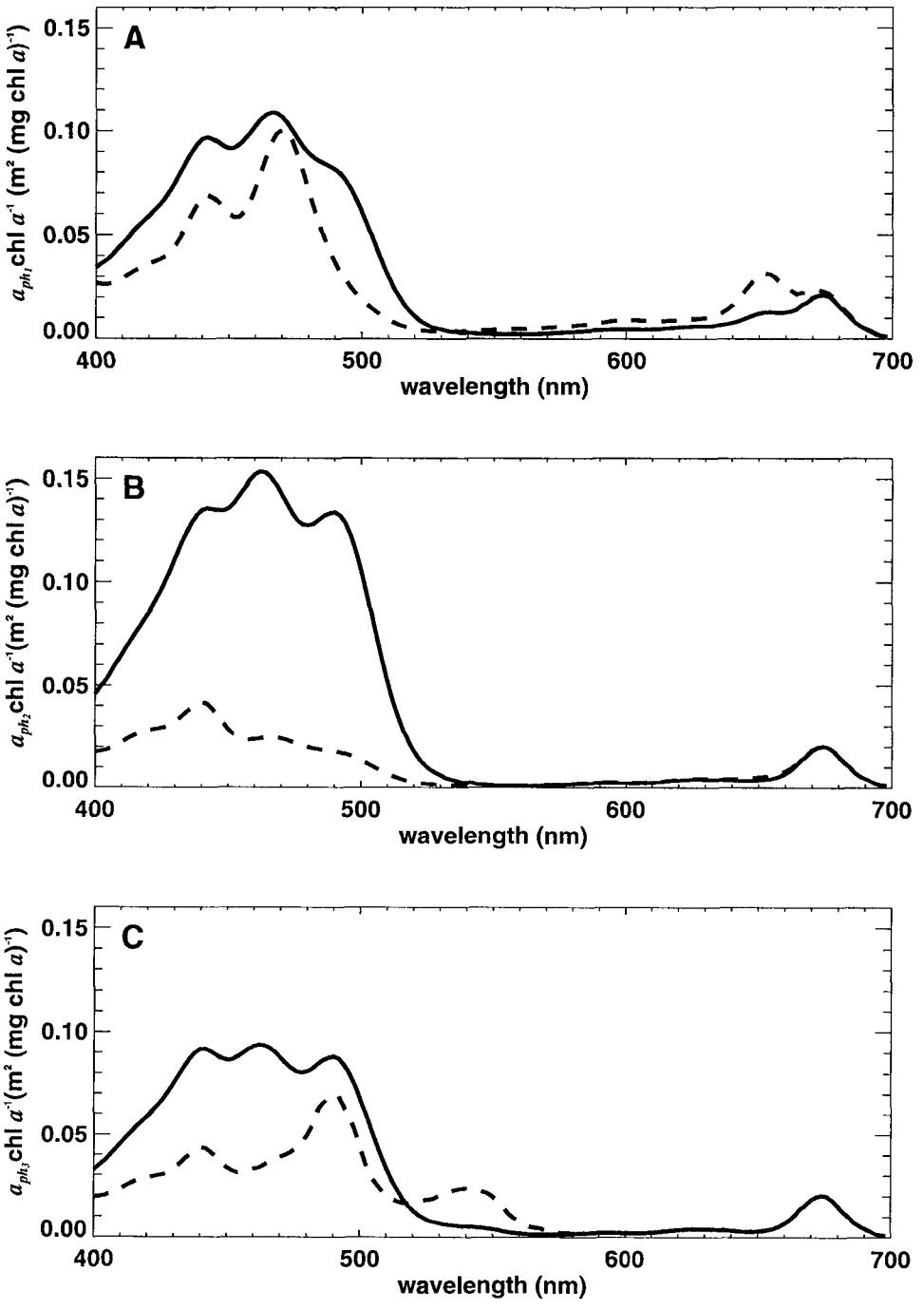

Fig. 3. The maximum (solid line) and minimum (dashed line) chlorophyll a-specific absorption as a function of wavelength for: A) algal group 1-low light-adapted *Prochlorococcus*, B) algal group 2-high light-adapted *Prochlorococcus*, C) algal group 3-*Synechococcus*, D) algal group 4-autotrophic eukaryotes, E) algal group 5-large diatoms, respectively. The carbon to chlorophyll a ratios used in the calculation of the specific absorption spectra are described in section 4.6.

Figure 3 continued.

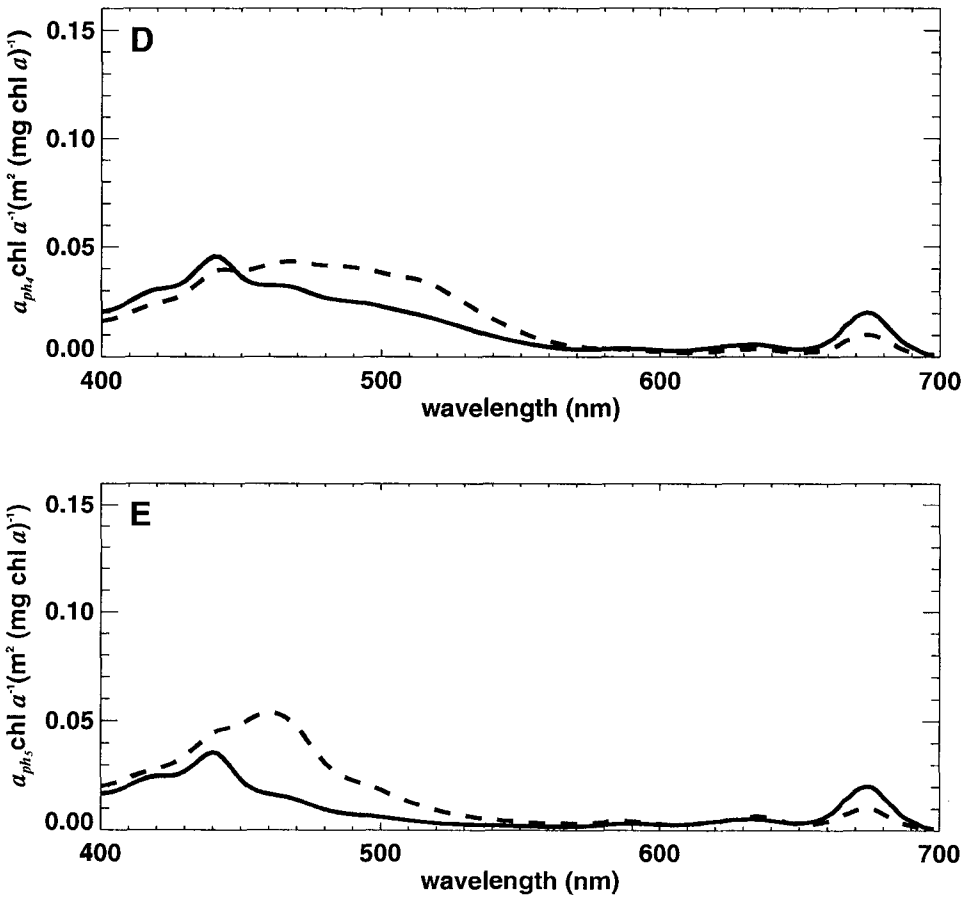

at 680 nm. The strongest light absorption occurs in algal groups 1 to 3. These absorption spectra determine the structure of the underwater light field and the magnitude of the irradiance at depth.

IV.2.4 Total spectral backscattering of light

The total backscattering component of light attenuation, $b'(\lambda, z)$, is the result of backscattering by sea water, $b_{bw}b_w(\lambda, z)$ and backscattering by particulate material, $b_{bp}b_p(\lambda, z)$ (Morel, 1988; Kyewalyanga et al., 1992), which is expressed as:

$$b'(\lambda, z) = b_{bw}\, b_w(\lambda, z) + b_{bp}\, b_p(\lambda, z), \tag{8}$$

where b_w and b_p are the total scattering coefficients of water and particulate materials, respectively. The relative proportion of photons that are backscattered by water and

particulate materials are b_{bw} and b_{bp}, respectively. The total scattering coefficient of water (b_w) was taken from Smith and Baker (1981), and b_{bw} was assumed to be spectrally invariant with a value of $0.5b_w$ (Smith and Baker, 1981; Morel, 1988; Kyewalyanga et al., 1992).

The total particulate scattering, $b_p(\lambda, z)$, is usually expressed as a function of the total chlorophyll a (chl $a(z)$) concentration at depth (Morel et al., 1991). For this study, the empirical relationship developed by Morel et al. (1991) which is of the form:

$$b_p(\lambda, z) = 0.30[chl\ a(z)]^{0.62}\left(\frac{550}{\lambda}\right), \tag{9}$$

was used to obtain the depth-dependent scattering of light by particulate matter. This power function relationship increases particulate scattering as chlorophyll a concentration increases. The relationship is expressed relative to the scattering that occurs at 550 nm. The total backscattering by particulate materials is also spectrally dependent and was included using the empirical formulation developed by Morel (1988) which is of the form:

$$b_{bp}\, b_p(\lambda, z) = 0.30[chl\ a(z)]^{0.62}\left[0.002 + 0.02(0.5 - 0.25\, log[chl\ a(z)])\left(\frac{550}{\lambda}\right)\right]. \tag{10}$$

IV.3 PHYTOPLANKTON STATE EQUATIONS

The basic state equation governing phytoplankton dynamics for each algal group (AG_i) is of the form:

$$\frac{\partial AG_i}{\partial t} + w\frac{\partial AG_i}{\partial z} - \frac{\partial}{\partial z}K_z\frac{\partial AG_i}{\partial z} = [min(\mu_{ll_i}, \mu_{nul_i})]AG_i - m_i AG_i - I_{AG_i}Z_s, \quad \text{for i} = 1, 5, \tag{11}$$

where the three terms on the left side represent changes in each algal group that are produced by local time (t) variations, vertical (z) advection (w), and vertical diffusive flux (K_z), respectively. The right side of Eq. (11) represents the biological processes

that provide sources and sinks of each algal group, which includes light- (μ_{ll_i}) and nutrient-limited (μ_{nul_i}) growth, natural mortality, and losses due to zooplankton grazing, respectively. Algal groups 1-4 are grazed by microzooplankton, and algal group 5 is grazed by mesozooplankton (Fig. 2). All of the phytoplankton growth and loss processes are expressed in terms of carbon. The definitions and units of the parameters used in the algal group equations are given in Table 6.

The realized net growth rate for each algal group, μ_i, is the minimum of the light- and nutrient-limited growth rates, which limits growth by the least available resource (e.g. Walsh (1975)). The basal growth rate on which μ_{ll_i} and μ_{nul_i} are based is determined from temperature (T) using the specific growth relationship given by Eppley (1972), which is of the form:

$$\mu_{mt_i}(z,t) = \mu_{m_i}(z,t)exp^{0.0633(T(z)-27)}, \tag{12}$$

where μ_{mt_i} is the temperature-dependent maximum growth rate for each algal group, which is calculated for each time and depth interval, and μ_{m_i} is the maximum growth rate at 27°C for each algal group (Table 7). Details of the formulations used to obtain μ_{ll_i} and μ_{nul_i} are given in sections 4.4 and 4.5, respectively.

Because ~80% of the daily production of algal groups 1-4 is removed by grazing in the equatorial Pacific (Landry et al., 1995), natural mortality is assumed to have no effect on these algal groups (Table 7). The natural mortality rate for algal group 5 (Table 7) is such that 15% of these phytoplankton cells are removed in one day. This rate is consistent with those measured by Dam et al. (1995) for large diatoms in the equatorial Pacific.

Losses due to grazing by microzooplankton (algal groups 1-4) and mesozooplankton (algal group 5) are obtained using the formulation given by Franks et al. (1986) which is of the form:

$$I_{AG_i} = g_{AG_i}\Lambda AG_i(1 - e^{-\Lambda AG_i}), \tag{13}$$

where g_{AG_i} is the maximum grazing rate of zooplankton on each algal group

Table 6
Definitions and units of variables or parameters used in the equations that describe the dynamics of phytoplankton particulate carbon, nitrogen, iron, and silicate for each algal group

Symbol	Definition	Units
μ_{ll}	Light-limited carbon specific growth rate	hr^{-1}
μ_{nul}	Nutrient-limited carbon specific growth rate	hr^{-1}
m	Phytoplankton specific death rate	hr^{-1}
μ	Realized net carbon specific growth rate	hr^{-1}
μ_{mt}	Maximum, temperature dependent carbon specific growth rate	hr^{-1}
μ_m	Maximum carbon specific growth rate at 27°C	d^{-1}
g_{AG}	Phytoplankton specific grazing coefficient	d^{-1}
Λ	Ivlev coefficient of grazing	$(mmol\ C\ m^{-3})^{-1}$
$\rho_{NO_3^-}$	Absolute nitrate transport flux	$\mu mol\ N\ l^{-1}\ d^{-1}$
$\rho_{NH_4^+}$	Absolute ammonium transport flux	$\mu mol\ N\ l^{-1}\ d^{-1}$
ρ_{Fe}	Absolute iron transport flux	$nmol\ Fe\ l^{-1}\ d^{-1}$
ρ_{Si}	Absolute silicate transport flux	$\mu mol\ Si\ l^{-1}\ d^{-1}$
α	Photosynthetic efficiency	$(\mu mol\ quanta\ m^{-2})^{-1}$
E_o	Scalar irradiance at depth z	$\mu mol\ quanta\ m^{-2}\ s^{-1}$
$E_o cp$	Compensation irradiance	$\mu mol\ quanta\ m^{-2}\ s^{-1}$
dr	The coefficient of exponential decay of light-limited growth rate	$(\mu mol\ quanta)^{-1}$
$E_o inb$	Inhibiting light level	$\mu mol\ quanta\ m^{-2}\ s^{-1}$
ϕ_m	Maximum quantum yield	$\mu mol\ C\ (\mu mol\ quanta)^{-1}$
$a^*_{ph_p}$	Photosynthetic absorption coefficient	m^{-1}
$K_{sNO_3^-}$	Half saturation constant for nitrate uptake	$\mu mol\ NO_3^-\ l^{-1}$
ψ	Nitrate uptake repression exponent	$(\mu mol\ NH_4^+\ l^{-1})^{-1}$
$K_{sNH_4^+}$	Half saturation constant for ammonium uptake	$\mu mol\ NO_3^-\ l^{-1}$
K_{sFe}	Half saturation constant for iron uptake	$nmol\ Fe\ l^{-1}$
K_{sSi}	Half saturation constant for silicate uptake	$\mu mol\ Si\ l^{-1}$

Table 6 continued.

Symbol	Definition	Units
K_{QN}	Subsistence quota for nitrogen-limited growth	μmol N (μmol C)$^{-1}$
Q_N	Cellular nitrogen status of the algal group	μmol N (μmol C)$^{-1}$
K_{QFe}	Subsistence quota for iron-limited growth	nmol Fe (μmol C)$^{-1}$
Q_{Fe}	Cellular iron status of the algal group	μmol Fe (μmol C)$^{-1}$
K_{QSi}	Subsistence quota for silicate-limited growth	μmol Si (μmol C)$^{-1}$
Q_{Si}	Cellular silicate status of the algal group	μmol Fe (μmol C)$^{-1}$
QN_{max}	Maximum allowed nitrogen to carbon ratio in each algal group	μmol N (μmol C)$^{-1}$
QFe_{max}	Maximum allowed iron to carbon ratio in each algal group	nmol Fe (μmol C)$^{-1}$
QSi_{max}	Maximum allowed silicate to carbon ratio in each algal group	μmol Si (μmol C)$^{-1}$
$\overline{\mu}$	Growth rate at maximum cellular nutrient concentrations	d^{-1}

(Table 7) and Λ is the Ivlev (1955) coefficient for zooplankton grazing (because Λ is a variable that is specific to zooplankton, its value is given in Table 12). This particular parameterization for zooplankton grazing losses provides model solutions that are stable for a wide range of parameter values (Franks et al., 1986).

Phytoplankton particulate nitrogen is an integral component of the dynamics governing each algal group because the nitrogen uptake and nitrogen-limited growth rate of each algal group are estimated as a function of particulate nitrogen (AGN_i) as:

$$\frac{\partial AGN_i}{\partial t} + w\frac{\partial AGN_i}{\partial z} - \frac{\partial}{\partial z}K_z\frac{\partial AGN_i}{\partial z} =$$

$$\rho_{NO3i} + \rho_{NH4i} - m_i AGN_i - I_{AGN_i} Z_{s+l}, \tag{14}$$

where the terms on the left side of Eq. (14) represent the same physical processes included in Eq. (11). The first two terms on the right side of Eq. (14) represent increases in algal group particulate nitrogen that occur as a result of nitrate and ammonium uptake, respectively. The third and fourth terms represent losses from the particulate nitrogen pool by natural mortality of each algal group and grazing by microzooplankton and mesozooplankton, represented by $Z_{(s+l)}$. Details of the approach used to obtain nitrate and ammonium uptake rates are given in section 4.5.

The iron concentration within the five algal groups ($AGFe_i$) is obtained using an equation of the form:

$$\frac{\partial AGFe_i}{\partial t} + w\frac{\partial AGFe_i}{\partial z} - \frac{\partial}{\partial z}K_z\frac{\partial AGFe_i}{\partial z} = \rho_{Fe_i} - m_i AGFe_i - I_{AGFe_i} Z_{(s+l)}, \tag{15}$$

where the physical processes governing iron concentration are given by the terms on the left side of Eq. (15). The biological source and sink terms on the right side of Eq. (15) represent uptake of iron by each algal group, loss of iron by natural mortality of the algal groups, and removal of iron via zooplankton grazing, respectively. The formulation used to parameterize iron uptake by the individual algal group is given in section 4.5.

Of the algal groups included in the model, only algal group 5, the diatoms, depend on silicate for growth (cf. Fig. 2). The effect of silicate on the dynamics of algal group 5 was modeled using an equation of the form:

$$\frac{\partial AGSi_5}{\partial t} + w\frac{\partial AGSi_5}{\partial z} - \frac{\partial}{\partial z}K_z\frac{\partial AGSi_5}{\partial z} = \rho_{Si_5} - m_5 AGSi_5 - I_{AGSi_5} Z_l, \tag{16}$$

where the terms on the left side represent physical processes similar to those in Eq. (11) and the terms on the right side represent the biological processes of silicate

Table 7
Values of parameters, defined in Table 6, used in the equations describing the dynamics of each algal group (AG)

Parameter	$AG1$	$AG2$	$AG3$	$AG4$	$AG5$
m	0^{1}	0^{1}	0^{1}	0^{1}	0.15^{1}
μ_m	$0.58^{2,3}$	$0.56^{2,3}$	$0.8^{2,4,5}$	1.2^{6}	1.66^{6}
g_{AG}	$4^{7,8}$	$4^{7,8}$	$4^{7,8}$	$4^{7,8}$	$5^{9,10}$
$E_o$cp	1.0^{2}	6^{2}	6^{2}	$10^{11,12}$	8^{11}
dr	0.1^{13}	0.001^{13}	—	—	—
$E_o$inb	40^{2}	105^{2}	—	—	—
ϕ_m	0.0833^{3}	0.0833^{3}	0.0833^{14}	0.0833^{14}	0.0833^{14}
K_{sNO_3}	0.1^{15}	0.1^{15}	0.167^{16}	0.417^{16}	2.29^{17}
ψ	1000^{16}	1000^{16}	6.5^{16}	2.6^{16}	1.462^{18}
K_{sNH_4}	0.05^{15}	0.05^{15}	0.083^{16}	0.208^{16}	2.18^{17}
K_{sFe}	0.01^{16}	0.01^{16}	0.01^{16}	0.02^{6}	$0.12^{19,20}$
K_{sSi}	—	—	—	—	1.2^{21}
K_{QN}	5.66^{5}	5.66^{5}	5.66^{5}	$14.00^{11,22,23,24}$	16.6^{25}
K_{QFe}	$2\ 10^{-3^{6}}$	$2\ 10^{-3^{6}}$	$2\ 10^{-3^{6}}$	$3.0\ 10^{-3^{6}}$	$5.5\ 10^{-3^{6}}$
K_{QSi}	—	—	—	—	0.18^{26}
QN_{max}	3.42^{5}	3.42^{5}	3.42^{5}	$5.5^{11,22,23,24}$	6.25^{25}
QFe_{max}	$31\ 10^{-3^{6}}$	$31\ 10^{-3^{6}}$	$31\ 10^{-3^{6}}$	$50\ 10^{-3^{6}}$	$50\ 10^{-3^{6}}$
QSi_{max}	—	—	—	—	0.315^{26}

Superscripts refer to the references that provide the source for the parameter value given in the table, and the citation is provided below. The parameters that are not required by a particular algal group are indicated by —. [1]Leonard et al. (1999); [2]Moore et al. (1995); [3]Partensky et al. (1993); [4]Cuhel and Waterbury (1984); [5]Kana and Glibert (1987a); [6]Sunda and Huntsman (1995); [7]Landry et al. (1995); [8]Verity et al. (1996); [9]Dam et al. (1995); [10]Roman and Gauzens (1997); [11]Richardson et al. (1983); [12]Sakshaug et al. (1987); [13]Bissett et al. (1999b); [14]Sakshaug et al. (1991); [15]Harrison et al. (1996); [16]See text for calculations; [17] Zhang and Zou (1997); [18]Wroblewski (1977); [19]Coale et al. (1996b); [20]Fitzwater et al. (1996); [21]Nelson and Treguer (1992); [22]Laws and Bannister (1980); [23]Sakshaug et al. (1989); [24]Flynn et al. (1994); [25]Geider et al. (1998); [26]Takeda (1998).

uptake by diatoms, and losses of silicate from cell natural mortality and grazing by mesozooplankton (Z_l), respectively. The formulations for silicate uptake is given in section 4.5.

IV.4 FORMULATION OF ALGAL GROUP LIGHT-LIMITED GROWTH

The light-limited growth rate for each phytoplankton algal group (μ_{ll_i}) is assumed to be governed by a hyperbolic tangent function (Jassby and Platt, 1976) that relates growth rate and irradiance as:

$$\mu_{ll_i}(z) = tanh\left[\frac{\alpha_i(E_o(z) - E_o cp_i)}{\mu_{mt_i}(z)}\right] e^{-dr_i(E_o(z)-E_o inb_i)}\mu_{mt_i}(z), \quad \text{for i} = 1,5, \qquad (17)$$

where α_i and μ_{mt_i} are the photosynthetic efficiency and temperature-dependent growth rate (obtained from Eq. (12)) for each algal group, respectively. The scalar irradiance at a depth z ($E_o(z)$) is obtained by spectrally-integrating the downwelling spectral irradiance ($E_d(\lambda, z)$) obtained using the irradiance model described in section 4.2.2. The compensation light flux ($E_o cp_i$), which is the irradiance value at which net growth is zero, is obtained for each algal group from experimental studies (Table 7). This value sets a depth limit on algal group production.

The exponential portion of Eq. (17) allows for light inhibition of algal growth, which occurs at a rate given by dr_i. The formulations used for light-dependent growth are such that light inhibition affects only algal groups 1 and 2 (Table 7). Experimental studies (Moore et al., 1995) show that the growth of these phytoplankton cells is limited by high-light environments. Algal groups 3 to 5 do not exhibit similar growth inhibition in high-light regimes (Anderson and Roels, 1981; Falkowski et al., 1985; Post et al., 1985; Kana and Glibert, 1987a,b; Sakshaug et al., 1989; Iriarte and Purdie, 1993; Moore et al., 1995).

The photosynthetic efficiency for each algal group (α_i) is obtained from scaling the spectrally-integrated specific absorption coefficient of the photosynthetically active

pigments for each algal group, $a^*_{ph_{pi}}$, by a maximum quantum yield of photosynthesis for each group (ϕ_{m_i}) (Kirk, 1994) as

$$\alpha_i(z) = \phi_{m_i}\, a^*_{ph_{pi}}(z). \tag{18}$$

The value of ϕ_m represents the moles of carbon that are fixed per mole quanta of light (Table 7). For this study, a value of 12 mole quanta needed to fix one mole carbon ($\phi^{-1}_{m_i}$) was used (Partensky et al., 1993), which gives a value of ϕ_m of 0.083 (Table 7). This value was experimentally determined and represents a conservative estimate of maximum photosynthesis quantum yield.

The spectrally-integrated specific absorption coefficient for the photosynthetically active pigments for each algal group is obtained by integrating the spectrally-dependent absorption spectra ($a_{ph_i}(\lambda, z)$, discussed in section 4.2.3) over the PAR portion of the irradiance spectrum (400-700 nm) as:

$$a^*_{ph_{pi}}(z) = \frac{\int_{400}^{700} a_{ph_i}(\lambda, z)\, E_d(\lambda, z)\, d\lambda}{\int_{400}^{700} E_d(\lambda, z)\, d\lambda}, \tag{19}$$

where $E_d(\lambda, z)$ is the spectral irradiance for each wavelength (λ) at depth (z) and is obtained from the underwater light model described in section 4.2.2. The value of the spectrally-integrated specific absorption coefficient is calculated at each depth for each algal group.

IV.5 FORMULATION OF ALGAL GROUP NUTRIENT-LIMITED GROWTH

The specific rates of phytoplankton nutrient uptake and growth can be uncoupled depending upon the nutritional status of the phytoplankton cell (Droop, 1973; Goldman, 1980, 1982; Goldman and Glibert, 1983). Thus, use of a parameterization that assumes that phytoplankton growth is a direct function of nutrient uptake is appropriate only for population growth at maximal rates (Goldman and Glibert, 1983) and does not allow for phytoplankton species assemblages to shift in relative abundance of the different algal groups in response to differential nutrient uptake rates,

cell physiology, and environmental variability. This study has objectives that focus on understanding the effects of physical and biological processes on phytoplankton community composition in the equatorial Pacific. Therefore, the nutrient limited growth rate (μ_{nul_i} in Eq. (11)) was formulated using separate parameterizations for nutrient uptake and growth rates as follows.

The rate at which the different algal groups remove nitrate (first term, right side of Eq. (14)) is related via a hyperbolic function to the ambient nitrate concentration as

$$\rho_{NO_3^- i}(z,t) = \mu_{mt_i}(z,t) AGN_i \left[\frac{NO_3^-}{K_{sNO_3^- i} + NO_3^-} e^{-\psi_i NH_4^+} \right], \tag{20}$$

where the maximum rate of uptake is determined by the temperature-dependent specific growth rate ($\mu_{mt_i}(z,t)$, Eq. (12)), and the nitrate concentration at which one-half the maximum rate is obtained as given by $K_{sNO_3^- i}$. Values of $K_{sNO_3^- i}$ measured for each algal group are given in Table 7. The uptake of nitrate is inhibited by the presence of ammonium (Wroblewski, 1977; Flynn, 1991; Price et al., 1994), and this process is represented by the exponential term in Eq. (20). The degree to which nitrate uptake is inhibited by ammonium is given by ψ_i and values for this coefficient for each algal group are given in Table 7. The inhibition value for diatoms, algal group 5, is similar to that used in other models that include this phytoplankton group (Wroblewski, 1977). The inhibition parameter values for algal groups 3 and 4 reflect the lower half saturation constants measured for these phytoplankton (Table 7). These nitrate uptake inhibition parameter values are estimated from the value used for diatoms by assuming an inverse relationship with nitrate uptake inhibition and cell size. This gives a nitrate uptake inhibition parameter value for algal groups 1 and 2 (Table 7) that prevents nitrate uptake by these phytoplankton. This is supported by studies that have shown that *Prochlorococcus* spp. are incapable of using nitrate as a nitrogen source (Miller and Castenholz, 2001; Moore et al., 2002b; Rocap et al., 2002; Scanlan and West, 2002).

The rate of nitrate uptake is also modified by the particulate nitrogen concentration of each algal group (AGN_i). Thus, Eq. (20) represents a nitrate transport flux into each algal group.

The uptake of ammonium is obtained for each algal group using a similar hyperbolic relationship of the form:

$$\rho_{NH_4^+ i}(z,t) = \mu_{mt_i}(z,t) AGN_i \left[\frac{NH_4^+}{K_{sNH_4^+ i} + NH_4^+} \right], \tag{21}$$

where the parameter definitions are similar to those in Eq. (20) and are given in Table 7.

The total nitrogen transfer flux for each algal group is given by the sum of the nitrate and ammonium fluxes ($\rho_{NO_3^- i}(z,t) + \rho_{NH_4^+ i}(z,t)$) and this determines the increase in algal group particulate nitrogen produced by ambient nutrient concentrations (first term right side of Eq. (14)).

The uptake of iron by each algal group is assumed to also follow a hyperbolic relationship with iron concentration:

$$\rho_{Fe_i}(z,t) = \mu_{mt_i}(z,t) AGFe_i \left[\frac{Fe}{K_{sFe_i} + Fe} \right], \tag{22}$$

where $AGFe_i$ is the cell iron content given by Eq. (15). Values for the iron uptake parameters are given in Table 7.

Similarly the uptake of silicate by algal group 5 is given by

$$\rho_{Si_5}(z,t) = \mu_{mt_5}(z,t) AGSi_5 \left[\frac{Si}{K_{sSi_5} + Si} \right], \tag{23}$$

where the cellular silicate concentration, $AGSi_5$, is given by Eq. (16). The silicate uptake parameter values are given in Table 7.

The ability of phytoplankton to take up excess nutrients for use at a later time, termed luxury consumption, is related to cell size, with large cells having a greater capacity for nutrient storage (Wheeler, 1983). For the algal groups included in this study, diatoms have the largest potential for luxury consumption, followed by the autotrophic eukaryotes and finally the smaller *Synechococcus* and *Prochlorococcus*

spp. Luxury uptake and storage of iron is also valid, and the largest luxury uptake occurs in the diatoms (Sunda and Huntsman, 1995, Table 7).

The effect of cellular nutrient concentrations in modifying the nutrient-limited growth rate ($\mu_{nul_i}(z,t)$) was included using a Droop (1973) equation which provides a realistic mathematical representation of growth under nutrient limiting conditions (Marra et al., 1990; Haney and Jackson, 1996) and is of the form:

$$\mu_{nul_i}(z,t) = \overline{\mu_i}(z,t)\left[1 - \frac{K_{QN_i}}{Q_{N_i}(z,t)}\right]\left[1 - \frac{K_{QFe_i}}{Q_{Fe_i}(z,t)}\right]\left[1 - \frac{K_{QSi_5}}{Q_{Si_5}(z,t)}\right], \qquad (24)$$

where $\overline{\mu_i}(z,t)$ is the algal group growth rate that occurs at maximum ratios of algal group particulate nitrogen to carbon (AGN_i:AG_i), particulate iron to carbon ($AGFe_i$:AG_i), and particulate silicate to carbon ($AGSi_5$:AG_5) ratios. The actual algal group particulate nitrogen (nitrate + ammonium) to carbon, particulate iron to carbon and particulate silicate to carbon ratios are represented by $Q_{N_i}(z,t)$, $Q_{Fe_i}(z,t)$, and $Q_{Si_5}(z,t)$ (note that silicate is only limiting for $AG5$), respectively. The subsistence algal nitrogen, iron, and silicate to carbon ratios are given by K_{QN_i}, K_{QFe_i}, and K_{QSi_5}, respectively. These subsistence quotas define the algal particulate nitrogen, iron, and silicate to carbon ratios ($Q_{N_i}(z,t)$, $Q_{Fe_i}(z,t)$, and $Q_{Si_5}(z,t)$) where zero growth rate for each algal group occurs (Droop, 1973), and values for these are given in Table 7.

The actual cellular nitrogen to carbon ratio that controls the nitrogen-based algal growth rate is obtained from

$$Q_{N_i}(z,t) = \frac{AGN_i + \rho_{NO_3^-i} + \rho_{NH_4^+i}}{AG_i}. \qquad (25)$$

The cellular nutrient ratios controlling iron- and silicate-based growth are similar:

$$Q_{Fe_i}(z,t) = \frac{AGFe_i + \rho_{Fe_i}}{AG_i} \quad \text{and} \quad Q_{Si_5}(z,t) = \frac{AGSi_5 + \rho_{Si_5}}{AG_5}. \qquad (26)$$

The actual growth rate (μ_{mt}, Eq. (12)) uses a true maximum growth rate ($\overline{\mu_i}$) which is reached when the algal group particulate nitrogen to carbon, particulate iron to

carbon, and particulate silicate to carbon ratios are maximized. Because μ_{mt} changes with time and depth, $\overline{\mu}_i$ is calculated for each time and depth from

$$\overline{\mu_i}(z,t) = \mu_{mt_i}(z,t)\left[1 - \frac{K_{QN_i}}{QN_{max_i}}\right]^{-1}\left[1 - \frac{K_{QFe_i}}{QFe_{max_i}}\right]^{-1}\left[1 - \frac{K_{QSi_5}}{QSi_{max_5}}\right]^{-1}, \quad (27)$$

which is a modified form of Eq. (24) in which $\mu_{mt_i}(z,t)$ replaces $\mu_{nul_i}(z,t)$ and the maximum particulate nitrogen to carbon, iron to carbon, and silicate to carbon ratios for each algal group are used, which are given by QN_{max_i}, QFe_{max_i}, QSi_{max_i}, respectively. Unlike the actual ratios calculated by using Eqs. (25) and (26), these are constant ratios and values for each group are given in Table 7.

IV.6 CARBON TO CHLOROPHYLL *a* RATIOS AND THE PIGMENT CONCENTRATIONS OF EACH ALGAL GROUP

IV.6.1 Carbon to chlorophyll ratios

The chemical composition of phytoplankton cells changes in response to variability in environmental conditions. This adjustment of cellular physiology is termed acclimation. Its importance to phytoplankton growth rate is indicated by variations of pigment to biomass ratios observed in vertical profiles (Cullen, 1982; Campbell et al., 1994). The assumption that biochemical composition (e.g. carbon to chlorophyll *a* ratio) is actively adjusted by phytoplankton cells to acclimate to prescribed environmental conditions (Geider and Osborne, 1987; Langdon, 1988; Cloern et al., 1995; Geider et al., 1998) is applied in the development of the present model. The carbon to chlorophyll *a* ratios of each algal group are not fixed in the model, rather these vary as a function of light- or nutrient-limitation.

The carbon to chlorophyll *a* ratio of each algal group, θ_i, is allowed to vary between some maximum and minimum value. The determination of the ratio at each time and depth depends on an optimal carbon to chlorophyll *a* ratio and a rate of change from the previous carbon to chlorophyll *a* ratio. For light-limited growth,

the optimal carbon to chlorophyll a ratio, $\theta_{opt_{ll}i}$, versus irradiance is described as a linear function of irradiance (Geider et al., 1986a; Geider and Osborne, 1987) as:

$$\theta_{opt_{ll}i}(z,t) = \theta_{O_{ll}i} + S_{\theta_{ll}i}E_o(z). \tag{28}$$

The intercepts, $\theta_{O_{ll}i}$ ($g\ g^{-1}$), and slopes, $S_{\theta_{ll}i}$ (μmol quanta $m^{-2}s^{-1})^{-1}$), used in Eq. (28) and the ranges of carbon to chlorophyll a for each algal group are given in Table 8.

Table 8
Values of parameters used to estimate light-limited carbon to chlorophyll a (C:chl a) ratios for each algal group (AG) included in the lower trophic level ecosystem model

AG	C:chl a ($g\ g^{-1}$)	Irradiance (μmol quanta $m^{-2}s^{-1}$)	$\theta_{O_{ll}}$	$S_{\theta_{ll}}$	Reference
1	20-100	0-100	20	0.8	1,2
2	15-150	0-450	15	0.30	1,2
3	30-160	0-1330	30	0.10	2,3,4
4	25-60	0-300	25	0.12	5,6,7
5	20-100	12-1200	20	0.067	8

The references from which the values were obtained are indicated in the last column, and the citations are as follows: 1. Partensky et al. (1993); 2. Moore et al. (1995) ; 3. Kana and Glibert (1987b) ; 4. Kana et al. (1992) ; 5. Laws and Bannister (1980); 6. Geider and Platt (1986b); 7. Geider and Osborne (1987); 8. Geider et al. (1998).

Similar linear equations are used to estimate the nitrogen-limited carbon to chlorophyll a ratios, $\theta_{opt_{nl}i}$, and iron-limited carbon to chlorophyll a ratios (Sakshaug et al., 1989; Sunda and Huntsman, 1995). However, for these ratios, the independent variables are the carbon to nitrogen $\left(\frac{AG_i}{AGN_i}\right)$ and carbon to iron $\left(\frac{AG_i}{AGFe_i}\right)$ ratios, respectively, rather than irradiance:

$$\theta_{opt_{nl}i}(z,t) = \theta_{0_{nl}i} + S_{\theta_{nl}i}\left(\frac{AG_i}{AGN_i}\right) \tag{29}$$

$$\theta_{opt_{Fel}i}(z,t) = \theta_{0_{Fel}i} + S_{\theta_{Fel}i}\left(\frac{AG_i}{AGFe_i}\right) \tag{30}$$

The slopes and intercepts for the nitrogen- and iron-limited carbon to chlorophyll a ratios for each algal group are given in Tables 9 and 10, respectively.

Table 9
Values of parameters used to estimate nitrogen-limited carbon to chlorophyll a ratios (C:chl a) for each algal group (AG) included in the lower trophic level ecosystem model

AG	C:chl a ($g\ g^{-1}$)	C:N (mol mol^{-1})	$\theta_{O_{nl}}$	$S_{\theta_{nl}}$	Reference
1	No change	—	—	—	1
2	No change	—	—	—	1
3	No change	—	—	—	2,3
4	60-150	6.625-14	-20	12.2	4
5	100-250	5.8-14.6	1.1	17	5

The references from which the values were obtained are indicated in the last column and the citation is provided below. The parameters that are not required by a particular algal group are indicated by —. 1. Moore et al. (1995); 2. Kana et al. (1992); 3. Glibert and Ray (1990); 4. Laws and Bannister (1980); 5. Geider et al. (1998).

The maximum of the light-, $\theta_{opt_{ll}i}(z,t)$, nitrogen-, $\theta_{opt_{nl}i}(z,t)$, and iron-limited, $\theta_{opt_{Fel}i}(z,t)$ carbon to chlorophyll a ratios is assumed to be the carbon to chlorophyll a ratio that the algal group strives to achieve. The change in the actual carbon to chlorophyll a ratio, θ_i, towards the optimal carbon to chlorophyll a ratio is determined by the growth rate, $\mu_i(z,t)$, calculated for the current time step for each algal group (Falkowski and Wirick, 1981):

Table 10
Values of parameters used to estimate iron-limited carbon to chlorophyll a ratios (C:chl a) for each algal group (AG) included in the lower trophic level ecosystem model

AG	C:chl a ($g\ g^{-1}$)	Fe:C ($\times 10^{-5}$) (mol mol^{-1})	$\theta_{O_{Fel}}$	$S_{\theta_{Fel}}$	Reference
1	No change	—	—	—	
2	No change	—	—	—	
3	236-336	1.49-3.8	400.16	-4.32×10^{6}	1
4	35-75	0.37-3.32	63.58	-0.939517×10^{6}	2
5	35-105	1.31-33.3	58	-0.9502×10^{6}	2

The references from which the values were obtained are indicated in the last column and the citation is provided below. The parameters that are not required by a particular algal group are indicated by —. 1. Kudo and Harrison (1997); 2. Sunda and Huntsman (1995).

$$\frac{\partial R_i}{\partial t} = \mu_i(z,t)(R_{w_i}(z,t) - R_i(z,t)), \tag{31}$$

where

$$R_{w_i}(z,t) = \{max[\theta_{opt_{lti}}(z,t), \theta_{opt_{nti}}(z,t), \theta_{opt_{Feli}}(z,t)]\}^{-1}$$

and

$$R_i(z,t) = \theta_i^{-1}(z,t)$$

in which $R_i(z,t)$ is the chlorophyll a to carbon ratio (chl a:C), $\theta_i^{-1}(z,t)$, $R_{w_i}(z,t)$ is the optimal chlorophyll a to carbon ratio which the phytoplankton try to obtain, and μ_i is the realized growth rate of each algal group, which is equal to the minimum of either the light- or nutrient-limited growth rate (section 4.3).

IV.6.2 Algal group pigment concentrations

The changes in accessory pigments are defined by their relationship to chlorophyll *a* (Table 11) and as a result co-vary with changes in chlorophyll *a*. The accessory pigment ratio is assumed to be a linear function of the carbon to chlorophyll *a* ratio in each algal group. The minimum and maximum accessory pigment to chlorophyll *a* values in Table 11 correspond to the maximum and minimum carbon to chlorophyll *a* ratio of each algal group that are given in Tables 8, 9, and 10. For example the chlorophyll *b* (chl *b*) concentration of algal group 1 is estimated as:

$$\text{chl } b = -0.020\, AG_1 + 2.4\,\text{chl } a, \tag{32}$$

where AG_1 and chl *a* represent the carbon and chlorophyll *a* concentrations, respectively, in algal group 1. The values of the slope (-0.020) and the intercept (2.4) are from Table 11. Other pigments in each algal group are estimated in a similar way.

Because $\mu_i(z,t)$ has to be greater than zero to affect a change in the chlorophyll *a* to carbon ratio (Eq. 31), pigment changes only occur when there is sufficient light or nutrients to support growth of the algal groups. Also because changes in chlorophyll *a* concentrations are dependent on the total light intensity without any spectral dependence (Eq. 18), changes in accessory pigments are only a function of the total photon flux which is consistent with observations (Jeffrey and Vesk, 1977; Glover et al., 1987; Hooks et al., 1988; Olson et al., 1988; Moore et al., 1995).

IV.7 ZOOPLANKTON STATE EQUATIONS

The governing equation for microzooplankton (Z_s) is assumed to be of the form:

$$\frac{\partial Z_s}{\partial t} + w\frac{\partial Z_s}{\partial z} - \frac{\partial}{\partial z}K_z\frac{\partial Z_s}{\partial z} = \sum_{i=1}^{4} \lambda^* I_{P_i} Z_s - I_{Z_s} Z_l - e_s Z_s - m_{z_s} Z_s, \quad \text{for i} = 1,4, \tag{33}$$

where the terms on the left side represent changes in concentration that are produced by local time variations, vertical advection, and vertical diffusion, respectively. The biological processes that provide gains and losses to the microzooplankton biomass,

Table 11
The values of accessory pigment to chlorophyll *a* ratios that correspond to the maximum and minimum carbon to chlorophyll *a* ratio of each algal group (*AG*) from Tables 8, 9, and 10

AG	chl *b*:chl *a*	chl *c*:chl *a*	PSC:chl *a*	PPC:chl *a*	PE:chl *a*	Ref
1	2.4-0.8	—	—	0.3-1.4	—	1
	slope=-0.020			slope=0.014		
2	0.2-0.06	—	—	0.3-2.5	—	1
	slope=-0.001			slope=0.016		
3	—	—	—	0.3-1.5	20-3	1,2,9
				slope=0.009	slope=-0.13	
4	—	0.34-0.17	2.0-0.5	0.10	—	3,4,5,
		slope=-0.005	slope=-0.012	constant		6,7,8
5	—	0.96-0.13	0.88-0.14		—	8
		slope=-0.0037	slope=-0.0033			

The pigments include chlorophyll *a* (chl *a*), chlorophyll *b* (chl *b*), chlorophyll *c* (chl *c*), photosynthetic carotenoids (PSC), photoprotective carotenoids (PPC), and phycoerythrin (PE). For algal group 5 the sum of the carotenoids (PSC+PPC) are formulated as a function of chlorophyll *a*. The references (Ref) from which the values were obtained are indicated in the last column and the citation is provided below. The parameters that are not required by a particular algal group are indicated by —.
1. Moore et al. (1995) ; 2. Kana and Glibert (1987b) ; 3. Jeffrey (1976); 4. Perry et al. (1981); 5. Haxo (1985) ; 6. Cleveland and Perry (1987) ; 7. Schofield et al. (1990) ; 8. Hoepffner and Sathyendranath (1992) ; 9. Barlow and Alberte (1985).

represented by the terms on the right side of Eq. (33), are assimilated ingestion of the grazed phytoplankton biomass, grazing on microzooplankton by mesozooplankton, excretion, and mortality, respectively.

Microzooplankton graze algal groups 1 to 4 and the assimilated ingestion represents the sum of the biomass grazed from these four algal pools. The efficiency at which the grazed algal biomass is assimilated is given by λ^*, which has the same value for all algal groups (Table 12).

Removal of microzooplankton by mesozooplankton grazing (I_{Z_s}) is parameterized similar to what was done for grazing on phytoplankton (Eq. (13)). The values used for the microzooplankton specific grazing rate (g_{Z_s}) and Ivlev constant (Λ) are given in Table 12.

The microzooplankton excretion loss rate is given by e_s and the value of this coefficient is given in Table 12. The microzooplankton mortality includes natural as well as predation mortality. This rate at which mortality occurs (m_{z_s}, Table 12) is such that 50% of the microzooplankton biomass is removed each day, which is consistent with observations (Dam et al., 1995; Zhang et al., 1995).

The equation governing the mesozooplankton (Z_l) dynamics is similar to Eq. (33) and is of the form

$$\frac{\partial Z_l}{\partial t} + w\frac{\partial Z_l}{\partial z} - \frac{\partial}{\partial z}K_z\frac{\partial Z_l}{\partial z} = \lambda^* I_{P_5} Z_l + \lambda^* I_{Z_s} Z_l - e_l Z_l - m_{z_l} Z_l. \qquad (34)$$

Increases in mesozooplankton biomass are supported by grazing on diatoms (algal group 5) and microzooplankton. The grazed biomass is assimilated with an efficiency given by λ^* (Table 12). Losses to the mesozooplankton biomass occur via excretion and mortality, and values for the rates at which these processes occur are given in Table 12.

IV.8 NUTRIENT STATE EQUATIONS

The ambient nutrient concentrations are an integral component of the dynamics governing the nutrient uptake by each algal group as described in section 4.5. The

Table 12
Definitions, values, and units of the parameters used in the microzooplankton, mesozooplankton, nutrient, large detritus, and small detritus governing equations

Symbol	Definition	Value	Units
Λ	Ivlev coefficient of grazing	1[1]	$(\text{mmol C m}^{-3})^{-1}$
λ^*	Zooplankton assimilation efficiency	0.75[1]	unitless
e_s	Mesozooplankton excretion rate	0.1[2,3]	d^{-1}
m_{Z_s}	Mesozooplankton death rate	0.6	d^{-1}
e_l	Microzooplankton excretion rate	0.1[2,3]	d^{-1}
m_{Z_l}	Microzooplankton death rate	0.5	d^{-1}
g_{Z_s}	Mesozooplankton specific grazing coefficient	15[4]	d^{-1}
c_a^*	Remineralization rate of detritus to ammonium	0.05[5]	d^{-1}
c_{Fe}^*	Remineralization rate of detritus to iron	0.1[5]	d^{-1}
FFe	Aeolian iron deposition at the surface	estimated	$\text{nmol l}^{-1}\ \text{d}^{-1}$
fe_{sol}	Soluble fraction of aeolian iron	0.1[6]	unitless
$fesca$	Particle scavenging loss term for iron	estimated	$\text{nmol l}^{-1}\ \text{d}^{-1}$
c_{Si}^*	Dissolution rate of detritus to silicate	0.1[7]	d^{-1}
sc_{des}	Small detritus sinking rate	10[5]	m d^{-1}
sc_{del}	Large detritus sinking rate	20[5]	m d^{-1}
c_c^*	Remineralization rate of detritus to carbon	0.1[5]	d^{-1}

Superscripts refer to the references that provide the source for the parameter value and the citations are as follows: [1]Leonard et al. (1999); [2]Landry et al. (1996); [3]Hutchins and Bruland (1995); [4]Dam et al. (1995); [5]Laws et al. (2000); [6]Duce and Tindale (1991); [7]Nelson et al. (1995).

nitrogen is partitioned into two components, recycled nitrogen, ammonium, and new nitrogen, nitrate. The basic state equation governing nitrate dynamics is of the form:

$$\frac{\partial NO_3^-}{\partial t} + w\frac{\partial NO_3^-}{\partial z} - \frac{\partial}{\partial z}K_z\frac{\partial NO_3^-}{\partial z} = -\sum_{i=1}^{5}\rho_{NO_3^- i}, \tag{35}$$

where the three terms on the left side represent changes in nitrate concentration that are produced by local time variations, vertical advection, and vertical diffusion, respectively. The only biological loss term for nitrate is uptake by each phytoplankton algal group (section 4.5), which is represented by the term on the right side of Eq. (35).

The basic state equation of ammonium is of the form:

$$\frac{\partial NH_4^+}{\partial t} + w\frac{\partial NH_4^+}{\partial z} - \frac{\partial}{\partial z}K_z\frac{\partial NH_4^+}{\partial z} =$$

$$\sum_{i=1}^{5}(-\rho_{NH_{4_i}^+}) + e_s Z_s\left(\frac{N}{C}\right)_{Z_s} + e_l Z_l\left(\frac{N}{C}\right)_{Z_l} + c_a De_s N + c_a De_l N, \tag{36}$$

where the three terms on the left represent the same physical processes included in the nitrate equation (Eq. (35)). The biological processes that provide gains and losses to the ambient ammonium concentration, represented by the terms on the right side of Eq. (36), are uptake by each algal group, excretion by microzooplankton, excretion by mesozooplankton, and remineralization of small detrital nitrogen ($De_s N$) and large detrital nitrogen ($De_l N$).

The loss term for ammonium represents the uptake by each phytoplankton algal group (section 4.5). The excretion losses by microzooplankton ($e_s Z_s$) and mesozooplankton ($e_s Z_s$), which are described in section 4.7, are assumed to directly enter the ammonium pool. The particulate carbon pools of each zooplankton group are converted to a nitrogen equivalent using a nitrogen to carbon ratio ($\frac{N}{C}$), for each group to estimate the amount of nitrogen in the excretion. This ratio is estimated by tracking the nitrogen to carbon ratio in the phytoplankton grazed by each zooplankton group, and it is calculated at each time and depth. Thus, this ratio is a dynamically evolving quantity rather than being a fixed constant value.

The other source for ammonium is the remineralization of small (De_sN) and large detrital nitrogen (De_lN) (Laws et al., 2000), which is described in section 4.9. The remineralization rate of detrital nitrogen to ammonium, $c_a(z)$, is assumed to be modified by temperature as:

$$c_a(z) = c_a^* T_{func}(z), \tag{37}$$

where

$$T_{func}(z) = e^{(0.0967(T(z)-25))}, \tag{38}$$

where $T(z)$ is water temperature in °C at depth (z). The temperature function ($T_{func}(z)$) for the equatorial Pacific is obtained from Christian and Karl (1995). The value used for remineralization rate of detrital nitrogen at 25°C, c_a^*, is given in Table 12.

The iron dynamics are assumed to be governed by an equation that is similar to that used for ammonium except for a surface deposition term (FFe) and a scavenged iron term ($fesca$):

$$\frac{\partial Fe}{\partial t} + w\frac{\partial Fe}{\partial z} - \frac{\partial}{\partial z}K_z\frac{\partial Fe}{\partial z} = \sum_{i=1}^{5}(-\rho_{Fe_i}) + e_s Z_s \left(\frac{Fe}{C}\right)_{Z_s} + e_l Z_l \left(\frac{Fe}{C}\right)_{Z_l} + c_{Fe} De_s Fe + c_{Fe} De_l Fe + \delta(z) FFe\, fe_{sol} - fesca(z), \tag{39}$$

where the three terms on the left represent the physical processes. The biological processes that provide gains and losses to the ambient iron concentration, represented by the terms on the right side of Eq. (39), are uptake by each algal group, excretion by microzooplankton, excretion by mesozooplankton, remineralization of small detrital iron (De_sFe) and large detrital iron (De_lFe), aeolian iron deposition, and scavenging of iron.

The particulate carbon pools of each zooplankton group are converted to an iron equivalent using an iron to carbon ratio $\left(\frac{Fe}{C}\right)$ for each group to estimate the amount

of iron produced by excretion. This ratio is estimated by tracking the iron to carbon ratio in the phytoplankton grazed by each zooplankton group, and it is calculated at each time and depth. The remineralization rate of detritus to iron, $c_{Fe}(z)$, is also assumed to vary as a function of temperature ($c^*_{Fe}T_{func}(z)$). The value used for remineralization rate of iron at 25°C, c^*_{Fe}, is given in Table 12.

The aeolian iron deposition (FFe) is simulated using the Kronecker delta (δ[z=0]=1; δ[z >0]=0) to ensure that the atmospheric iron flux is applied at the air-sea interface only. The value for the soluble iron fraction of the aeolian input (fe_{sol}, section 4.10) is given in Table 12.

The particle scavenging iron loss term ($fesca(z)$) is adopted from Moore et al. (2002a). It is assumed that at low iron concentrations (< 0.6 nM) most dissolved iron is bound to organic ligands, but is still weakly particle reactive and at iron concentrations above 0.6 nM particle scavenging rates increase rapidly with increasing iron concentrations. For these assumptions, the iron scavenging can be modeled as:

$$fesca(z) = 2.74\ 10^{-5}\ Fe(z) \quad \text{for } Fe(z)\ < 0.6 \text{ nM}, \tag{40}$$

and

$$fesca(z) = 1.644\ 10^{-5} + 0.0274(Fe(z) - 0.6)\frac{Fe(z) - 0.6}{Fe(z) + 1.4} \quad \text{for } Fe(z)\ > 0.6 \text{ nM}, \tag{41}$$

the scavenged iron is added to the small detrital pool which may remineralize during sinking.

The basic state equation of silicate, which is only used by algal group 5, the diatoms, is of the form

$$\frac{\partial Si}{\partial t} + w\frac{\partial Si}{\partial z} - \frac{\partial}{\partial z}K_z\frac{\partial Si}{\partial z} = -\rho_{Si_5} + c_{Si}De_lSi. \tag{42}$$

The physical and biological processes that affect silicate processes are similar to those included in the nitrate equation (Eq. (35)) except for the addition of silicate through dissolution of large detritus silicate ($c_{Si}De_lSi$) (Nelson et al., 1995).

The loss term for silicate is via uptake by algal group 5 only, as represented by the first term on the right side of Eq. (42). The dissolution rate of detrital silicate, $c_{Si}(z)$, is assumed to follow the temperature function given by Eq. (38) ($c^*_{Si}T_{func}(z)$), and the value used for dissolution rate of silicate at 25°C, c^*_{Si}, is given in Table 12.

IV.9 DETRITUS STATE EQUATIONS

The governing equation for small detrital carbon (De_s) is assumed to be of the form:

$$\frac{\partial De_s}{\partial t} + (w + sc_{des})\frac{\partial De_s}{\partial z} - \frac{\partial}{\partial z}K_z\frac{\partial De_s}{\partial z} =$$
$$\sum_{i=1}^{4}[m_i P_i + (1-\lambda^*)I_{P_i}Z_s] + (e_s + m_{Zs})Z_s - c_c De_s, \qquad (43)$$

where the three terms on the left side represent changes in De_s that are produced by local time variations, vertical advection and sinking (sc_{des}), and vertical diffusive fluxes, respectively. Sinking of the small detritus pool is assumed to occur at a constant rate. The right side of Eq. (43) represents the biological processes that provide sources and sinks of De_s, which includes a source term through the death and unassimilated grazed fraction of algal groups 1 to 4, excretion and mortality of microzooplankton, and a loss term due to remineralization of De_s, respectively. Remineralization of small detritus carbon is modified by temperature ($c^*_c T_{func}(z)$) similar to what was done for remineralization of nitrogen (Eq. 37). The definitions, values, and units of the parameters used in the De_s equations are given in Table 12.

The equation governing the large detrital carbon (De_l) dynamics is similar to Eq. (43) and is of the form:

$$\frac{\partial De_l}{\partial t}+(w+sc_{del})\frac{\partial De_l}{\partial z}-\frac{\partial}{\partial z}K_z\frac{\partial De_l}{\partial z} = m_5P_5+(1-\lambda^*)(I_{P_5}+I_{Z_s})Z_l+(e_l+m_{Zl})Z_l-c_cDe_l. \qquad (44)$$

where increases in large detrital carbon are supported by mortality of algal group 5, the unassimilated fraction (1-λ^*) of algal group 5 and the microzooplankton biomass

that are grazed by mesozooplankton, and excretion (e_l) and mortality (m_{Zl}) by mesozooplankton, respectively. Loss from the large detrital carbon occurs via remineralization (c_c) which is assumed to occur in a similar manner to small detrital carbon. The values for the rates at which these processes occur are given in Table 12.

The state equations for detrital nitrogen, iron, and silicate are similar to Eqs. (43) and (44) except that scavenged iron is assumed to transfer into the small detrital iron pool, and only the large detrital pool is available to provide input to the silicate pool via remineralization (Fig. 2).

IV.10 MODEL IMPLEMENTATION

IV.10.1 Numerical methods

The one-dimensional lower trophic level model was implemented with a coordinate system with the origin at the sea surface and the vertical coordinate positive downward. The model domain extends from the sea surface to 120 m, which is below the 1% light level. This is sufficiently deep to include the total phytoplankton production in the upper waters of the equatorial Pacific.

The system of equations describing the physical and biological dynamics of the state equations (Eqs. 11, 14-16, 33-36, 39, 42-44) was solved numerically using a Crank-Nicholson scheme (Crank, 1956). This numerical integration scheme is unconditionally stable for the parameter ranges used in this study. The vertical coordinate was represented at 1-m intervals, which is sufficient resolution to define features such as the deep chlorophyll maximum that occurs in equatorial Pacific waters (Lindley et al., 1995). A one-hour interval was used for the time integration, which allows resolution of the diurnal periodicity in phytoplankton growth kinetics.

IV.10.2 Surface and bottom boundary conditions for Cold Tongue simulations

Surface boundary conditions were specified as no flux conditions (i.e. Neumann conditions) for all model state variables except for iron. For iron, the daily atmospheric dust flux in g m^{-2} hr^{-1}, obtained from Ginoux et al. (2001), was used to specify an input. This input was specified from the sum of four dust size classes (0.1-1, 1-2, 2-3 and 3-6 μm). The mass fraction of iron in the mineral dust aerosol was assumed to be 0.05 for the first size class and 0.012 for the remaining size classes (Fung et al., 2000). The soluble iron fraction (fe_{sol}, Eq. (39)) was taken to be 0.1 (Duce et al., 1991; Duce and Tindale, 1991). The dust flux in g m^{-2} hr^{-1} was converted to a flux in nmol l^{-1} hr^{-1} (FFe in Eq. 39) by using appropriate scaling factors. It was assumed that the dust deposited on 1 m^{-2} at the sea surface was introduced to a 1 m^{-3} water volume.

The bottom boundary conditions for nitrate, silicate and iron were specified using a temperature-nutrient relationship. The nitrate (NO_3^-) and iron (Fe) dependencies on temperature (T) were taken from Barber and Chavez (1991) and Leonard et al. (1999), respectively, and are given as

$$NO_3^-(z,t) = 66.69 - 3.89\,T(z,t) + 0.06\,T(z,t)^2, \tag{45}$$

$$Fe(z,t) = 0.499 - 0.019\,T(z,t), \tag{46}$$

where NO_3^- and Fe are in μmol l^{-1} and nmol l^{-1}, respectively. The depth and time varying temperature was obtained from the time series measured at TAO mooring arrays (Chapter 3).

A silicate (Si) to temperature (T) regression was developed using data from four 1992 JGOFS EqPac cruises:

$$Si(z,t) = 26.3462 - 0.895590\,T(z,t). \tag{47}$$

An ammonium to temperature relationship does not exist and therefore the Christian et al. (2002a) simulation was used to set the ammonium bottom boundary conditions at 120 m. The time interval of the Christian et al. (2002a) simulation was 6 days, so these values were linearly interpolated to 1-hour time intervals, to be consistent with the time integration of the model used in this study.

IV.10.3 Initial vertical profiles

Initial profiles of phytoplankton, small and large zooplankton and detritus, and ammonium were obtained from the Christian et al. (2002a) simulation at 20 depth intervals and linearly interpolated to 1-m depth intervals. The small and large phytoplankton compartments obtained from the Christian et al. (2002a) simulation were partitioned into 5 algal groups based on the relative ratios of these algal groups measured during the JGOFS cruises (Landry et al., 1996; Iriarte and Fryxell, 1995). The initial profiles of nitrate, iron, and silicate were estimated using the nutrient to temperature relations. Very small (0.0001 μmol C l^{-1}) threshold values were set for the phytoplankton and zooplankton state variables, so that these concentrations do not become zero. this provides a refuge for these ecosystem components so they can respond when conditions become favorable for growth.

IV.10.4 Boundary conditions for the Warm Pool

The nitrate to temperature and silicate to temperature regressions at 120 m are estimated using the climatological data at 0°N, 165°E from Conkright et al. (2002) as

$$NO_3^-(z,t) = 35.39 - 1.18\,T(z,t) \tag{48}$$

and

$$Si(z,t) = 15.9 - 0.50\,T(z,t), \tag{49}$$

where NO_3^- and Si are in μmol l^{-1}.

The iron to temperature regression is the modified form of the iron to temperature regression developed for 0°N, 140°W. For 0°N, 165°E, the regression is substituted to match the corresponding temperatures at 120 m as

$$Fe(z,t) = 0.499 - 0.013\,T(z,t), \tag{50}$$

where Fe is in nmol l^{-1}.

Because an ammonium to temperature relationship does not exist, the results of the Christian et al. (2002a) simulation are used to set the ammonium bottom boundary conditions at 120.

IV.10.5 Nutrient and light limitation conditions

Nutrient uptake is calculated separately from carbon growth and all nutrients taken up by phytoplankton are added to the particulate nutrient pool of each algal group (see section 4.3). During light limitation, the nutrient uptake rate can greatly exceed that of the light-limited carbon growth rate. For example, the cellular nitrogen to carbon (AGN_1:AG_1) ratio and cellular iron to carbon ($AGFe_1$:AG_1) ratio for algal group 1 are allowed to drop to minima of 5.5 μmol N (μmol C)$^{-1}$ and 0.031 nmol Fe (μmol C)$^{-1}$, respectively, during uptake of nitrogen and iron (Table 7). Nutrient uptake continues over 24 hours and is subject to the minimum carbon to nutrient ratios. The minimum carbon to nutrient ratios of each AG and for each limiting nutrient are given in Table 7 in the form of maximum nutrient to carbon ratios (e.g., $Q_{N_{max}}$ for nitrogen to carbon ratio).

Light begins to inhibit algal group 1 and algal group 2 at 40 and 105 μmol quanta m^{-2} s^{-1}, and a zero growth rate is reached at 110 and 10300 μmol quanta m^{-2} s^{-1}, respectively (Moore et al., 1995). The zero growth light intensities were determined by extrapolating the log-linear plot of growth versus irradiance given in Moore et al. (1995) to its zero intercept. Inhibition is assumed to exponentially reduce the maximum growth rate (see section 4.4).

CHAPTER V

RESULTS

V.1 REFERENCE SIMULATION

The ecosystem model described in the previous section was first used to establish a reference simulation that provides the basis for comparisons with other simulations that are designed to test model sensitivity to variations in processes and parameter values. The reference simulation is for one year, 1992, and for a site at 0°N, 140°W. This time and location corresponds to the U.S. JGOFS EqPac cruises (Murray et al., 1995). The observations from these cruises (Table 2, Chapter 3) provide verification of the results obtained from the reference simulation. The time period of the reference simulation includes an El Niño event and the transition from El Niño to non-El Niño (normal) conditions (Murray et al., 1992).

The environmental time series input to the ecosystem model are described in the following section. This is followed by descriptions of the simulated depth-time distribution of the state variables and of the derived quantities obtained from the reference simulation.

V.1.1 Reference simulation forcing

The surface temperature time series (Fig. 4A) obtained at 0°N, 140°W from the TAO mooring shows values of 28 to 29°C from January to about May 1992 which is indicative of El Niño conditions (Murray et al., 1992). The range of temperature variability during this time is small, being less than 2°C. In May 1992, the surface temperature decreases by about 4°C over two months to about 25°C. This decrease is associated with the transition from El Niño to non-El Niño conditions. For the remainder of 1992 surface temperature remains around 25°C, which is reflective of the cooler temperatures associated with non-El Niño conditions in this part of the equatorial Pacific (Philander, 1990). The latter portion of the surface temperature time series (Fig. 4A) shows some high frequency variability, such as the events that

occur at Year Day (YD) 210, YD260, and YD310. This variability, which occurs with about a 20-day time scale, is associated with TIWs (Qiao and Weisberg, 1995; Yu et al., 1995; Friedrichs and Hofmann, 2001).

The subsurface temperatures at 120 m started to drop by the end of February, indicating the waning of El Niño conditions. Wunsch and Gill (1976) and Friedrichs and Hofmann (2001) show that physical variability in the central equatorial Pacific is also present at frequencies shorter than the 20-day events, and that these short period events produce subsurface temperature oscillations of 2-4°C, with periods of 6-8-days (Fig. 4A). These temperature oscillations are consistent with the period of the IGWs (Wunsch and Gill, 1976).

The vertical velocity time series used to force the ecosystem model (Fig. 4B) was calculated from the TAO mooring temperature observations as described in section 3.1. The vertical velocities during the first three months of 1992 show the passage of a low frequency wave with a period of 60 days which is associated with a Kelvin wave (Kessler et al., 1995). During the same time vertical velocities show periods of strong upwelling and downwelling, with maximum magnitudes of ± 30 m d^{-1}. These strong upwelling/downwelling velocities are associated with IGWs. From about YD100 through the transition to non-El Niño conditions at about YD200 (late summer) the magnitude of the vertical velocity is reduced (± 10 m d^{-1}) and is characterized by variability that occurs at a 6-8-day interval, which is associated with IGWs. The latter portion of the vertical velocity time series (YD210 onwards) is characterized by higher vertical velocities (10-20 m d^{-1}), and 7 strong upwelling/downwelling events, which occurred with a frequency of $\sim$20-days. These events are associated with the passage of TIWs (Qiao and Weisberg, 1995; Friedrichs and Hofmann, 2001).

The mixed layer depth time series (Fig. 4C) computed from temperature measurements as described in section 3.1, shows depths in excess of 100 m during El Niño conditions. These depths are consistent with the deeper mixed layers that occur in the eastern equatorial Pacific during El Niño conditions, which were measured during the S1 and TS1 cruises (not shown). As the eastern Pacific transitioned to non-El Niño conditions, mixed layer depths decreased and remained between 20 and 40 m

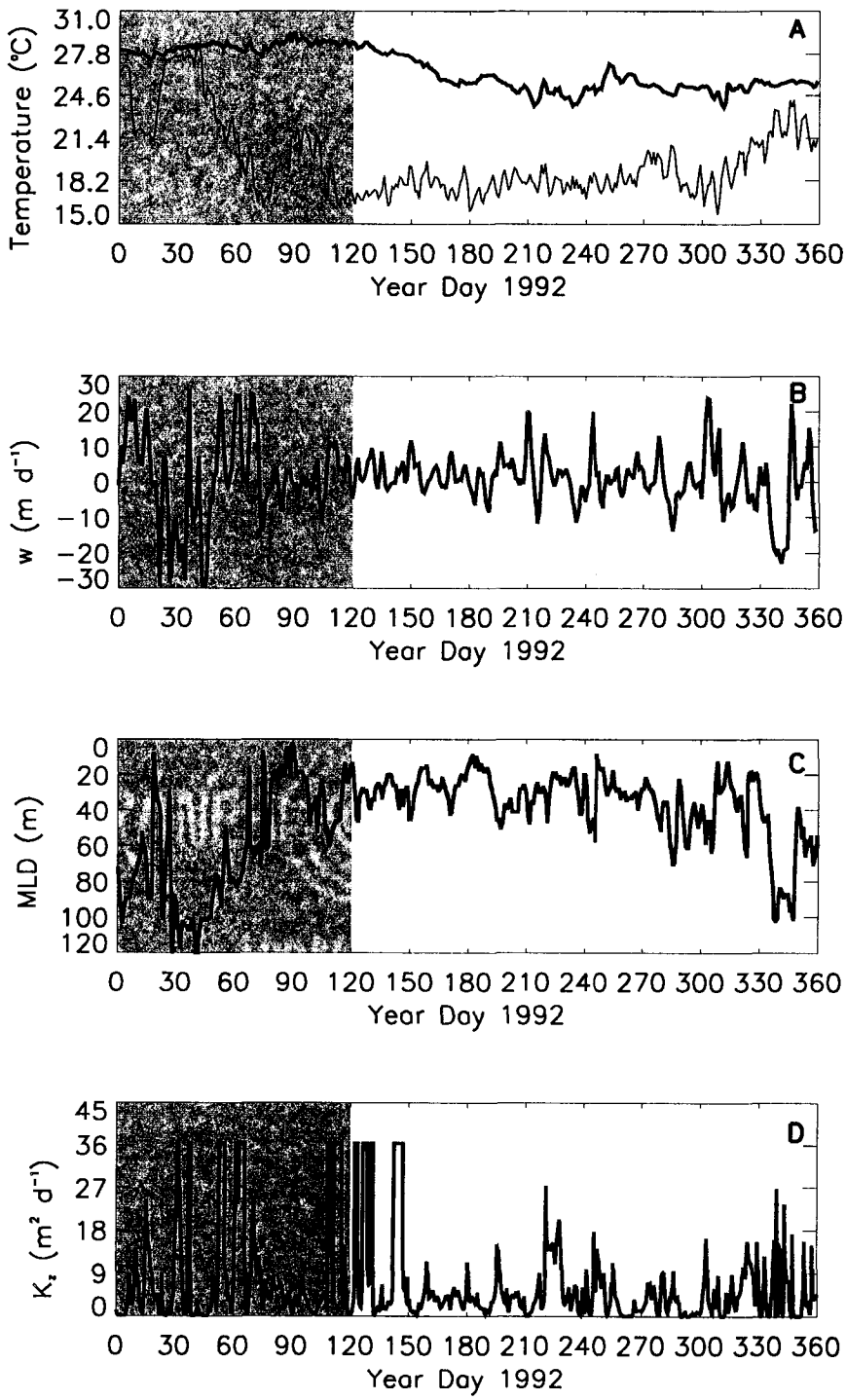

Fig. 4. Time series of (A) surface temperature (thick solid line) and temperature at 120 m (thin solid line), (B) vertical velocity (w) at 40 m, (C) mixed layer depth (MLD), and (D) vertical diffusivity coefficient (K_z) at 25 m estimated from observations obtained from the TAO mooring at 0°N, 140°W as discussed in Chapter 3. Shaded regions denote the El Niño season.

for most of the remainder of 1992. The higher frequency variations in mixed layer depth observed from about YD100 to YD330 are associated with the passage of TIWs and IGWs. The extended period of relatively shallow mixed layer depths from about YD150 to YD190 is the result of isotherm shoaling during the transition period. The rapid deepening of the mixed layer to 100 m at about YD330 is associated with a period of strong downwelling (Fig. 4B).

The time series of the vertical diffusivity coefficient (K_z) at 25 m (Fig. 4D), which is computed as described in section 3.1, shows high values from about YD20 to YD75 that correspond to the time of maximum downwelling velocities (Fig. 4B) and mixed layer depth (Fig. 4C). The maximum value for this coefficient is 36 $m^2 d^{-1}$, that is set in the Pacanowski and Philander (1981) formulations. The maximum value of K_z is reached when the shear of the horizontal currents (u, v) is high. From about YD110 to YD150, during the transition to non-El Niño conditions, the vertical diffusivity coefficient remains relatively high because of high current shear. From YD150 throughout the remainder of 1992, the value of K_z fluctuates between near zero and about 20 m^2 d^{-1}, with only occasional higher values. The high frequency variations in K_z during the latter portion of the time series are produced by TIWs and IGWs. The values of K_z derived from the TAO mooring observations using the Pacanowski and Philander (1981) formulations are consistent with those reported in other studies of the mixing dynamics of the equatorial Pacific (Peters et al., 1981).

The simulated downwelling irradiance just below the sea surface changes between 50 and ~500 μmol quanta m^2 s^{-1} during the first five months of 1992 (Fig. 5A). The large fluctuations and reduced irradiance during this time result from extensive cloud cover that is characteristic of El Niño conditions in the eastern equatorial Pacific (Philander, 1990). After transition to non-El Niño conditions, fluctuations in the simulated irradiance just below the sea surface are dampened and the high frequency fluctuations that occur are consistent with the clear skies and reduced cloudiness that occurs when these conditions prevail (Philander, 1990). The irradiance level increases during the spring and into the summer, reaching a maximum of about 500 μmol quanta m^2 s^{-1} in late summer to early Fall. The decrease of about 50

μmol quanta m^2 s^{-1} in late Fall to early winter is produced by seasonal decreases in solar radiation at this location (Foley et al., 1997). The pattern of the simulated irradiance at various depths throughout the upper 100 m of the water column (Fig. 5B) is similar to that just below the surface (Fig. 5A). However, the magnitude of irradiance is diminished, essentially nearly zero at 100 m (Fig. 5B). In general, the 10% and 1% light levels are located between 70-90 m and 100-120 m, respectively, throughout 1992. These values are consistent with other estimates of euphotic zone depths for this region (Walsh et al., 1995).

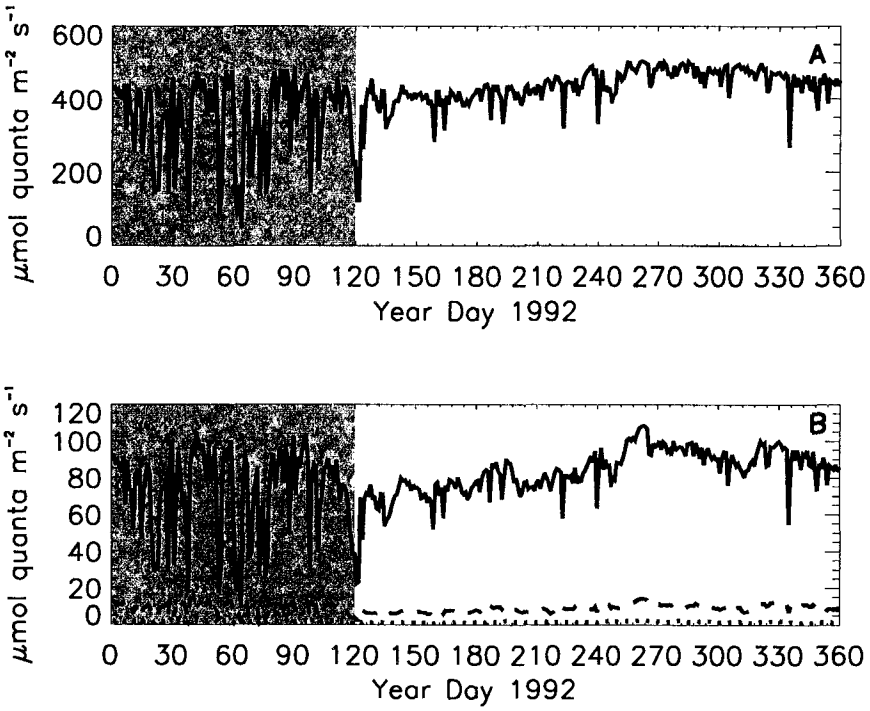

Fig. 5. Time series of (A) simulated daily integrated downwelling irradiance (PAR) just below the surface and simulated daily integrated downwelling irradiance arriving at (B) 20 m (solid line), 60 m (dashed line), and 100 m (dotted line). The depth-dependent irradiance values are obtained from the irradiance model described in section 3.2. Shaded regions denote the El Niño season.

V.1.2 Simulation of algal groups

The simulated depth-time distributions in the upper 100 m of the five algal groups at 0°N, 140°W for 1992 show the general features of low biomass during the first 100 days followed by increased biomass from about YD120 on and persisting for the remainder of 1992 (Fig. 6). The initial low biomass corresponds to El Niño conditions (see previous section) and deep mixed layers (Fig. 4C). Throughout the latter part of the simulations each algal group shows episodic increases/decreases in biomass, with these events lasting for 6 to 20 days. The integrated annual biomass in the upper 120 m of the ocean estimated from these simulated algal group distributions was 61,667 mmol C m^{-2} (Table 13).

The simulated depth-time distribution of the low light-limited *Prochlorococcus* (Fig. 6A) shows that this algal group has very low concentrations during El Niño conditions and blooms only after the transition to non-El Niño conditions. The biomass maximum for this algal group occurs below the mixed layer at depths greater than 40 m (Fig. 6A). The maximum concentration obtained for this algal group during the one-year simulation was 0.34 μmol C l^{-1} and occurred at 50 m on YD117.

The high-light adapted *Prochlorococcus* occurs in the upper water column, generally above 40 m (Fig. 6B). The simulated depth-time distribution for this algal group shows a large bloom, maximum concentration of 0.47 μmol C l^{-1}, that persists from about YD115 to YD180. This bloom occurs just after the transition from El Niño to non-El Niño conditions (Fig. 5). Throughout the latter portion of the simulation, algal group 2 shows episodic blooms, but the magnitude is less than the first large bloom. A small duration, but relatively high biomass bloom, occurred at the end of the simulation between YD320 and YD330.

The simulated depth-time distribution for algal group 3, *Synechecoccus*, shows the most variability of all five algal groups (Fig. 6C). This algal group blooms repeatedly over the course of the one-year simulation. The blooms are of short duration, 10 to 20 days, and are characterized by biomass greater than 0.3 μmol C l^{-1}. The maximum simulated biomass for this algal group was 0.39 μmol C l^{-1} which occurred

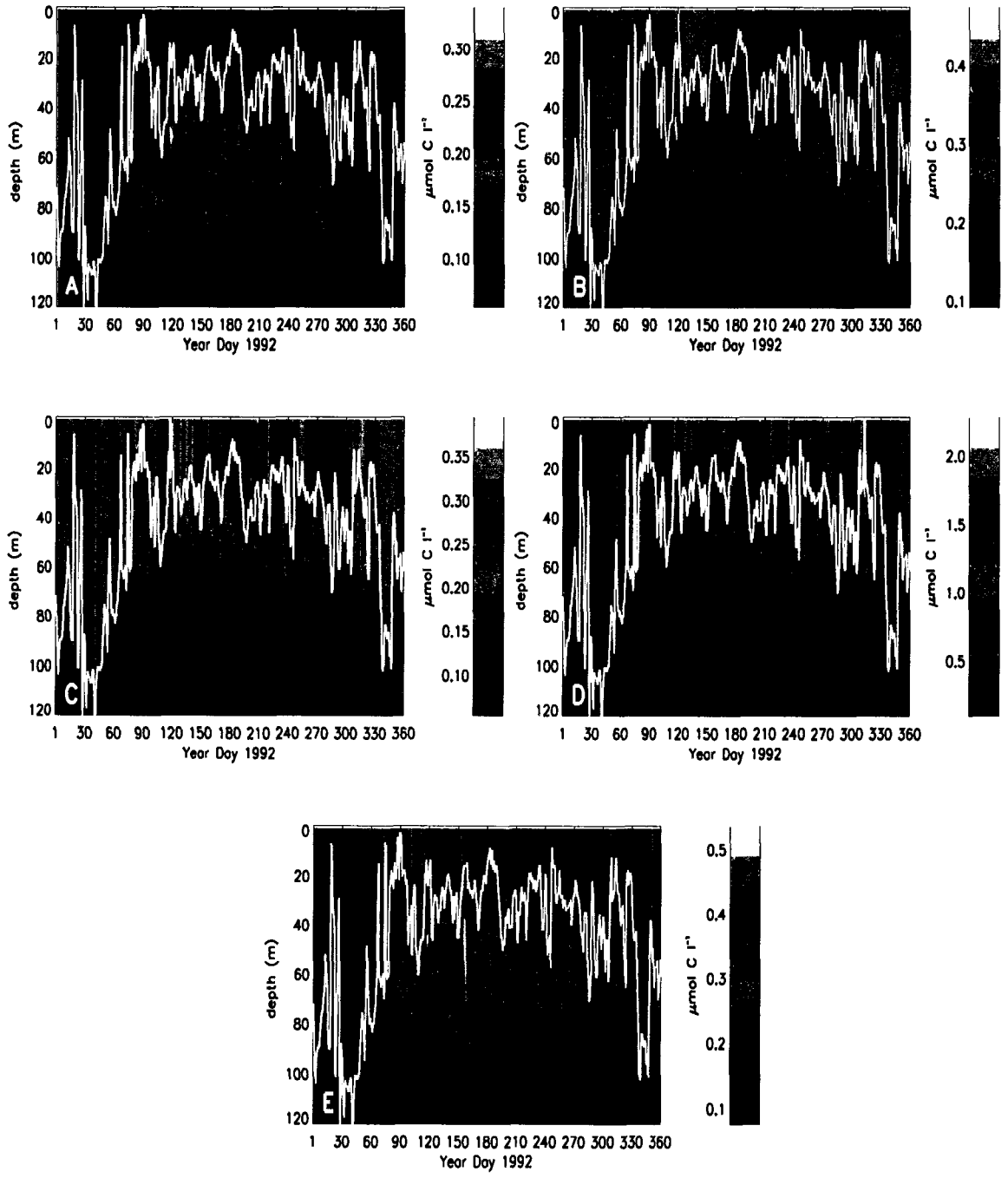

Fig. 6. Simulated depth-time distributions of daily-averaged algal biomass (μmol C l^{-1}) of (A) low light-adapted *Prochlorococcus* (algal group 1), (B) high light-adapted *Prochlorococcus* (algal group 2), (C) *Synechococcus* (algal group 3), (D) autotrophic eukaryotes (algal group 4), and (E) large diatoms (algal group 5). Overlaid solid white line represents the mixed layer depth, which is obtained as described in section 3.1. Lighter colors indicate higher concentrations.

Table 13
Annual integrated carbon biomass (Biomass, mmol C m^{-2} yr^{-1}), percentage of total biomass, annual integrated primary production (PP, mmol C m^{-2} yr^{-1}), and percentage of total primary production for each algal group (AG) calculated from the reference simulation done at 0°N, 140°W for 1992

	Biomass	Total biomass (%)	PP	Total PP (%)
$AG1$	4,888	8	390	2
$AG2$	10,831	18	2,597	12
$AG3$	7,527	13	2,634	12
$AG4$	31,060	50	15,689	69
$AG5$	7,358	12	1,166	6

on YD117 in the upper 10 m of the water column (Fig. 6C). However, despite the numerous episodic blooms of this algal group, the biomass integrated over 120 m for *Synechecoccus* (21 $m$mol C m^{-2}) is less than that for *Prochlorococcus* (43 $m$mol C m^{-2}).

The simulated biomass for algal group 4, the autotrophic eukaryotes, is the highest of all five algal groups (Fig. 6D, Table 13). This algal group showed 12 intense blooms during the one-year simulation (Fig. 6D), which are at least double the background biomass concentration of this group. The highest biomass (2.27 μmol C l^{-1}) was associated with the bloom that occurred between YD300 and YD330. The majority (52%) of the biomass of algal group 4 occurs in the mixed layer at depths shallower than 45 m.

The simulated biomass of algal group 5, the large diatoms, occurred mostly below the mixed layer (Fig. 6E). Maxima in biomass are confined to short duration (8 days) intense (e.g., 0.54 μmol C l^{-1} on YD117) blooms, the majority of which occurs during the first 210 days of the simulation. The contribution of this algal group to the overall water column biomass is only 12% (Table 13) over the one-year simulation. Similar to algal group 1, the diatoms are essentially not present during the initial part of 1992 when El Niño conditions prevail.

Chlorophyll a distributions

The simulated time-depth distribution of chlorophyll *a* concentrations obtained from the sum of all five algal groups (Fig. 7) shows patterns that are similar to those for the simulated biomass distributions. A deep chlorophyll maximum always exists during the year, but it is lower and deeper during the El Niño period compared to the rest of the year.

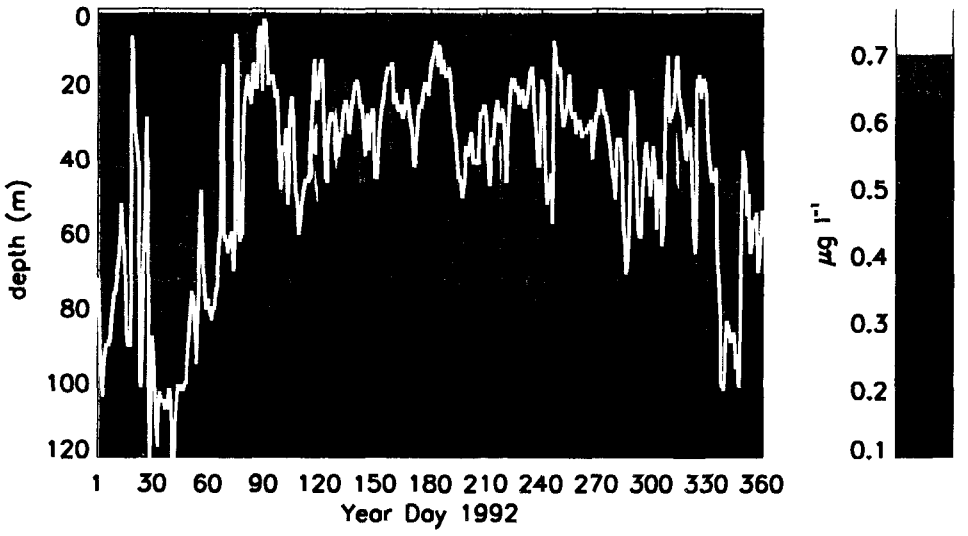

Fig. 7. Simulated depth-time distribution of daily-averaged chlorophyll *a* (μg l^{-1}) obtained from the sum of all five algal groups. Overlaid solid white line represents the mixed layer depth, which is obtained as described in section 3.1. Lighter colors indicate higher concentrations.

The simulated chlorophyll *a* concentrations show a non-homogeneous distribution in the mixed layer. At the surface, chlorophyll *a* concentrations are low and then increase towards the bottom of the mixed layer. The deep chlorophyll maximum is generally located just below the mixed layer during most of the year, but during periods of extensive deepening of the mixed layer (YD25-40 and YD340-350) it is situated above the mixed layer. At around 100 m, chlorophyll *a* concentrations drop below 0.15 μg l^{-1}.

During the first three months of the year chlorophyll *a* concentrations are lower in

the mixed layer compared to the rest of the year. A weak deep chlorophyll maximum is observed around 80 m during this time; whereas, during the rest of the year it is stronger with a maximum value of 0.75 μg l^{-1} on YD127 at 35 m. Throughout the year, there are three periods (YD120-140, YD200-240, YD300-330) when the deep chlorophyll maxima is well developed and is characterized by high chlorophyll *a* concentrations.

Simulated algal group rates

Primary production

The simulated depth-time distribution of primary production for the five algal groups (Fig. 8) shows patterns that are similar to those for the simulated biomass distributions. Primary production is low during El Niño conditions, increases during non-El Niño conditions and occurs in episodic events of varying duration. The primary production patterns (Fig. 8) are vertically less dispersed compared to the vertical biomass distributions (Fig. 6).

The simulated primary production for algal group 1 (Fig. 8A) occurs in a narrow band below the mixed layer between 45 and 70 m. Maximum production occurs between YD80 and YD160, with the maximum value of 0.065 μmol C l^{-1} d^{-1} on YD116 at 49 m. Overall, algal group 1 accounted for only 2% of the annual integrated primary production at 0°N, 140°W (Table 13). In contrast, primary production of the high-light adapted *Prochlorococcus* occurs at shallower depths (with maximum concentration of 0.23 μmol C l^{-1} d^{-1} at 16 m on YD130), mainly above 40 m throughout the one-year simulation (Fig. 8B). The most intense primary production event by this algal group, however, occurred between YD120 and YD150. This one event accounts for 20% of the simulated primary production of the algal group for 1992.

The simulated primary production for algal groups 3 and 4 is confined to the upper 20-40 m and occurs in several episodic events during the one-year simulation. The timing of the maxima in primary production for the two algal groups is similar. However, the primary production of algal group 4 is considerably higher than that of algal group 3, 15,689 mmol C m^{-2} yr^{-1} versus 2,634 mmol C m^{-2} yr^{-1}, respectively (Table 13).

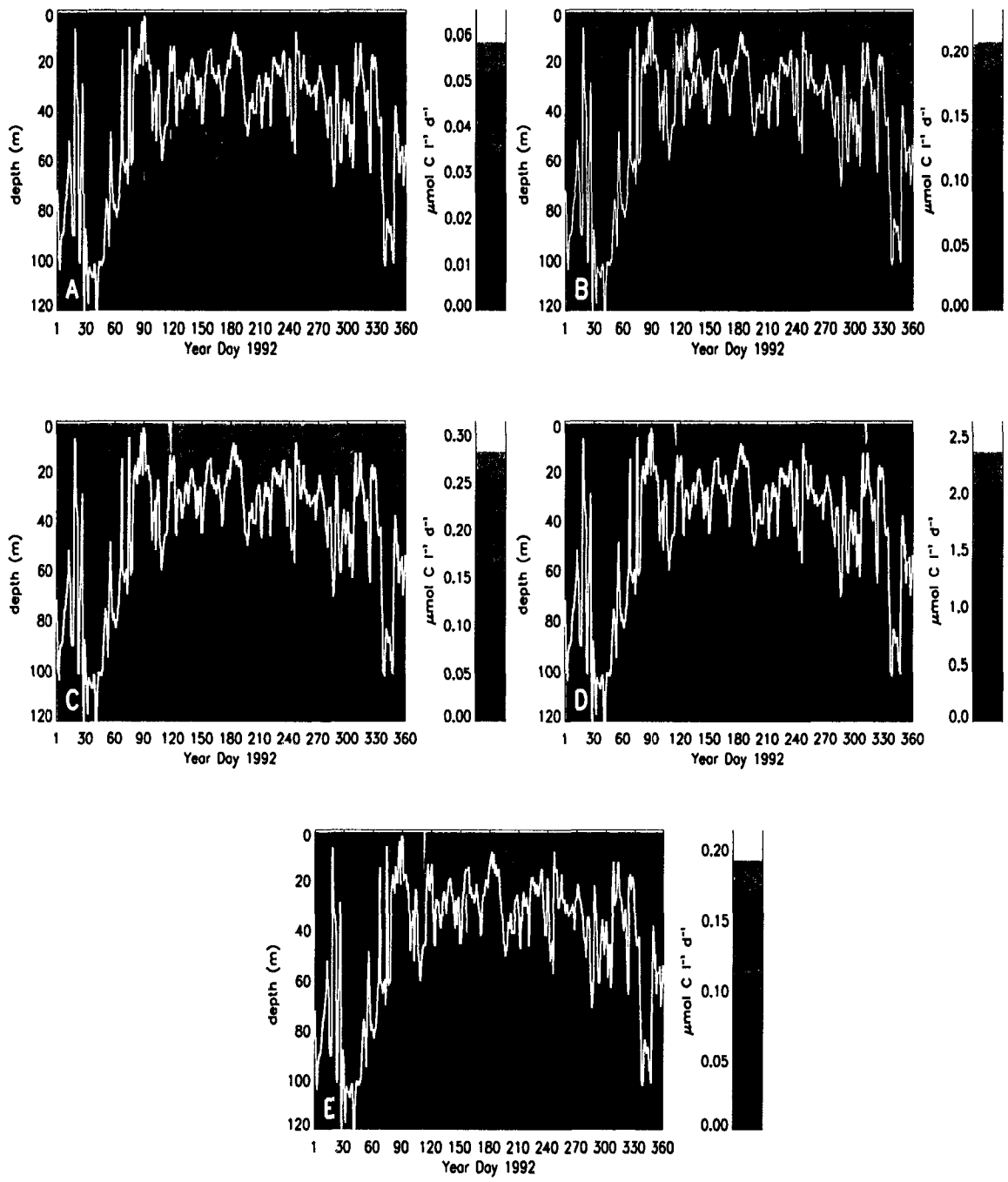

Fig. 8. Simulated depth-time distributions of daily-averaged algal primary production (μmol C l^{-1} d^{-1}) of (A) low light-adapted *Prochlorococcus* (algal group 1), (B) high light-adapted *Prochlorococcus* (algal group 2), (C) *Synechococcus* (algal group 3), (D) autotrophic eukaryotes (algal group 4), and (E) large diatoms (algal group 5). Overlaid solid white line represents the mixed layer depth, which is obtained as described in section 3.1. Lighter colors indicate higher rates.

The primary production associated with algal group 5 occurs in a band that is centered about 40 m. The highest primary production by this group occurs on YD155 at 30 m. The only appreciable primary production by this algal group above 40 m occurs in a short duration pulse at YD112. The overall pattern of primary production for this algal group is one of short duration intense pulses, and as such differs from what is observed for the other algal groups. As a result, the contribution of this algal group to the integrated annual primary production is only 6% (Table 13).

Growth rates

The maximum daily growth rates for each algal group occur at different depths and days (Figs. 9A-E, 10A-E, 11A-E). All groups reach their maximum actual growth rates during the first half of the year (Table 14) and the highest and the lowest light-limited growth rates for all algal groups occur when El Niño conditions prevail (Figs. 9A-E). The narrow bands of low light-limited growth rates are distributed among high light-limited growth rates during this part of the year, resulting in a high variability in light-limited growth rates (Figs. 9A-E). The highest nutrient-limited growth rates are also observed during El Niño conditions (Figs. 10A-E), but these high growth rates generally occur below the mixed layer, except for algal group 1. Within the mixed layer, all algal groups, except algal group 1 are nutrient-limited (Figs. 10A-E) and the levels of nutrient limitation experienced by each algal group show temporal variability.

The simulated depth and time distribution of the light-limited growth rate for algal group 1 increases from a value of zero at the surface to a maximum value between 40 and 60 m, after which it decreases (Fig. 9A). There are short periods of high light-limited growth rates reached by this group, that occur at shallow depths (i.e. 20 m). These periods are especially common during El Niño conditions, such as the event on YD60-YD75 at $\sim$20 m. The simulated distribution of the nutrient-limited growth rate of this group shows little variation over the one-year simulation (Fig. 10A). In the surface waters, algal group 1 is strongly light inhibited and nutrient

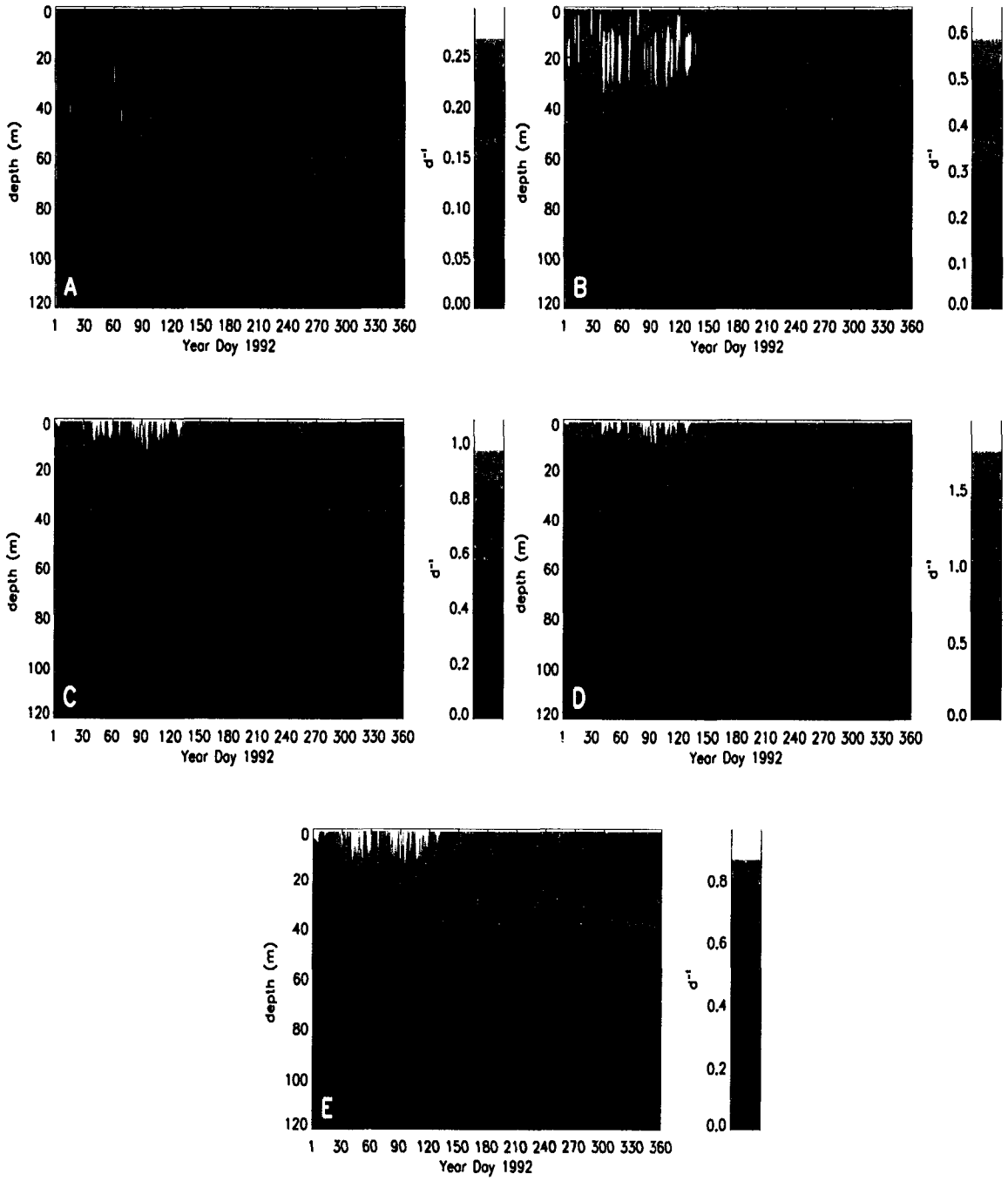

Fig. 9. Simulated depth-time distributions of daily averaged light-limited growth rates (d^{-1}) of (A) low light-adapted *Prochlorococcus* (algal group 1), (B) high light-adapted *Prochlorococcus* (algal group 2), (C) *Synechococcus* (algal group 3), (D) autotrophic eukaryotes (algal group 4), and (E) large diatoms (algal group 5). Lighter colors indicate higher rates.

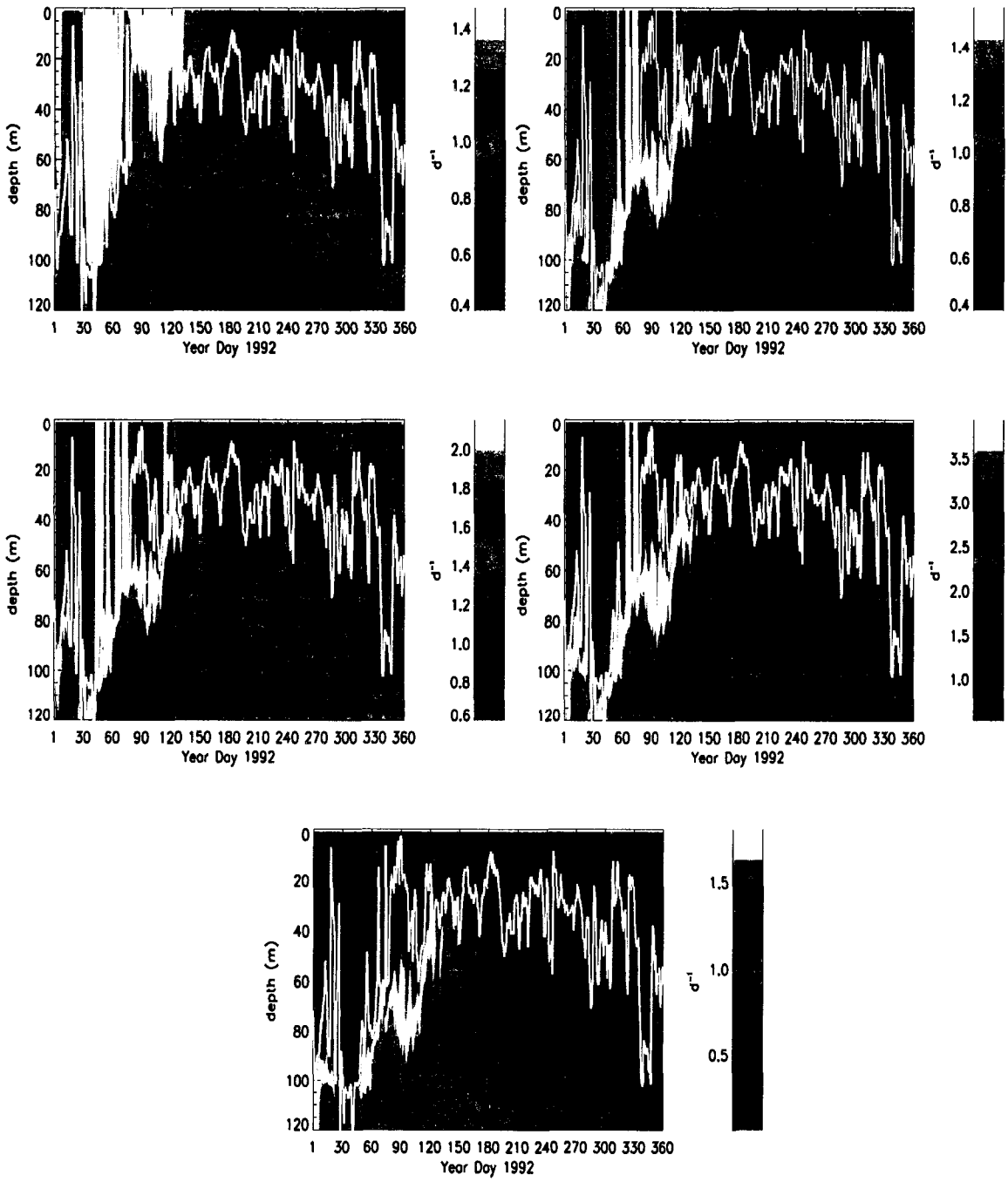

Fig. 10. Simulated depth-time distributions of daily averaged nutrient-limited growth rates (d^{-1}) of (A) low light-adapted *Prochlorococcus* (algal group 1), (B) high light-adapted *Prochlorococcus* (algal group 2), (C) *Synechococcus* (algal group 3), (D) autotrophic eukaryotes (algal group 4), and (E) large diatoms (algal group 5). Overlaid solid white line represents the mixed layer depth, which is obtained as described in section 3.1. Lighter colors indicate higher rates.

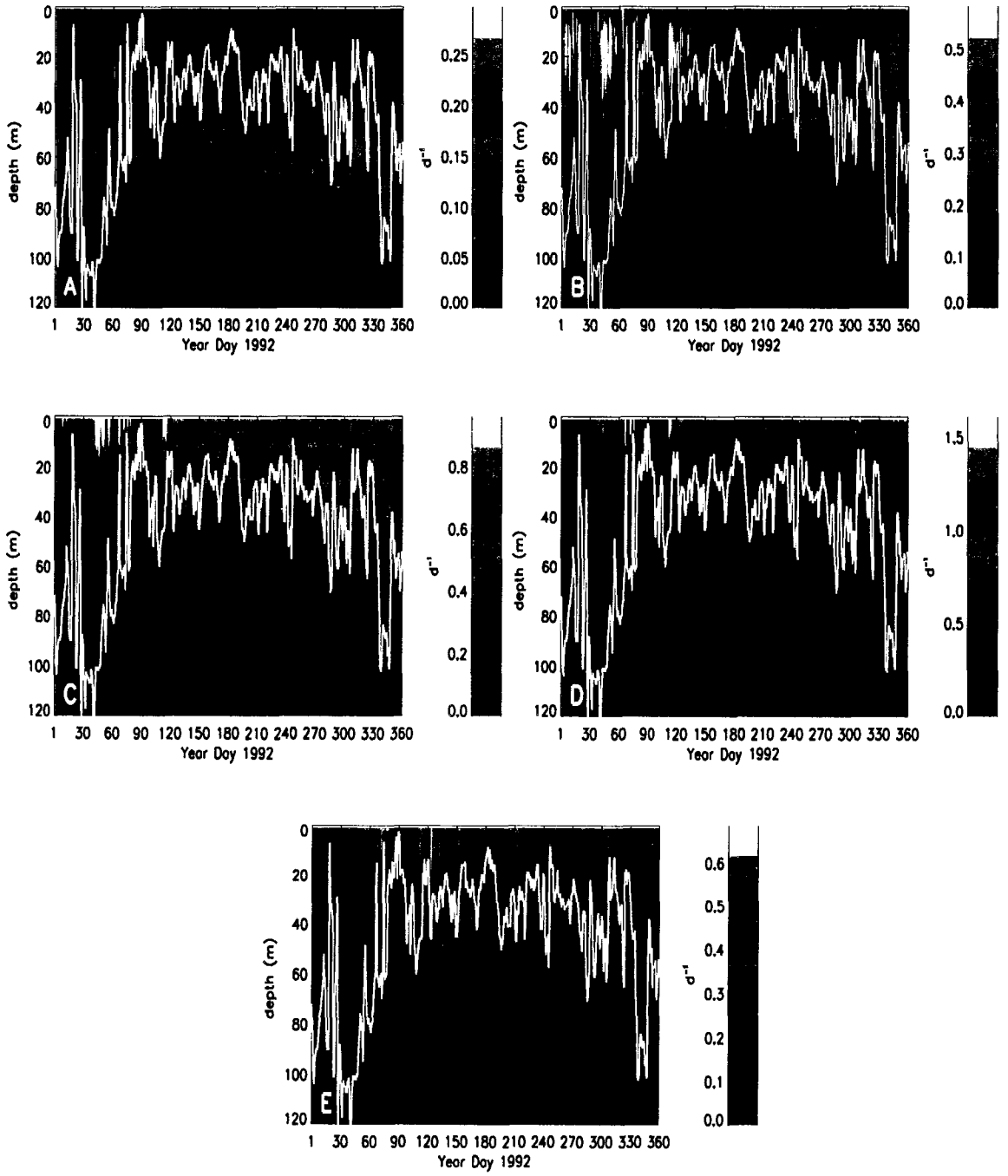

Fig. 11. Simulated depth-time distributions of daily averaged actual growth rates (d^{-1}) of (A) low light-adapted *Prochlorococcus* (algal group 1), (B) high light-adapted *Prochlorococcus* (algal group 2), (C) *Synechococcus* (algal group 3), (D) autotrophic eukaryotes (algal group 4), and (E) large diatoms (algal group 5). Overlaid solid white line represents the mixed layer depth, which is obtained as described in section 3.1. Lighter colors indicate higher rates.

Table 14
Maximum (Max) actual growth rate, day of occurrence, and depth of occurrence for each algal group

	Max growth rate (d^{-1})	Time of occurrence (YD)	Depth (m)
*AG*1	1.32	38	75
*AG*2	1.56	113	13
*AG*3	2.18	113	surface
*AG*4	3.9	64	surface
*AG*5	1.77	109	59

Maximum rates were obtained from the reference simulation done at 0°N, 140°W for 1992.

limitation has a very weak effect on this algal group (Figs. 9A and 10A). As a result, the actual growth rate of algal group 1 is similar to the light-limited growth rate distribution (Figs. 11 and 9A) for this group. This indicates that the growth of this group is controlled mainly by light.

In the surface waters, the light-limited growth rate of algal group 2 is below its maximum value due to light inhibition and it reaches its maximum value between 10-30 m (Fig. 9B). Similar to algal group 1, short periods of high light-limited growth rate values of this algal group occur at shallow depths when El Niño conditions are present. Nutrient limitation on the growth rate of algal group 2 occurs for short periods during YD70-YD100, YD180-YD200, and YD250-YD260 in the mixed layer. As a result, the combined effects of light inhibition (Fig. 9B) and nutrient limitation (Fig. 10B) control the growth rate of algal group 2, and the actual growth rate (Fig. 11B) of this group reflects the effects of both processes.

The effect of light limitation on the growth rates of algal groups 3 to 5 is similar (Figs. 9C-E). These groups do not experience any light limitation in the surface waters and their growth rates gradually decline below 20 m, dropping to zero around

80 m. The influence of nutrient limitation on growth is less on algal group 3 compared to algal groups 4 and 5 (Figs. 10C-E). Algal group 5 is most strongly limited by nutrients compared to the other algal groups. The combined effect of light and nutrients on algal groups 3 to 5 is such that the daily-averaged actual growth rates of these algal groups are mainly controlled by nutrient limitation in the mixed layer and by light limitation below the mixed layer (Figs. 11C-E).

Algal group cellular nutrient ratios

Cellular nutrient to carbon ratios of the algal groups are good indicators of nutrient-limited growth. The simulated cellular nitrogen to carbon ratios stay at their maximum values for all algal groups except algal group 2 (Figs. 12A-E). This indicates that only algal group 2 is limited by nitrogen during the year. The cellular nitrogen to carbon ratios for this group show considerable temporal variability during the year and that nitrogen limitation occurs primarily in the mixed layer. During the warm El Niño period the cellular nitrogen to carbon ratios are at or close to their maximum values and stay below maximum values for the rest of the year. The cellular nitrogen to carbon ratios of algal group 2 are homogeneous within the mixed layer, and they reach their maximum values just below the mixed layer.

The cellular iron to carbon ratios of all groups are homogeneous within the mixed layer and begin to increase at the bottom of the mixed layer, reaching their maximum values 5 to 30 m below the mixed layer (Figs. 13A-E). The cellular iron to carbon ratios of algal group 1 are always at their maximum values (Fig. 13A), which indicates that this group is not iron limited. Cellular iron to carbon ratios of algal groups 2 and 3 remain lower than their maximum values within the mixed layer except for YD60-75, YD210-225, and YD310-320 (Figs. 13B and C). The cellular iron to carbon ratios for algal groups 4 and 5 are at their minimum values within the mixed layer during most of the year (Figs. 13D and E). For these groups, the cellular iron to carbon ratios never reach their maximum value within the mixed layer, with the exception of algal group 4, which reaches its maximum ratio value at YD307.

In the model, only algal group 5 has a cellular silicate compartment (Fig. 2). The

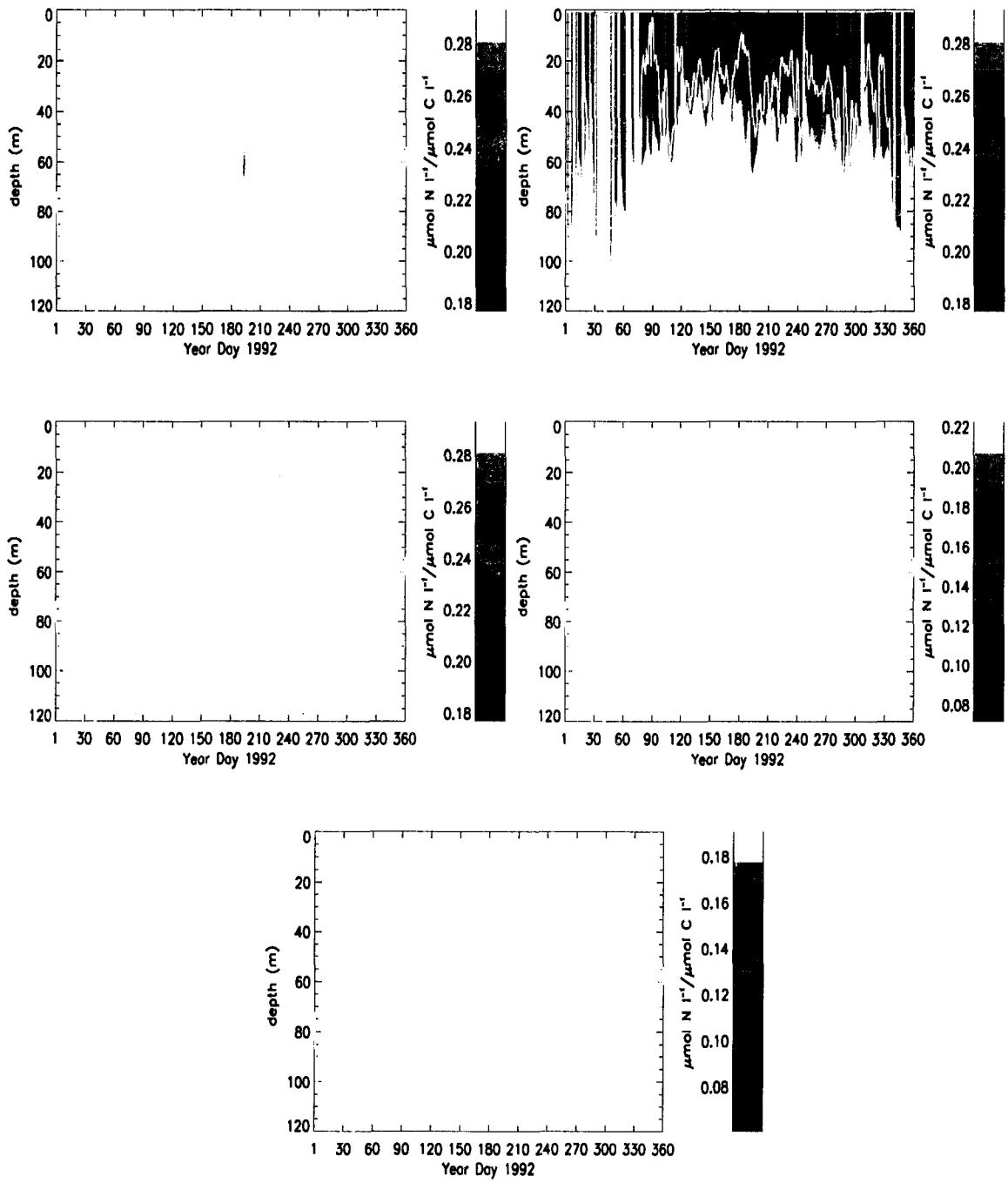

Fig. 12. Simulated depth-time distributions of cellular nitrogen to carbon ratios (μmol N l^{-1}/μmol C l^{-1}) of (A) low light-adapted *Prochlorococcus* (algal group 1), (B) high light-adapted *Prochlorococcus* (algal group 2), (C) *Synechococcus* (algal group 3), (D) autotrophic eukaryotes (algal group 4), and (E) large diatoms (algal group 5). Overlaid solid white line represents the mixed layer depth, which is obtained as described in section 3.1. Lighter colors indicate higher ratios.

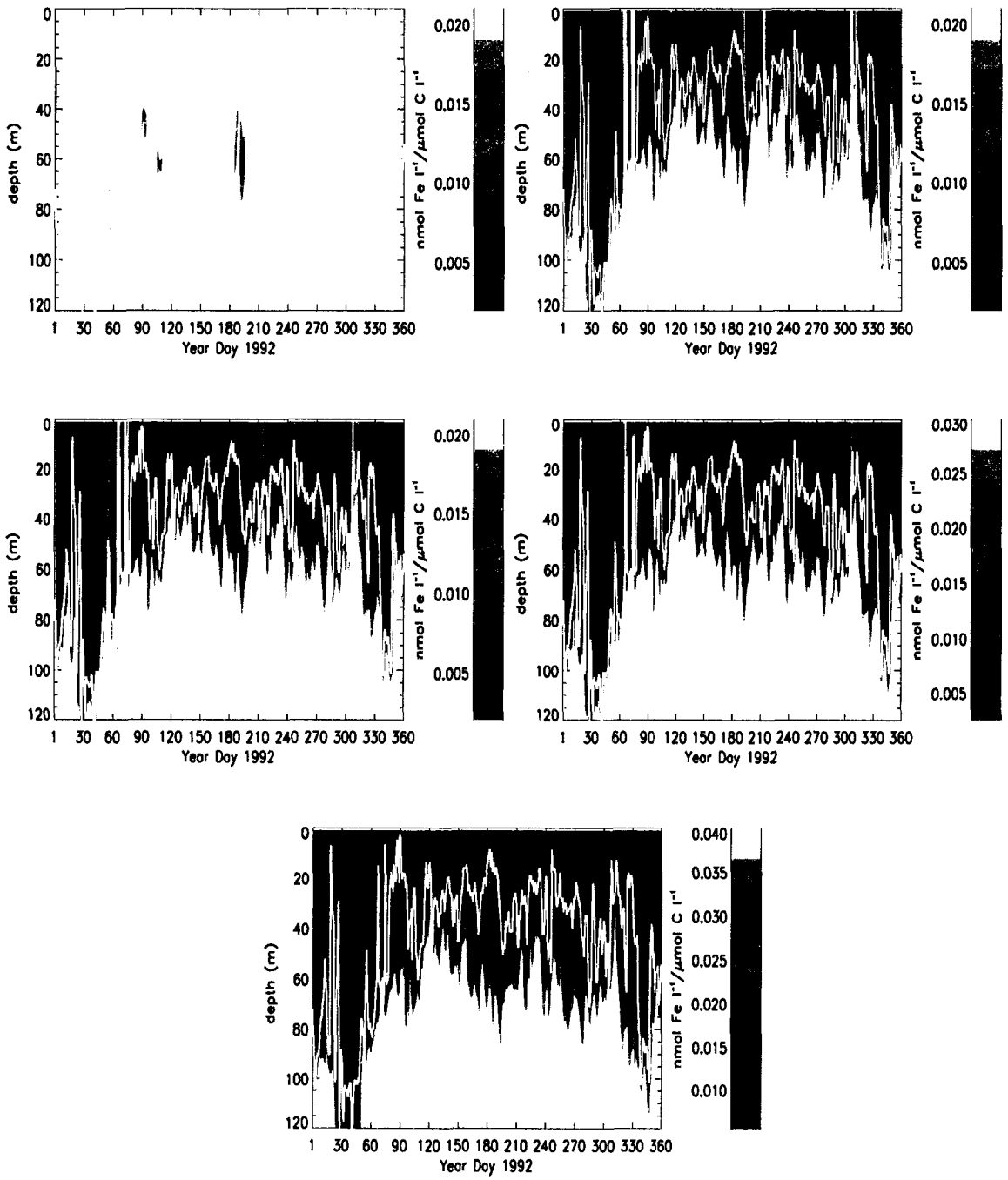

Fig. 13. Simulated depth-time distributions of cellular iron to carbon ratios (nmol Fe l^{-1}/μmol C l^{-1}) of (A) low light-adapted *Prochlorococcus* (algal group 1), (B) high light-adapted *Prochlorococcus* (algal group 2), (C) *Synechococcus* (algal group 3), (D) autotrophic eukaryotes (algal group 4), and (E) large diatoms (algal group 5). Overlaid solid white line represents the mixed layer depth, which is obtained as described in section 3.1. Lighter colors indicate higher ratios.

cellular silicate to carbon ratios (not shown) for this algal group are always at their maximum value, indicating that this group is not silicate limited.

V.1.3 Zooplankton

The simulated depth-time distributions show little temporal variability in microzooplankton biomass concentration throughout the year (Fig. 14A). However, in contrast, considerable temporal variability occurs in the mesozooplankton concentration (Fig. 14B). The distribution of mesozooplankton shows the general features of low biomass during the first 100 days, followed by increased biomass which persists for the remainder of 1992. The initial low mesozooplankton biomass corresponds to El Niño conditions and deep mixed layers. Throughout the latter part of the year, the micro- and mesozooplankton show episodic increases/decreases in biomass, although these fluctuations are very weak for microzooplankton. These events persist for 6 to 20 days.

The simulated depth-time distribution of microzooplankton concentrations remains relatively constant ($\sim$0.3 μmol C l^{-1}) in the upper 50 m and rapidly drops below 0.05 μmol C l^{-1} between 50 and 80 m. In the mixed layer, the highest peak in microzooplankton concentration occurs on YD65 (0.6 μmol C l^{-1}) and during the rest of the year variability in the microzooplankton biomass is low ($\pm$1 μmol C l^{-1}).

Mesozooplankton are more confined to the surface waters compared to the microzooplankton (Fig. 14B). Their concentration drops from an average of 0.4 μmol C l^{-1} to below 0.1 μmol C l^{-1}, right below the mixed layer. The peak concentrations of mesozooplankton are correlated with peaks in algal primary production (Fig. 8), showing a maximum value of 1.5 μmol C l^{-1} on YD315.

V.1.4 Nutrients

The simulated depth-time distributions of nitrate, iron, and silicate concentrations in the upper 100 m show the general features of low nutrient conditions during the first 100 days, which correspond to El Niño conditions, followed by increased

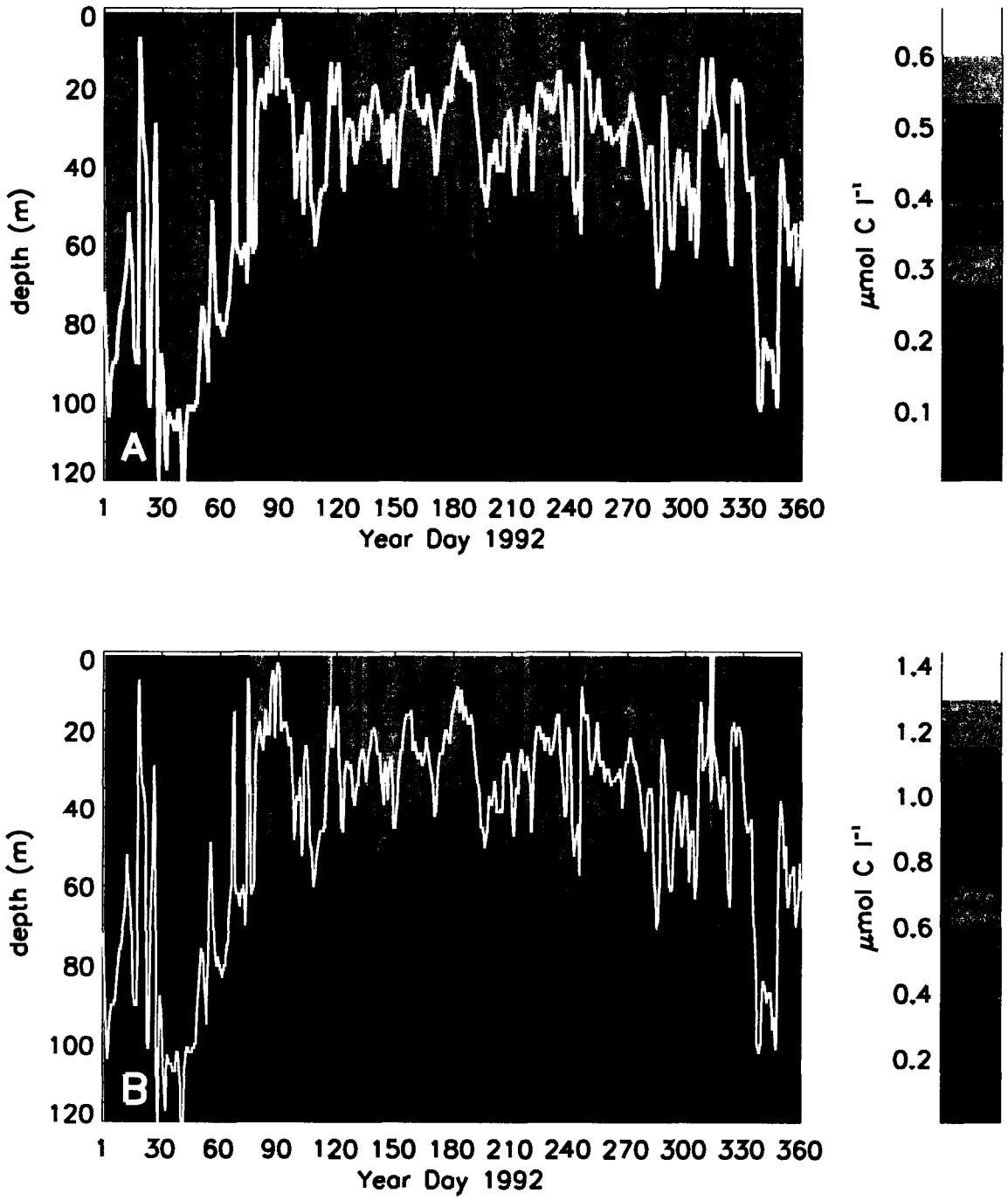

Fig. 14. Simulated depth-time distributions of biomass (μmol C l^{-1}) of (A) microzooplankton, and (B) mesozooplankton. Overlaid solid white line represents the mixed layer depth, which is obtained as described in section 3.1. Lighter colors indicate higher concentrations.

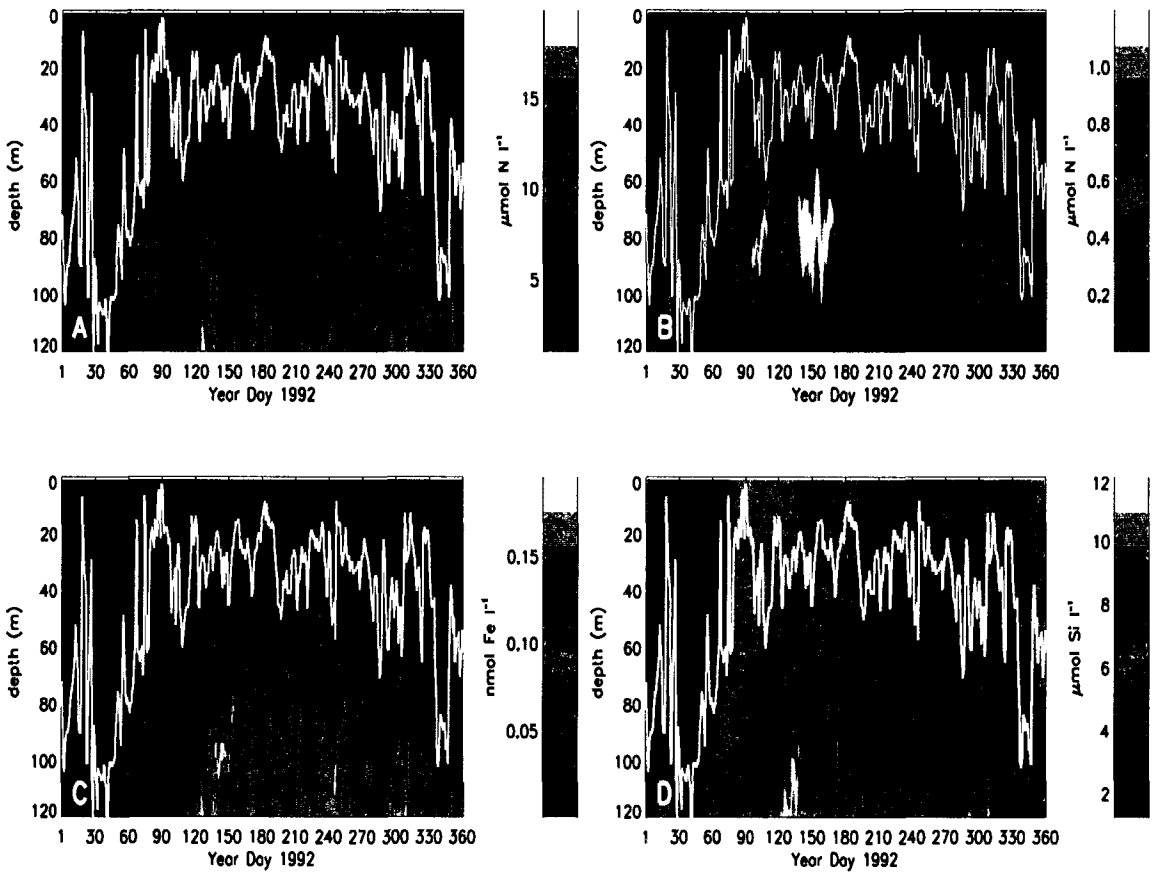

Fig. 15. Simulated depth-time distributions of concentrations of (A) nitrate (μmol l^{-1}), (B) ammonium (μmol l^{-1}), (C) iron (nmol l^{-1}), and (D) silicate (μmol l^{-1}). Overlaid solid white line represents the mixed layer depth, which is obtained as described in section 3.1. Lighter colors indicate higher concentrations.

concentrations at about YD120, which persists for the remainder of 1992 (Figs. 15A, C and D). The simulated ammonium distribution (Fig. 15B) differs from the other nutrients in that its concentration is higher between YD70 and YD180 compared to the rest of the year. Distributions of all nutrients are homogeneous within the mixed layer. All nutrients increase with depth except for ammonium which forms a maximum below the mixed layer between 70-100 m, after which it decreases with depth.

The simulated nitrate concentrations are lower during El Niño conditions, although this nutrient is never depleted (>2 μmol l^{-1}) within the water column (Fig. 15). The minimum nitrate concentration in the mixed layer was 2 μmol l^{-1} on YD197, which corresponds to an extended period of low nitrate values between YD165 and YD220 (Fig. 15A). The temporal variability in nitrate concentration is low ($\pm$5 μmol l^{-1}) within the mixed layer, but the variability increases towards 120 m ($\pm$15 μmol^{-1}). Increases in nitrate concentration coincide with episodic upwelling events that persist for 6 to 20 days (Fig. 4).

Simulated ammonium is depleted (<0.1 μmol l^{-1}) within the mixed layer (Fig. 15B) where phytoplankton demand for this nutrient is high. The ammonium maximum occurs below the mixed layer where the majority of nitrogen regeneration occurs. The peaks in simulated ammonium concentration follow increases in algal group primary production (Figs. 8A-E). Ammonium concentrations are higher during the first half of the year with maximum values of 1.1 μmol l^{-1} between YD130 and YD175. These maxima follow persistently high primary production values observed during YD105-165 (Fig. 8).

Simulated iron concentrations are lower during El Niño conditions (Fig. 15C). Similar to ammonium, iron is also depleted in the mixed layer (<0.03 nmol l^{-1}). Iron concentrations are higher during the second half of the year below the mixed layer, showing a maximum value of 0.195 nmol l^{-1} on YD308 at 120 m. Simulations show that the strongest injection of iron into the mixed layer occurs around YD315.

Silicate follows a similar trend to nitrate (Fig. 15D). Silicate is never depleted within the water column and attains a minimum value of 1.8 μmol l^{-1} on YD43.

V.1.5 Particulate carbon fluxes

The flux of organic particulate carbon is obtained from the sum of the small and large detrital carbon fluxes at 120 m (section 4.9) and is used to determine the carbon export out of the upper 120 m at 0°N, 140°W. Daily particulate carbon fluxes through the model bottom boundary at 120 m show high temporal variability during the year (Fig. 16). Similar to primary production, carbon export is also lower during

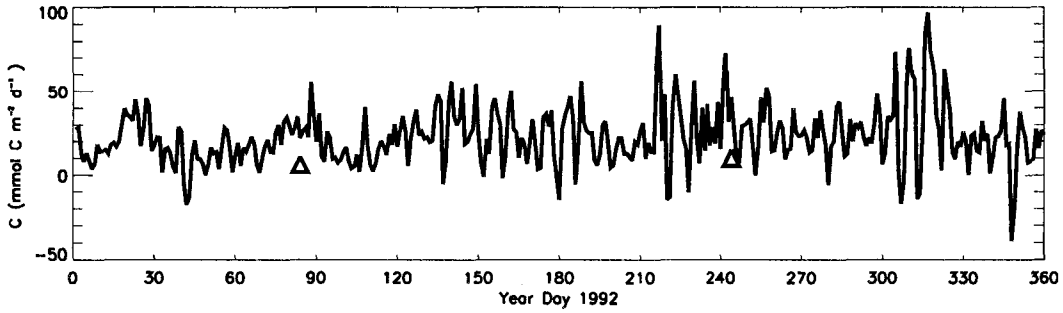

Fig. 16. Simulated time distribution of organic particulate carbon fluxes (mmol C m^{-2} d^{-1}) at 120 m. Positive values indicate that the flux is towards the ocean bottom and the negative values indicate that the flux is towards the ocean surface. The carbon fluxes at 120 m (△) measured during the two U.S. JGOFS EqPac survey cruises, S1 and S2, are shown for comparison.

the El Niño period.

The export carbon fluxes are highest when a downwelling event (Fig. 4B) follows a period of high primary production, such as the events that occur on YD15-30, YD75-90, YD 120-170, YD220-240, and YD300-320 (Fig. 8). The latter two peaks in export production, which occur during the second part of the year, are considerably higher than the three peaks that occur during the first part of the year. The annual integrated particulate carbon flux past 120 m is 10,416 mmol C m^{-2} yr^{-1}. A similar calculation for the carbon flux past 50 m yields an annual value of 10,735 mmol C m^{-2} yr^{-1} . The small decrease in these estimated carbon fluxes indicate the effect of remineralization processes on the vertical flux of particulate carbon.

V.1.6 Simulated upper water column carbon budget

Analyses of the distributions obtained from the reference simulation indicate that microzooplankton grazing of algal groups 2-4 (~40 mmol C m^{-2} d^{-1}) provides the primary pathway for carbon transfer between the primary and secondary producers (Fig. 17). The removal of small phytoplankton by micrograzers is 71%, which is consistent with observations (Landry et al., 1995) which show 53-83% of small

phytoplankton grazed by microzooplankton. Dam et al. (1995) reported that mesozooplankton only removed 1-12% of the daily primary production, almost all due to grazing on diatoms (Bidigare and Ondrusek, 1996). The simulated mesozooplankton grazing removes only 4% of the daily production as diatoms which is consistent with observations. The simulated microzooplankton contribution to mesozooplankton grazing is ~80% (19 mmol C m^{-2} d^{-1}) and Zhang et al. (1995) reported that small animals (200-500 μm) contributed more than 50% (range 34-80%) of total mesozooplankton grazing.

The simulated carbon transfer between the two zooplankton compartments and the two detritus compartments are similar (~29 mmol C m^{-2} d^{-1}) (Fig. 17). The removal of particulate carbon through remineralization comprises a major part of both small and large detrital carbon pools. About 72% of the simulated small detrital carbon and 50% of the simulated large detrital carbon are converted to dissolved organic carbon in the euphotic zone (0-120 m).

The simulated annual-averaged vertical distributions of carbon production and removal suggest that microzooplankton grazing exceeds algal group 1 production above 40 m (Fig. 18A), thereby removing all the daily production, because the growth rate of this group is inhibited by light at the surface (Fig. 9A). Between 40 and 80 m the daily production exceeds grazing removal, although most (66%) of the daily production by this algal group is removed by microzooplankton. Below 80 m, grazing again exceeds primary production because of low algal growth rates due to light limitation (Fig. 9A).

Except in the top ~3 m, the simulated production rate of algal group 2 is higher than its removal by microzooplankton grazing throughout the upper 60 m (Fig. 18B). This group is much less inhibited by light at the surface compared to algal group 1 (Figs. 9A and B). However, below 60 m grazing removal exceeds algal group 2 production due to light limitation (Fig. 9B).

The simulated primary production and grazing removal characteristics are similar for algal groups 3 and 4 (Figs. 18C and D). From the surface to about 50 m, the simulated daily production exceeds the micrograzer removal of production. However,

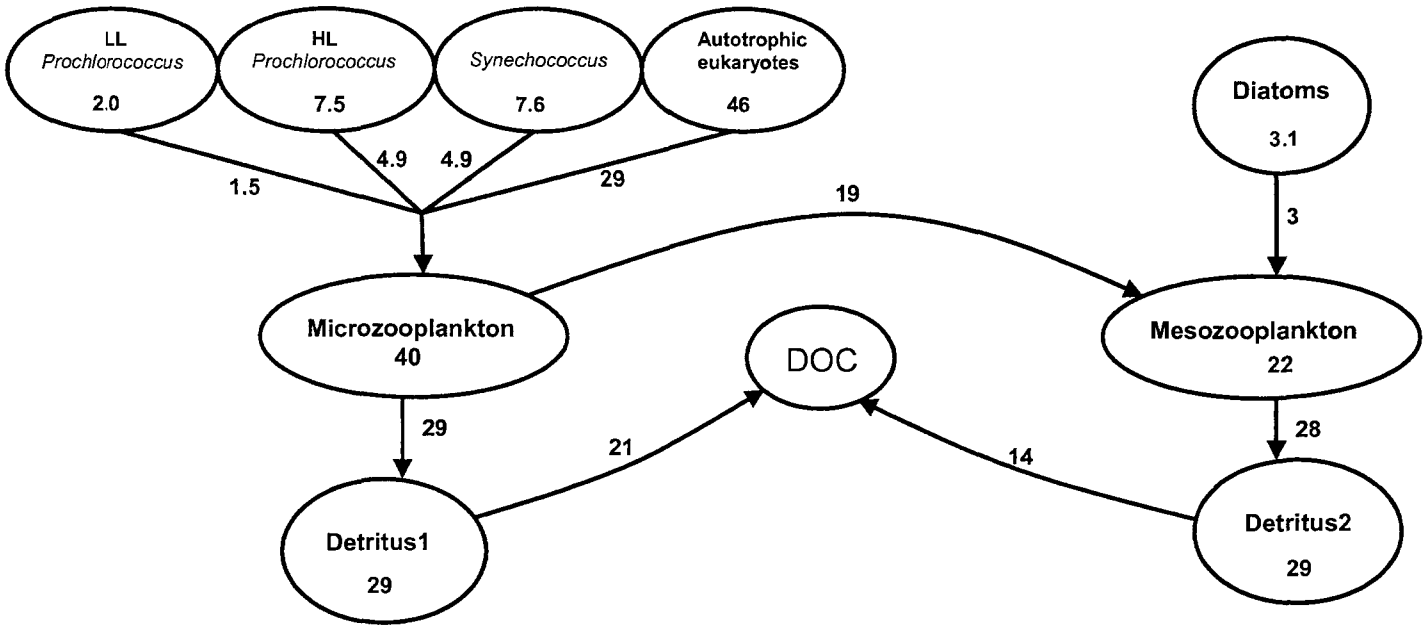

Fig. 17. Flowchart of the simulated carbon budget (mmol C m^{-2} d^{-1}) obtained for the lower trophic level model structure used in this study. Arrows indicate the direction of carbon transfer between model compartments. The ecosystem variables are daily averaged over the euphotic zone (0-120 m). The numbers in the algal group and zooplankton compartments are the net daily primary production and assimilated part of grazed carbon, respectively. Arrows between algal groups and zooplankton compartments and the arrow between microzooplankton and mesozooplankton compartments indicate net daily grazing. Arrows between zooplankton and small (Detritus1) detritus and large (Detritus2) detritus compartments indicate the carbon loss by zooplankton as unassimilated grazing, mortality and excretion. Arrows between the detritus compartments and the dissolved organic carbon (DOC, which is not tracked in the model) indicate the loss of carbon from the detritus compartments by remineralization. Abbreviations on the flow chart are: LL- low light-adapted; HL-high light-adapted; DOC-dissolved organic carbon.

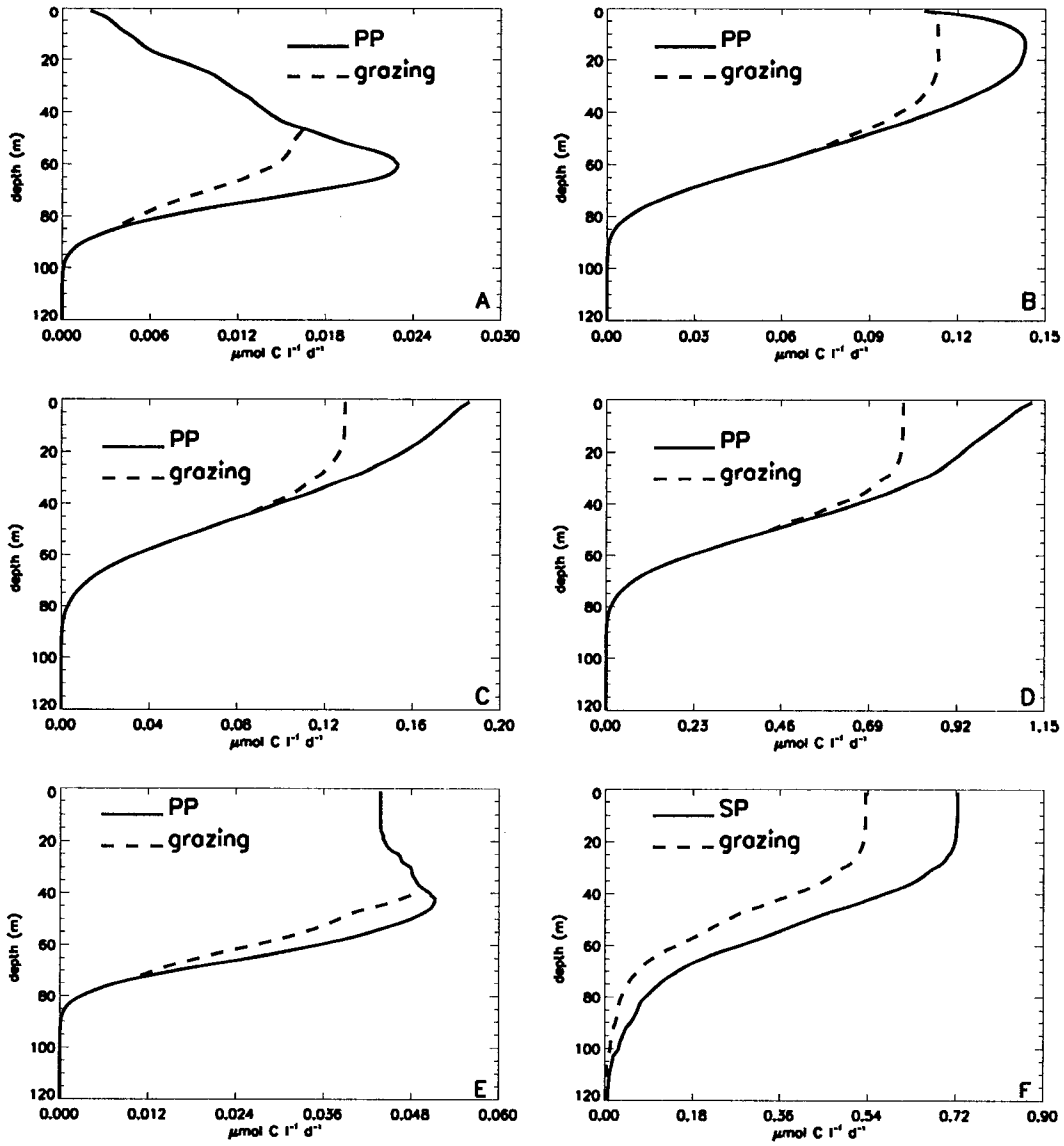

Fig. 18. Simulated profiles of annual-averaged carbon production (solid line) and removal of carbon production by grazing (dashed line) (mmol C l^{-1} d^{-1}) of (A) low light-adapted *Prochlorococcus* (algal group 1), (B) high light-adapted *Prochlorococcus* (algal group 2), (C) *Synechococcus* (algal group 3), (D) autotrophic eukaryotes (algal group 4), (E) large diatoms (algal group 5) and (F) microzooplankton. Microzooplankton grazes algal groups 1-4 and mesozooplankton grazes algal group 5 and microzooplankton, as explained in section 4.1. Abbreviations used are: PP- primary production by algal groups; SP- secondary production by microzooplankton.

~60% of algal group 3 and 4 production is lost to grazing at the surface and this value gradually increases to 100% towards 50 m. Below 50 m, growth becomes light limited (Figs. 9C and D) and all the daily production is removed by micrograzers.

Only mesozooplankton graze on algal group 5 (Fig. 2), which results in the production and removal of carbon resulting from this interaction different from that obtained for (Fig. 18E) algal groups 3 and 4 (Figs. 18C and D). Grazing removes all the daily algal group 5 production in the upper 45 m (Fig. 9E), although the growth of this group is not inhibited by light over this depth range as is the case for algal groups 1 and 2. However, nutrient limitation is a strong effect on this algal group in the surface waters (Fig. 10E), which extensively reduces growth rates. Between 40 and 70 meters nutrient limitation is less, which allows algal group 5 production to exceed removal by mesozooplankton. Below 80 m, all of the algal group 5 daily production is removed by grazers, similar to other groups.

The simulated mesozooplankton production is supported by grazing of algal group 5 as well as by grazing of microzooplankton (Fig. 2). The simulated profiles show that daily microzooplankton secondary production exceeds removal by mesozooplankton throughout the whole water column (Fig. 18F). Both microzooplankton production and grazing removal decrease uniformly towards 120 m, and grazing removal corresponds to ~65% of daily secondary production by microzooplankton throughout the water column.

V.1.7 Model-data comparison

The biogeochemical data available from the U.S. JGOFS EqPac field studies (Murray et al., 1994, 1995) provide measurements of many of the variables included in the lower trophic level ecosystem model (Table 2). These measurements are used for comparison with the simulated distributions for specific days and depths, as well as for comparisons on a depth-integrated basis. No direct measurements of phytoplankton biomass are available from the field studies. Thus, the cell count data obtained during the cruises (Table 2) were converted to algal group biomass as explained in Chapter 3 for comparison with model results.

Some of the estimated physical and optical terms used in the simulations were also compared with cruise data. The mixed layer depth and underwater spectral irradiance values obtained at the nominal wavelengths (410, 441, 488, 520, 550, 560, 589, 633, 656, 671, 683, 694 nm) during TS1 and TS2 cruises compare well with the simulated values (not shown).

The simulated mixed layer biomass concentrations of each algal group (Fig. 19A) and the 120-m integrated values (Fig. 19B) agree well with the corresponding concentrations calculated for the same time period from the U.S. JGOFS EqPac cruise data. The simulated distribution shows three blooms of *Prochlorococcus* (algal groups 1 and 2) between YD110-YD160, YD200-YD255, and YD300-YD320, for which the biomass is as high as measured biomass during TS2.

The simulated time distribution of the algal groups shows a wide range of temporal variability, including a strong 6-8-day periodicity. This high frequency variability is not captured in cruise observations. However, general features observed during the cruises are reproduced by the simulations. The observations and simulation results show that the phytoplankton biomass is dominated by algal group 4 throughout the year, with algal group 1 + 2 being secondary in dominance (Figs. 19A and B). Early in the year, during El Niño conditions, the simulated and observed distributions show that the biomass associated with algal group 4 (autotrophic eukaryotes) and algal group 1 + 2 are similar and that algal group 3 dominates over algal group 5. Both observations and model results show that during the latter part of the year, the biomass of algal group 4 is double that of algal group 1 + 2. Also, the observations and simulations show increases in the biomass of algal groups 3 and 5 during the second part of the year and the magnitude of this increase is comparable for both groups. The simulated distributions show that the temporal variability in the biomass of algal group 5 is higher than that for algal group 3 and that algal group 5 dominates over algal group 3 occasionally. Measurements from the second U.S. JGOFS time series cruise on YD295 showed exceptionally high diatom concentrations compared to other measurements on this cruise (1 versus 0.2 μmol C l^{-1} in the mixed layer). This single large increase in diatom biomass (algal group 5) is not

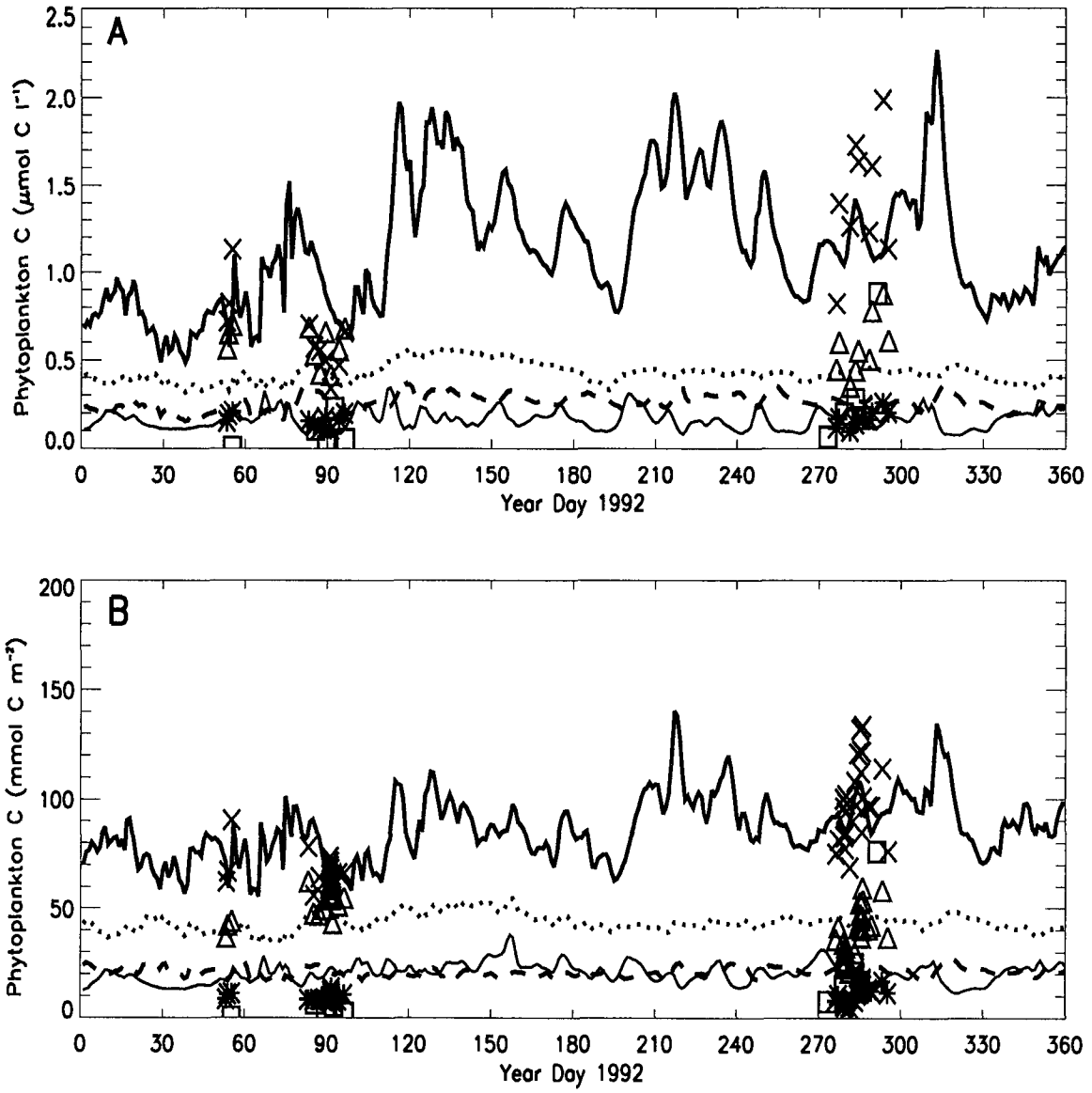

Fig. 19. Simulated time distribution of the combined low light-adapted and high light-adapted *Prochlorococcus* (dotted line), *Synechococcus* (dashed line), autotrophic eukaryotes (thick solid line), and large diatoms (thin solid line) in (A) the mixed layer (μmol C l^{-1}), and (B) integrated (mmol C m^{-2}) from the surface to 120 m. The corresponding measurements for each algal group from the four U.S. JGOFS EqPac cruises are shown by $\triangle$, $*$, $\times$, and $\square$, respectively. Measurements from the cruises do not distinguish between the two ecotypes of *Prochlorococcus* spp. Therefore, the simulated biomass values of algal groups 1 and 2 are summed up for comparison with the cruise measurements.

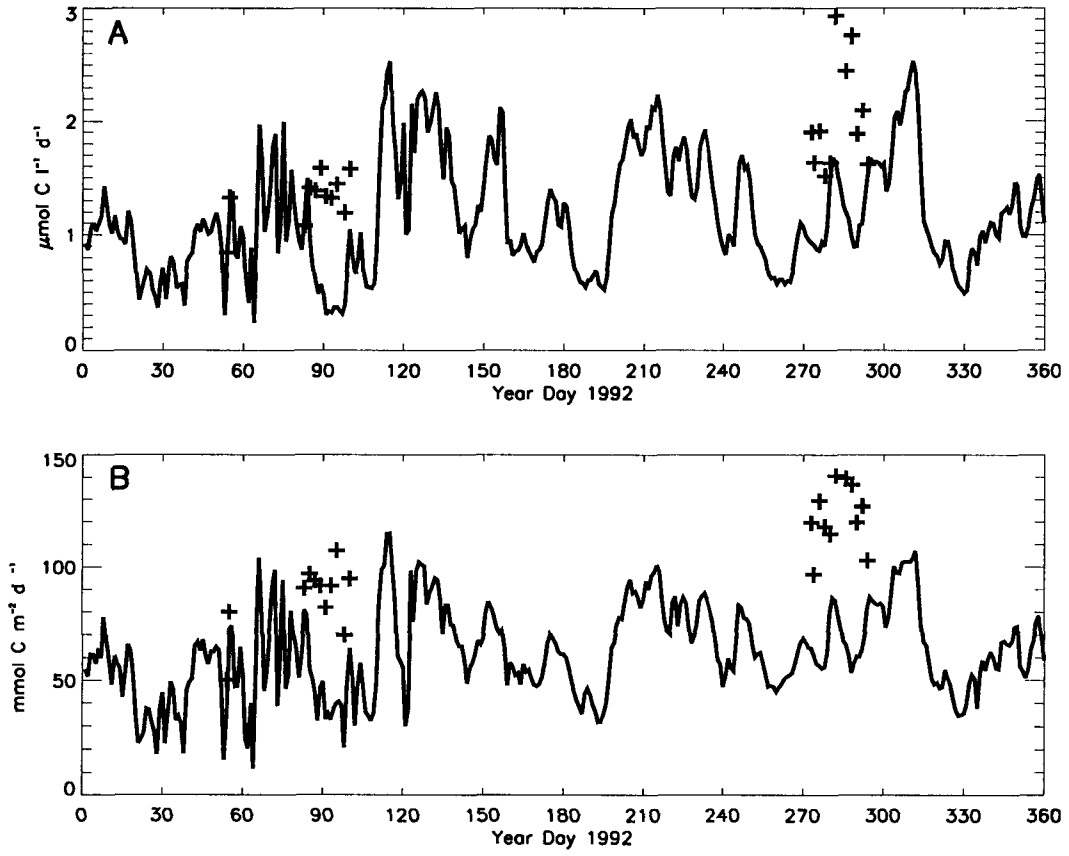

Fig. 20. Simulated time distribution of daily-averaged primary production (A) in the mixed layer (μmol C $l^{-1}d^{-1}$) and (B) integrated (mmol C $m^{-2}d^{-1}$) from the surface to 120 m. The corresponding measurements from the four U.S. JGOFS EqPac cruises are shown with +.

reproduced in the simulation.

The simulated mixed layer and integrated primary production underestimates measured values from the U.S. JGOFS cruises (Figs. 20A and B). However, the simulated primary production values do reproduce the relative increase in primary production observed during the TS2 cruise which occurred during the latter part of the year. Primary production goes through several maxima/minima cycles during the year with the maximum rate of 2.62 μmol C l^{-1} d^{-1} occurring on YD315. The simulated maxima in primary production on YD115-Y160, YD200-YD255, and YD300-YD315 are comparable to the primary production rates measured during the TS2 cruise.

The simulated and observed accessory pigments in the mixed layer are in reasonable agreement (Fig. 21A). Comparison between the simulated and observed integrated accessory pigments (Fig. 21B) shows that the model-derived chlorophyll *a* overestimates the concentrations measured during the cruises (S1 and TS1) in the first part of the year. Observations indicate that below 60 m chlorophyll *a* and other pigment concentrations were higher during the S1 and TS1 cruises compared to S2 and TS2 cruises, whereas surface values were slightly lower during S1 and TS1. The model successfully reproduces this difference in the chlorophyll *a* and pigment concentrations between two seasons (Figs. 21A and B).

The vertical profiles of chlorophyll *a* measured during the two U.S. JGOFS time series cruises provide an additional comparison for the simulated chlorophyll *a* values (Figs. 22A and B). The measured chlorophyll *a* profiles show a deep chlorophyll maximum between 50 and 80 m during the first cruise (YD83 to YD98), which is deeper than the chlorophyll maximum observed during the second cruise (YD272 to YD284) which occurred between 45 and 65 m. The simulated chlorophyll *a* profile reproduces the change in depth and the magnitude of the deep chlorophyll maxima observed between the two cruises. The chlorophyll *a* concentrations obtained during the TS1 cruises show that chlorophyll *a* concentrations below 80 m are as high as the surface values, which are underestimated by the model (Fig. 22A).

The simulated concentrations of nitrate and ammonium compare well with concentrations measured during the U.S. JGOFS EqPac cruises (Figs. 23A and B). However, the simulated mixed layer silicate concentrations overestimated observed silicate concentrations. Below the mixed layer, the decrease in ammonium concentrations seen in the TS2 cruise data is reproduced in the simulated distributions.

The measured iron concentrations (Fig. 24A) in the surface waters were typically below the detection limit for this micronutrient. The simulated surface water iron concentration was near zero throughout the year. The simulated iron concentrations at 120 m (Fig. 24B) was within the range measured during the U.S. JGOFS time series cruises.

The simulated micro- and mesozooplankton biomass and distribution are difficult

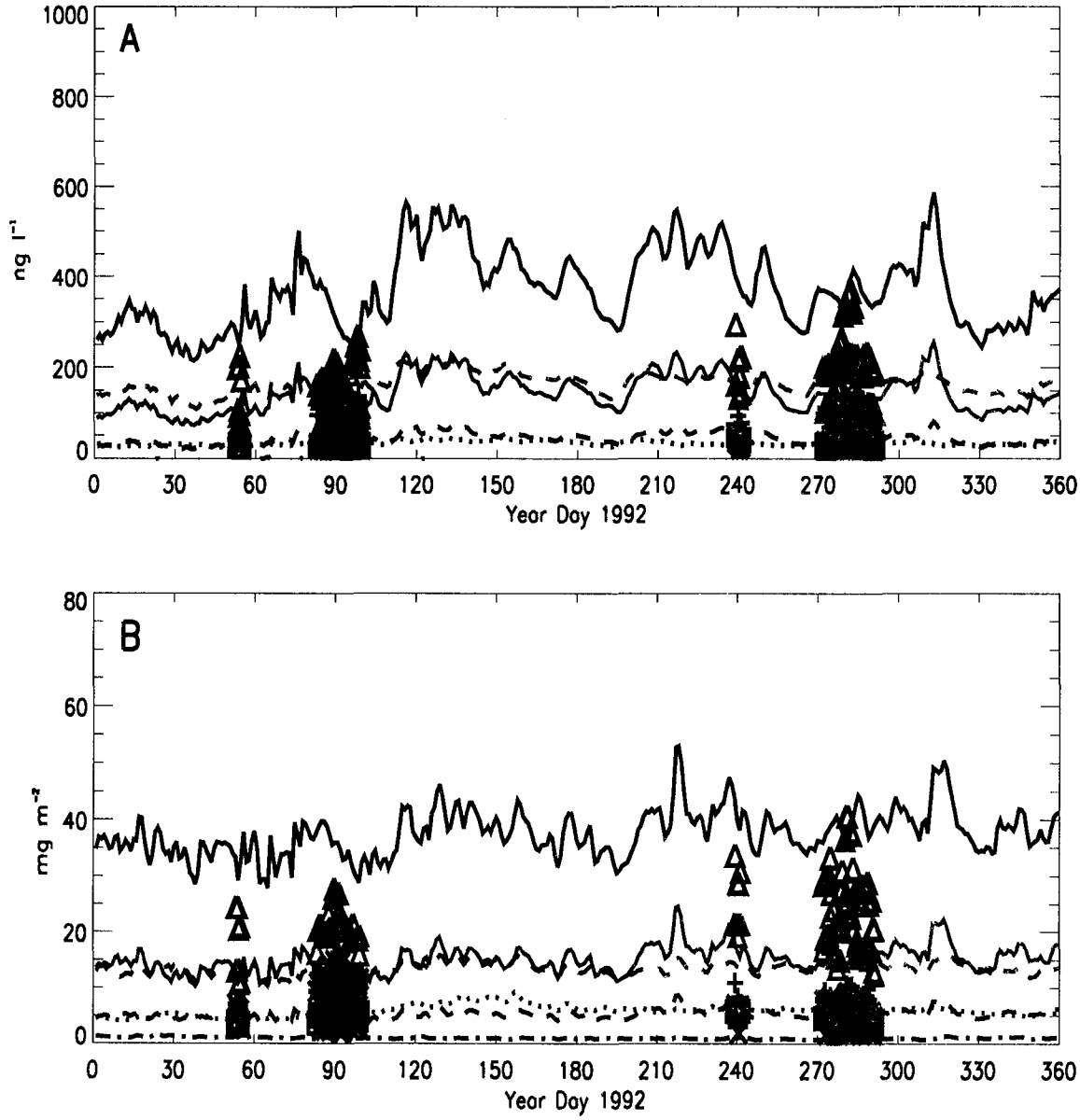

Fig. 21. Simulated time distribution of daily-averaged chlorophyll a (solid black line), chlorophyll b (dashed black line), chlorophyll c (dotted black line), photoprotective carotenoids (dashed lighter color (light blue) line), photosynthetic carotenoids (solid lighter color (orange) line), and phycoerithyrin (dashed and dotted black line) (A) in the mixed layer (μg l^{-1}) and (B) integrated (mg l^{-2}) from surface to 120 m. The corresponding pigment measurements from the four U.S. JGOFS EqPac cruises are shown with black $\triangle$, $*$, $\square$, $+$, lighter color (orange) $\triangle$ and $\times$, respectively.

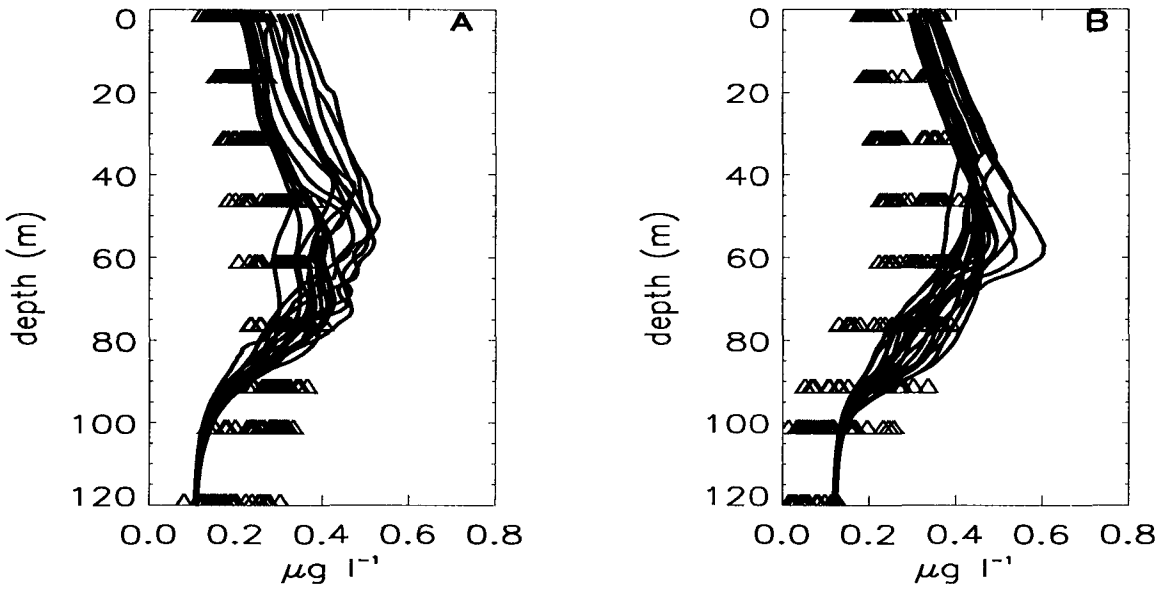

Fig. 22. Simulated profiles of chlorophyll a (μg l^{-1}) for (A) YD83-YD98 and (B) YD272-YD284. The corresponding chlorophyll a measurements ($\triangle$) from the two U.S. JGOFS EqPac time series cruises are shown for comparison.

to verify with measurements. However, some limited data are available (Table 2, Chapter 3). The simulated micro- and mesozooplankton concentrations are almost double the values measured during the U.S. JGOFS cruises ($\sim$18 versus $\sim$10 mmol m^{-2} for microzooplankton and $\sim$25 versus $\sim$12 mmol m^{-2} for mesozooplankton). Direct comparison of the simulated and observed zooplankton biomass is problematic because they do not necessarily represent the same quantity. Thus, agreement within a factor of 2 is taken to be acceptable.

Similarly, little data are available for comparison with the simulated surface carbon fluxes (Fig. 16). The limited measurements that are available can be subject to considerable experimental error (Dunne and Murray, 1999). However, comparison of the simulated organic particulate carbon flux to measurements made during the U.S. JGOFS EqPac cruise is promising (Fig. 16). The simulated fluxes overestimate the measured fluxes, but direct comparisons between the two are difficult because the measured and simulated fluxes may not represent the same quantities. The

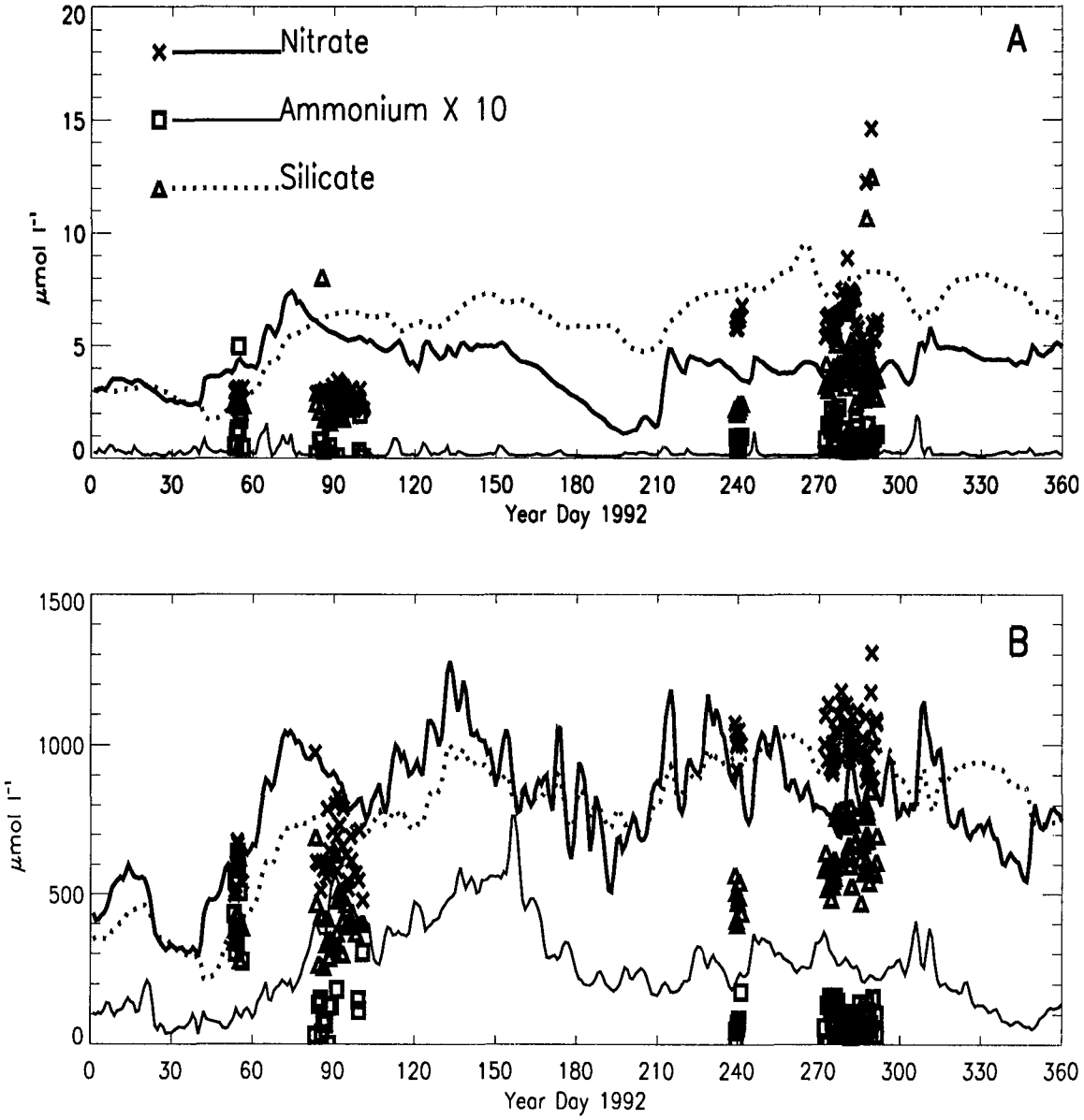

Fig. 23. Simulated time distribution of daily-averaged nitrate (thick solid line), ammonium (thin solid line), and silicate (dotted line) (A) in the mixed layer (μmol l^{-1}) and (B) integrated (mmol m^{-2}) from the surface to 120 m. The corresponding measurements for nitrate ($\times$), ammonium ($\square$), and silicate ($\triangle$) from the four U.S. JGOFS EqPac cruises are shown for comparison. Ammonium concentrations are scaled by a factor of 10 for comparison purposes.

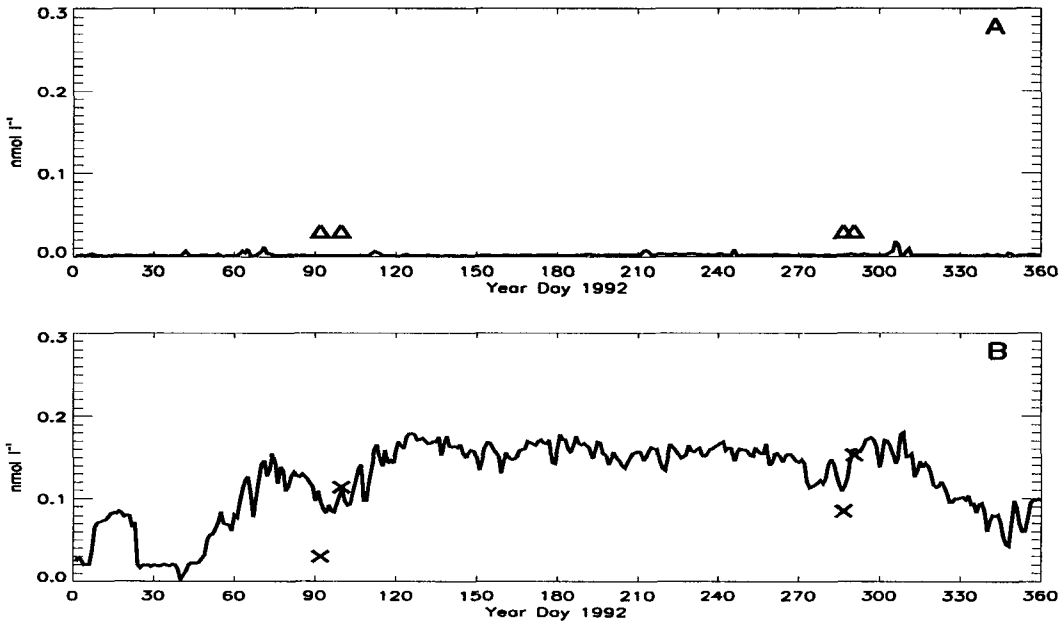

Fig. 24. Simulated time distribution of daily-averaged iron (A) in the mixed layer (nmol l^{-1}) and (B) at 120 m. The corresponding iron measurements (×) from U.S. JGOFS EqPac cruises are shown for comparison. Measured iron concentrations that are below the detection limit for iron (0.03 nmol l^{-1}) are indicated by △.

simulated and observed organic particulate carbon fluxes show an increase in the latter part of 1992.

V.2 MODEL SENSITIVITY TO MODEL STRUCTURE

V.2.1 Algal group effect

To investigate the effect of each algal group on the structure and function of the lower trophic level ecosystem, simulations were done in which particular algal groups were eliminated from the model structure. The simulated annual integrated biomass, primary production, and annual carbon flux were calculated for each of these simulations and compared to the equivalent values obtained from the reference simulation. This provides a measure of the relative effect of each algal group.

The absence of algal group 4 has the most effect on the annual integrated biomass

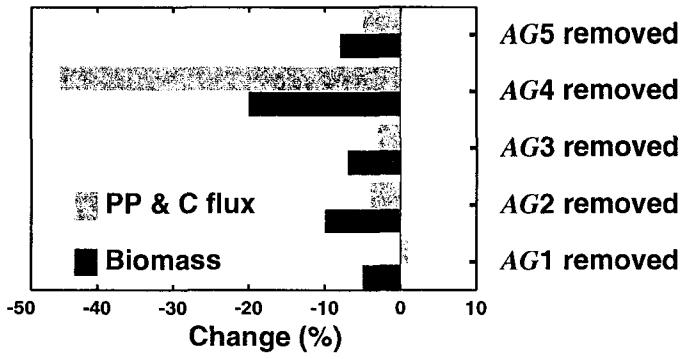

Fig. 25. Change (%) in annual integrated biomass, primary production (PP), and carbon fluxes (C flux) at 120 m produced when each algal group is removed from the model structure. The bars show the difference between the reference simulation and simulations with the modified model structure. The primary production and carbon flux changes are of similar magnitudes and are shown by a single bar.

relative to the biomass obtained from the reference simulation (Fig. 25). Without algal group 4, the annual integrated biomass is 20% less compared to the reference simulation results. The absence of algal groups 1, 2, 3, and 5 results in a reduction in the annual integrated biomass of 10% or less. The main characteristics of algal group 4, which gives it an advantage over other groups, is that it can adapt well to low nutrient conditions, contrary to algal group 5, and it can avoid grazing pressure better compared to smaller forms (i.e. algal groups 1-3) as explained in Chapter 4.

Removal of algal group 4 results in a 45% decrease in annual integrated primary production relative to the reference simulation. Considering that the reference simulation results indicate that this group is responsible for 69% of the annual primary production (Table 13), this results indicate that other groups replace 35% of carbon originally produced by this group. The absence of algal groups 2, 3, and 5 results in reductions in integrated primary production of 5% or less. Removal of algal group 1 actually results in an increase in integrated primary production of about 1%. The effect of the absence of each algal group on carbon fluxes is similar in magnitude to the effect on primary production (Fig. 25).

V.2.2 Nutrient uptake

A unique characteristic of the lower trophic level ecosystem model is that *Prochlorococcus* spp., algal groups 1 and 2, do not take up nitrate but only use ammonium (Moore et al., 2002b). Modifications of the model structure to allow these algal groups to use nitrate results in increased *Prochlorococcus* spp. primary production of 17%, which corresponds to an increase of 7% in the primary production of the whole algal community. This modification in *Prochlorococcus* spp. nutrient uptake dynamics does not cause a significant change in the primary production of the other algal groups.

V.3 MODEL SENSITIVITY TO MODEL DYNAMICS

V.3.1 Iron concentration

The response of the lower trophic level ecosystem to changes in iron concentration was examined by doubling or halving the iron concentration at the base of the euphotic zone. Doubling the iron concentration at the base of the euphotic zone does not produce an iron replete upper ocean. Iron concentration in surface waters still remains below the detection limit of 0.03 nmol l^{-1}. The increased iron at the base of the euphotic zone only affects the iron concentration during upwelling of waters from 120 m. It has little influence during downwelling periods.

Annual integrated primary production increases by 33% when the iron concentration at the base of the euphotic zone is doubled. Algal group 4 shows the largest response to increased iron, with a primary production increase of 46% (Fig. 26). Algal groups 2 and 3 show increased primary production of 7% and 5%, respectively (Fig. 26). Increased iron results in reduction of the integrated primary production of algal groups 1 and 5 of 12% and 10%, respectively (Fig. 26).

The increased iron concentration at 120 m results in only a 10% increase in the annual integrated biomass of the phytoplankton community. The increases in annual integrated biomass of algal groups 3 and 4 are less than the increases in their primary production values (Fig. 26). Increased iron concentration does not affect algal group

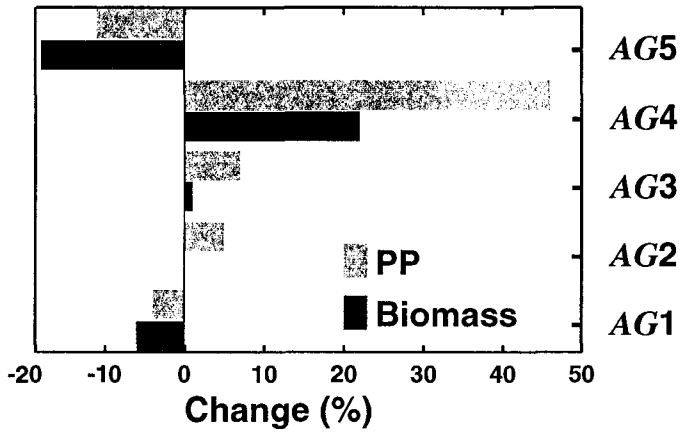

Fig. 26. Change (%) in annual biomass and primary production (PP) of each algal group (*AG*) in response to doubling the iron concentrations at 120 m. The bars show the percent difference between the reference simulation and the modified model run.

2 biomass, but produces a decrease in the biomass of algal groups 1 and 5, that is larger than the decrease in their primary production.

The magnitude of response of the lower trophic levels to a 50% reduction in iron concentration at the base of the euphotic zone is less than their response to a 2 fold increase in iron (Fig. 27). The reduction in iron concentration gives a decrease in annual primary production of 21%, and a decrease in annual integrated biomass of 6%. Algal group 4 is the most affected by decreased iron, with a 27% decrease in primary production.

Unlike the macronutrients, iron can be provided by atmospheric deposition and removed by particle scavenging. Elimination of the atmospheric iron flux results in a 16% decrease in annual integrated primary production and carbon fluxes (Fig. 27). Algal group 4 responds most strongly to the loss of this iron source, with reductions in primary production rate and biomass of 11% and 19%, respectively. Iron scavenging by particles, in contrast, does not have an appreciable effect on primary production, producing only a 4% decrease when not active (Fig. 27). This result agrees well with

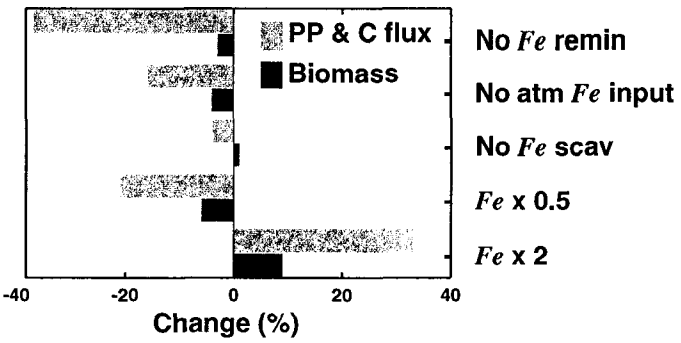

Fig. 27. Change (%) in annual integrated biomass, primary production (PP), and carbon flux (C flux) at 120 m in response to modifications in the manner in which iron is supplied. The bars show the percent difference obtained between the reference simulation and simulations in which iron (Fe) concentrations at 120 m are doubled ($Fe \times 2$), reduced by 50% ($Fe \times 0.5$), no iron scavenging (scav), no atmospheric (atm) iron deposition and no remineralization (remin)..

observations, that show that at low iron concentrations ($< \sim 0.6$ nM) most (>99%) of the dissolved iron is bound to organic ligands and is not strongly particle reactive (Van den Berg, 1995; Rue and Bruland, 1995, 1997). Overall, comparison of the effects of the different modifications to the iron sources (Fig. 27), shows that the changes in primary production and carbon fluxes are always greater than biomass changes.

V.3.2 Silicate concentration

The reference simulation results indicate that algal group 5 is not silicate limited because silicate values were rarely below 3 μmol l^{-1}. To test the response of the algal groups to reduced silicate concentrations, silicate at the bottom of the euphotic zone was reduced by 50%. This reduction resulted in a $\sim$50% decrease in integrated silicate concentration (not shown). However, reducing silicate at the bottom of the euphotic zone mainly reduces the high silicate concentrations that occur during upwelling events and does not affect the low silicate values during downwelling periods.

Therefore, only a slight decrease of 1% in primary production of algal group 5 results from reduced silicate concentrations.

V.4 PARAMETER SENSITIVITY

Many of the parameters used in marine ecosystem models are not well constrained by measurements (Doney, 1999). Information on zooplankton grazing rates is very limited (Armstrong, 1994). Little information is available on cellular nutrient concentration ratios of different algal groups (Sunda and Huntsman, 1995; Geider et al., 1998; Takeda, 1998). Also, there are still many unanswered questions concerning the recycling (remineralization) of iron in oceanic surface waters (Bruland et al., 1994; Wells et al., 1995; Johnson et al., 1997; Fung et al., 2000; Jickells and Spokes, 2002).

In this study, the sensitivity of the model solutions to variations in zooplankton grazing rates, cellular nutrient concentration ratios, and iron remineralization was tested. In previous studies Friedrichs and Hofmann (2001) used ±25% difference of original parameter values and Fennel et al. (2003) used a difference of ±50%. In this study a difference of ±25% is preferred, because this difference is within the variance of environmental conditions for the grazing rates (Landry et al., 1995; Verity et al., 1996), cellular nutrient concentrations Sunda and Huntsman (1995) and iron remineralization (Bruland et al., 1994; Johnson et al., 1997). The effect of variations in these parameters was assessed using yearly primary production, vertical carbon fluxes at 120 m, carbon biomass of the 5 algal groups, and the concentrations of nutrients as diagnostics.

Grazing

At 0°N, 140°W in the equatorial Pacific grazers, particularly microzooplankton, remove most of the daily production of phytoplankton biomass (Landry et al., 1997). To explore the influence of grazing on primary production and biomass, grazing rates of microzooplankton and mesozooplankton were varied by ±25% of their value used in the reference simulation (cf. Tables 7 and 12).

Simulation results show that the magnitude of the phytoplankton biomass depends strongly on the grazing parameters. Variation of the microzooplankton grazing rates of ±25% produces ~±19% changes in primary production and biomass. This magnitude of change is indicative of an ecosystem under top-down control (Klein and Steele, 1985). A similar change in primary production and biomass is observed when the grazing rates of mesozooplankton are varied, but the nature of the change is complex. For example, reduced grazing pressure on microzooplankton by mesozooplankton results in increased grazing pressure on phytoplankton by microzooplankton which reduces the phytoplankton biomass. Variations in the mesozooplankton grazing rate have the strongest influence on algal group 5, because this group is directly grazed by mesozooplankton. A 25% decrease in the mesozooplankton grazing rate resulted in a 27% increase in algal group 5 annual primary production and biomass and produced a shift towards a diatom-dominated phytoplankton community.

Cellular iron to carbon ratios

In the model, growth rates of the algal groups are estimated as a function of cellular nutrient concentrations (section 4.5). Specified minimum cellular nutrient to carbon ratios set the limit for zero growth rate. Because iron is the primary nutrient limiting phytoplankton growth at 0°N, 140°W, only variations in the cellular iron to carbon ratio (K_{QFe_i}, Table 7) were tested.

Perturbing minimum cellular iron to carbon ratios by ±25% results in a ±11% variation in primary production and export flux and no significant effect in biomass relative to the reference simulation. The effect of changing the iron to carbon ratio is greatest for algal groups 4 and 5 compared to the other algal groups. For example, decreasing the minimum limit of iron to carbon ratios by 25% results in an increase of 20% in algal group 4 primary production, and essentially no effect on algal group 1.

Iron remineralization

Recycled iron via remineralization is responsible for 40% of the simulated annual

primary production and about 3% of the annual integrated biomass (Fig. 27). The effect of recycled iron on the primary production differs for each algal group. Algal group 4 responds most strongly, with its production reduced by half when iron remineralization is not active. The primary production of algal groups 2 and 3 also decrease (30 and 37% decrease, respectively). However, the absence of iron remineralization enhances the primary production of algal groups 1 and 5 by 20 and 30%, respectively.

V.5 MODEL SENSITIVITY TO PHYSICAL FORCING

Effects of modified physical forcing fields

To investigate the effects of variations in environmental forcing on the lower trophic levels, the model was forced with time series of vertical velocity (w), diffusivity coefficient (K_z), mixed layer depth, temperature (T), and light that were modified relative to the ones used in the reference simulation. Temperatures at 120 m determine the concentrations of nutrients, which are carried into surface waters via upwelling, mixing in the mixed layer, and diffusion. The light field is one of the main driving mechanisms for algal growth (section 4.4). The effect of the modified environmental time series was assessed by comparing the annual phytoplankton biomass and primary production estimates and carbon fluxes at 120 obtained from the simulations.

Primary production is most sensitive to decreased vertical velocity (Fig. 28), with a 50% decrease in vertical velocity producing a 46% decrease in annual primary production. The response of the annual integrated phytoplankton biomass to reduced vertical velocities is less, with only an 11% reduction. Increasing vertical velocities by 50% results in a 32% increase in annual primary production (Fig. 28). Annual biomass increases by 10%, indicating a decoupling in the responses of primary production and biomass. The change in carbon flux resulting from decreased vertical velocity is similar to what is seen for primary production, with a 58% decrease at 120 m. Increasing vertical velocity produces only a 15% increase in carbon flux at

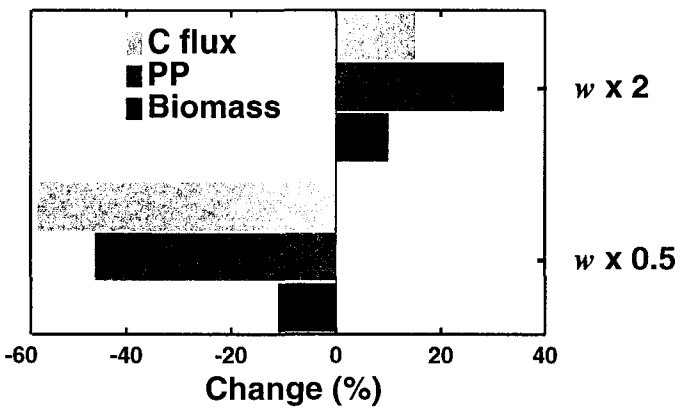

Fig. 28. Change (%) in annual biomass, primary production (PP), and carbon fluxes (C flux) at 120 m in response to modifications in the vertical velocity time series that is input into the model. The bars show the percent difference between the reference simulation and simulations in which the vertical velocities (w) at 120 m were doubled ($2 \times w$) and reduced by 50% ($0.5 \times w$).

120 m.

Changes in the vertical velocity fields produce changes in the amount of nutrients injected into the upper ocean, which in turn affects the relative abundance of the five algal groups. Decreased vertical velocities favor algal groups 1 and 5 (Fig. 29). Algal group 5 is diminished somewhat by decreased vertical velocities, but less so than algal groups 2 to 4. Algal group 4 annual primary production is reduced by ~50% by a 50% reduction in vertical velocities.

Increased vertical velocities shift the phytoplankton community assemblage towards larger algal groups, with the primary production of algal groups 4 and 5 increasing by 43% and 22%, respectively. Although the primary production of algal group 5 increases considerably, its biomass is essentially unchanged from that in the reference simulation. Primary production associated with the other groups is only slightly modified by increased vertical velocities (Fig. 29).

Fixing the mixed layer at 44 m produces a shallower mixed layer during El Niño conditions and a deeper mixed layer later in the year (cf. Fig. 4C). The deeper mixed layer post-El Niño results in an annual increase in primary production of 17%. A

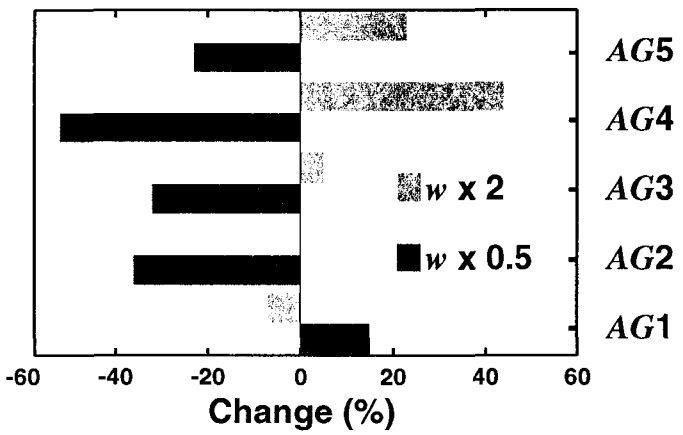

Fig. 29. Change (%) in annual primary production of each algal group in response to modifications in the vertical velocity time series that is input into the model. The bars show the percent difference between the reference simulation and simulations in which the vertical velocities (w) at 120 m were doubled ($2 \times w$) and reduced by 50% ($0.5 \times w$).

deeper mixed layer favors all of the groups, except algal group 1. A deeper mixed layer results in these phytoplankton cells being moved into the high-light surface waters, which produces light inhibition of growth.

A constant minimal vertical diffusive flux (K_z) of 0.036 m^2 d^{-1} decreases the annual primary production and carbon flux by 13% and 14%, respectively. The effect of diffusive fluxes on each algal group differs. A reduced vertical diffusive flux results in a decrease in primary production for algal groups 2 to 4, with algal group 4 being the most affected group with a decrease in primary production of 15%. The primary production of algal group 1 increases by 28% in response to reduced vertical diffusion, and primary production of algal group 5 increases slightly (1%).

Decreased vertical diffusive fluxes result in a decrease in total annual algal biomass, although this decrease (5%) is much less than the decrease in annual integrated primary production. The change in algal group biomass to decreased vertical diffusivity is small relative to the change in their primary production. Algal group 1 is the most affected group, with a 17% increase in biomass. The biomass of the

other algal groups decreases with algal group 5 being the most affected group (11% decrease in biomass).

Temperature not only determines the nutrient levels at the bottom of the model domain (section 4.10), but it also affects the growth rates of algal groups (section 4.3). Thus, a 5°C increase in temperature results in a decrease in nutrient concentrations and an increase in phytoplankton growth rates. The opposite occurs for a decrease in temperature. Simulations in which the temperature was decreased or increased by 5°C resulted in a small (5%) decrease in total annual primary production.

The effect of cloud cover on photosynthetic potential of the algal groups was investigated with simulations that did not include cloud reduction of the surface irradiance (i.e. clear sky). These simulations show that the effect of cloud cover on the total annual primary production is small (4% increase) for 1992 because the cloud cover in the region was not extensive for this time. Comparison of the simulations with and without clouds, however, shows that clouds can inhibit or dampen phytoplankton blooms. For example, with clear sky conditions a phytoplankton bloom occurs between YD60 and YD90, which is not present in the simulations that include cloud cover.

The effect of cloud cover on each algal group also differs with small groups (algal groups 1 to 3) being the most affected groups. The removal of cloud cover results in an increase in primary production of algal groups 1 to 3 by ~8%; whereas, the increase in primary production of algal group 4 is less (1%) and primary production by algal group 5 is decreased by 3%.

Relative effects of physical forcings at different frequencies

The environmental time series used to force the reference simulation exhibit variability over a wide range of time scales. To investigate the effect of variability at the different time scales, the model was forced with a constant mean vertical velocity for 1992 (1.6 m d^{-1}), time series that were 40-day low-pass filtered (Figs. 30A-D), which retain low frequency motions such as Kelvin waves, and time series that were 20-day high-pass filtered (Figs. 31A-D), which retain high frequency motions such as TIWs

and IGWs.

For a constant positive vertical velocity (upwelling) recycled iron is not removed from the surface waters and as a result accumulates below the mixed layer. This artificial accumulation of iron results in a 25% increase in phytoplankton primary production. A constant vertical velocity removes the high frequency variability in the phytoplankton biomass and increases the difference in biomass between the first and latter parts of 1992.

Modification of the vertical velocity field by filtering out high or low frequency motions reduces the advective input of recycled iron from the lower boundary of the model, which artificially accumulates iron below the mixed layer. As a result, the high and low-pass filtered vertical velocity fields yield increased primary production of 47% and 15%, respectively.

Analysis of the frequencies of the motions in the vertical velocity fields shows that in 1992 motions with periods of 42-75 days dominated, which is reflected in the phytoplankton distributions obtained from the reference simulation (Fig. 19). The 40-day low-pass filtered time series (Figs. 30A-D) produces periodicity in the simulated algal groups with frequencies of 42-75 days (Figs. 32A and B). Moreover, the low frequency motions are responsible for the sustained ($\sim$40 days) decreases in algal biomass, such as those that occur during YD30-YD60, YD70-YD120, and YD160-YD220 (Figs. 32A and B). The amplitudes of the fluctuations in biomass are larger than those seen in the reference simulation. For example, the biomass of algal group 4 in the mixed layer increases by a factor of 5 between YD102 and YD123 (Fig. 32A); whereas, the reference simulation shows a tripling in biomass for this algal group during the same time period (Fig. 19A). A similar trend is also observed for algal group 5.

The time series analysis of the vertical velocities also showed significant variability at frequencies of 8-26-days, which includes TIWs (20-day period, Qiao and Weisberg, 1995; Yu et al., 1995) and IGWs (6-8-day period, Wunsch and Gill, 1976; Friedrichs and Hofmann, 2001). Input of the high-pass filtered environmental time series (Figs. 31A-D) shows that these high frequency motions produce fluctuations

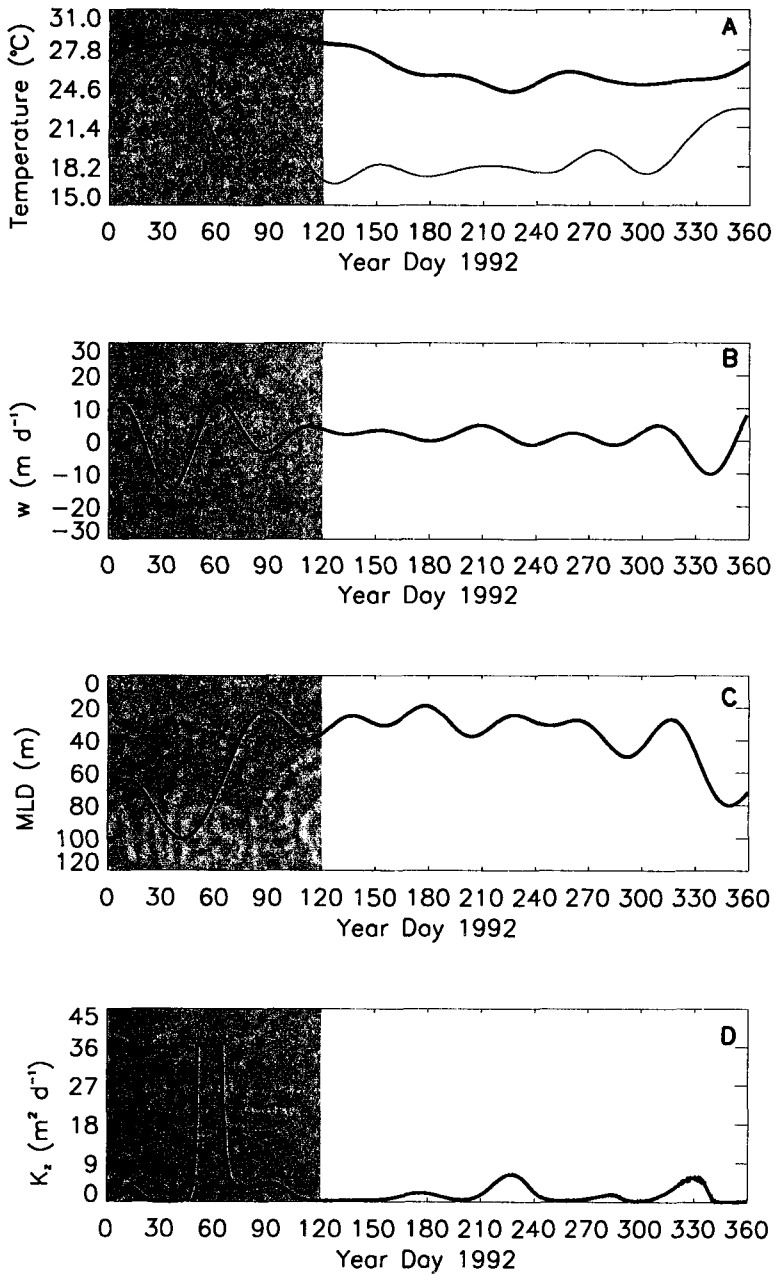

Fig. 30. Time series of 40-day low-pass filtered (A) surface temperature (thick solid line) and temperature at 120 m (thin solid line), (B) vertical velocity (w) at 40 m, (C) mixed layer depth (MLD), and (D) vertical diffusivity coefficient (K_z) at 25 m estimated from observations obtained from the TAO mooring at 0°N, 140°W as discussed in Chapter 3. Fast Fourier Transform (FFT) is used to determine the frequency spectra and to low-pass filter the time series. By using the FFT the high frequency motions with periods lower than 40 days are removed. Shaded regions denote the El Niño season.

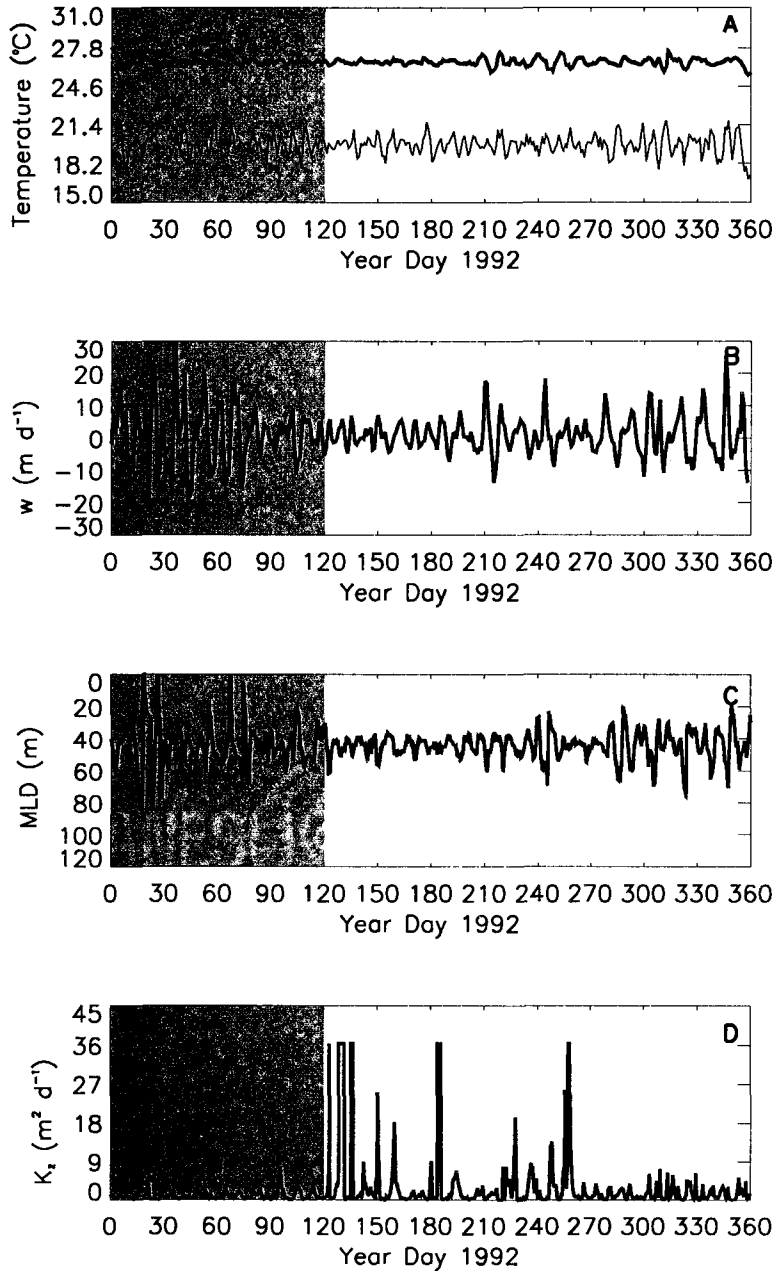

Fig. 31. Time series of 20-day high-pass filtered (A) surface temperature (thick solid line) and temperature at 120 m (thin solid line), (B) vertical velocity (w) at 40 m, (C) mixed layer depth (MLD), and (D) vertical diffusivity coefficient (K_z) at 25 m estimated from observations obtained from the TAO mooring at 0°N, 140°W as discussed in Chapter 3. Fast Fourier Transform is used to determine the frequency spectra and to high-pass filter the time series. By using the FFT the low frequency motions with periods higher than 20 days are removed. Shaded regions denote the El Niño season.

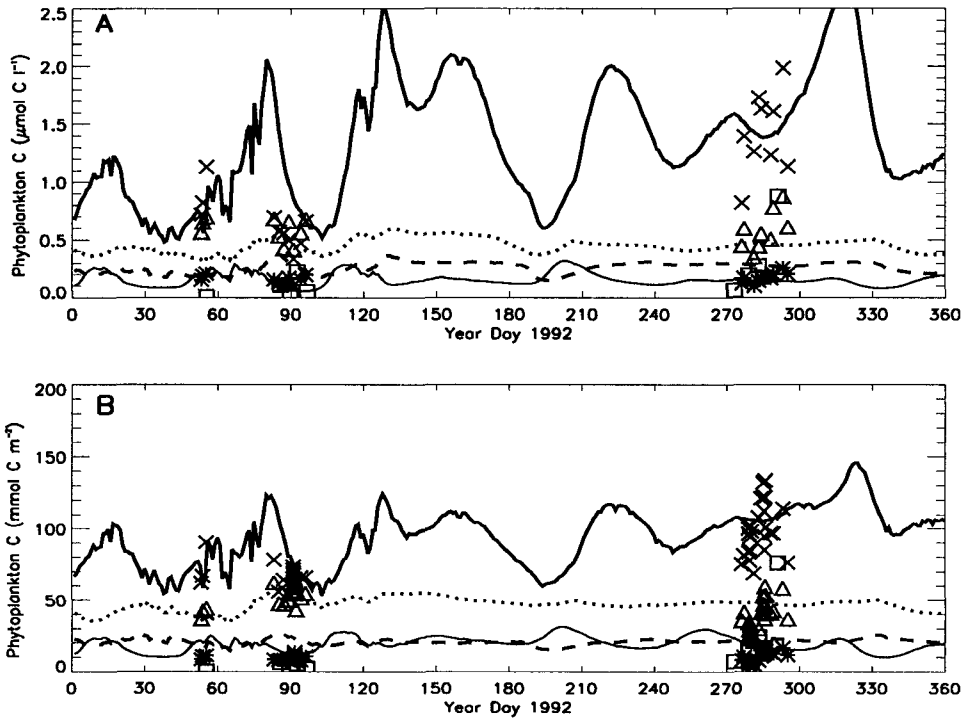

Fig. 32. Same as Fig. 19, but using the 40-day low-pass filtered environmental time series shown in Figs. 30A-D.

in phytoplankton biomass that have smaller amplitudes than those produced by the low frequency time series (Fig. 33A and B). Also, the amplitude of the variability is smaller compared to the biomass distributions obtained from the reference simulation. Total phytoplankton biomass is higher than observations (Fig. 33), and the difference in biomass (relative to the reference simulation) between the El Niño part of the year and the rest of the year decreases.

The highest simulated algal biomass occurs on YD285 (Fig. 33B) which happens to coincide with the time of observations made during the U.S. JGOFS TS2 cruise. The algal biomass for the rest of the simulations is lower, which is in contrast to the reference simulation results which show three other periods with algal biomass that is higher than observed during the TS2 cruise. The high frequency environmental time series result in increases in the biomass of algal groups 4 and 5 during the El Niño period relative to the other groups.

The accumulation of iron below the mixed layer that occurs in response to the

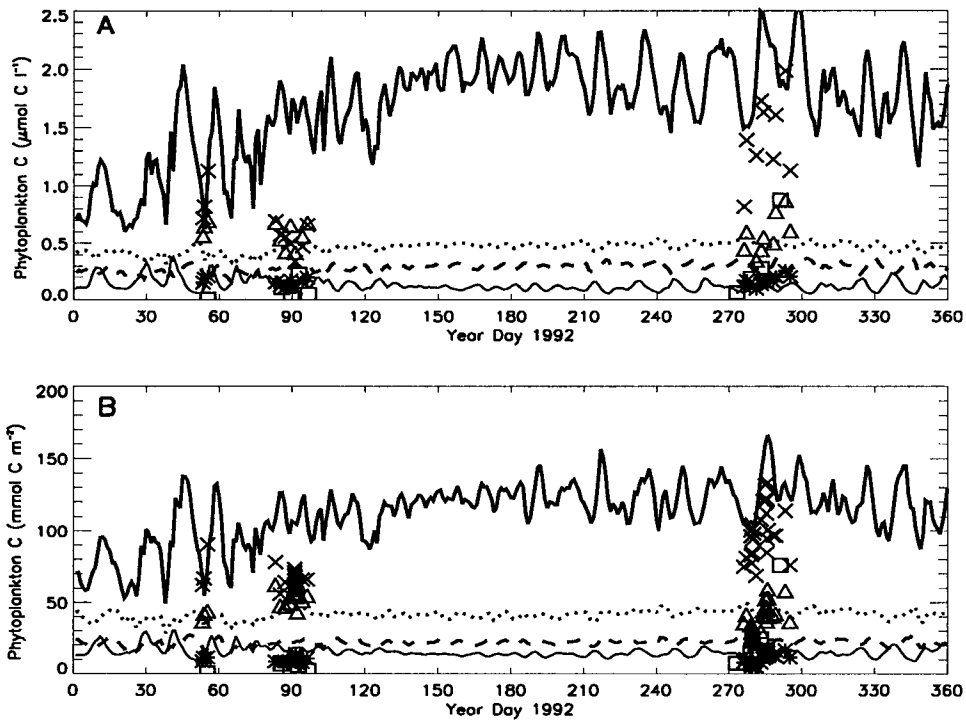

Fig. 33. Same as Fig. 19, but using the 20-day high-pass filtered environmental time series shown in Figs. 31A-D.

high or low-pass filtered environmental time series was eliminated by setting the iron remineralization rate to a very low value (0.01 d^{-1}). For comparison, an equivalent simulation was done with the reference model. Without the effect of iron accumulation, the annual phytoplankton primary production and annual carbon flux decrease by ~5% in response to low frequency events. High frequency motions increase the annual primary production and the annual carbon flux increases by ~30%.

V.6 LONG TERM SIMULATIONS (1991-1999)

The ecosystem model described in chapter 4 was used to do a ~8-year simulation (1991-1999) at 0°N, 140°W (the Cold Tongue region). The TAO data that are used to construct the environmental time series that are input to the model are almost continuous during this time. More important for this study, the 1990s were characterized by three El Niño events (1991-1993, 1994-1995, and 1997-1998) and two La Niña

events (1995-1996 and 1998-1999). This period also featured the strongest El Niño of the century (1997-1998) (McPhaden, 1999), as well as two consecutive periods of El Niño conditions during 1991-1995 without an intervening cold episode. Equivalent 9-year simulations were done for the Warm Pool (0°N, 165°E) as comparison. The Southern Oscillation Index (SOI), which is a measure of large-scale fluctuations in air pressure between the western and eastern tropical Pacific (Trenberth and Hoar, 1996), is used to determine the warm and cold ENSO phases for 1991-1999.

V.6.1 Cold Tongue environmental time series

The temperature time series (Fig. 34A) obtained at 0°N, 140°W from the TAO mooring shows prolonged periods of negative SOI values that coincide with abnormally warm (>28°C, at the surface) ocean waters, which are conditions that are typical of El Niño events (Philander, 1990). Conversely, prolonged periods of positive SOI values coincide with abnormally cold (<24°C, at the surface) ocean waters, which is typical of La Niña conditions. The time series of the SOI and sea surface temperatures (Fig. 34A) indicate that the ENSO cycle (El Niño to La Niña) has an average period of about four years at 0°N, 140°W.

The temperature and SOI time series (Fig. 34A) show that a warm event (El Niño) starts to develop in September 1991 which persists until the end of April 1992. After April 1992, the system shifts into a cold phase with SOI values being close to zero. This cold phase is sustained until the beginning of 1993 when the SOI becomes negative and stays negative until the end of the year. During 1993 the warm waters (28°C) are confined to the surface between March and June and do not penetrate below 60 m. Towards the end of 1993 the system shifts into a cold phase with the SOI index being close to zero. This is followed by the 1994-1995 El Niño which persists until mid-1995. The first La Niña of the decade is observed when surface water temperatures drop to 22°C at the end of 1995. The SOI stays positive until February 1997 after which the strongest recorded ENSO occurs. The SOI stays negative until the beginning of 1998, and the surface waters remain near 30°C for almost a year. During this period the surface ocean is completely stratified

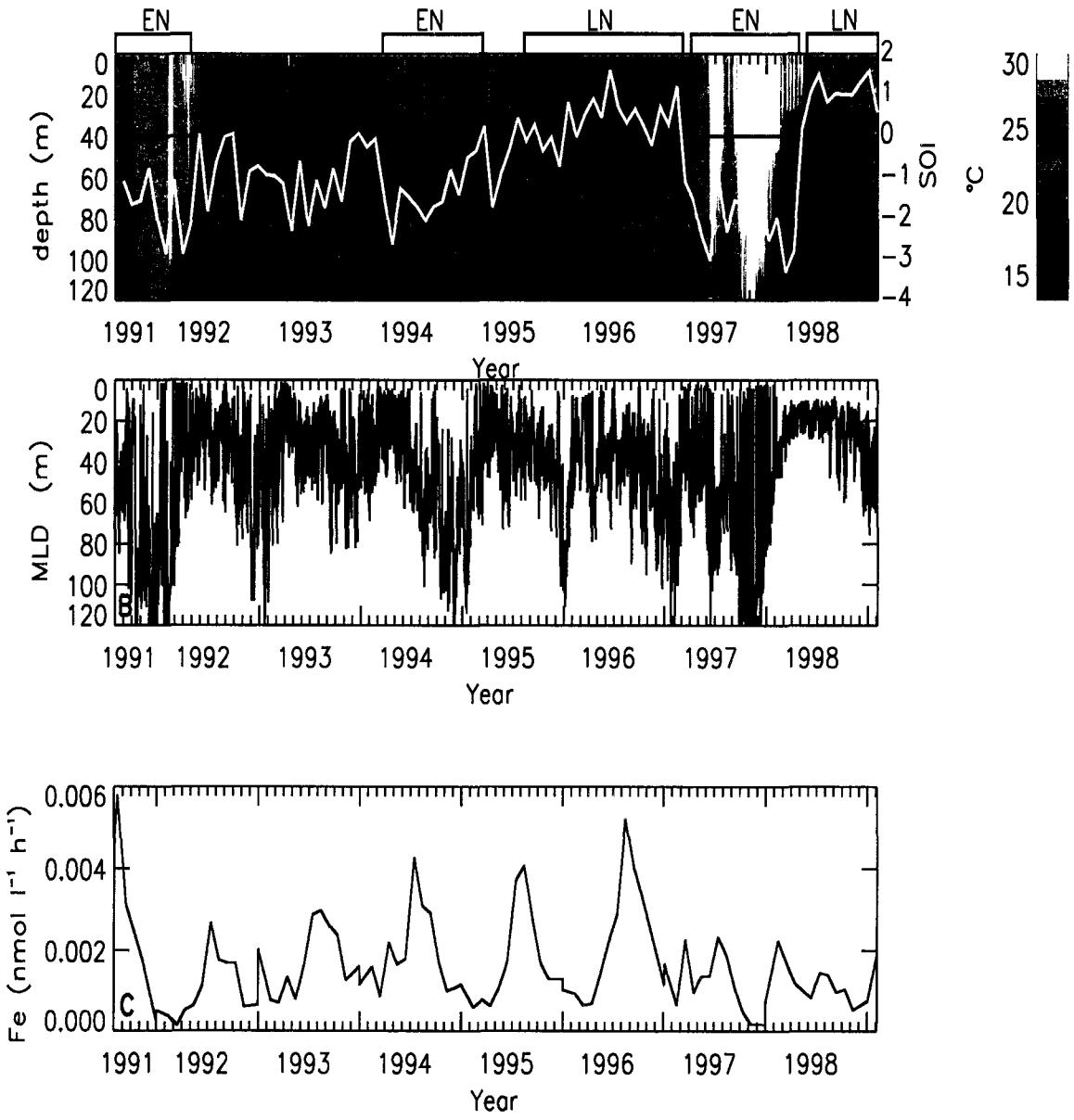

Fig. 34. (A) Depth-time distribution of temperature, time series of (B) estimated mixed layer depth (MLD) and, (C) aeolian iron flux (Ginoux et al., 2001) for 1991 to 1999. The temperature and mixed layer depth are from the TAO mooring at 0°N, 140°W. The Southern Oscillation Index (SOI), obtained from the U.S. Department of Commerce National Oceanic and Atmospheric Administration (http://www.elnino.noaa.gov/) is shown, by the white line and the black line indicates the zero SOI. The time periods of El Niños (EN, red) and La Niñas (LN, blue) are shown. Lighter colors indicate higher temperature.

with warm (30°C) waters extending to 120 m. Towards the end of 1997 the system starts to shift into a La Niña phase, and the coldest surface temperatures (~20°C) of the decade are observed during 1998.

The buildup and waning of 1991-1992 and 1997-1998 El Niños show similar characteristics. At the beginning of the 1991-1992 and 1997-1998 El Niños the warming of the surface waters occurred rapidly and warm waters immediately penetrated to 100 m deep. However, cooling is more gradual, and the subsurface waters, around 120 m, start to cool in the middle of the El Niño event and cold waters reach ~60 m before the buildup of the cold episodes.

The time series of temperature (Fig. 34A) at the bottom of the model domain can also give indications about the state of the EUC. Equatorial Under Current is generally indicated by temperatures between 15°C and 20°C in the equatorial Pacific (Halpern, 1980; Tomczak and Godfrey, 1994). The temperature time series show that EUC is missing within the euphotic zone during the three El Niño events (1991, 1994, and 1997). However, during the cold phases of the ENSO, the temperatures at 120 m are below 20°C indicating the intrusion of EUC into the euphotic zone. In particular during the 1997 La Niña the 20°C isotherm is lifted up to the sea surface, indicating that during this period, EUC is reaching the sea surface.

The mixed layer depth time series (Fig. 34B), which is computed from temperature measurements as described in section 3.1, shows depths in excess of 100 m during the El Niño episodes. During the cold phases, the mixed layer depths are shallow, averaging 30 m. The shoaling of mixed layer depths during the cold phases is the result of shoaling of the isotherms during these periods.

The mixed layer depths are persistently shallow throughout 1998, which corresponds to the strong La Niña episode. A sharp decrease in mixed layer depth occurs towards the end of 1997, and during 1998 the mixed layer depth stays at ~20 m, and shows little variation at depth.

The aeolian iron flux obtained from Ginoux et al. (2001) indicates a strong annual variability in iron deposition (Fig. 34C). The lowest deposition occurs during

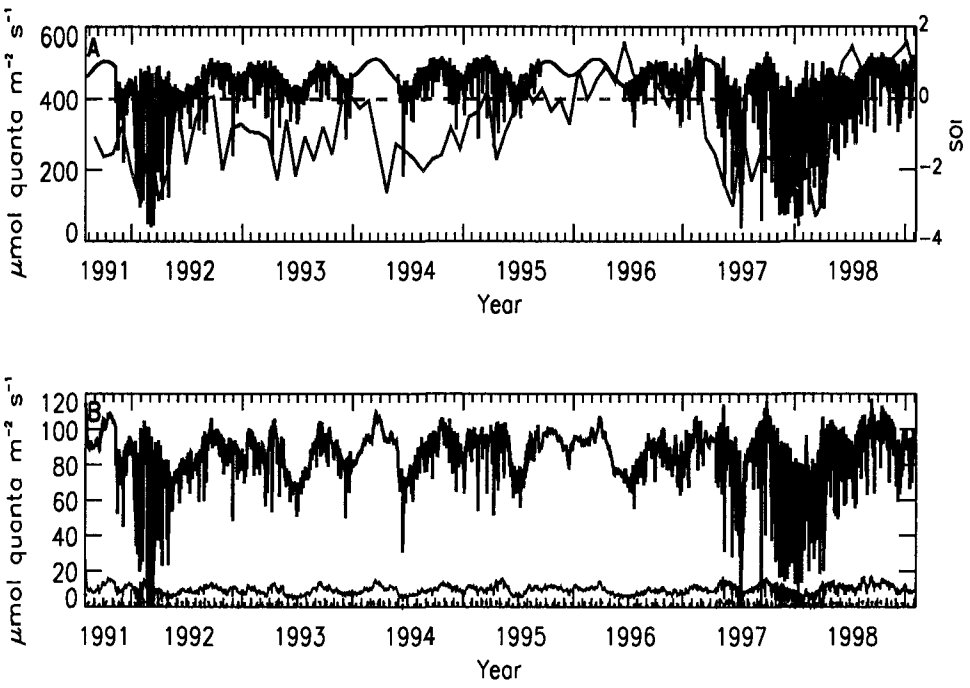

Fig. 35. Time series of simulated (A) integrated downwelling irradiance (PAR) just below the surface and (B) daily integrated downwelling irradiance arriving at 20 m (solid line), 60 m (thin solid line), and 100 m (dotted line). These results are obtained for the Cold Tongue region at 0°N, 140°W from the model described in section 4.2. The Southern Oscillation Index (SOI), obtained from the U.S. Department of Commerce National Oceanic and Atmospheric Administration (http://www.elnino.noaa.gov/) is shown by the dashed grey line and the solid grey line indicates the zero SOI.

February-April and the highest during August-October. Years 1991 and 1996 correspond to a high dust deposition period and in 1992 and 1998 iron deposition is low.

The simulated downwelling irradiance field shows that the effect of cloud cover is correlated with the SOI in the Cold Tongue region (Figs. 35A and B). During times of strong negative SOI, cloud cover can reduce the intensity of the surface irradiance by 80%. The strongest effect of cloud cover on the downwelling irradiance was observed during the 1992 and 1997-1998 El Niño events. While the cloud cover can significantly reduce the irradiance, its effect on the depth of the euphotic zone is minimal, producing only a 3 m decrease in the euphotic zone depth during high cloud cover periods.

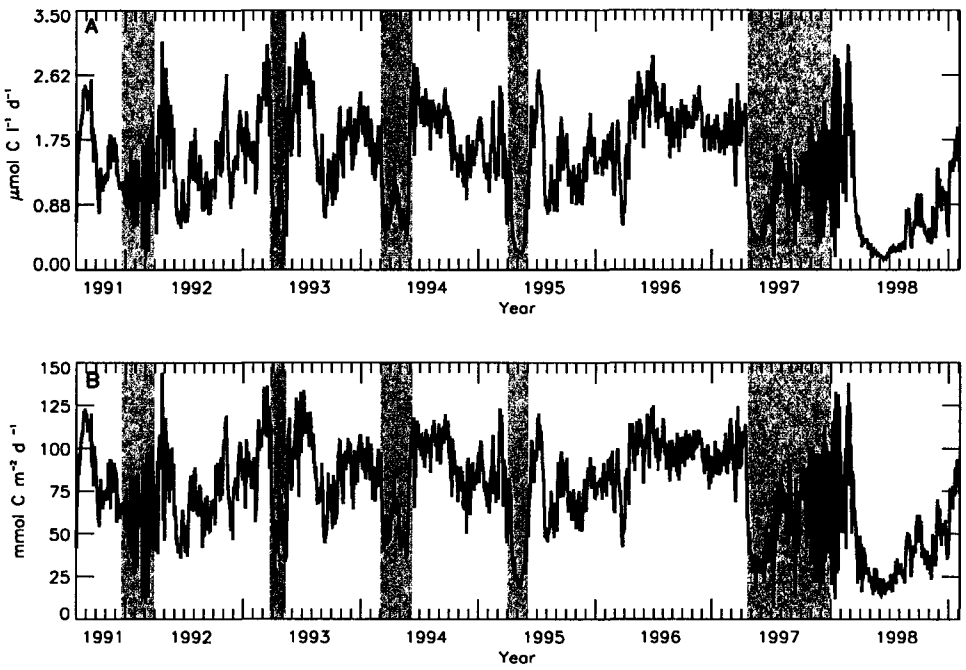

Fig. 36. Simulated time distribution of primary production (A) in the mixed layer, and (B) integrated over the water column (120 m) in the Cold Tongue. Shaded regions denote the peak periods of the negative phases of the Southern Oscillation Index (SOI).

V.6.2 Phytoplankton

The simulated time evolution of primary production at 0°N, 140°W for 1991 to 1999 (Fig. 36) shows that the transition periods between El Niño and La Niña events are the times of greatest change in primary production. The times of negative change in the SOI coincide with low simulated primary production values (Figs. 36A and B). The lowest primary production values occurred during the 1997 (10 mmol C m^{-2} d^{-1}), 1992 (12 mmol C m^{-2} d^{-1}), and 1995 (20 mmol C m^{-2} d^{-1}) El Niño events. Once the SOI starts to shift towards positive, the simulated primary production begins to increase and reaches values that are about a factor of 6 greater than those during the negative SOI phase.

The recovery from El Niño conditions begins prior to full development of La Niña conditions. Observations show that the intrusion of cold waters into the euphotic zone

starts ~4 months before the SOI turns positive (Fig. 34A). During this period the estimated mixed layer depth is still deep compared to the post El Niño phases (Fig. 34B). This combination of cold water intrusion with deep mixed layers introduces nutrients, especially iron in the surface waters, and results in the simulated La Niña bloom at the time when the SOI shifts towards positive (Figs. 36A and B). During periods of persistently high SOI, such as during 1996 and early 1997, the algal groups can sustain high primary production rates (Fig. 36).

The simulated depth-time distributions of the five algae groups at 0°N, 140°W for 1991-1999 (Figs. 37A-E) show that algal groups 2 to 4 bloom during the end of the negative phases of SOI. The times of highest biomass of algal groups 1 and 5 coincide with low biomass periods of other groups.

Algal group 4 dominates the algal biomass at all times (Fig. 37) and undergoes large blooms in May-August 1993, April 1994, May-June 1995, April 1996-March 1997, and February-April 1998. The biomass of algal groups 2 and 3 is also high during these times, but show less temporal variability than algal group 4. The largest blooms of algal group 1 and 5 are in April-June 1995 and February-August 1998. During April-May 1998 the biomass of algal group 5 is similar to the biomass of algal group 4.

The spatial and temporal variations in the algal groups seen in the one-year reference simulation (Figs. 6A-E) also occur at interannual scales. In the 9-year simulation, maxima in biomass of algal group 1 occur below the mixed layer (Fig. 37A) and maxima of algal group 2 occur in the mixed layer (Fig. 37B). *Synechococcus* spp. (algal group 3) is less abundant compared to *Prochlorococcus* (algal group 2 + 3, Fig. 37C), with the average water column biomass of the two being 21 *m*mol C m^{-3} and 41 *m*mol C m^{-3}, respectively. The majority of the biomass of algal group 4 is at depths shallower than 45 m (Fig. 37D) and that for algal group 5 is at depths deeper than 45 m (Fig. 37E).

The simulated time-depth distribution of chlorophyll *a* concentrations obtained from the sum of all five algal groups (Fig. 38) shows that chlorophyll *a* in the mixed layer varies from 0.3 to up to 1.0 $\mu g\, l^{-1}$ on interannual time scales. A deep chlorophyll

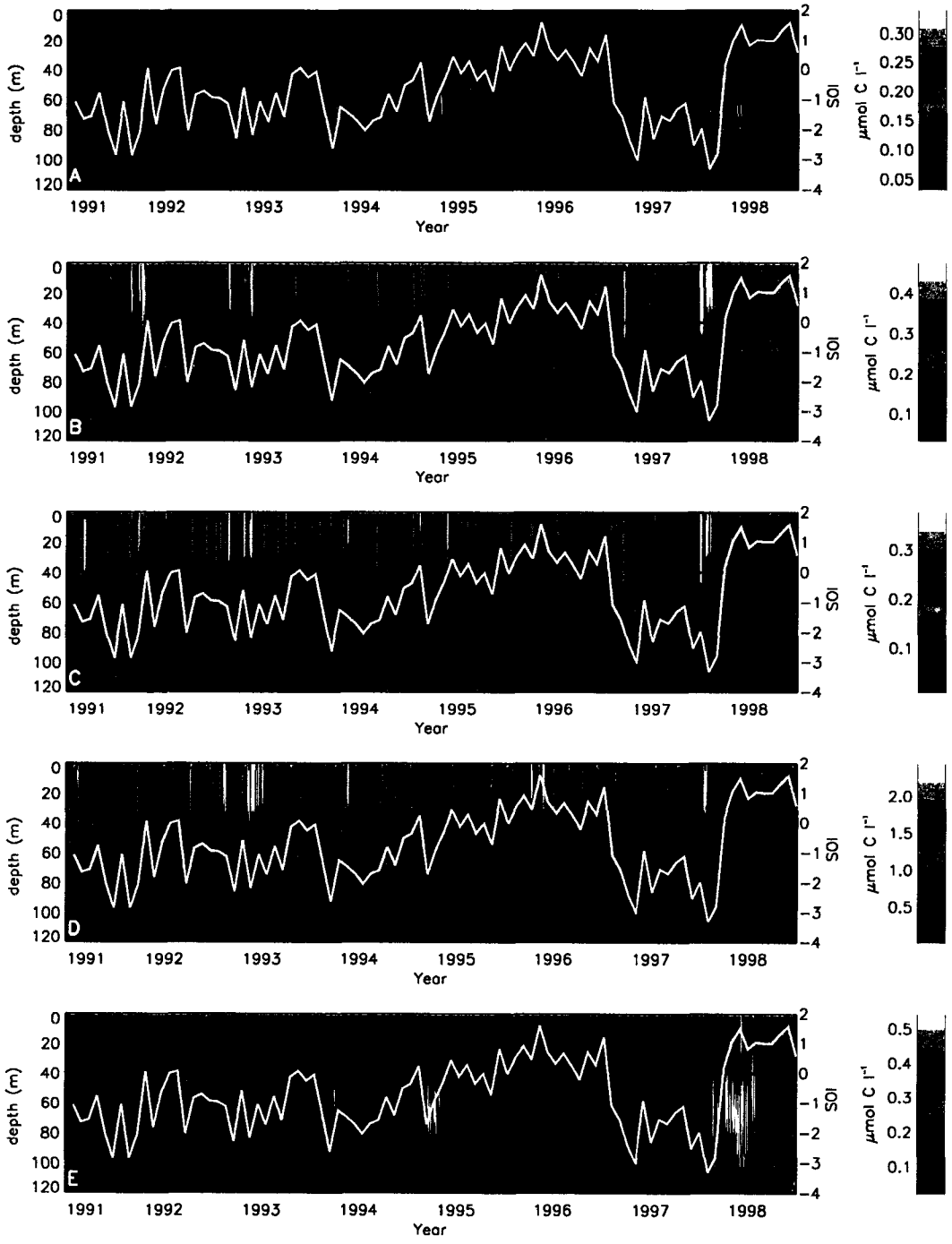

Fig. 37. Simulated depth-time biomass (μmol C l^{-1}) distributions of (A) low light-adapted *Prochlorococcus* (algal group 1), (B) high light-adapted *Prochlorococcus* (algal group 2), (C) *Synechococcus* (algal group 3), (D) autotrophic eukaryotes (algal group 4), and (E) large diatoms (algal group 5) in the Cold Tongue region at 0°N, 140°W. The Southern Oscillation Index (SOI) obtained from the U.S. Department of Commerce National Oceanic and Atmospheric Administration (http://www.elnino.noaa.gov/) is shown by the white line and the red line indicates the zero SOI. Lighter colors indicate higher concentrations.

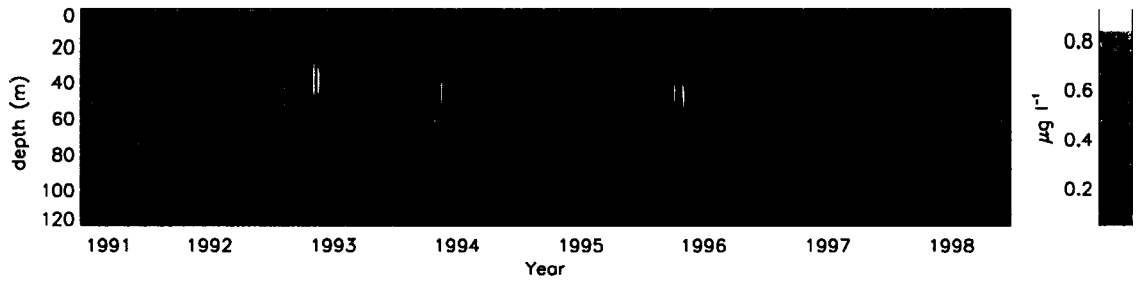

Fig. 38. Simulated depth-time distribution of chlorophyll a (μg l^{-1}) at 0°N, 140°W obtained from the sum of all five algal groups. Lighter colors indicate higher concentrations.

maximum is always present at 0°N, 140°W even during the 1997 El Niño period, when surface chlorophyll a values are particularly low (<0.2 μg l^{-1}). During the nine-year simulation there were 10 periods where the surface chlorophyll a values are above 0.6 μg l^{-1} (e.g., May-July 1993, March 1998) (Figs. 38 and 39). The deep chlorophyll maximum concentrations at these times are ~0.8 μg l^{-1} (Fig. 38). Also, there are periods with subsurface chlorophyll a values of ~0.8 μg l^{-1}, which correspond to surface chlorophyll a values below 0.4 μg l^{-1} (e.g., April 1998, Fig. 38).

The comparison of simulated chlorophyll a versus SeaWiFS chlorophyll a (Fig. 39) shows that the simulated La Niña bloom occurs earlier than the observed bloom but with a similar magnitude. The observed sharp decrease in chlorophyll a after La Niña bloom and the peak at the end of 1998 are reproduced by the simulated chlorophyll distribution. The high frequency oscillations that occur with 6-20-day periodicity in the simulated chlorophyll a fields are also consistent with the SeaWiFS chlorophyll a observations.

V.6.3 Nutrients

The simulated depth-time concentration distributions in the upper 120 m of the three macronutrients and one micronutrient at 0°N, 140°W are low during the El Niño periods and high during the La Niña periods (Figs. 40 A-D). The lowest nutrient

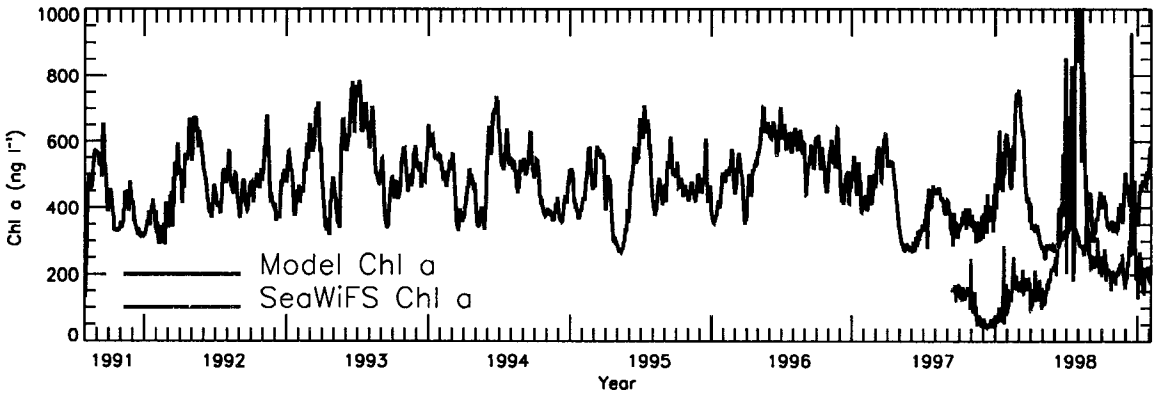

Fig. 39. Comparison of simulated chlorophyll *a* (black) with chlorophyll *a* derived from Sea-viewing Wide Field of view Sensor (SeaWiFS) measurements (grey) at at 0°N, 140°W. The SeaWiFS data set begins in Fall 1997.

concentrations occur during the middle of the warm El Niño periods (negative SOI) after which they increase towards the end of the negative phase of SOI. All nutrients are close to depletion during the 1997 El Niño and concentrations are especially low during the 1991 and 1994 El Niño periods (Figs. 40 A-D). Nitrate, iron, and silicate reach their highest values during the initial part of the positive SOI phases. The highest simulated nutrient concentrations at 120 m occur during the 1998 La Niña. During the 1997-1998 ENSO, nutrient concentrations start to increase at the end of the SOI negative phase.

Simulated nitrate concentrations are particularly low during the three El Niño periods (1991, 1994, and 1997, Fig. 40A) and decrease to a minimum of $\sim$2 μg l^{-1} in 1997. The highest nitrate concentrations occur in mid-1998 in association with the 1998 La Niña.

Ammonium is generally depleted (<0.1 μmol l^{-1}) within the mixed layer during most of the decade (Fig. 40A). The ammonium concentrations reach maximum values during the last 4 months of the negative SOI phase (March 1992, June 1993, March 1995, and February 1998).

Similar to ammonium, iron is also depleted in the mixed layer (<0.03 nmol l^{-1}).

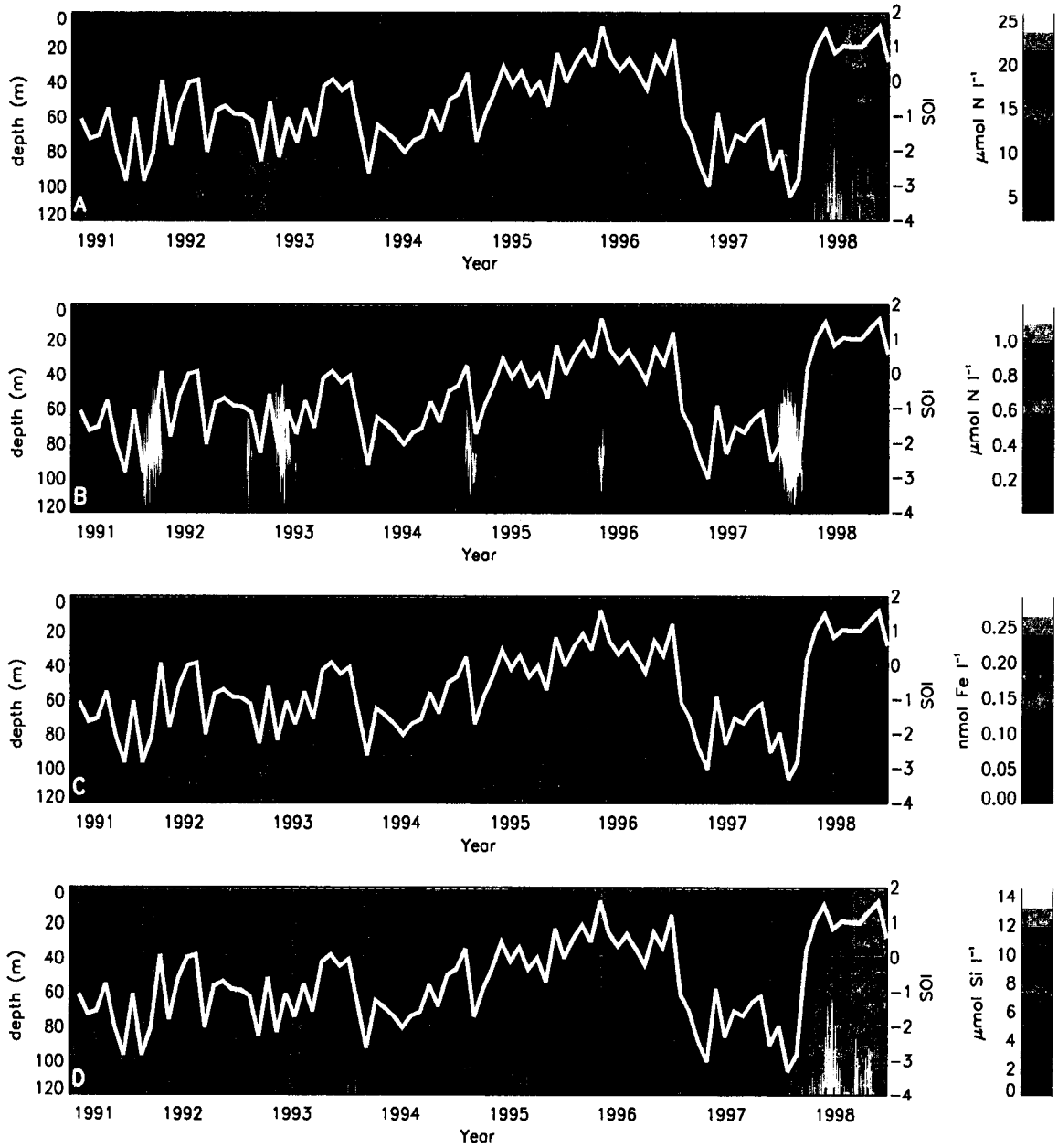

Fig. 40. Simulated depth-time distributions of the concentrations of (A) nitrate, (B) ammonium, (C) iron, and (D) silicate in the Cold Tongue. The Southern Oscillation Index (SOI), obtained from the U.S. Department of Commerce National Oceanic and Atmospheric Administration (http://www.elnino.noaa.gov/) is shown by the white line and the red line indicates the zero SOI. Lighter colors indicate higher concentrations.

Simulated iron concentrations are almost completely depleted within the whole water column during the three El Niño periods (1991, 1994, and 1997). High iron values coincide with both high nitrate and high ammonium values. For example, at the beginning of 1998, similar to ammonium, an iron maximum (0.25 nmol l^{-1}) occurs around 80 m. The highest iron concentrations (0.3 nmol l^{-1}) occur at 120 m in mid-1998, similar to the nitrate concentrations.

The simulated silicate distribution follows a pattern similar to nitrate (Fig. 40D). Simulated silicate concentrations are low during the three El Niño periods (1991, 1994, and 1997), although concentrations are never depleted during the 1991 and 1994 El Niños. Contrary to nitrate, silicate is completely depleted ($\sim$0 μg l^{-1}) in the upper 100 m during the 1997 El Niño. The highest silicate concentrations also occur during mid-1998, associated with the 1998 La Niña.

Impact of time variable iron deposition on primary production

Using a mean constant aeolian iron deposition instead of using the time variable iron deposition (Fig. 34C) does not change the integrated annual primary production in the Cold Tongue region. The maximum difference in primary production between the two model runs is 0.5 μmol C l^{-1} d^{-1} (Fig. 41A). This small difference indicates that the time variability in aeolian iron deposition is not strong enough to significantly alter the annual integrated production of phytoplankton blooms in the Cold Tongue region (Fig. 36A).

The effect of a time invariant iron deposition is shown best by the difference in primary production obtained from the reference simulation and the constant iron source simulation (Fig. 41A). The largest difference occurs during years 1995 and 1996 when iron deposition is particulary high (Fig. 34C). However the percent difference in primary production between the two models runs (Fig. 41B) does not follow this pattern. Variable iron deposition increased primary production up to 40% during year 1995 and also decreased primary production up to 100% in 1998 (Fig. 41B). The difference in primary production for 1995 and 1998 is high (Fig. 41B), although the actual reduction in primary production is small (Fig. 41A). During these periods the actual simulated primary production is low (Fig. 36A). The large percent change

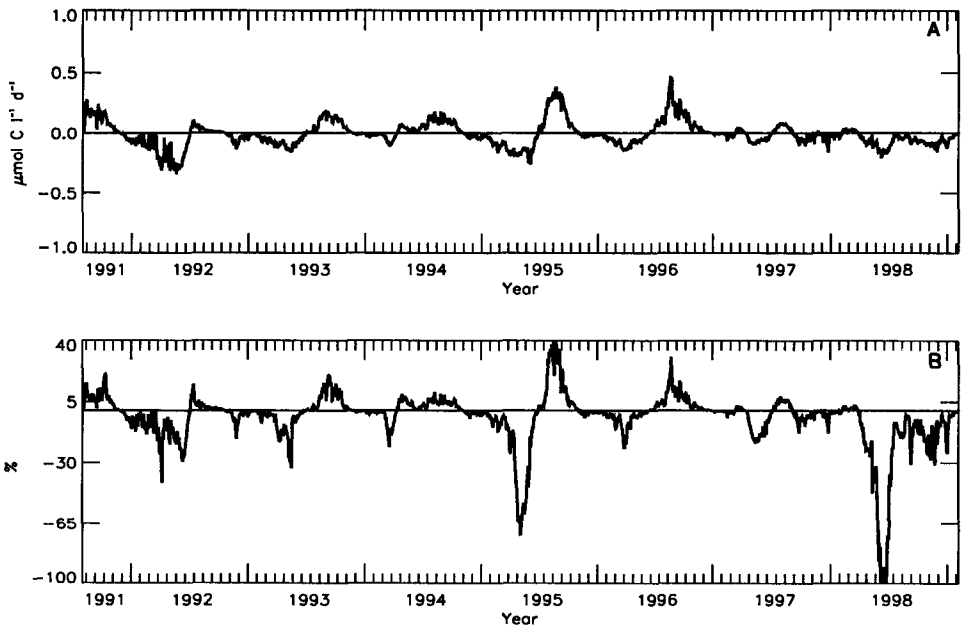

Fig. 41. Change in primary production in the Cold Tongue mixed layer in response to setting the aeolian iron deposition to a mean value of 0.013 nmol l^{-1} h^{-1}. Actual (A) and percent (%) (B) difference between the reference simulation and the simulation in which a constant (time invariant) aeolian iron deposition is used. Straight solid lines in both panels indicate the zero difference between two model runs.

due to variations in the iron input source suggests that aeolian iron deposition is responsible of a major part of primary production during these seasons.

V.7 DIEL VARIATIONS IN MIXED LAYER DEPTH

The deepest seasonal mixed layers (~120 m) occur during the El Niño periods (Fig. 34B) and the shallowest (10-30 m) occur during La Niña conditions in the Cold Tongue region. Superimposed on the seasonal change is strong diurnal variability in mixed layer depth (Fig. 42), which is caused by the diurnal heating of the surface waters. Heating stratifies the surface waters during the day, and convective cooling mixes the water at night (Price et al., 1986; Schudlich and Price, 1992). Recently, by using a neutrally buoyant float in the northeast Pacific Ocean D'Asaro et al. (1996) proved that the depth of the active mixing shows variability between day and night.

In the equatorial Pacific Ocean variations in the depth of the diel mixed layer

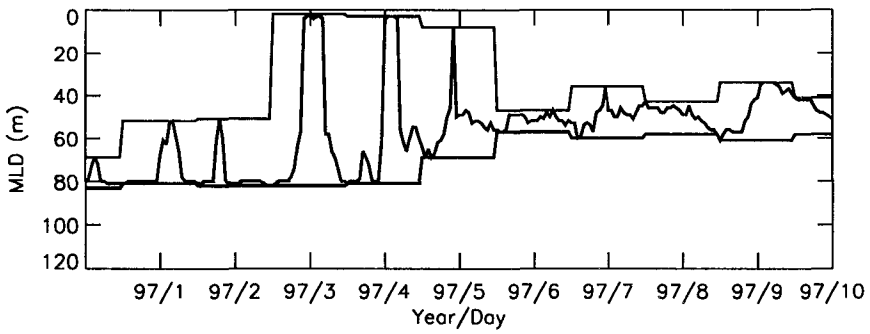

Fig. 42. Mixed layer depth (MLD) during the first 10 days of year 1997 estimated from temperature measurements from the TAO mooring at 0°N, 140°W. The upper and lower solid lines indicate the nighttime and daytime mixed layer depths, respectively.

using the 1°C difference from the SST criterion, are up to 110 m during El Niño periods, but are seldom over 25 m during La Niñas. The strongest diel fluctuations in the mixed layer depth are estimated for the 1997-1998 El Niño, which are as great as 110 m.

Night-time mixed layer deepening entrains nutrient-rich waters into the mixed layer and dilutes the phytoplankton biomass. Daytime shoaling of the mixed layer confines these nutrient-rich waters to a high light environment that accelerates biological production. Simulations that use a mixed layer depth that undergoes a diurnal deepening and shallowing show that this process can significantly affect the distribution of chlorophyll a, and influence primary production by pumping nutrients upward and by controlling light levels experienced by phytoplankton (not shown). Many of the biochemical pools included in the lower trophic level model have strong gradients in the upper 100 m of the ocean and high frequency oscillations in the depth of mixing can be important in enhancing vertical exchange in surface waters. Those components of the lower trophic level ecosystem with high surface concentrations (i.e. phytoplankton and zooplankton) are mixed downwards, while those with concentrations that increase with depth (i.e. nutrients) are pumped upward.

Inclusion of a diurnally-varying mixed layer depth increases the simulated annual

primary production by 9% compared to using only a daytime (minimum) mixed layer depth. The night-time (maximum) mixed layer depth produces only a 1.4% increase in annual primary production, relative to the value obtained using a variable mixed layer depth.

The diurnal dilution of phytoplankton biomass provides a mechanism for transporting particulate matter downward and out of the surface layer. However, the simulation results suggest that this may not be a significant contributor to export fluxes, consistent with observations (Gardner et al., 1999). The simulated carbon flux at 120 m is 9% higher for a diurnally varying mixed layer relative to the value obtained from simulations that used the daytime (minimum) mixed layer depth.

V.8 COMPARISON OF TWO ECOSYSTEMS, COLD TONGUE VERSUS WARM POOL

V.8.1 Warm Pool environmental time series

The effect of the SOI on the Warm Pool differs from that observed for the Cold Tongue region. The water temperatures at 120 m begin cooling right after the SOI switches to the negative phase (El Niño) and continue to decrease during the negative phase (Fig. 43A) unlike the Cold Tongue where El Niño conditions correspond to anomalously warm waters. During the positive phases of SOI (La Niña) water temperatures in the Warm Pool region are warmer than usual (Fig. 43A).

The surface waters in the Warm Pool stayed around 29°C throughout the decade of the 1990s, except for two cold periods (27°C) at the end of 1995 and during 1998 (Fig. 43A). The warmest waters at 120 m are observed during the end of the 1995-1996 La Niña which corresponds to a cool period in the Cold Tongue. The coldest waters are observed towards the end of the 1997 El Niño; whereas, during this period anomalously warm waters extend down to 100 m in the Cold Tongue region. The other cold period is during 1995, which corresponds to the end of the 1994-1995 El Niño.

The estimated mean mixed layer depths in the Warm Pool region are deeper

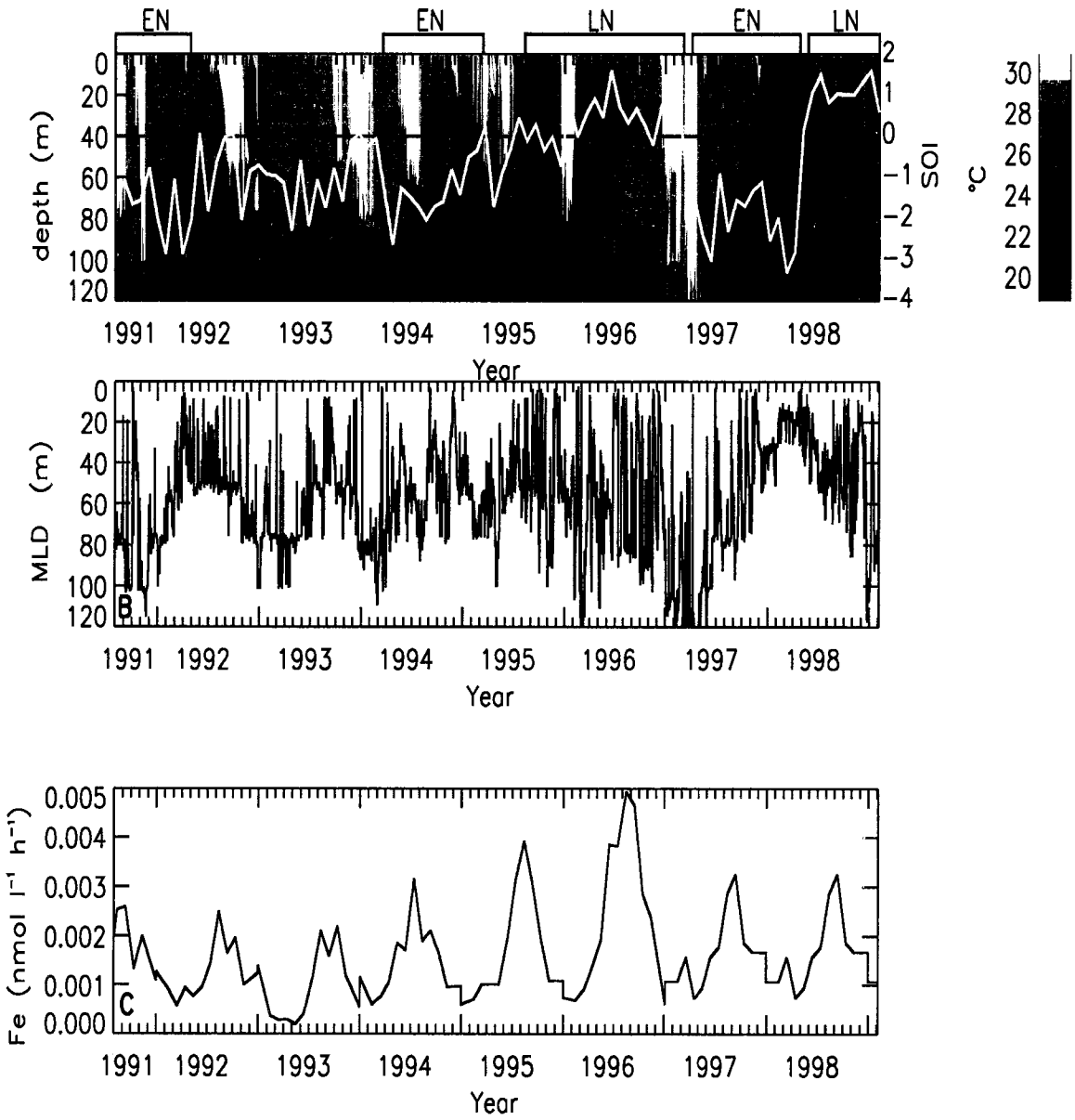

Fig. 43. Depth-time distribution of (A) temperature, (B) estimated mixed layer depth (MLD) and, (C) aeolian iron flux (Ginoux et al., 2001) for 1991 to 1999 for the Warm Pool (0°N, 165°E) region. The temperature and MLD are from the TAO mooring at 0°N, 165°E. The Southern Oscillation Index (SOI), obtained from the U.S. Department of Commerce National Oceanic and Atmospheric Administration (http://www.elnino.noaa.gov/) is shown by the white line and the black line indicates the zero SOI. The time periods of El Niños (EN, red) and La Niñas (LN, blue) are shown. Lighter colors indicate higher temperature.

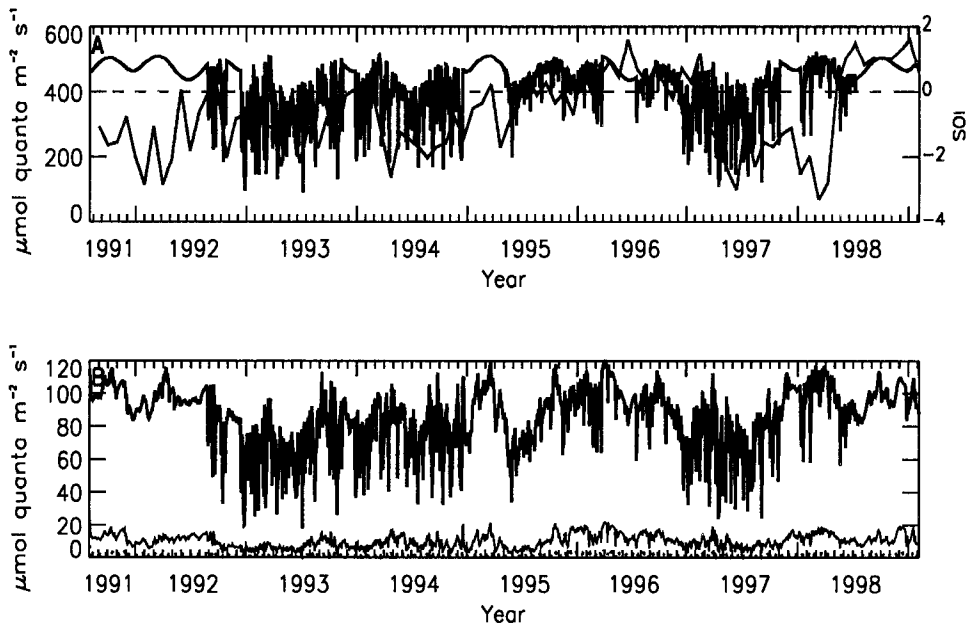

Fig. 44. Time series of simulated (A) integrated downwelling irradiance (PAR) just below the surface and (B) daily integrated downwelling irradiance arriving at 20 m (solid line), 60 m (thin solid line), and 100 m (dotted line). These results are obtained for the Warm Pool region at 0°N, 165°E from the model described in section 4.2. The Southern Oscillation Index (SOI), obtained from the U.S. Department of Commerce National Oceanic and Atmospheric Administration (http://www.elnino.noaa.gov/) is shown by the solid grey line and the dashed grey line indicates the zero SOI.

than those estimated for the Cold Tongue region (average depth of 59 versus 44 m). Unlike in the Cold Tongue region, the estimated mixed layer depths associated with the La Niña episodes are deeper than those that occur during the El Niño events in the Warm Pool (Fig. 43B). During the El Niño periods of 1994 and 1997 mixed layer depths stay particularly shallow (~30 m). The mixed layer depth extends to 120 m at the beginning of the 1997 El Niño and shoals afterwards as the event develops.

The aeolian iron flux obtained from Ginoux et al. (2001) for the Warm Pool indicates a strong annual variability in iron deposition similar to what is obtained for the Cold Tongue region (Fig. 43C). The least iron deposition occurs during February-April and the highest during August-October. Year 1996 corresponds to a high dust deposition period.

The annual cycle of the irradiance in the Warm Pool is similar to the Cold Tongue, and the variability in annual irradiance is low in both regions (± 50 μmol quanta m^2 s^{-1}). The general cloud cover is higher in the Warm Pool compared to the Cold Tongue. There is no linear correlation between the SOI and the cloud cover in the Warm Pool. The start of the high cloud cover occurs towards the end of the positive phase of SOI and continues as the SOI switches to negative (Figs. 44A and B). During the 1990s cloud cover was consistently high in the region except for the second part of 1995.

V.8.2 Phytoplankton

The simulated annual integrated primary production in the Warm Pool is 20% lower than that obtained for the Cold Tongue. However, there is only a small difference (5%) in integrated algal biomass between the two regions, although the distribution of each algal group biomass shows distinct differences between the two regions.

The simulated depth-time distributions of the five algae groups at 0°N, 165°E for 1991-1999 indicate that in the Warm Pool the highest algal group biomass concentrations occur during the El Niño phases (Figs. 45A-E) contrary to what happens in the Cold Tongue region (Figs. 37A-E). Algal group 4 dominates the phytoplankton community assemblage in the Warm Pool (Figs. 45A-E), but this dominance is not continuous as it is in the Cold Tongue (Figs. 37A-E). During cold periods algal group 4 becomes dominant and during warm periods the biomass of *Prochlorococcus* spp. (algal group 1 + 2) is as high as that of algal group 4.

The annual biomass of algal group 1 in the Warm Pool is 60% higher than its biomass in the Cold Tongue. The highest algal group 1 biomass corresponds to the negative SOI phases, and the lowest biomass values for this group correspond to the beginning of the 1997 El Niño (Fig. 45A). The simulated annual biomass of algal groups 2 and 3 is slightly higher and lower, respectively, relative to the values obtained from the Cold Tongue simulations.

The biomass distribution patterns of algal groups 2-4 are similar and these groups

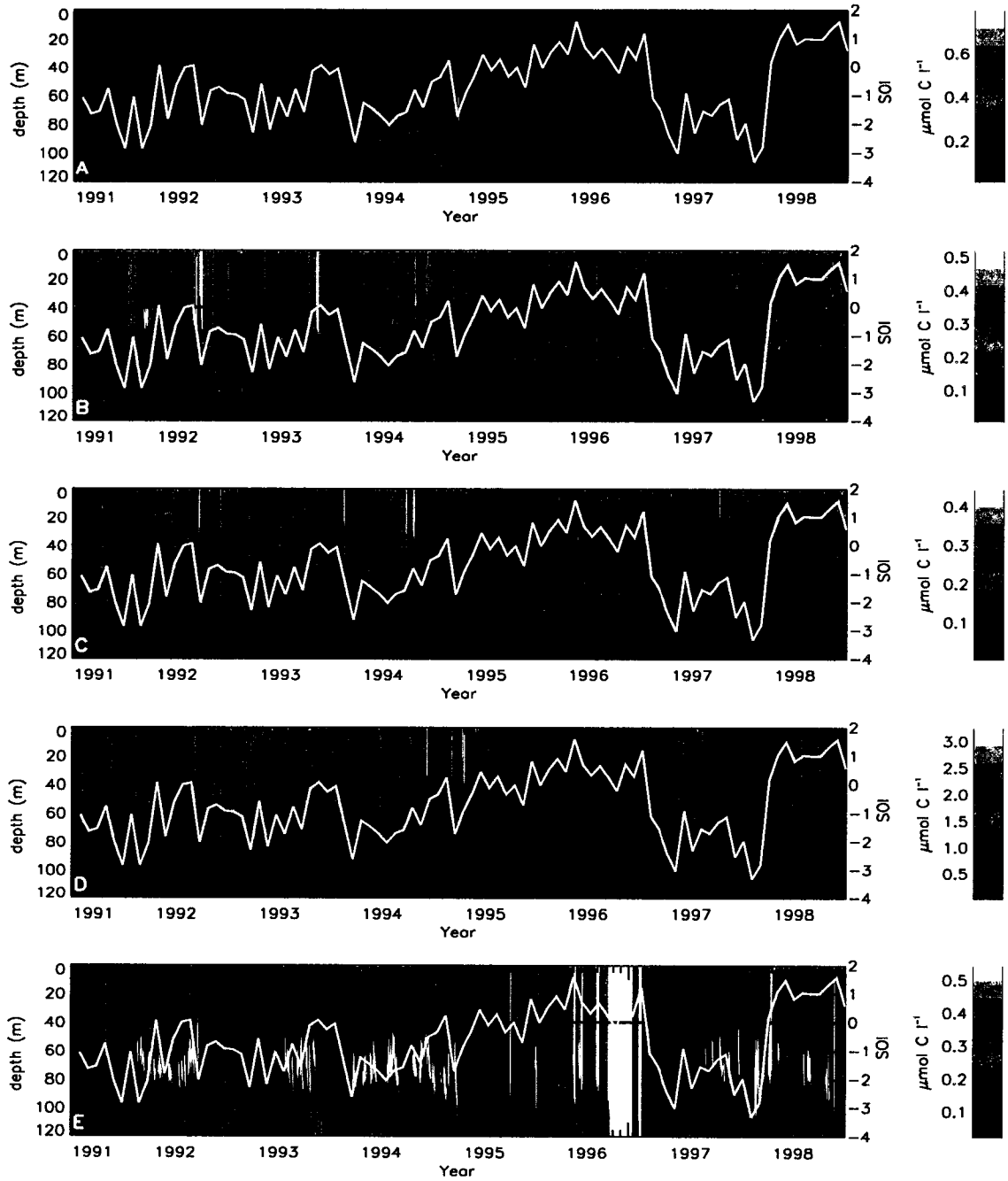

Fig. 45. Simulated depth-time biomass (μmol C l^{-1}) distributions of (A) low light-adapted *Prochlorococcus* (algal group 1), (B) high light-adapted *Prochlorococcus* (algal group 2), (C) *Synechococcus* (algal group 3), (D) autotrophic eukaryotes (algal group 4), and (E) large diatoms (algal group 5) in the Warm Pool region at 0°N, 165°E. The Southern Oscillation Index (SOI) obtained from the U.S. Department of Commerce National Oceanic and Atmospheric Administration (http://www.elnino.noaa.gov/) is shown by the white line and the red line indicates the zero SOI. Lighter colors indicate higher concentrations.

show episodic blooms from 1991 to the end of 1995, which corresponds to a period of negative SOI (Fig. 45B-D). The biomass of these groups are at their lowest during the 1995-1996 La Niña, and they bloom during the 1997 El Niño. Towards the beginning of the 1998 La Niña, a substantial decrease in the biomass of these algal groups occurs, which is followed by another bloom in the middle of the 1998 La Niña period.

The maximum biomass of algal group 5 coincides with the times and depths at which the biomass of other groups are low (Fig. 45E), similar to what occurs in the Cold Tongue simulations (Fig. 37E). The highest biomass of this group generally occurs below the mixed layer depth (mid-1992, 1994, and 1998). The exception occurs at the end of the 1996, which corresponds to the end of 1996 La Niña, when the total algal biomass is particularly low. The deep mixed layer occurring during this period uniformly distributes the biomass in the water column (Fig. 34B). A second surface bloom by algal group 5 occurs during the 1998 La Niña.

Simulations indicate that the deep chlorophyll maximum in the Warm Pool (Fig. 46) is in general deeper than the deep chlorophyll maximum in the Cold Tongue (Fig. 38) ($\sim$50 m versus $\sim$65 m). The surface chlorophyll *a* values in the Warm Pool are low, with a mean concentration of 0.25 μg l^{-1}. During the warm periods chlorophyll *a* concentrations are below 0.2 μg l^{-1} and increase to 0.4 μg l^{-1} during the cold periods. The highest simulated chlorophyll *a* values (1.1 μg l^{-1}) are at 40 m during 1995, which corresponds to the end of the 1994-1995 El Niño when cold waters reach the surface (Fig. 43A). During this period the highest surface values are 0.8 μg l^{-1} (Fig. 47).

The comparison of simulated chlorophyll *a* versus SeaWiFS chlorophyll *a* (Fig. 47) shows that the simulated bloom associated with El Niño conditions occurs earlier than observed, similar to what was seen in the simulated chlorophyll distributions for the Cold Tongue region (Fig. 39). The magnitude of the simulated bloom is similar to the observed values.

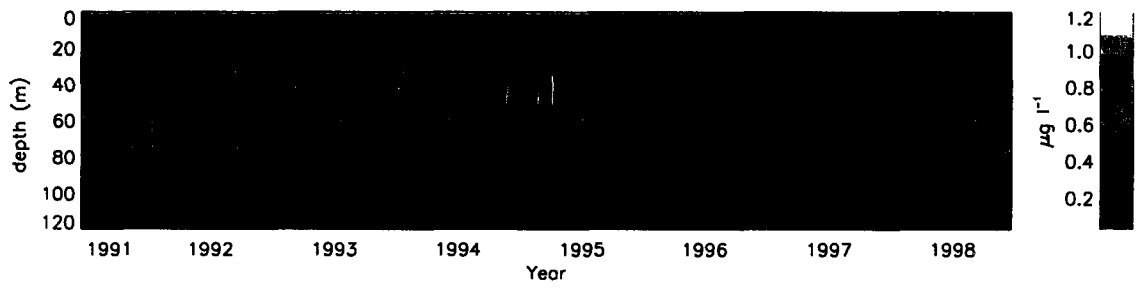

Fig. 46. Simulated depth-time distributions of chlorophyll a (μg l^{-1}) obtained from the sum of all five algal groups in the Warm Pool at 0°N, 165°E for 1991-1999. Lighter colors indicate higher concentrations.

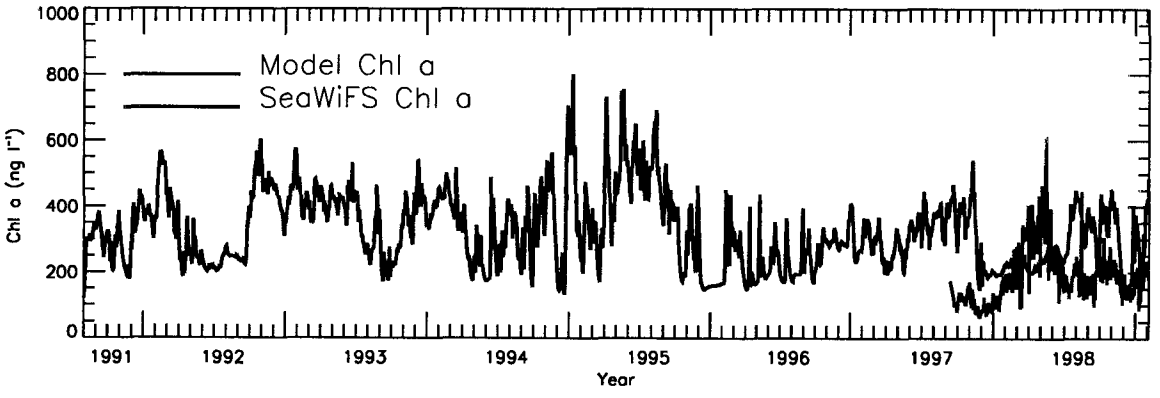

Fig. 47. Comparison of simulated chlorophyll a (black) with chlorophyll a derived from Sea-viewing Wide Field of view Sensor (SeaWiFS) measurements (grey) at 0°N, 165°E. The SeaWiFS data set begins in Fall 1997.

V.8.3 Nutrients

The simulated depth-time concentrations in the upper 120 m of the four nutrients in the Warm Pool at 0°N, 165°E are low during La Niña periods and high during El Niño periods (Figs. 48 A-D). The highest nutrient concentrations occur during the negative phases of SOI and the lowest concentrations occur during La Niña (positive SOI) periods. During the 1995-1996 La Niña, the lowest concentrations of all nutrients occur. Nitrate, ammonium and iron were completely depleted above 80 m during 1996 and the silicate concentrations gradually decrease from 4 μmol l^{-1} to below 1 μmol l^{-1} during this year.

The simulated distributions indicate that surface nitrate levels in the Warm Pool are much lower (annual mean of 1.2 μmol l^{-1}, Fig. 48A) than those in the Cold Tongue (annual mean of 8.9 μmol l^{-1}, Fig. 40A). The highest nitrate levels occur in the Warm Pool during the 1997-1998 and 1991-1993 El Niños. During the rest of the decade nitrate is depleted (<1 μmol l^{-1}) in the surface waters.

In general ammonium concentrations are very low (<0.1 μmol l^{-1}) above 40 m. There is a strong (~1 μmol l^{-1}) ammonium maximum centered at ~80 m (Fig. 48B), which persists throughout the 1990s, except for the 1995-1996 La Niña period. The strength of this ammonium maximum differs from that seen in the Cold Tongue simulations where ammonium maxima values rarely reached 1 μmol l^{-1} (Fig. 40B).

The Warm Pool simulations show that this region is also iron depleted (Fig. 48C), similar to what was found for the Cold Tongue (Fig. 40C). The iron concentrations are also very low above 40 m (<0.1 nmol l^{-1}), although the mean surface iron concentration is more than double the mean iron concentration in the Cold Tongue (0.07 versus 0.03 nmol l^{-1}, respectively). The highest simulated iron concentrations occurred during the 1994-1995 El Niño.

The simulated silicate concentrations in the Warm Pool (Fig. 48D) are lower than those obtained for the Cold Tongue (Fig. 40D). However, silicate concentrations in the Warm Pool are never depleted, except at the beginning of 1997 (~0.5 μg l^{-1}), which corresponds to the end of the 1995-1996 La Niña. For a persistent negative

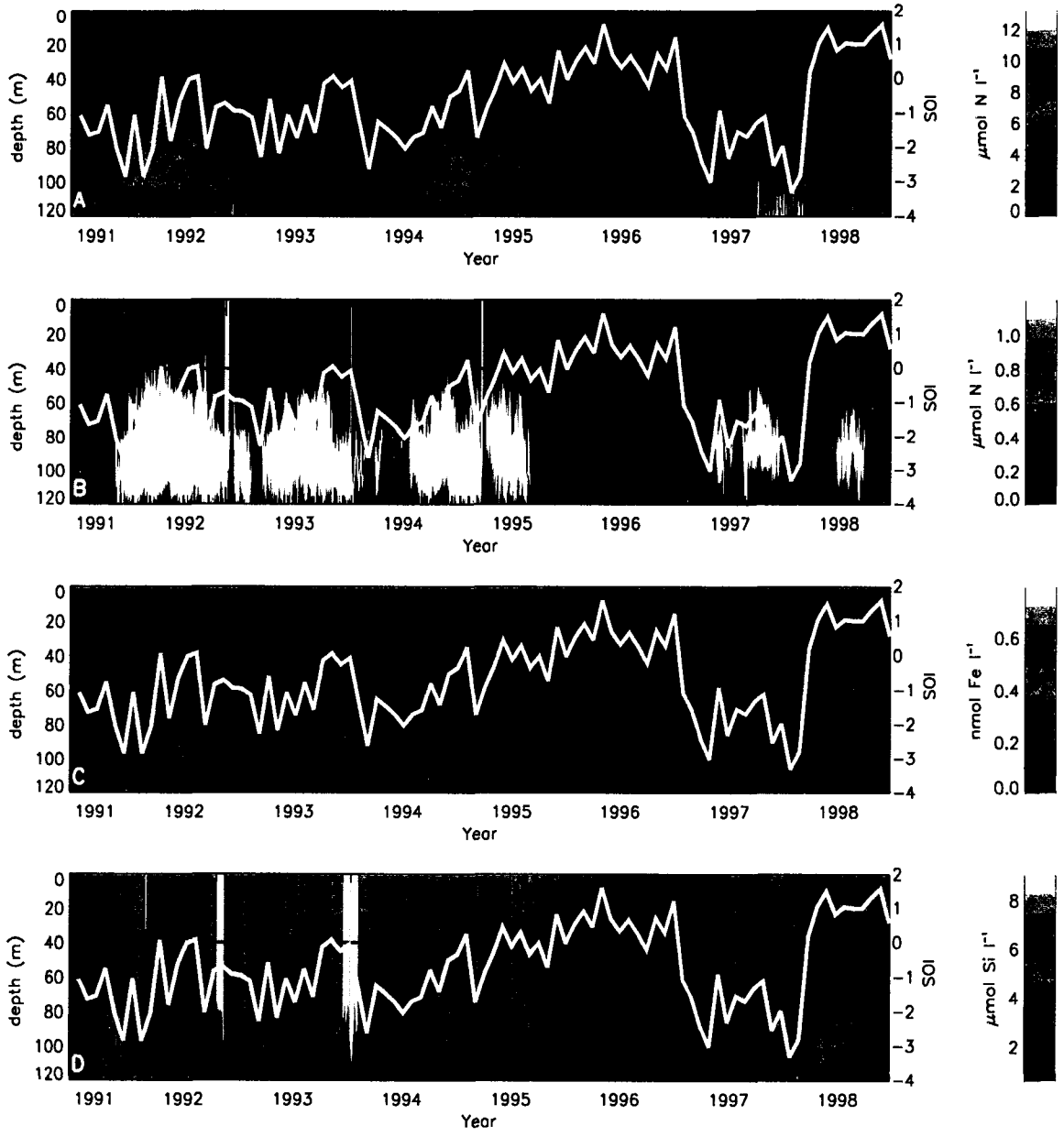

Fig. 48. Simulated depth-time distributions of the concentrations of (A) nitrate, (B) ammonium, (C) iron, and (D) silicate in the Warm Pool. The Southern Oscillation Index (SOI), obtained from the U.S. Department of Commerce National Oceanic and Atmospheric Administration (http://www.elnino.noaa.gov/) is shown by the white line and the red line indicates the zero SOI. Lighter colors indicate higher concentrations.

Table 15
Comparison of simulated nitrate (NO_3^-), ammonium (NH_4^+), silicate ($Si(OH)_4$), and primary production (PP) values with their corresponding values measured during the 1994 FLUPAC and 1996 Zonal Flux cruises

	Unit	Time	Observed	Modeled
NO_3^- surface (0-30 m)	μmol l^{-1}	29/9/1994	0.003	0.002
NO_3^- total (0-120 m)	mmol m^{-2}	29/9/1994	172	499
NO_3^- surface (0-30 m)	μmol l^{-1}	22/4/1996	2.61	0.82
NO_3^- total (0-120 m)	mmol m^{-2}	22/4/1996	313	265
NH_4^+ surface (0-30 m)	μmol l^{-1}	29/9/1994	0.01	0.01
NH_4^+ total (0-120 m)	mmol m^{-2}	29/9/1994	3.6	62
NH_4^+ surface (0-30 m)	μmol l^{-1}	22/4/1996	0.9	0.01
NH_4^+ total (0-120 m)	mmol m^{-2}	22/4/1996	94.4	11
$Si(OH)_4$ surface (0-30 m)	μmol l^{-1}	29/9/1994	1.7	3.5
$Si(OH)_4$ total (0-120 m)	mmol m^{-2}	29/9/1994	325	470
$Si(OH)_4$ surface (0-30 m)	μmol l^{-1}	22/4/1996	4.75	3.14
$Si(OH)_4$ total (0-120 m)	mmol m^{-2}	22/4/1996	480	334
PP surface (0-30 m)	μmol l^{-1} d^{-1}	3/10/1994	0.85	2
PP total (0-120 m)	mmol m^{-2} d^{-1}	3/10/1994	74	95.57
PP surface (0-30 m)	μmol l^{-1} d^{-1}	22/4/1996	1.5	0.3
PP total (0-120 m)	mmol m^{-2} d^{-1}	22/4/1996	93.8	47

SOI, which corresponds to upwelling of cold waters at 120 m and surface stratification (Fig. 43A), silicate tends to accumulate in the mixed layer. During the 1991-1993 El Niño when these conditions prevailed in the Warm Pool region, the simulated silicate concentrations are above 8 nmol l^{-1} in the mixed layer.

V.8.4 Model-data comparison

The lower trophic level ecosystem model was not explicitly developed for the Warm Pool, and as a result the Warm Pool simulations provide additional model sensitivity studies. The simulated distributions are compared with measurements made during two cruises that took place in the Warm Pool to provide an assessment of the general applicability of the model structure (Table 15). The details of the data collected during the 1994 FLUPAC and 1996 Zonal Flux cruises are described in Chapter 3.

Overall, the simulated nutrient and primary production values compare well with

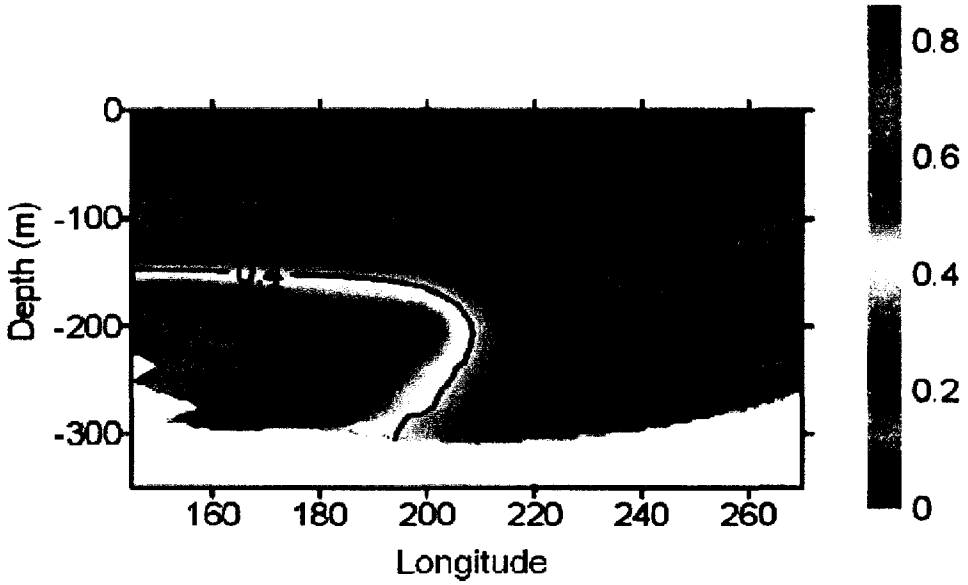

Fig. 49. Vertical distribution of iron concentration (nM) along the equator in the Pacific Ocean. The section was constructed from two iron profiles reported by Nakayama et al. (1995) at 150°E and 158°W, EqPac measurements reported by Gordon et al. (1997) at 140°W and PlumEx profiles reported by Gordon et al. (1998) at 93°W (adapted from Johnson et al. (2002)). Sampling locations where iron was measured are indicated by circles.

measurements, but these comparisons are not strong when done for specific days (Table 15). However, it should be noted that the measurements have poor space and time resolution and as a result may not be directly comparable to the simulated values.

The observed and simulated surface concentrations of nitrate and ammonium compare well during the 1994 FLUPAC cruise, which corresponds to an El Niño period. The observed surface silicate concentrations are lower than the simulated values during this time. The model overestimates the 120-m integrated nutrient values compared to those obtained from nutrient measurements made during the 1994 FLUPAC cruise. The model underestimates both the surface and integrated nutrient concentrations compared to measured values from the 1996 Zonal Flux cruise, which corresponds to the 1995-1996 La Niña period. As a result of this mismatch in the nutrient concentrations, the simulated primary production values for 1994 overestimate the values measured in 1994 and underestimate the 1996 measured values.

No direct iron measurements are available for 0°N, 165°E. However, some historical data for this region are available (Johnson et al., 2002). Comparisons of the simulated iron concentrations to the historical iron measurements show that the simulated values are realistic in that iron levels above 80 m are less than 0.1 nmol l^{-1} (Fig. 49 vs. Fig. 48C). Observed iron concentrations at 120 m are about 0.2 nmol l^{-1} (Fig. 49), which is also consistent with simulated concentrations.

V.8.5 Iron dynamics

To test the effect of iron on limiting production in the Warm Pool a simulation was done using the iron-temperature relationship developed for the Cold Tongue (Eq. 46). The resultant annual primary production values are about 50% of those obtained for the Cold Tongue region (27,022 versus 14,338 mmol C m^{-2} yr^{-1}). The iron-temperature relationship developed for the Warm Pool (Eq. 50) results in an increase of annual primary production by almost 75%, but this value is still 22% lower than the annual primary production estimated for the Cold Tongue.

The pattern of aeolian iron deposition differs between the two regions (Fig. 34C versus 43C), but the mean hourly deposition in both regions is almost the same ($\sim$0.038 nmol l^{-1} hr^{-1}). The simulations indicate that the effect of aeolian iron deposition on the Warm Pool ecosystem is somewhat stronger than its effect on the Cold Tongue ecosystem. Elimination of iron via aeolian deposition decreases the annual primary production of the Warm Pool by 20% and that of the Cold Tongue by 17%. Algal group 4 in the Warm Pool ecosystem is the most affected by no aeolian deposition, showing a 24% decrease in annual primary production.

The simulated iron remineralization has a substantial influence on the Warm Pool carbon production, accounting for 50% of the annual primary production. This is higher than the 40% annual primary production in the Cold Tongue that is supported by iron remineralization.

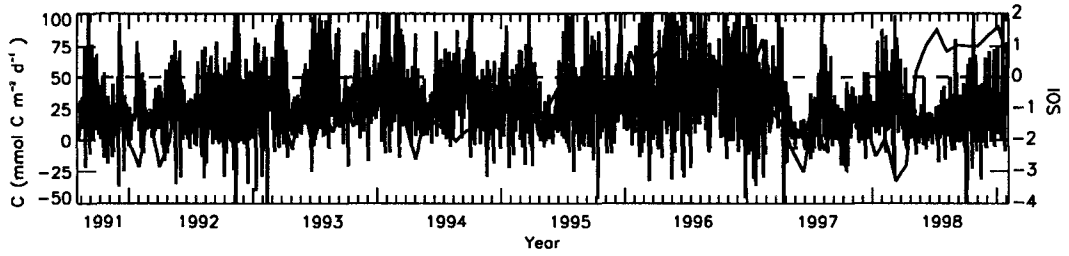

Fig. 50. Simulated time distribution of particulate carbon export fluxes at 120 m in the Cold Tongue. The Southern Oscillation Index (SOI), obtained from the U.S. Department of Commerce National Oceanic and Atmospheric Administration (http://www.elnino.noaa.gov/) is shown by the lighter color (green) line and the dashed (red) line indicates the zero SOI.

V.8.6 Export production

The simulated annual carbon fluxes at the base of the euphotic zone (120 m) in the Warm Pool are 22% lower than the equivalent carbon flux calculated for the Cold Tongue. These results are consistent with observations, which showed that the mean POC flux in the Warm Pool is ~15% lower than that in the Cold Tongue region (Dunne et al., 2000).

The simulated particulate carbon export fluxes in the Cold tongue are correlated with the SOI (Fig. 50). During the cold (positive) phases of SOI the carbon export is high compared to the warm (negative) phases of SOI, except at the beginning of 1997, when high export production is seen in the simulated time series (Fig. 50). In contrast, there is no apparent correlation between export carbon production and the SOI in the Warm Pool (Fig. 51). The periods of highest simulated export carbon production coincide with the negative phases of SOI. During 1996, when the SOI is persistently positive, the export carbon production in the Warm Pool is near zero.

In both regions export carbon production values are variable. For example, in the Cold Tongue (Fig. 50) the export carbon fluxes are ~3 times higher during the 1995-1996 La Niña than those during the 1994 El Niño. In the Warm Pool low frequency variability dominates the simulated export carbon flux (Fig. 51), whereas the Cold Tongue export carbon flux shows more influence from high frequency motions (Fig. 50). In the Warm Pool, the difference in the simulated export carbon flux between

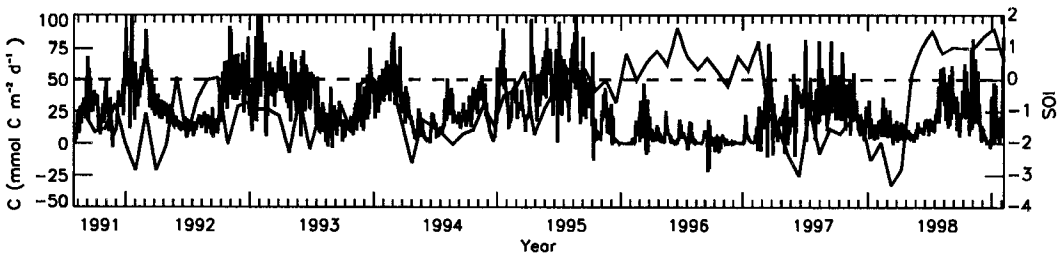

Fig. 51. Simulated time distribution of particulate carbon export fluxes at 120 m in the Warm Pool. The Southern Oscillation Index (SOI), obtained from the U.S. Department of Commerce National Oceanic and Atmospheric Administration (http://www.elnino.noaa.gov/) is shown by the lighter color (green) line and the dashed (red) line indicates the zero SOI.

the cold and warm phases can increase by a factor of five.

CHAPTER VI

DISCUSSION

The modeling approach used in this study provides a framework for testing in a quantitative manner the understanding of factors that control phytoplankton biomass, growth rate, primary production, and export production in the equatorial Pacific Ocean. The simulated model state variables and ratios show the importance of interaction between the algal groups in defining the composition of the phytoplankton community and its primary production and carbon flux. In this section, the performance of the algal group-based ecosystem model is discussed as well as the results of the model sensitivity simulations that are described in Chapter 4. Specifically, the discussion focuses on the cause and effect of the patterns seen in the simulated distributions, interprets the nonlinear interactions that occur between biomass, primary production, and carbon fluxes, discusses the influence of the environment on carbon production and export, and analyzes the implications of climate variability for the lower trophic level ecosystem. In section 6.5 the differences in ENSO effects on the Cold Tongue and the Warm Pool ecosystems are discussed.

VI.1 CAUSE AND EFFECT OF PATTERNS IN MODEL STATE VARIABLES AND DERIVED FIELDS

VI.1.1 Phytoplankton structure

Many of the ecosystem models developed for the equatorial Pacific Ocean (e.g., Chai et al., 1996; Loukos et al., 1997; Leonard et al., 1999; McClain et al., 1999; Friedrichs and Hofmann, 2001; Christian et al., 2002a) include one or two species of plankton (i.e. nanoplankton and netplankton) which underrepresents the dynamics of the phytoplankton community. For example, in the two-species models that include iron (e.g., Leonard et al., 1999; Christian et al., 2002a), it is assumed that the large phytoplankton growth rates are strongly limited by iron and that the maximal rates of grazing mortality are less for these cells than for the small phytoplankton.

These assumptions allow the netplankton to escape grazing control under strong upwelling conditions and become dominant because the small phytoplankton remain under strong grazer control. However, in the equatorial Pacific the netplankton (e.g., diatoms) do not exceed 15% of the total biomass even under strong upwelling conditions (Chavez, 1989; Iriarte and Fryxell, 1995; Bidigare and Ondrusek, 1996). Moreover, Bidigare and Ondrusek (1996) suggested that in the equatorial Pacific region some nanoplankton do not experience strong grazer control and that they bloom during strong upwelling conditions.

The multiple algal group model (section 4.1) used in this study avoids these limitations in dynamics by including algal group 4 (i.e. autotrophic eukaryotes), which falls between the large and small phytoplankton groups used in other models (e.g., Christian et al., 2002a), and by inclusion of three smaller forms (algal groups 1 to 3). Algal group 4 responds strongly to strong upwelling conditions and blooms. The biomass of the smaller phytoplankton forms is controlled by microzooplankton. Algal group 5 is controlled by mesozooplankton and remains below 15% of the total biomass. The choice of the model structure used in this study is also in keeping with the current understanding of the lower trophic levels of the equatorial Pacific (Chavez, 1989; Iriarte and Fryxell, 1995; Lindley et al., 1995; Bidigare and Ondrusek, 1996; Coale et al., 1996b; Chavez et al., 1996; Landry et al., 1996; Latasa et al., 1997; Higgins and Mackey, 2000; Landry et al., 2000a) and the U.S. JGOFS EqPac results (section 5.1.7).

Based on model-derived results, Christian et al. (2002b) concluded that the iron-mediated removal of surface nitrate by phytoplankton was such that significant inputs of iron were needed to prevent the accumulation of nitrate in surface waters of the equatorial Pacific. This result implies that phytoplankton in equatorial waters must have small iron quotas (e.g., less than 0.003 nmol Fe (μmol C)$^{-1}$). However, the inclusion of variable cellular nutrient quotas, as done in the model used in this study, removes the need for assuming uniformly low cellular iron quotas. The nitrogen to carbon ratios of each algal group remain high (Figs. 12A-E), allowing nitrate to be deposited in the cells, which in turn allows the cellular iron to carbon ratios to be

low and variable in the surface waters (Figs. 13A-E). Only the cellular iron quotas of algal groups 4 and 5 decrease to 0.003 nmol Fe $(\mu\text{mol C})^{-1}$ (Figs. 13D and E).

Inclusion of multiple algal groups resolves some basic problems associated with simulating phytoplankton growth and production. This structure also makes it possible to analyze the effect of each group on carbon biomass, production, and flux. The results of the simulations (section 5.2.1) show that all algal groups have a considerable effect on phytoplankton carbon biomass, but that not all have a strong effect on primary production and carbon flux (Fig. 25). This indicates that carbon cycle models need to include the few key algal groups that have the primary influence on primary production and export variability. It is possible to combine algal groups 1-3 (low-light adapted *Prochlorococcus*, high-light adapted *Prochlorococcus* and *Synechococcus*) under one group (e.g. cyanobacteria group) to form a three algal group model for use in carbon cycle models. The first three groups comprise a separate group because of their distinctive nutrient utilization characteristics, as explained in section 4.1, and because the carbon budget estimations (Fig. 17) show that these three groups are responsible for a substantial percentage (27%) of the carbon transfer between the primary producers and the higher trophic levels (section 5.1.6.). A group (i.e. autotrophic eukaryotes) that falls between large diatoms and this cyanobacteria group is essential as explained above. Both the sensitivity studies (Fig. 25) and the carbon budget estimations (section 5.1.6.) show that algal group 5 is responsible for ~8% of the carbon export to higher trophic levels, although the contribution by this group to carbon export small, because of reduced growth rates due to iron limitation. However, this group should be retained in carbon cycle models because iron enrichment experiments done in equatorial Pacific waters (Coale et al., 1996b) showed that large diatoms can be a major contributor to carbon production under iron replete conditions.

Algal group biomass and primary production

The physiological differences in algal groups are also reflected in the vertical distribution patterns of biomass and primary production rate. The primary production

resulting from algal group 1 is confined to a narrow band around 60 m (Fig. 8A), with the biomass of this group being more dispersed (Fig. 6A). Primary production by algal groups 2-4 occurs mainly in the upper 60 m of the water column (Fig. 8B-D), but the simulated distributions show that these phytoplankton are also abundant below the surface waters (Fig. 6B-D), which is consistent with observations (Landry et al., 1996). The biomass dispersion of these groups occurs by vertical advection and diffusion, and mixing in the mixed layer. The primary production of algal group 5 is confined to the bottom of the mixed layer and is mixed upwards by convection. Deepening of the mixed layer can increase the phytoplankton production by pumping nutrients into the euphotic zone. However, when the mixed layer extends below the euphotic zone, which occurred between YD15-60 in the reference simulation, primary production ceases as the cells are moved out of the lighted part of the water column (Figs. 8A-E). Similarly, mixing upwards benefits some algal groups, such as groups 3 and 4, because of increased light (Figs. 8C and D). Other algal groups, such as groups 1 and 2, stop growing because of photoinhibition (Figs. 8A and B). Light inhibition of growth is stronger for algal group 1 compared to algal group 2, and as a result the biomass of algal group 1 in surface waters is lower than its biomass below the mixed layer (Fig. 6A). Algal group 2, in comparison, is abundant within the mixed layer (Fig. 6B).

Within the mixed layer, algal groups 1 to 3 show less temporal variability compared to algal groups 4 and 5, because heavy grazing by microzooplankton on the smaller cells buffers the variability in their biomass. The distribution of the simulated biomass of algal group 5 is higher below the mixed layer compared to the surface waters (Fig. 6E). Nutrient limitation (especially iron limitation) is stronger for algal group 5 compared to the others (Fig. 13E). Although light levels are lower below the mixed layer, nutrient concentrations are higher, and this results in optimal growth conditions for this algal group. Also, the simulated mesozooplankton are abundant in the mixed layer (Fig. 14B) which results in removal of algal group 5 in the mixed layer at a rate that is higher than that below the mixed layer. This decrease in grazing pressure towards deeper waters contributes to the increase in algal group 5

biomass towards the bottom of the euphotic zone.

The simulated phytoplankton biomass during YD110-YD160, YD200-YD255, and YD300-YD320 was higher than that observed during the U.S. JGOFS EqPac TS2 cruise (Fig. 19). The TS2 cruise occurred during the passage of a relatively weak TIW (Friedrichs and Hofmann, 2001) and the thermocline depth during the TS2 cruise was deeper than during the YD110-YD160, YD200-YD255, and YD300-YD320 periods (Fig. 4A). The highest simulated phytoplankton biomass values occurred during YD300-YD320, which corresponds to the passage of strong TIWs which can be seen in vertical velocity fields (Fig. 4B). These blooms also correspond to relatively shallow mixed layer depths and cold water temperatures representative of high nutrient concentrations (Figs. 4B and C).

Towards the end of the El Niño period during YD45-75, three consecutive strong IGWs appear in the vertical velocity fields (Fig. 4B) as shifts in velocity from ~20 m d^{-1} to 0 m d^{-1} over 6-8-days. The passage of the IGWs do not trigger phytoplankton blooms, because this period also coincides with the passage of a Kelvin wave, which produces a deep thermocline and deep mixed layer depths (Figs. 4A and C).

The simulated algal group biomass abundance and distribution are realistic as determined from comparison with measurements (section 5.1.7). However, the simulated primary production values underestimated observed rates (Figs. 20A and B). One potential reason for this mismatch is that the simulated and measured primary production rates may not represent the same processes. During the U.S. JGOFS EqPac cruises net daily particulate carbon production resulting from autotrophic and heterotrophic processes was estimated (Barber et al., 1996). The simulated primary production estimates are based on only production by autotrophic algae. Kirchman et al. (1995) argued that the ratio of heterotrophic bacteria production to primary production was around 0.15 during the TS1 and TS2 cruises. If the observed primary production rates are reduced by 15%, than the simulated mixed layer primary production values (Fig. 20A) fall within the observed limits. However, the simulated integrated primary production values are still lower than the observations (Fig. 20B).

Algal group physiology

Algal groups 1 and 2 cannot use nitrate as a nitrogen source (section 4.5), and as a result ammonium is depleted in the surface waters (Fig. 15B). However, the cellular nitrogen to carbon ratios for algal group 1 stay at their maximum values; whereas, those for algal group 2 are below their maximum values (Figs. 12A and B). This arises because algal group 1 is not limited by ammonium at the surface, it is already light limited. Similarly, the cellular iron to carbon ratios of algal group 1 are always maximum (Fig. 13A), which indicates that this group is not iron limited either. The inability of *Prochlorococcus* spp. to use nitrate has a considerable effect on the simulated primary production and carbon fluxes (section 5.2.2) and implies that this level of physiological detail needs to be included in biogeochemical and carbon cycling models.

The simulated cellular iron to carbon ratios of algal groups 1-5 indicate that all groups, except algal group 1, are limited by iron, but that the strength of the iron limitation varies between species (Figs. 13A-E). Algal group 5 is most limited by iron, because the cellular iron to carbon ratios of this group generally stay at their minimum value within the mixed layer (Fig. 13E). Algal groups 2 and 3 are less iron-limited because their iron to carbon ratios remain above the minimum specified iron to carbon ratios of these groups (Figs. 13B and C).

The simulated maximum light-limited (Figs. 9A-E) and nutrient-limited phytoplankton growth rates (Figs. 10A and B) are higher during the first five months of 1992, because higher water temperatures during this time result in higher temperature dependent maximum growth rates ($\mu_{mt}(z,t)$) for each group. This results in the maximum growth rates of algal groups 2-5 occurring just below the mixed layer during the first five months of 1992, although the nutrient concentrations increase towards deeper waters (120 m). Each algal group reaches its maximum growth rate at different depths and times (Table 14), which reflects the physiological differences among different groups.

The effects of clouds are also reflected in the growth rates of algal groups. The effects of clouds on algal groups 1 and 2 are counterintuitive in that cloudy periods

weaken the effect of light inhibition on these groups. This result was especially significant during the first four months of 1992 and resulted in an increase in growth rates of algal groups 1 and 2 in the surface waters (Figs. 9A and B). However, although the cloud cover results in an increase in the surface growth rates of algal groups 1 and 2, it does not increase the overall primary production rate of these groups. The decrease in the irradiance reaching the sea surface means less light inhibition for the algal cells at the surface, but results in light limitation of growth occurring at shallower depths. This produces an upwards shift in the primary production vertical profile of algal groups 1 and 2 without increasing the overall primary production. The decrease in irradiance during cloudy times resulted in decreased growth rates for the other algal groups which appears in the simulated distribution as vertical bands of reduced growth rates (Figs. 9C-E).

Nutrients

Observations (Martin et al., 1989; Bruland et al., 1994; Johnson et al., 1997) show that the vertical profile of iron in the ocean follows a nutrient-type (e.g., nitrate) distribution. The simulated vertical iron distributions support these observations and suggest that the vertical iron distributions show characteristics of both new- (nitrate) and recycled-nitrogen (ammonium) (Figs. 15A and B). The simulated iron concentration is high at the bottom of the euphotic zone (120 m) due to upwelling of iron-rich waters and is also as high near 80 m due to efficient remineralization of iron in sinking particles (Fig. 15C). This is consistent with recent observations that show that iron is rapidly recycled in the surface waters (Hutchins et al., 1993; DiTullio et al., 1993; Barbeau et al., 1996).

The simulated silicate concentrations are always >2 μmol l^{-1} in the upper 120 m which is in agreement with observations from the U.S. JGOFS EqPac cruises (Fig. 15D). The half saturation constant for silicate uptake by diatoms is below this value (Nelson and Treguer, 1992). Simulations using a higher silicate half saturation constant (3 μmol l^{-1}) did not differ from the reference simulation. Thus, results for 0°N, 140°W are counter to the suggestion that low silica inputs to the equatorial upwelling

system is a primary cause of the low new production of organic carbon (Dugdale and Wilkerson, 1998).

Zooplankton

Dam et al. (1995) showed that the bulk of the diet of mesozooplankton in equatorial Pacific waters is not phytoplankton, but rather the mesozooplankton may consume most of the microzooplankton production. The simulated distributions support this theory and show that 63% (9,790 μmol C year^{-1}) of the microzooplankton production is cropped by mesozooplankton. High mesozooplankton grazing results in a low variability in microzooplankton biomass (Fig. 14A), and therefore, the variability in phytoplankton concentration is not reflected in the microzooplankton biomass. Any increase in microzooplankton concentration is rapidly removed by mesozooplankton. Thus, variability in mesozooplankton biomass has a similar structure to phytoplankton primary production (Fig. 14B).

Carbon export

The simulated export carbon fluxes are largely controlled by inputs of subsurface nitrate and sinking of particulate matter, as suggested by Eppley and Peterson (1979). However, analysis of the factors controlling the export carbon flux indicate that the conceptual model of Eppley and Peterson (1979) needs to be expanded to include multiple limiting nutrients, such as iron and ammonium. This agrees with the results of other modeling studies (Christian et al., 2002a; Moore et al., 2002a).

The simulated particulate carbon fluxes are driven by primary production, downwelling vertical velocities, and sinking and they are reduced with depth via remineralization (Fig. 16). Downwelling, increases the transportation of particulate material out of the surface waters, therefore the highest carbon export values occur during the downwelling periods that follow a high carbon production period (e.g., YD15-30, YD75-90, YD120-170, YD220-240, and YD300-320, section 5.1.5).

Moreover, the variability in the simulated carbon fluxes is mainly regulated by the vertical velocities rather than being a direct reflection of carbon production. For

example, the two consecutive peaks in carbon flux that occur between YD300 and YD330 (Fig. 16), coincide with two periods of downwelling vertical velocities.

Water temperature also affects the simulated export carbon flux because of the dependency of particulate carbon remineralization on temperature. Warm temperatures during the first part of 1992 (Fig. 4A) produce faster particle remineralization, thus reducing carbon export. For example during the El Niño period (YD1-120), temperatures are such that remineralization rates are almost double the remineralization rates of the cold non-El Niño period.

The model-data comparisons of the export carbon fluxes show that the simulated values overestimate the observations (Fig. 16). One possible explanation for this mismatch is that other macrozooplankton, which are not included in this model, remove biogenic material in the surface waters and can increase the removal of particulate carbon from the surface waters (Wiebe et al., 1979; Steinberg et al., 2001). Also flux feeders (organisms with mucus nets that collect settling particles, Jackson, 1993) that graze below the mixed layer and vertically migrating zooplankton can remove carbon (Longhurst and Harrison, 1988) from the surface layers. The effect of other zooplankton species and vertical migration are not included in the model.

VI.2 MODEL INTERACTIONS AND FEEDBACKS

The competition for light and nutrients and differential grazing by micro- and mesozooplankton on each algal group regulate the interactions between algal groups. The sensitivity analyses (section 5.2) shows that removal of algal group 4 decreases the simulated annual primary production by 45% (Fig. 23). Algal group 4 contributes 69% of the annual primary production. The other groups replace algal group 4 to a certain extent, but their physiological characteristics do not allow complete replacement. Similar results are obtained when the other algal groups were eliminated. Algal group 1 is the only group whose absence results in an increase in primary production (1%). The nutrients that algal group 1 normally consumes below the mixed layer are taken up by other phytoplankton in the mixed layer (i.e. algal group 4),

resulting in a slightly higher production (Fig. 25).

The simulated phytoplankton biomass is strongly controlled by zooplankton (section 5.4). Increases in primary production stimulate zooplankton grazing which produces increases in zooplankton biomass, resulting in more effective grazing. As primary production decreases, the zooplankton biomass decreases, releasing the grazing pressure on phytoplankton. These interactions between primary production and zooplankton grazing lead to a buffering effect on phytoplankton biomass variability and the variability in primary production is not directly reflected on phytoplankton biomass.

The results from this study support the suggestion that iron regulation and grazing jointly constrain the standing stocks of production (Landry et al., 1997). However, principal control on the simulated algal biomass is from grazing rather than iron, and changes in primary production and carbon export are mainly driven by variability in iron concentration. In general, primary production and export carbon flux respond more to changes in environmental forcing of biological processes (Fig. 52) than does phytoplankton biomass; the changes in the two are not linear. The exception is modifications in the strength of the grazing rate, which gives an identical change in primary production and biomass.

Reducing the sinking rates of the small and large detrital pools provides an example of the nonlinear interactions in the lower trophic level model. Reduced sinking rates retains detritus in the euphotic zone longer and thus enhances nutrient production via remineralization. The export carbon flux is then reduced due to less available particulate matter and lower sinking velocities. However, the increased recycling of nitrogen and iron resulted in unrealistic accumulations of recycled nutrients in the euphotic zone (Fig. 53), which results in high carbon production and increased particulate carbon concentrations. The net result is that reduced detritus sinking rates do not change the export carbon fluxes, but rather result in unrealistically high primary production, and ammonium and iron concentrations.

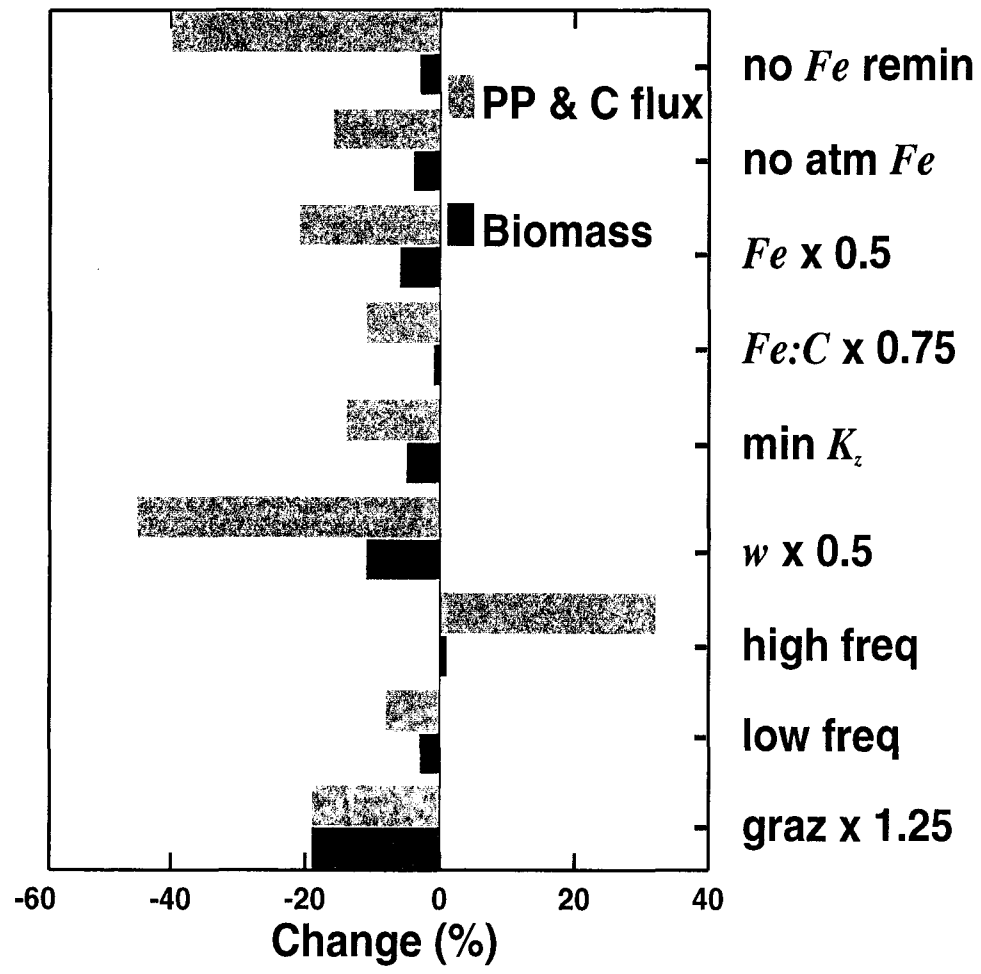

Fig. 52. Change (%) in annual integrated biomass, primary production (PP), and carbon flux (C flux) at 120 meters in response to modifications in model structure. The bars show the difference obtained between the reference simulation and the simulations in which no iron (Fe) remineralization (remin), no atmospheric (atm) iron deposition, iron concentrations at 120 reduced by 50% ($Fe \times 0.5$), the maximum cellular iron to carbon ($Fe{:}C$) ratios decreased by 25%, vertical diffusion coefficient (K_z) set to a minimum (min) value, vertical velocity (w) decreased by 50%, model run with filtered 40-day low-pass filtered high frequency (freq) forcings and 20-day low-pass filtered high frequency forcings and after grazing (graz) rates of micro- and mesozooplankton increased by 25%. The primary production and carbon flux changes are of similar magnitude and are shown by a single bar.

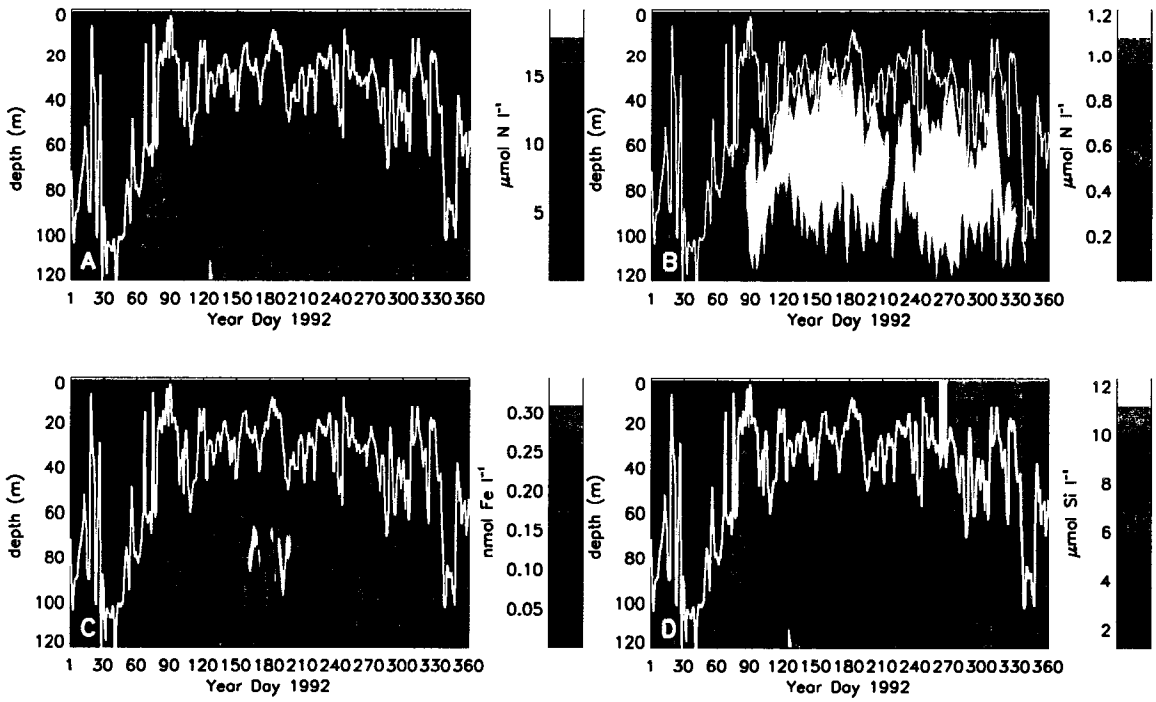

Fig. 53. Same as Fig. 15, but using the reduced detritus sinking rates. Lighter colors indicate higher concentrations.

VI.3 ENVIRONMENTAL EFFECTS

Because the algal group-based ecosystem model is forced with observed time series of temperature, vertical velocity, and mixed layer depth it is possible to determine the effect of environmental variability on carbon biomass, primary production, and export production. In particular, the effects of low- and high-frequency physical variability on primary production and export production is of interest for the equatorial Pacific.

Friedrichs and Hofmann (2001) showed variability resulting from IGWs (6-8-d) and TIWs (20-d) dominated the vertical velocity fields at 0°N, 140°W. The effect of these high frequency motions appears in the MLD, T and K_z time series input to the ecosystem model (Figs. 4A-D). The distribution of simulated phytoplankton shows a wide range of temporal variability, and the effect of high frequency variability is

clearly seen on simulated phytoplankton biomass and primary production (Figs. 19B and 20B) and this is reflected in the export carbon fluxes (Fig. 16).

Forcing of the ecosystem at 0°N, 140°W with only low-frequency variability (e.g., absence of IGWs, TIWs) reduced annual integrated primary production by 5% relative to the reference simulation because iron flux to the surface waters is underestimated (section 5.5). This supports the results in Friedrichs and Hofmann (2001) that showed if the IGWs are not resolved by the forcing fields the net effect of IGWs and TIWs will need to be parameterized in ecosystem models in order to get realistic primary production estimates in the eastern equatorial Pacific.

The high frequency variability in the simulated phytoplankton biomass decreases when a mean vertical velocity of 1.8 m s^{-1} is input to the ecosystem model. This indicates that the vertical velocity field is producing much of the temporal and spatial variability in phytoplankton biomass. However, the increase in phytoplankton biomass between the first and latter parts of 1992 arises from the initial deeper thermocline which results in reduced upwelling and reduced nutrients injected into the surface. This is consistent with field study results (Barber et al., 1996) that show that the biological processes at 0°N, 140°W are sensitive to changes in thermocline depth.

Variability in the eastern equatorial Pacific also exists on annual/interannual time scales. Recent studies (Chavez et al., 1998; Strutton and Chavez, 2000) demonstrated the influence of Kelvin waves on phytoplankton production during the 1997 El Niño. The biological response to the Kelvin waves during the 1997 El Niño was a depression in primary production. A similar event occurred during 1992 El Niño, the 40-d low-pass filtered time series of temperature, vertical velocity and mixed layer depth show a low frequency event occurring during the first 75 days of 1992 (Fig. 4A-C), which reflects passage of a Kelvin wave associated with an ongoing El Niño. The period between YD15-YD50 corresponds to a strong downwelling event, the effect of which is low simulated primary production during this time (Figs. 20A and B).

VI.4 CLIMATE CHANGE IMPLICATIONS

The results of the simulations that used modified iron and vertical advection conditions provide good proxies for considering the potential effects of climate variability in the eastern equatorial Pacific. Inferences from the results of these simulations are given in the sections that follow.

Change in iron input

Sarmiento et al. (2004) suggest that changes in ocean stratification are likely to be one of the main effects of climate warming. In the eastern equatorial Pacific, under stratified conditions, the thermocline deepens as observed during El Niño conditions (Wyrtki, 1975, 1985; Philander, 1990; Hansen, 1990). The observations (Coale et al., 1996a; Chavez et al., 1999; Strutton and Chavez, 2000; Picaut et al., 2002) indicate that the main effect of the change in thermocline depth is a reduction in the iron concentrations at the base of the euphotic zone.

The simulations show that a decrease in iron concentration at the base of the euphotic zone shifts the phytoplankton community assemblage towards small algal forms (algal groups 1-3) and algal group 5 (section 5.3) and that the primary production of algal groups 2, 3, and 4 decreases. Algal group 4 experiences a large decrease in primary production for reduced iron conditions. Algal groups 1-3 adapt better to low iron concentrations in the simulations, which is consistent with observations that indicate that these groups are more efficient at iron uptake under low iron conditions compared to the larger algal groups (Sunda and Huntsman, 1995, 1997). The primary production of algal group 1 showed a 9% increase under low iron concentration conditions, because the decrease in pigment concentrations in the mixed layer due to reduction in biomass of the other algal groups resulted in increased downwelling irradiance. Also, the nutrient concentrations are higher and grazing pressure is lower below the mixed layer and algal group 1 can take advantage of these conditions (Figs. 11A-E).

There is no evidence that the climate change can increase iron concentrations

in the deep ocean, however Wells et al. (1999) reported that in the geological past the tectonic processes could have an influence on periodic iron inputs into the eastern equatorial Pacific Ocean. Cycles of plankton productivity recorded in eastern equatorial Pacific sediments may therefore reflect the influence of tectonic processes superimposed on the effects of global climate forcing. The simulations show that increasing iron at the base of the euphotic zone (120 m) can result in increased primary production and carbon flux (33%) even when there is no change in environmental conditions (e.g., vertical velocities). Increasing iron at 120 m without changing the vertical advection results in an increase in primary production during upwelling periods only, which shows that phytoplankton at 0°N, 140°W are strongly iron limited even during upwelling periods.

An increase in iron concentrations at the bottom of the euphotic zone shifts the phytoplankton community assemblage towards algal group 4 (section 5.3.1, Fig. 26). This is consistent with the results of iron enrichment experiments (Landry et al., 2000a) which show that iron fertilization produces only a small increase in the biomass of *Prochlorococcus* spp. and *Synechococcus* and a large increase in the biomass of autotrophic eukaryotes. Landry et al. (2000a) also suggested that the relative constancy of the smaller-size forms might be the effect of grazers. The simulation results support this suggestion and show that for increased iron conditions the primary production of algal groups 2 and 3 increases $\sim$10%, but that the increase in biomass is insignificant (Fig. 26).

Increased iron concentration actually decreases the simulated primary production of algal group 5. The model structure is such that increased production of algal groups produces increases in mesozooplankton and hence increased grazing pressure which decreases production of this algal group 5. This is not consistent with results from iron enrichment experiments that show that microzooplankton biomass increases with increased iron concentrations (Landry et al., 2000a). However, a subsequent study by Landry et al. (2000b) showed that the grazing rate of mesozooplankton can increase (3 fold) in response to iron enrichment. However, the standing stock of mesozooplankton is strongly controlled by predation, which is not included

in the current model structure.

Siegenthaler and Sarmiento (1993) suggested that climate change might also influence the carbon export rate by causing a more rapid remineralization of organic particles. With the model structure used in this study, changes in water temperature also affect the remineralization rates of particulate matter (section 5.4) and at 0°N, 140°W sustained growth of the algal groups depends on remineralised iron. The simulations show that a decrease of 40% in annual integrated primary production can occur in response to decreased remineralization (Fig. 27), which could be produced by reduced water temperatures. The simulations further suggest that increased stratification and increased water temperatures can increase remineralization of nutrients, thereby, increasing primary production. These potential temperature dependencies need to be included in carbon cycling and climate models developed for the equatorial Pacific.

The effect of recycled iron differs for each algal group. Algal group 4 is the most affected group, with primary production reduced by 50% and biomass reduced by 3% when iron remineralization is not active.

Martin et al. (1989, 1990) hypothesized that the increase in carbon export due to aeolian iron input can result in the drawdown of atmospheric carbon dioxide. The simulations show that the absence of aeolian iron fluxes produces an 18% decrease in primary production and carbon export (section 5.3.1). Considering relatively low aeolian iron input at 0°N, 140°W (Duce and Tindale, 1991; Ginoux et al., 2001), this strong sensitivity of export carbon production suggests that atmospheric iron inputs are responsible for a considerable amount of phytoplankton carbon production. Thus, this process needs further study and refinement and needs to be included in future carbon cycle models developed for the equatorial Pacific.

Change in vertical advection

Climate change may result in shifts in the rate of upwelling to the surface ocean due to the projected changes in the degree of stratification (Sarmiento et al., 1998). The simulations that used vertical velocity time series with a modified magnitude

showed that decreased vertical velocities resulted in decreased iron input which produced changes in algal group relative abundance and production (Fig. 28).

Increased vertical velocity shifted the phytoplankton community towards the larger algal groups 4 and 5 (Fig. 29). Although the primary production of algal group 5 increased considerably, the biomass of this group showed an insignificant change, because the increased mesozooplankton grazing converts algal group 5 primary production to secondary production.

The main differences between the simulations obtained with modified iron concentrations and modified vertical velocities is seen in the response of the annual integrated biomass, primary production, and carbon export. Changes in biomass are correlated with increased or decreased vertical velocities (Fig. 28). However, the general linear relation between primary production and carbon flux does not hold for these conditions. The simulated export carbon flux and primary production are similar for reduced vertical velocities. However, the export carbon flux shows a modest response (15% increase) to increased vertical velocities; whereas, the primary production response is about double (32%) this value (Fig. 28). Vertical velocities not only affect the amount of nutrients injected into the surface water, but also influence the sinking velocities of particulate materials (section 3.9). Increased vertical velocities decrease sinking of particles during upwelling times (positive vertical velocity), which generally corresponds to high carbon production. When the sinking speed of particles decreases, this results in enhanced remineralization of carbon and other nutrients, thus decreasing particulate material and enhancing carbon production as a feedback loop. The effect of the increase in sinking velocities during downwelling (negative vertical velocity) periods is relatively weaker, because these periods correspond to low carbon production.

Deepening of the thermocline, which reduces the vertical velocities in the model (section 3.1), results in decreases in simulated annual primary production and carbon export. However, the decrease in carbon export is higher than the decrease in primary production (Fig. 28). This suggests that a decrease in vertical velocities would diminish the carbon export at a higher rate than it reduces the carbon production.

VI.5 EFFECT OF ENSO ON THE COLD TONGUE AND THE WARM POOL ECOSYSTEMS

VI.5.1 Cold Tongue

The rate of primary production in the Cold Tongue is directly related to the phase of the SOI, with decreased production associated with decreasing and negative SOI values, which occur during El Niños (Figs. 20A and B). These periods correspond to low nutrient concentrations at the base of the euphotic zone (Figs. 40A-D), because the EUC, which pumps nutrient-rich (e.g., iron) cold waters into surface waters, is weaker and deeper during El Niños (Barber et al., 1996).

During the mature phases of La Niñas, the simulated algal primary production and biomass is not as high compared to the biomass and primary production at the beginning of La Niñas. Although during the mature phases of La Niñas the upwelling of nutrients is stronger (Figs. 40A-D), the mixed layer depths are much shallower due to shallow thermocline depths and the water temperatures are lower (Figs. 34A and B). The shallow mixed layer depths result in reduced mixing of nutrient rich waters into the surface waters and low temperatures result in reduced growth rates and reduced recycling of iron and ammonium.

Based on simulations of the lower trophic levels of the Cold Tongue, Leonard et al. (1999) suggested that primary production in this region can show considerable interannual variability, with 50% more primary production occurring during non-ENSO conditions compared to El Niño conditions. The simulated primary production estimates from this study agree with this conclusion and further suggest a 3-fold short-term variability in primary production between the end of the El Niño and beginning of La Niña. Leonard et al. (1999) also showed that netplankton concentrations decrease substantially during El Niño periods. Direct comparison of netplankton concentrations between this study and that done by Leonard et al. (1999) is difficult because of the different phytoplankton community structure used in the two models. However, the simulated biomass of autotrophic eukaryotes and diatoms obtained in this study (Figs. 37D and E), shows a substantial decrease during El

Niño periods.

Recent studies showed that primary production in the Cold Tongue is affected by TIWs (Chavez et al., 1999; Friedrichs and Hofmann, 2001) and Kelvin waves (Chavez et al., 1998; Murtugudde et al., 1999). The simulated carbon export dynamics obtained from 0°N, 140°W (Fig. 50) is enhanced when TIWs are present and diminished when Kelvin waves occur, such as what occurred during the latter part of 1992 and the beginning of 1997, respectively. The simulated changes in carbon export productions in response to environmental structure variability are consistent with the observations by Dunne et al. (2000). During the second part of 1992 and the beginning of 1997, the simulated iron inputs in the Cold Tongue at 120 m (from the EUC) are closely linked to the passage of TIWs and Kelvin waves (Fig. 40C), which agrees with previous studies (Barber et al., 1996; Foley et al., 1997; Friedrichs and Hofmann, 2001).

VI.5.2 Effect of diurnal mixing in the Cold Tongue

Variability in the mixed layer and diel changes in mixed layer depth significantly affect the simulated distribution of chlorophyll *a* and influence primary production rates by pumping nutrients upward and controlling the light levels experienced by phytoplankton. Many of the biochemical variables included in the lower trophic level model have strong gradients in the upper 100 m of the ocean. Thus, oscillations in the depth of mixing is an important component of vertical exchange in the surface waters. Biochemical quantities with high surface concentrations (e.g., phytoplankton) are mixed downward, those with concentrations that increase with depth (e.g., nutrients) are pumped upwards.

The simulated nutrient distributions reflect observations that show that heating stratifies the surface waters at 0°N, 140°W during the day and convective cooling mixes the water at night (Gardner et al., 1995). Night-time deepening entrains nutrient-rich waters into the mixed layer and day-time shoaling of the mixed layer confines these nutrient-rich waters to high-light levels that accelerate biological production.

Denman and Marra (1986) showed that large variations in the depth that phytoplankton are mixed can affect their growth rates because of differences in the light field within the mixed layer. Simulation results suggest that during the night, the phytoplankton biomass is diluted as the mixed layer depth increases, which results in intrusion of nutrients into the surface waters. However, during the day the mixed layer depth shoals and production increases as light levels increase, resulting in an increase in biomass. This diurnal dilution allows the phytoplankton to take advantage of high nutrients below the day-time mixed layer. Thus, model result show that annual primary production is 9% higher when the diurnal mixed layer variability is included compared to using only a day-time (minimum) mixed layer depth. However, using the night-time (maximum) mixed layer depth produces a 1.4% increase in annual primary production. This small increase is due to the intrusion of nutrients into the surface waters during the day. This indicates that the stratification of surface waters and shoaling of the mixed layer during the day should not have a big influence on the light-dependent growth of phytoplankton in the eastern equatorial Pacific.

The effect of the variability of the mixed layer depth on particle export out of the euphotic zone has long been discussed. Kerr and Kuiper (1997) suggested that if the mixed layer depth in the ocean does not show variability and the particles are assumed to sink at a constant rate, there would be an equal flux of particles out of the mixed layer under steady state conditions regardless of the presence or absence of convective mixing. However, the variability in the mixed layer in the open ocean can potentially affect the export of particles from the mixed layer. Gardner et al. (1995) argued that the effect of diel changes in the mixed layer depth may enhance the carbon removal out of the euphotic zone. Diel changes in the mixed layer depth can isolate particles from mixing in the surface waters as the mixed layer shoal during the day. This would allow the particles below the mixed layer depth to settle at their sinking speed. This would be especially effective on fast sinking particles which can settle deeper than the mixed layer depth of the following evening. In this manner particles can be pumped from the surface waters. Contrary to this, Alldredge et al. (1987) argued that night-time increase in the intensity of mixing would redistribute

the particulate material within the mixed layer, thus prolonging their residence time in the euphotic zone. However, the simulation results show that the increase in carbon export from the euphotic zone for a diurnally varying mixed layer relative to the value obtained from simulations that used the day-time (minimum) mixed layer depth is identical to the increase in carbon production between two simulations. Thus, increases in carbon export are primarily a function of primary production and are not greatly affected by the downward transport of particulate matter due to the diurnal deepening of the mixed layer or by the redistribution of particulate matter throughout the mixed layer. It is possible that pumping of particulate material out of the euphotic zone and redistribution of particulate material throughout the mixed layer are counterbalanced.

VI.5.3 Warm Pool

The environmental conditions in the Warm Pool differ considerably from those in the Cold Tongue. The upper ocean in the Warm Pool is highly stratified and water temperatures from the surface to 120 m are in general warmer than those in the Cold Tongue. The warmest water temperatures in the Warm Pool occurred during La Niña periods and the strongest cooling occurred during the 1997-1998 El Niño (Fig. 43A).

The simulated nutrient distributions show increased levels at the base of the euphotic zone in the Warm Pool during El Niño conditions (Figs. 48A-D). This arises because the EUC, which pumps the nutrient-rich cold waters into the surface, shoals in the eastern Pacific during El Niños (Barber et al., 1996; Le Borgne et al., 2002). As a result the highest primary production and algal biomass concentrations in the Warm Pool occur during El Niño phases instead of during La Niña phases; as occurs in the Cold Tongue. The highest simulated chlorophyll *a* concentrations (Fig. 47) occur during the 1995 El Niño because cold nutrient-rich waters reached to the surface and the mixed layer depth extended to 90 m (Fig. 34B). The maxima in chlorophyll *a* coincided with the deepening of the mixed layer depth. During the 1997 El Niño cold waters also reach the surface but during this period the estimated mixed

layer depths are very shallow (~20 m) therefore the simulated primary production is not as high as during the 1995 El Niño.

Le Borgne et al. (2002) suggested that while iron limits primary production in the Cold Tongue, macronutrients control the primary production in the Warm Pool region. The simulations from the Cold Tongue and the Warm Pool regions show that the primary production and carbon export flux in the Cold Tongue is higher than the Warm Pool, although the iron levels are much higher in the Warm Pool. This suggests that in the Cold Tongue the high rates of primary production relative to the Warm Pool is not due to iron but it is the effect of high macronutrient concentrations in the region. Model results further suggest that the primary production is mainly controlled by iron in the Cold Tongue; whereas, the combined effects of macronutrients and iron control the Warm Pool primary productivity.

The phytoplankton assemblage in the Warm Pool consists of the normal background levels of small phytoplankton (*Prochlorococcus* spp., *Synechococcus*). The larger phytoplankton become abundant during periods of upwelling, which introduces nutrients to the surface. This produces algal biomass, mean organism size, and export fluxes that are greater than what occurs in the normally nutrient-depleted waters of the Warm Pool. However, the difference in annual simulated carbon export between the Warm Pool and Cold Tongue is small (22% higher in the Cold Tongue) because of the limitation of primary production in the upwelling zone by iron and, possibly by other nutrients. These results are consistent with observations (Le Borgne et al., 2002).

However, the nutrient and primary production observations obtained during the FLUPAC and Zonal Flux cruises at specific days show mismatches with simulated distributions (section 5.8.3). The October 1994 FLUPAC cruises took place under El Niño conditions and April 1996 Zonal Flux cruises took place under normal conditions. During the FLUPAC cruises, the thermocline was elevated in the Warm Pool region and intrusions of nutrient-rich cold waters were observed at the bottom of the euphotic zone (Fig. 43A). During the Zonal Flux cruises the thermocline was depressed in the Warm Pool region and nitrate levels were low at 120 m (Dunne

et al., 2000). The simulated nutrient concentrations (Figs. 48A, B and D) and primary production rates in the Warm Pool were higher during October 1994 compared to April 1996, however the observations show that the nutrient concentrations and primary production rates were higher during April 1996. The observed depletion of nitrate in the upper 70 m during the 1994 FLUPAC cruises may be produced by the "barrier layer", which is defined as the difference between the thickness of the isothermal layer and the mixed layer (determined by a defined change in density), with the isothermal layer generally being greater than or equal to the mixed layer (Le Borgne et al., 2002). The barrier layer is produced by the difference between the depth of the isohaline and the isothermal layers in the Warm Pool region (Sprintall and McPhaden, 1994). This feature is not correctly represented by the environmental time series input to the model and its absence may explain some of the discrepancies in simulated and observed quantities.

The high salinity barrier layer that is present between the mixed layer and the thermocline suppresses nutrient fluxes (Le Borgne et al., 2002). The mixed layer depth time series input into the model are estimated from a defined change (1°C) in temperature from the SST (which corresponds to the thickness of the isothermal layer) which may result in mixed layer depths that are deeper than actual depths. Also, the mixed layer in the model is assumed to be homogeneous, an assumption which is not strictly correct (Archer, 1999). Therefore, the mechanism that keeps high nutrient waters from mixing into surface waters under stratified conditions is missing in the model dynamics, allowing nutrients to penetrate into surface waters in the Warm Pool during the cold phases of ENSO.

The simulated iron concentrations indicate that the iron-temperature regression developed for the Warm Pool (section 4.10.3) gives results consistent with the observations (Johnson et al., 2002). The iron-temperature regression developed for the cold waters at 0°N, 140°W gives low iron concentrations at the base of the euphotic zone, which results in 50% less simulated annual primary production in the Warm Pool relative to the Cold Tongue and accumulation of macronutrients in the surface waters. These results indicate that the iron-temperature relationship undergoes

regional variations and that this relationship needs to be developed using *in situ* measurements for the area of interest.

VI.6 1997-1998 EL NIÑO-LA NIÑA

The onset of the 1997 El Niño started with the eastward propagation of an equatorially trapped Kelvin wave (Chavez et al., 1998; Strutton and Chavez, 2000). Observations (Chavez et al., 1998; Strutton and Chavez, 2000) show that the biological response to the Kelvin waves was manifest as a depression in primary production at the beginning of 1997, followed by an increase in primary production to a rate of 100 mmol C m^{-2} d^{-1}. A second Kelvin wave in late April 1997 resulted in another depression in primary production rate of 33 mmol C m^{-2} d^{-1} at the beginning of May (Chavez et al., 1998). The simulated primary production rates for May 1997 are consistent with these observations (Fig. 37A-E) in that the effect of the downwelling Kelvin wave at the beginning of 1997 is apparent. The simulated distributions show a rapid decrease in primary production during May 1997, which then begins to increase gradually in late June.

The onset of the 1997 El Niño in the simulated distributions is consistent with observations (Fig. 37A-E). However, the maximum in the simulated chlorophyll *a* bloom that is associated with the 1998 La Niña occurs during February 1998, which is inconsistent with SeaWiFS-derived chlorophyll *a* concentrations which show that the maximum surface bloom occurs in June-July. The reason for this mismatch may be seen in the simulated nutrient fields.

During early 1998, the simulated ammonium and iron concentrations increase in the Cold Tongue (Fig. 40B and C). The increase in iron is due to the combined effects of upwelling and high remineralization rates. Towards the end of the 1997 El Niño, the EUC at 0°N, 140°W starts to shoal which injects nutrient-rich waters into the upper water column. At the same time, the surface waters are warm, which results in high algal growth rates and remineralization rates. Intrusion of nutrients into the euphotic zone initiates a phytoplankton bloom and high remineralization of

iron and ammonium strengthens the magnitude of this bloom. During the 1997 El Niño, the water properties in the Cold Tongue were similar to typical Warm Pool conditions. The surface waters were strongly stratified, with warm waters extending to the bottom of the euphotic zone. For such conditions, it is possible that the depths of the isohaline and isothermal layers differed, as happens in the Warm Pool, and these dynamics are not included in the current model structure. Therefore, this mechanism, which retains high nutrient waters, could also have been in effect in the Cold Tongue during the 1997-1998 ENSO conditions. The result is an earlier La Niña bloom in the simulated chlorophyll distributions than indicated by the SeaWiFS-derived chlorophyll *a* observations.

The simulated chlorophyll *a* concentrations remain low in the Cold Tongue region during April-July because anomalously low water temperatures result in low growth rates. The estimated mixed layer depths for April-June are also low (Fig. 34B), which reduces the intrusion of nutrient-rich waters into the surface waters. Also, Murtugudde et al. (1999) and Picaut et al. (2002) showed that the persistent northerly winds towards the end of 1997-1998 El Niño resulted in a northward shift of the equatorial divergence. The first bloom after the El Niño appeared several degrees to the north of the equator during February 1998 (Murtugudde et al., 1999). This was a relatively weak bloom with chlorophyll concentrations of 0.3 mg m^{-3} and it moved towards the equator during February-June 1998. The unusually strong (> 1.0 mg m^{-3} chlorophyll *a*) 1998 bloom appeared on the equator in June and persisted until the end of August (Murtugudde et al., 1999). These observations suggest that non-local effects can also be an important factor in regulating the chlorophyll biomass on the equator. Part of the mismatch between the observed and modeled chlorophyll *a* during 1998 La Ninã may be due to horizontal advection of phytoplankton into the Cold Tongue region. Thus, non-local factors can contribute to differences in the timing and/or intensity of blooms in the simulated and satellite-derived chlorophyll *a* concentrations. The model structure used in this study does not have the capability of including non-local effects. This highlights the need for development of full three-dimensional models for the equatorial Pacific lower trophic levels.

During the development of the phytoplankton bloom associated with the 1998 La Niña, the mixed layer at 0°N, 140°W deepened, despite a shallow thermocline, resulting in entrainment of nutrients into the surface layer (Murtugudde, personal communication). However, during this period, the mixed layer depths input into the model remain shallow (Fig. 34B) due to the shallow thermocline depths. These results show the importance of and need for inclusion of the range of possible dynamics that effect mixed layer depth (e.g., effect of salinity). The approach used to estimate the mixed layer depths for this study is not sufficiently robust to include all of the relevant dynamics. Future studies should include a mixed layer dynamics that allows for the effects of El Niño processes.

The warm phase of the ENSO ends earlier in the Warm Pool compared to the Cold Tongue (Fig. 43A versus 34A). Upwelling of cold waters begins in May 1997 and by January 1998 the cold phase reaches its peak with cold waters extending to the surface (Fig. 43A). For these conditions, the simulated chlorophyll *a* bloom that is associated with the 1997 El Niño occurs during June-December 1997. The equivalent bloom in the SeaWiFS-derived chlorophyll time series (Fig. 47) begins in January 1998. The lack of the correct mixed layer dynamics in the model in the Warm Pool potentially underlies the mismatch in the simulated and observed chlorophyll blooms.

The effect of temperature on algal growth rates and nutrient remineralization rates can also affect the realism of the Warm Pool simulations. A better representation of temperature effect on algal growth and better information on the remineralization rates of iron and ammonium is needed to increase the model performance for environmental conditions that show extreme variability at short time scales (e.g., ENSO conditions).

CHAPTER VII

CONCLUSIONS

The results of this study are in agreement with generally accepted explanations for ecosystem processes in the equatorial Pacific region. The phytoplankton are nutrient limited and are dominated by small forms. Even the dominant groups usually produce less than their physiologically maximal rates, they are cropped to low abundances by microzooplankton grazers, and their sustained growth is dependent on the remineralized products of grazing. However, this study further emphasizes the importance of using a multi-component lower trophic level ecosystem model that includes detailed algal physiology and realistic micronutrient dynamics in order to investigate interactions in structuring the phytoplankton community assemblage and in regulating the export carbon flux in the equatorial Pacific. The simulations obtained from the lower trophic level ecosystem model show that a multi-algal group structure is needed to realistically represent the dynamics that underlie variations in phytoplankton community structure. Also, variable cellular nutrient quotas for the algal groups allows for realistic nutrient uptake dynamics.

In the Cold Tongue region at 0°N, 140°W, the simulated autotrophic eukaryotes and *Prochlorococcus* spp. dominate the phytoplankton community. During the El Niño period a shift towards smaller forms occur (e.g., *Prochlorococcus* spp. and *Synechecoccus*); whereas, under non-El Niño conditions phytoplankton assemblage shifts towards autotrophic eukaryotes.

The simulated primary production is most sensitive to the variations in the thermocline depth as it is closely linked to the mixed layer depth and to the amount of iron at the base of the euphotic zone. The shoaling of the thermocline induces upwelling in the model and an increase in vertical advection shifts the system towards larger algal groups (autotrophic eukaryotes and large diatoms). Analysis of the model results show that, in general, there is a strong coupling between the change in carbon production and export. However, the effect of vertical advection on carbon production and export is different from other environmental factors due to its direct effect

on particulate carbon sinking rates. High-frequency variability in vertical advection and temperature is an important mechanism driving the carbon export. Filtering out low frequency physical forcing (retaining the high frequency physical forcing) drives the system towards larger algal forms and results in a 30% increase in carbon production and export. This variability in the simulated annual carbon production caused by TIWs and IGWs has a strong influence on the carbon export from the surface waters. This result illustrates that using carbon cycle models coupled with Ocean Global Circulation Models which are incapable of resolving high frequency events would result in unrealistic estimations of variability in carbon export from the surface waters.

All algal groups have a considerable effect on simulated phytoplankton carbon biomass, but not all have a strong effect on primary production and carbon export. This indicates that it may not be necessary to represent a broad spectrum of algal groups in carbon cycle models, because a few key groups appear to have a large influence on primary production and export variability. Combining algal groups 1-3 (low-light adapted *Prochlorococcus*, high-light adapted *Prochlorococcus* and *Synechococcus*) as a cyanobacteria group and retaining algal groups 4 and 5 as distinct groups may be sufficient for modeling large-scale carbon export from equatorial Pacific waters.

This study showed that grazing is the principal control on simulated algal biomass and that primary production and carbon export are mainly driven by iron availability at 0°N, 140°W. The inability of *Prochlorococcus* spp. to use nitrate has a considerable effect on simulated primary production and carbon fluxes which can lead to nitrogen limitation even in the HNLC regions. The explanation for the relative constancy of these small ammonium-dependent species, which is now attributed only to grazing pressure, should be extended to include both nitrogen limitation and grazing constraints.

This study supports the hypothesis that iron has a nutrient-type (e.g., nitrate) profile in the oceans (Martin et al., 1989; Bruland et al., 1994; Johnson et al., 1997).

However, the simulated vertical distributions further suggest that iron shows characteristics of both new-(nitrate) and recycled-nitrogen (ammonium). Recycled iron is an important component of the ecosystem dynamics, because sustained growth of algal groups depends on remineralized iron which accounts for 40% of the annual primary production in the Cold Tongue region. Model results also show that phytoplankton in the Cold Tongue are strongly iron limited even during upwelling periods. The algal uptake and iron remineralization formulations included in the model are based on limited observations. In order to better assess the effects of iron on the lower trophic levels and the carbon export, better understanding of iron uptake dynamics by various algal groups, remineralization processes of iron, aeolian iron fluxes, and iron solubility is needed.

For the Cold Tongue region, the ENSO warm phase results in a shift to small algal forms (e.g., *Prochlorococcus* spp. and *Synechecoccus*) and low primary productivity. For the Warm Pool region, the phytoplankton community biomass is increasingly dominated by larger algal forms (e.g., autotrophic eukaryotes) and primary production is enhanced.

The simulations from the Cold Tongue and the Warm Pool regions show that the primary production and carbon export flux in the Cold Tongue are higher than those for the Warm Pool, although the iron levels are much higher in the Warm Pool. This suggests that the higher primary production levels in the Cold Tongue are not due to iron, but rather are a result of the high macro-nutrient concentrations in the region. Although the simulated primary production is higher in the Cold Tongue compared to the Warm Pool, the phytoplankton growth rates are still well below their physical potentials mainly due to iron control. The combined effects of macronutrients and iron control the Warm Pool primary productivity. Although it is hypothesized that the lower trophic level dynamics in the Warm Pool region is mainly regulated by macronutrients (Le Borgne et al., 2002), the effect of iron regulation on phytoplankton in the region is not known. The effect of nutrient dynamics in regulating the Warm Pool primary productivity is still an area of investigation.

Although there are many potential avenues for better representation of the biology

in the lower trophic level ecosystem model used in this study, it is the representation of the physical dynamics that provides the primary constraints on the realism of the simulated distributions. In particular the changes in mixed layer dynamics and vertical advection associated with the transition periods from highly stratified conditions to upwelling conditions (ENSO) are not well represented by the approach used to specify the environmental structure. Future studies should include a mixed layer dynamics model that allows for more robust responses in the environment to ENSO conditions. This can be achieved by fully coupling the ecosystem model to a three-dimensional model that includes a realistic mixing scheme (e.g., Chen et al., 1994; Murtugudde et al., 1996), which would resolve high frequency variability resulting from the physical forcing fields (e.g., temperature, mixed layer depth, vertical velocity).

Thus, the research described in this study provides a framework for future global and basin-scale studies of multi-component ecosystem modeling that includes detailed algal physiology. With the rapid advances in computer technology, it will be possible to combine sophisticated components for both ecosystems and biogeochemical dynamics in a global and basin-scale modeling framework in the very near future. Today it is difficult to validate such global and basin-scale models because current satellite ocean color instruments provide only a poor indicator of the biological activity in the ocean through chlorophyll *a* concentration. However, the work to monitor phytoplankton species and physiology from space is already on its way (Sathyendranath et al., 2001; Alvain et al., 2005) and will provide data for calibration and validation for multi-component ecosystem modeling.

REFERENCES

Alldredge, A. L., Gotschalk, C. C., MacIntyre, S., 1987. Evidence for sustained residence of macrocrustacean fecal pellets in surface waters off Southern California. Deep-Sea Research 34, 1641–1652.

Alvain, S., Moulin, C., Dandonneau, Y., Breon, F. M., 2005. Remote sensing of phytoplankton groups in case 1 waters from global SeaWiFS imagery. Deep-Sea Research I , –Submitted.

Anderson, S. M., Roels, O. A., 1981. Effects of light intensity on nitrate and nitrite uptake and excretion by *Chaetoceros curvisetus*. Marine Biology 62 (4), 257–261.

Archer, D., 1999. Modeling CO_2 in the ocean: A review. In: Bouwman, A. F. (Ed.), Scaling of trace gas fluxes between terrestrial and aquatic ecosystems and the Atmosphere. Elsevier, Amsterdam.

Archer, D. E., Takahashi, T., Sutherland, S., Goddard, J., Chipman, D., Rodgers, K., Ogura, H., 1996. Daily, seasonal, and interannual variability of sea surface carbon and nutrient concentration in the equatorial Pacific Ocean. Deep-Sea Research II 43, 779–808.

Armstrong, R. A., 1994. Grazing limitation and nutrient limitation in marine ecosystems: Steady state solutions of an ecosystem model with multiple food chains. Limnology and Oceanography 39 (3), 597–608.

Armstrong, R. A., 1999. An optimization-based model of iron-light-ammonium colimitation of nitrate uptake and phytoplankton growth. Limnology and Oceanography 44 (6), 1436–1446.

Baker, K. S., Frounin, R., 1987. Relation between photosynthetically available radiation and total insolation at the ocean surface under clear skies. Limnology and Oceanography 32 (6), 1370–1377.

Barbeau, K., Moffet, J., Caron, D., Croot, P., Erdner, D., 1996. Role of protozoan grazing in relieving iron limitation of phytoplankton. Nature 380, 61–64.

Barber, R. T., Chavez, F. P., 1991. Regulation of primary productivity rate in the equatorial Pacific. Limnology and Oceanography 36 (8), 1803–1815.

Barber, R. T., Sanderson, M. P., Lindley, S. T., Chai, F., Newton, J., Trees, C. C., Foley, D. G., Chavez, F. P., 1996. Primary productivity and its regulation in the equatorial Pacific during and following the 1991-1992 El Niño. Deep-Sea Research II 43 (4-6), 933–969.

Barlow, R. G., Alberte, R. S., 1985. Photosynthetic characteristics of phycoerythrin-containing marine *Synechococcus* spp. 1. Responses to growth photon flux density. Marine Biology 86 (1), 63–74.

Behrenfeld, M. J., Bale, A. J., Kolber, Z. S., Aiken, J., Falkowski, P. G., 1996. Confirmation of iron limitation of phytoplankton photosynthesis in the equatorial Pacific Ocean. Nature 383 (6600), 508–511.

Bidigare, R. R., Ondrusek, M. E., 1996. Spatial and temporal variability of phytoplankton pigment distributions in the central equatorial Pacific Ocean. Deep-Sea Research II 43 (4-6), 809–833.

Bidigare, R. R., Ondrusek, M. E., Morrow, J. H., Kiefer, D. A., 1990. *In vivo* absorption properties of algal pigments. Tech. Rep. 10, SPIE-The International Society for Optical Engineering, Bellingham, WA.

Binder, B. J., Chisholm, S. W., Olson, R. J., Frankel, S. L., Worden, A. Z., 1996. Dynamics of picophytoplankton, ultraphytoplankton and bacteria in the central equatorial Pacific. Deep-Sea Research II 43 (4-6), 907–931.

Bissett, W. P., Walsh, J. J., Dieterle, D. A., Carder, K. L., 1999a. Carbon cycling in the upper waters of the Sargasso Sea: 1. Numerical simulation of differential carbon and nitrogen fluxes. Deep-Sea Research I 46 (2), 205–269.

Bissett, W. P., Walsh, J. J., Dieterle, D. A., Carder, K. L., 1999b. Carbon cycling in the upper waters of the Sargasso Sea: II. Numerical simulation of apparent and inherent optical properties. Deep-Sea Research I 46 (2), 271–317.

Blanchot, J., Rodier, M., Le Bouteiller, A., 1992. Effect of El Niño Southern Oscillation events on the distribution and abundance of phytoplankton in the western Pacific Tropical Ocean along 165°E. Journal of Plankton Research 14 (1), 137–156.

Bruland, K. W., Orians, K. J., Cowen, J. P., 1994. Reactive trace metals in the stratified central north Pacific. Geochimica et Cosmochimica Acta 58, 3171–3182.

Campbell, L., Nolla, H. A., Vaulot, D., 1994. The importance of *Prochlorococcus* to community structure in the central north Pacific Ocean. Limnology and Oceanography 39, 954–961.

Campbell, L., Vaulot, D., 1993. Photosynthetic picoplankton community structure in the Subtropical North Pacific Ocean near Hawaii (station ALOHA). Deep-Sea Research I 40, 2043–2060.

Cavender-Bares, K. S., Mann, E., Chisholm, S. W., Ondrusek, M., Bidigare, R., 1999. Differential response of equatorial Pacific phytoplankton to iron fertilization. Limnology and Oceanography 44, 237–246.

Chai, F., Lindley, S. T., Barber, R. T., 1996. Origin and maintenance of a high nitrate condition in the equatorial Pacific. Deep-Sea Research II 43 (4-6), 1031–1064.

Chavez, F., Buck, K. R., Coale, K. H., Martin, J. H., DiTullio, G. R., Welschmeyer, N. A., Jacobson, A. C., Barber, R. T., 1991. Growth rates, grazing, sinking and iron limitation of equatorial Pacific phytoplankton. Limnology and Oceanography 36, 1816–1827.

Chavez, F. P., 1989. Size distribution of phytoplankton in the central and eastern Pacific Ocean. Global Biogeochemical Cycles 3, 27–35.

Chavez, F. P., Buck, K. R., Service, S. K., Newton, J., Barber, R. T., 1996. Phytoplankton variability in the eastern and central Tropical Pacific. Deep-Sea Research II 43, 809–833.

Chavez, F. P., Strutton, P. G., Friedrich, G. E., Feely, R. A., Feldman, G. C., Foley, D. G., McPhaden, M. J., 1999. Biological and chemical response of the equatorial Pacific Ocean to the 1997-98 El Niño. Science 286 (5447), 2126–2131.

Chavez, F. P., Strutton, P. G., McPhaden, M. J., 1998. Biological-physical coupling in the central equatorial Pacific during the onset of the 1997-98 El Niño. Geophysical Research Letters 25 (19), 3543–3546.

Chen, D., Rothstein, L. M., Busalacchi, A. J., 1994. A hybrid vertical mixing scheme and its application to tropical ocean models. Journal of Physical Oceanography 24 (10), 2156–2179.

Chisholm, S. W., Olson, R. J., Zettler, E. R., Goericke, R., Waterbury, J. B., Welschmeyer, N. A., 1988. A novel free-living prochlorophyte abundancy in the oceanic euphotic zone. Nature 334, 340–343.

Christian, J. R., Karl, D. M., 1995. Bacterial ectoenzymes in marine waters: activity ratios and temperature responses in three oceanic provinces. Limnology and Oceanography 40, 1042–1049.

Christian, J. R., Verschell, M. A., Murtugudde, R., Busalacchi, A. J., McClain, C. R., 2002a. Biogeochemical modelling of the tropical Pacific Ocean. I. Seasonal and interannual variability. Deep-Sea Research II 49, 509–543.

Christian, J. R., Verschell, M. A., Murtugudde, R., Busalacchi, A. J., McClain, C. R., 2002b. Biogeochemical modelling of the tropical Pacific Ocean. II: Iron biogeochemistry. Deep-Sea Research II 49, 545–565.

Cleveland, J. S., Perry, M. J., 1987. Quantum yield, relative specific absorption and fluorescence in nitrogen-limited *Chaetoceros gracilis*. Marine Biology 94 (4), 489–497.

Cloern, J. E., Grenz, C., Vidergar-Lucas, L., 1995. An empirical model of the phytoplankton chlorophyll:carbon ratio – the conversion factor between productivity and growth. Limnology and Oceanography 40, 1313–1321.

Coale, K. H., Fitzwater, S. E., Gordon, R. M., Johnson, K. S., Barber, R. T., 1996b. Control of community growth and export production by upwelled iron in the equatorial Pacific Ocean. Nature 379 (6566), 621–624.

Coale, K. H., Johnson, K. S., Fitzwater, S., Gordon, R., Tanner, S., Chavez, F., Ferioli, L., Sakamoto, C., Rogers, P., Millero, F., Steinberg, P., Nightingale, P., Cooper, D., Cochlan, W. P., R, K., 1996a. A massive phytoplankton bloom induced by an ecosystem-scale iron fertilization experiment in the equatorial Pacific Ocean. Nature 383 (6600), 495–501.

Conkright, M. E., Garcia, H. E., O'Brien, T. D., Locarnini, R. A., Boyer, T. P., Stephens, C., Antonov, J. I., 2002. World Ocean Atlas 2001, Volume 4: Nutrients. S. Levitus. U.S. Government Printing Office, Washington, D.C., NOAA Atlas NESDIS 52 Edition, 392 pp.

Crank, J., 1956. The mathematics of diffusion. Oxford University Press, Oxford.

Cuhel, R. L., Waterbury, J. B., 1984. Biochemical composition and short term nutrient incorporation patterns in a unicellular marine cyanobacterium, *Synechococcus* (WH7803). Limnology and Oceanography 29 (2), 370–374.

Cullen, J. J., 1982. The deep chlorophyll maximum: comparing vertical profiles of chlorophyll *a*. Canadian Journal of Fisheries and Aquatic Sciences 39, 791–803.

Cullen, J. J., 1991. Hypotheses to explain high-nutrient conditions in the open sea. Limnology and Oceanography 36, 1578–1599.

Cullen, J. J., Lewis, M. R., Davis, C. O., Barber, R. T., 1992. Photosynthetic characteristics and estimated growth rates indicate grazing is the proximate control of primary production in the equatorial Pacific. Journal of Geophysical Research 97 (C1), 639–654.

Dam, H. G., Zhang, X., Butler, M., Roman, M. R., 1995. Mesozooplankton grazing and metabolism at the equator in the central Pacific: Implications for carbon and nitrogen fluxes. Deep-Sea Research II 42 (2-3), 735–756.

D'Asaro, E. A., Farmer, D. M., Osse, J. T., Dairiki, G. T., 1996. A lagrangian float. Journal of Atmospheric and Oceanic Technology. 13, 130–1246.

Denman, K. L., Marra, J., 1986. Modeling the time dependent photoadaptation to fluctuating light. In: Nihoul, J. C. J. (Ed.), Marine interface ecohydrodynamics. Elsevier, Amsterdam, pp. 341–359.

DiTullio, G., Hutchins, D., Bruland, K., 1993. Interaction of iron and major nutrients controls phytoplankton growth and species composition in the tropical north Pacific Ocean. Limnology and Oceanography 38, 495–508.

Doney, S. C., 1999. Major challenges confronting marine biogeochemical modeling. Global Biogeochemical Cycles 13, 705–714.

Droop, M. R., 1973. Some thoughts on nutrient limitation in algae. Journal of Phycology 9 (3), 264–272.

Duce, R. A., Tindale, N. W., 1991. Atmospheric transport of iron and its deposition in the ocean. Limnology and Oceanography 36, 1715–1726.

Duce, R. A., et al., 1991. The atmospheric input of trace species to the world ocean. Global Biogeochemical Cycles 5, 193–259.

Dugdale, R. C., Wilkerson, F. P., 1998. Silicate regulation of new production in the equatorial Pacific upwelling. Nature 391, 270–273.

Dunne, J. P., Murray, J. W., 1999. Sensitivity of ^{234}Th export to physical processes in the Central Equatorial Pacific. Deep-Sea Research I 46, 831–854.

Dunne, J. P., Murray, J. W., Rodier, M., Hansell, D. A., 2000. Export flux in the western and central equatorial Pacific: zonal and temporal variability. Deep-Sea Research I 47, 901–936.

Eppley, R. W., 1972. Temperature and phytoplankton growth in the sea. Fishery Bulletin 70, 1063–1085.

Eppley, R. W., Peterson, B. J., 1979. Particulate organic matter flux and planktonic organic matter in the surface layer of the ocean. Deep-Sea Research I 30, 311–323.

Falkowski, P. G., Dubinsky, Z., Wyman, K., 1985. Growth-irradiance relationships in phytoplankton. Limnology and Oceanography 30 (2), 311–321.

Falkowski, P. G., Wirick, C. D., 1981. A simulation model of the effects of vertical mixing on primary productivity. Marine Biology 65 (1), 69–75.

Fennel, K., Abbott, M. R., Spitz, Y. H., Richman, J. G., Nelson, D. M., 2003. Modeling controls of phytoplankton production in the southwest Pacific sector of the Southern Ocean. Deep-Sea Research II 50, 769–798.

Firing, E., Lukas, R., Sadler, J., Wyrtki, K., 1983. Equatorial undercurrent disappears during 1982-83 El Niño. Science 222, 1121–1123.

Fitzwater, S. E., Coale, K. H., Gordon, R. M., Johnson, K. S., Ondrusek, M. E., 1996. Iron deficiency and phytoplankton growth in the equatorial Pacific. Deep-Sea Research II 43 (4-6), 995–1015.

Flament, P., Kennan, S. C., Knox, R. A., Niiler, P., Bernstein, R., 1996. The three-dimensional structure of an upper ocean vortex in the Tropical Pacific. Nature 382, 610–613.

Flynn, K. J., 1991. Algal carbon-nitrogen metabolism: A biochemical basis for modelling the interactions between nitrate and ammonium uptake. Journal of Plankton Research 13 (2), 373–i387.

Flynn, K. J., Davidson, K., Leftley, J. W., 1994. Carbon-nitrogen relations at whole-cell and free-amino-acid levels during batch growth of *Isochrysis galbana* (Prymnesiophyceae) under conditions of alternating light and dark. Marine Biology 118 (2), 229–237.

Foley, D. G., Dickey, T. D., McPhaden, M. J., Bidigare, R. R., Lewis, M. R., Barber, R. T., Lindley, S. T., Garside, C., Manov, D. V., McNeil, J. D., 1997. Longwaves and primary productivity variations in the equatorial Pacific at 0°, 140°W. Deep-Sea Research II 44 (9-10), 1801–1826.

Franks, P. J. S., Wroblewski, J. S., Flierl, G. R., 1986. Behavior of a simple plankton model with food-level acclimation by herbivores. Marine Biology 91 (1), 121–129.

Friedrichs, M. A. M., Hofmann, E. E., 2001. Physical control of biological processes in the central equatorial Pacific Ocean. Deep-Sea Research I 48 (4), 1023–1069.

Frost, B., 1991. The role of grazing in nutrient-rich areas of the open sea. Limnology and Oceanography 36, 1616–1630.

Frost, B., Franzen, N. C., 1992. Grazing and iron limitation in the control of phytoplankton stock and nutrient concentration; a chemostat analog of the Pacific equatorial upwelling zone. Marine Ecology Progress Series 83, 291–303.

Fung, I. Y., Meyn, S. K., Tegen, I., Doney, S. C., John, J. G., Bishop, J. K. B., 2000. Iron supply and demand in the upper ocean. Global Biogeochemical Cycles 14, 281–295.

Gardner, W. D., Gundersen, J. S., Richardson, M. J., Walsh, I. D., 1999. The role of seasonal and diel changes in mixed-layer depth on carbon and chlorophyll distributions in the Arabian Sea. Deep-Sea Research II 46, 1833–1858.

Gardner, W. D., Pyo, C. S., Richardson, M. J., Walsh, I. D., 1995. The oceanic mixed-layer pump. Deep-Sea Research II 42, 757–775.

Geider, R. J., MacIntyre, H. L., Kana, T. M., 1996. A dynamic model of photoadaptation in phytoplankton. Limnology and Oceanography 41 (1), 1–15.

Geider, R. J., MacIntyre, H. L., Kana, T. M., 1998. A dynamic regulatory model of phytoplanktonic acclimation to light, nutrients, and temperature. Limnology and Oceanography 43 (4), 679–694.

Geider, R. J., Osborne, B. A., 1987. Light absorption by a marine diatom: Experimental observations and theoretical calculations of the package effect in a small *Thalassiosira* species. Marine Biology 96 (2), 299–308.

Geider, R. J., Osborne, B. A., Raven, J. A., 1986a. Growth, photosynthesis and maintenance metabolic cost in the diatom *Phaeodactylum tricornutum* at very low light levels. Journal of Phycology 22 (1), 39–48.

Geider, R. J., Platt, T., 1986b. A mechanistic model of photoadaptation in microalgae. Marine Ecology Progress Series 30 (1), 85–92.

Ginoux, P., Chin, M., Tegen, I., Prospero, J., Holben, B., Dubovik, O., Lin, S. J., 2001. Sources and distributions of dust aerosols simulated with the GOCART model. Journal of Geophysical Research 106, 20225–20273.

Glibert, P. M., Ray, R. T., 1990. Different patterns of growth and nitrogen uptake in two clones of marine *Synechoccus* spp. Marine Biology 107 (2), 273–280.

Glover, H. E., Keller, M. D., Spinrad, R. W., 1987. The effects of light quality and intensity on photosynthesis and growth of marine eukaryotic and prokaryotic phytoplankton clones. Journal of Experimental Marine Biology and Ecology 105 (2-3), 137–159.

Goldman, J. C., 1980. Physiological processes, nutrient availability, and the concept of relative growth rate in marine phytoplankton ecology. In: Falkowski, P. G. (Ed.), Primary Productivity in the Sea. Plenum Press, New York, pp. 179–194.

Goldman, J. C., 1982. Comparative rapid ammonium uptake by four species of marine phytoplankton. Limnology and Oceanography 27 (5), 814–827.

Goldman, J. C., Glibert, P. M., 1983. Inorganic nitrogen uptake by phytoplankton. In: Carpenter, E., Carpone, D. G. (Eds.), Nitrogen in the Marine Environment. Academic Press, New York, pp. 233–274.

Gordon, R. M., Coale, K. H., Johnson, K. S., 1997. Iron distributions in the equatorial Pacific: Implications for new production. Limnology and Oceanography 42 (3), 419–431.

Gordon, R. M., Johnson, K. S., Coale, K. H., 1998. The behavior of iron and other trace elements during the IronEx I and PlumEx experiments in the Equatorial Pacific. Deep-Sea Research II 45, 995–1041.

Gregg, W. W., Carder, K. L., 1990. A simple spectral solar irradiance model for cloudless maritime atmospheres. Limnology and Oceanography 35 (8), 1657–1675.

Halpern, D., 1980. A Pacific equatorial temperature section from 172°E to 110°W during Winter and Spring 1979. Deep-Sea Research 27, 931–940.

Halpern, D., Knox, R. A., Luther, D. S., 1988. Observations of 20-days period meridional current oscillations in the upper ocean along the Pacific equator. Journal of Physical Oceanography 18, 1514–1534.

Haney, J. A., Jackson, G. A., 1996. Modeling phytoplankton growth rates. Journal of Plankton Research 18 (1), 63–85.

Hansen, D. V., 1990. Physical aspects of the El Niño event of 1982-1983. In: Glenn, P. (Ed.), Global ecological consequences of the 1982-1983 El Niño-Southern Oscillation. Elsevier, Amsterdam, p. 563.

Harrison, W. G., Harris, L. R., Irwin, B. D., 1996. The kinetics of nitrogen utilization in the oceanic mixed layer: Nitrate and ammonium interactions at nanomolar concentrations. Limnology and Oceanography 41 (1), 16–32.

Haxo, F. T., 1985. Photosynthetic action spectrum of the coccolithophorid, *Emiliani huxlei* (Haptophyceae): 19' Hexanoyloxyfucoxanthin as antenna pigment. Journal of Phycology 21, 282–287.

Higgins, H. W., Mackey, D. J., 2000. Algal class abundances, estimated from chlorophyll and carotenoid pigments, in the western equatorial Pacific under El Niño and non-El Niño conditions. Deep-Sea Research I 47 (8), 1461–1483.

Hoepffner, N., Sathyendranath, S., 1992. Bio-optical characteristics of coastal waters: Absorption spectra of phytoplankton and pigment distribution in the western North Atlantic. Limnology and Oceanography 37 (8), 1660–1679.

Hooks, C. E., Bidigare, R. R., Keller, M. D., Guillard, R. R. L., 1988. Coccoid eukaryotic marine ultraplankters with four different HPLC pigment signatures. Journal of Phycology 24 (4), 571–580.

Hutchins, D. A., Bruland, K. W., 1995. Fe, Zn, Mn and N transfer between size classes in a coastal phytoplankton community: Trace metal and major nutrient recycling compared. Journal of Marine Research 53 (2), 297–313.

Hutchins, D. A., DiTullio, G. R., Bruland, K. W., 1993. Iron and regenerated production: Evidence for biological iron recycling in two marine environments. Limnology and Oceanography 38, 1242–1255.

Iriarte, A., Purdie, D. A., 1993. Photosynthesis and growth response of the oceanic picoplankter *Pycnococcus provasolii* Guillard (clone Omega 48-23) (Chlorophyta) to variations in irradiance, photoperiod and temperature. Journal of Experimental Marine Biology and Ecology 168 (2), 239–257.

Iriarte, J. L., Fryxell, G. A., 1995. Microphytoplankton at the equatorial Pacific (140°W) during the JGOFS EqPac Time Series studies: March to April and October 1992. Deep-Sea Research II 42 (2-3), 559–583.

Ivlev, V. S., 1955. Experimental ecology of the feeding of fishes. Yale University Press, New Haven, translated from Russian by D. Scott.

Jackson, G. A., 1993. Flux feeding as a mechanism for zooplankton grazing and its implications for vertical particulate flux. Limnology and Oceanography 38, 1328–1331.

Jassby, A. D., Platt, R., 1976. Mathematical formulation of the relationship between photosynthesis and light for phytoplankton. Limnology and Oceanography 21 (4), 540–547.

Jeffrey, S., 1976. The occurrence of chlorophyll c1 and c2 in algae. Journal of Phycology 12 (3), 349–354.

Jeffrey, S. W., Vesk, M., 1977. Effect of blue-green light on photosynthetic pigments and chloroplast structure in the marine diatom *Stephanopyxis turris*. Journal of Phycology 13 (3), 271–279.

Jickells, T., Spokes, L., 2002. Atmospheric iron inputs to the oceans. In: Turner, D., Hunter, K. (Eds.), Biogeochemistry of iron in seawater. Wiley, New York.

Johnson, K. S., Gordon, R. M., Coale, K. H., 1997. What controls dissolved iron concentrations in the World Wcean? Marine Chemistry 57, 137–161.

Johnson, K. S., Moore, J. K., Smith, W. O., 2002. A report on the U.S. JGOFS workshop on iron dynamics in the carbon cycle. Tech. rep., Moss Landing, California.

Kaczmarska, I., Fryxell, G. A., 1995. Microphytoplankton of the Equatorial Pacific: 140°W meridianal transect during the 1992 El Niño. Deep-Sea Research II 42, 535–558.

Kana, T. M., Feiwel, N. L., Flynn, L. C., 1992. Nitrogen starvation in marine *Synechococcus* strains: Clonal differences in phycobiliprotein breakdown and energy coupling. Marine Ecology Progress Series 88 (1), 75–82.

Kana, T. M., Glibert, P. M., 1987a. Effect of irradiances up to 2000 μE m^{-2} s^{-1} on marine *Synechococcus* WH7803. I. Growth, pigmentation, and cell composition. Deep-Sea Research 34 (4A), 479–495.

Kana, T. M., Glibert, P. M., 1987b. Effect of irradiances up to 2000 μE m^{-2} s^{-1} on marine *Synechococcus* WH7803. II. Photosynthetic response and mechanism. Deep-Sea Research 34 (4A), 497–516.

Kerr, R. C., Kuiper, G. S., 1997. Particle settling through a diffusive-type thermohaline staircase in the ocean. Deep-Sea Research 44, 399–412.

Kessler, W. S., McPhaden, M., Weickmann, K. M., 1995. Forcing of intraseasonal Kelvin waves in the equatorial Pacific. Journal of Geophysical Research 100 (C6), 10,613–10,631.

Kirchman, D., Rich, J., Barber, R. T., 1995. Biomass and biomass production of heterotrophic bacteria along 140°W in the equatorial Pacific: Effect of temperature on the microbial loop. Deep-Sea Research II 42, 603–680.

Kirk, J. T. O., 1994. Light and photosynthesis in aquatic ecosystems. Cambridge University Press, Great Britain.

Klein, P., Steele, J. H., 1985. Some physical factors affecting ecosystems. Journal of Marine Research 43, 337–350.

Kudo, I., Harrison, P. J., 1997. Effect of iron nutrition on the marine cyanobacterium *Synechococcus* grown on different N sources and irradiances. Journal of Phycology 33 (2), 232–240.

Kyewalyanga, M., Platt, T., Sathyendranath, S., 1992. Ocean primary production calculated by spectral and broad-band models. Marine Ecology Progress Series 85 (1-2), 171–185.

Landry, M. R., Barber, R. T., Bidigare, R. R., Chai, F., Coale, K. H., Dam, H. G., Lewis, M. R., Lindley, S. T., McCarthy, J. J., Roman, M. R., Stoecker, D. K., Verity, P. G., White, J. R., 1997. Iron and grazing constraints on primary production in the central equatorial Pacific: An EqPac synthesis. Limnology and Oceanography 42 (3), 405–418.

Landry, M. R., Constantinou, J., Latasa, M., Brown, S. L., Bidigare, R. R., Ondrusek, M. E., 2000b. Biological response to iron fertilization in the eastern equatorial Pacific (IronEx II). 3. Dynamics of phytoplankton growth and microzooplankton grazing. Marine Ecology Progress Series 201, 57–72.

Landry, M. R., Kirshtein, J., Constantinou, J., 1995. A refined dilution technique for measuring the community grazing impact of microzooplankton, with experimental tests in the central equatorial Pacific. Marine Ecology Progress Series 120 (1-3), 53–63.

Landry, M. R., Kirshtein, J., Constantinou, J., 1996. Abundances and distributions of picoplankton populations in the central equatorial Pacific from 12°N to 12°S, 140°W. Deep-Sea Research II 43 (4-6), 871–890.

Landry, M. R., Ondrusek, M. E., Tanner, S. J., Brown, S. L., Constantinou, J., Bidigare, R. R., Coale, K. H., Fitzwater, S., 2000a. Biological response to iron fertilization in the eastern equatorial Pacific (IronEx II). 1. Microplankton community abundances and biomass. Marine Ecology Progress Series 201, 17–42.

Langdon, C., 1988. On the causes of interspecific differences in growth-irradiance relationship for phytoplankton. II. A general review. Journal of Plankton Research 10, 1291–1312.

Latasa, M., Landry, M. R., Schlueter, L., Bidigare, R. R., 1997. Pigment-specific growth and grazing rates of phytoplankton in the central equatorial Pacific. Limnology and Oceanography 42 (2), 289–298.

Laws, E. A., Bannister, T. T., 1980. Nutrient- and light-limited growth of *Thalassiosira fluviatilis* in continious culture, with implications for phytoplankton growth in the ocean. Limnology and Oceanography 25 (3), 457–473.

Laws, E. A., Falkowski, P. G., Smith, W. O., Ducklow, H., McCarthy, J. J., 2000. Temperature effects on export production in the open ocean. Global Biogeochemical Cycles 14, 1231–1246.

Le Borgne, R., Feely, R. A., Mackey, D. J., 2002. Carbon fluxes in the equatorial Pacific: A synthesis of the JGOFS programme. Deep-Sea Research II 49, 2425–2442.

Leonard, C. L., McClain, C. R., Murtugudde, R., Hofmann, E. E., Harding, L. W. J., 1999. An iron-based ecosystem model of the central equatorial Pacific. Journal of Geophysical Research 104 (C1), 1325–1341.

Li, W. K. W., Zohary, T., Yacobi, Y. Z., Wood, A. M., 1993. Ultraphytoplankton in the eastern Mediterranean Sea: Towards deriving phytoplankton biomass from flow cytometric measurements of abundance fluorescence and light scatter. Marine Ecology Progress Series 102, 79–87.

Lindley, S. T., Bidigare, R. R., Barber, R. T., 1995. Phytoplankton photosynthesis parameters along 140°W in the equatorial Pacific. Deep-Sea Research II 42 (2-3), 441–463.

Longhurst, A. R., Harrison, W. G., 1988. Vertical nitrogen flux from the oceanic photic zone by diel migrant zooplankton and nekton. Deep-Sea Research I 35, 881–889.

Loukos, H., Frost, B., Harrison, D. E., Murray, J. W., 1997. An ecosystem model with iron limitation of primary production in the equatorial Pacific at 140°W. Deep-Sea Research II 44 (9-10), 2221–2249.

Lukas, R., Lindstorm, E., 1991. The mixed layer of the western equatorial Pacific. Journal of Geophysical Research 96, 3343–3357.

Mackey, D. J., Parslow, J., Higgins, H. W., Griffiths, F. B., O'Sullivan, J. E., 1995. Plankton productivity and biomass in the western equatorial Pacific: Biological and physical controls. Deep-Sea Research II 42 (2-3), 499–533.

Mackey, D. J., Parslow, J. S., Griffiths, F. B., Higgins, H. W., Tilbrook, B., 1997. Phytoplankton productivity and the carbon cycle in the western equatorial Pacific under El Niño and non-El Niño conditions. Deep-Sea Research II 44, 1951–1978.

Marra, J., Bidigare, R. R., Dickey, T. D., 1990. Nutrients and mixing, chlorophyll and phytoplankton growth. Deep-Sea Research 37 (1A), 127–143.

Martin, J. H., Broenkow, W. W., Fitzwater, S. E., Gordon, R. M., 1990. Yes, it does: A reply to the comment by Banse. Limnology and Oceanography 35 (3), 775–777.

Martin, J. H., Gordon, R. M., Fitzwater, S., Broenkow, W. W., 1989. VERTEX: phytoplankton/iron studies in the Gulf of Alaska. Deep-Sea Research I 36, 649–680.

Martin, J. H., Gordon, R. M., Fitzwater, S. E., 1991. The case for iron. Limnology and Oceanography 36 (8), 1793–1802.

Martin, J. H., et al., 1994. Testing the iron hypothesis in ecosystems of the equatorial Pacific Ocean. Nature 371 (6493), 123–129.

McClain, C. R., Murtugudde, R., Signorini, S., 1999. A simulation of biological processes in the equatorial Pacific Warm Pool at 165°E. Journal of Geophysical Research 104 (C8), 18,305–18,322.

McPhaden, M. J., 1999. Genesis and evolution of the 1997-1998 El Niño. Science 283, 950–954.

McPhaden, M. J., Busalacchi, A. J., Cheney, R., Donguy, J.-R., Gage, K. S., Halpern, D., Ji, M., Julian, P., Meyers, G., Mitchum, G. T., Niiler, P. P., Picaut, J., Reynolds, R. W., Smith, N., Takeuchi, K., 1998. The Tropical Ocean-Global Atmosphere observing system: A decade of progress. Journal of Geophysical Research 103 (C7), 14,169–14,240.

Miller, S. R., Castenholz, R. W., 2001. Ecological physiology of *Synechococcus* sp. strain sh-94-5, a naturally occurring cyanobacterium deficient in nitrate assimilation. Applied Environmental Microbiology 67 (7), 3002–3009.

Moore, J. K., Doney, S. C., Kleypas, J. A., Glover, D. M., Fung, I. Y., 2002a. An intermediate complexity marine ecosystem model for the global domain. Deep-Sea Research II 49, 403–462.

Moore, L. R., Goericke, R., Chisholm, S. W., 1995. Comparative physiology of *Synechococcus* and *Prochlorococcus*: Influence of light and temperature on growth, pigments, fluorescence and absorptive properties. Marine Ecology Progress Series 116 (1-3), 259–275.

Moore, L. R., Post, A. F., Rocap, G., Chisholm, S. W., 2002b. Utilization of different nitrogen sources by the marine cyanobacteria *Prochlorococcus* and *Synechococcus*. Limnology and Oceanography 47 (4), 989–996.

Morel, A., 1988. Optical modeling of the upper ocean in relation to its biogenous matter content (case 1 water). Journal of Geophysical Research 93 (C9), 10749–10768.

Morel, F. M., Hudson, R. J. M., Price, N. M., 1991. Limitation of productivity by trace metals in the sea. Limnology and Oceanography 36, 1742–1755.

Murray, J., Johnson, E., Garside, C., 1995. A U.S. JGOFS process study in the equatorial Pacific (EqPac): Introduction. Deep-Sea Research II 42 (2-3), 275–293.

Murray, J. W., Barber, R. T., Roman, M. R., Bacon, M. P., Feely, R. A., 1994. Physical and biological controls on carbon cycling in the equatorial Pacific. Science 266, 58–65.

Murray, J. W., Leinen, M. W., Feely, R. A., Toggweiler, J. R., Wanninkhof, R., 1992. EqPac: A process study in the central equatorial Pacific. Oceanography 5, 134–142.

Murtugudde, R., Seager, R., Busalacchi, 1996. Simulation of the tropical oceans with an ocean GCM coupled to an atmospheric mixed-layer model. Journal of Climate 9 (8), 1795–1815.

Murtugudde, R. G., Signorini, S. R., Christian, S. R., Busalacchi, A. J., McClain, C. R., Picaut, J., 1999. Ocean color variability of the tropical Indo-Pacific basin observed by SeaWiFS during 1997-1998. Journal of Geophysical Research 104, 18351–18366.

Nakayama, E., Obata, H., Okamura, K., Isshiki, K., Karatani, H., Kimoto, T., 1995. Iron and manganese in the atmosphere and oceanic waters. In: Sakai, H., Nozaki, Y. (Eds.), Biogeochemical processes and ocean flux in the western Pacific. Terra Scientific Publishing, Tokyo, pp. 53–68.

Nelson, D. M., Treguer, P., 1992. Role of silicon as a limiting nutrient to Antarctic diatoms: Evidence from kinetic studies in the Ross Sea ice-edge zone. Marine Ecology Progress Series 80, 255–264.

Nelson, D. M., Treguer, P., Brzezinski, M. A., Leynaert, A., Queaguiner, B., 1995. Production and dissolution of biogenic silica in the ocean: Revised global estimates, comparison with regional data and relationship to biogenic sedimentation. Global Biogeochemical Cycles 9, 359–372.

Olson, R. J., Chisholm, S. W., Zettler, E. R., Armbrust, E. V., 1988. Analysis of *Synechococcus* pigment types in the sea using single and dual beam flow cytometry. Deep-Sea Research 35 (3), 425–440.

Pacanowski, R. C., Philander, S. G. H., 1981. Parameterization of vertical mixing in numerical models of tropical oceans. Journal of Physical Oceanography 11 (11), 1443–1451.

Partensky, F., Hess, W. R., Vaulot, D., 1999. *Prochlorococcus*, a marine photosynthetic prokaryote of global significance. Microbiology and Molecular Biology Reviews 63 (1), 106–127.

Partensky, F., Hoepffner, N., Li, W. K. W., Ulloa, O., Vaulot, D., 1993. Photoacclimation of *Prochlorococcus sp.* (Prochlorophyta) strains isolated from the North Atlantic and the Mediterranean Sea. Plant Physiology 101 (1), 285–296.

Perry, M. J., Talbot, M. C., Alberte, R. S., 1981. Photoadaption in marine phytoplankton: Response of the photosynthetic unit. Marine Biology 62 (2–3), 91–101.

Peters, H., Gregg, M. C., Caldwell, D. R., Moum, J. N., 1981. Equatorial vertical mixing. In: Katz, E. J., Witte, J. M. (Eds.), Further Progress in Equatorial Oceanography: A Report of the U.S. TOGA Workshop on the Dynamics of the Equatorial Oceans. Nova Univ. Press., pp. 101–120.

Philander, G., 1990. El Niño, La Niña, and the Southern Oscillation. Academic Press, Inc., Princeton, New Jersey.

Picaut, J., Hackert, E., Busalacchi, A. J., Murtugudde, R., Lagerloef, G. S. E., 2002. Mechanisms of the 1997-1998 El Niño-La Niña, as inferred from space-based observations. Journal of Geophysical Research 107, 1–20.

Picaut, J., Ioualalen, M., Menkes, C., Delcroix, T., McPhaden, M. J., 1996. Mechanism of the zonal displacements of the Pacific Warm Pool: Implications for ENSO. Science 274 (5292), 1486–1489.

Post, A. F., Dubinsky, Z., Wyman, K., Falkowski, P. G., 1985. Physiological response of a marine planktonic diatom to transitions in growth irradiance. Marine Ecology Progress Series 25 (2), 141–149.

Price, F., Weller, R., Pinkel, R., 1986. Diurnal cycling: Observations and models of the upper ocean response to diurnal heating, cooling, and wind mixing. Journal of Geophysical Research 91, 8411–8427.

Price, N. M., Ahner, B. A., Morel, F. M. M., 1994. The equatorial Pacific Ocean: Grazer-controlled phytoplankton populations in an iron-limited ecosystem. Limnology and Oceanography 39 (3), 520–534.

Qiao, L., Weisberg, R. H., 1995. Tropical instability wave kinematics: Observations from the tropical instability wave experiment. Journal of Geophysical Research 100, 8677–8693.

Quinn, W. H., Neal, V. T., Antunez de Mayolo, S. E., 1987. El Niño occurrences over the past four and a half centuries. Journal of Geophysical Research 92, 14449–14461.

Radenac, M. H., Rodier, M., 1996. Nitrate and chlorophyll distributions in relation to thermohaline and current structures in the western tropical Pacific during 1985-1989. Deep-Sea Research II 43 (4-6), 725–752.

Richardson, K., Beardall, J., Raven, J. A., 1983. Adaptation of unicellular algae to irradiance: An analysis of strategies. New Phytologist 93 (2), 157–191.

Rippka, R., Coursin, T., Hess, W., Lichtle, C., Scanlan, D. J., Palinska, K. A., Iteman, I., Partensky, F., Houmard, J., Herdman, M., 2000. *Prochlorococcus marinus* subsp. *pastoris* subsp. nov. strain pcc 9511, the first axenic chlorophyll a(2)/b(2)-containing cyanobacterium (*Oxyphotobacteria*). International Journal of Systematic and Evolutionary Microbiology 50 (5), 1833–1847.

Rocap, G., Distel, D. L., Waterbury, J. B., Chisholm, S. W., 2002. Resolution of *Prochlorococcus* and *Synechococcus* ecotypes by using 16S-23S ribosomal DNA internal transcribed spacer sequences. Applied Environmental Microbiology 68 (3), 1180–1191.

Rodier, M., Le Borgne, R., 1997. Export flux of particles at the equator in the western and central Pacific Ocean. Deep-Sea Research II 44, 2085–2113.

Roman, M. R., Dam, H. G., Gauzens, A. L., Urban-Rich, J., Foley, D. G., Dickey, T. D., 1995. Zooplankton variability on the equator at 140°W during the JGOFS EqPac study. Deep-Sea Research II 42, 673–693.

Roman, M. R., Gauzens, A. L., 1997. Copepod grazing in the equatorial Pacific. Limnology and Oceanography 42 (4), 623–634.

Rue, E. L., Bruland, K. W., 1995. Complexation of iron(III) by natural organic ligands in the central North Pacific as determined by a new competitive ligand equilibration/adsorptive cathodic stripping voltammetric method. Marine Chemistry 50, 117–138.

Rue, E. L., Bruland, K. W., 1997. The role of organic complexation on ambient iron chemistry in the equatorial Pacific Ocean and the response of a mesoscale iron addition experiment. Limnology and Oceanography 42, 901–910.

Sakshaug, E., Andresen, K., Kiefer, D. A., 1989. A steady state description of growth and light absorption in the marine planktonic diatom *Skeletonema costatum.* Limnology and Oceanography 34 (1), 198–205.

Sakshaug, E., Demers, S., Yentsch, C. M., 1987. *Thalassiosira oceanica* and *T. pseudonana* : Two different photoadaptational responses. Marine Ecology Progress Series 41 (3), 275–282.

Sakshaug, E., Johnsen, G., Andresen, K., Vernet, M., 1991. Modeling of light-dependent algal photosynthesis and growth: Experiments with the Barents Sea diatoms *Thalassiosira nordenskioeldii* and *Chaetoceros furcellatus.* Deep-Sea Research I 38 (4A), 415–430.

Sarmiento, J. L., Hughes, T. M. C., Stouffer, R. J., Manabe, S., 1998. Simulated response of the ocean carbon cycle to anthropogenic climate warming. Nature 393, 245–249.

Sarmiento, J. L., Slater, R., Barber, R., Bopp, L., Doney, S. C., Hirst, A. C., Kleypas, J., Matear, R., Mikolajewicz, U., Monfray, P., Soldatov, V., Spall, S. A., Stouffer, R., 2004. Response of ocean ecosystems to climate warming. Global Biogeochemical Cycles 18, art. GB3003.

Sathyendranath, S., Cota, G., Stuart, V., Maass, H., Platt, T., 2001. Remote sensing of phytoplankton pigments: a comparison of empirical and theoretical approaches. International Journal of Remote Sensing 22, 249–273.

Scanlan, D. J., West, N. J., 2002. Molecular ecology of the marine cyanobacterial genera *Prochlorococcus* and *Synechococcus*. FEMS Microbiology Ecology 40, 1–12.

Schofield, O., Bidigare, R. R., Prezelin, B. B., 1990. Spectral photosynthesis, quantum yield and blue-green light enhancement of productivity rates in the diatom *Chaetoceros gracile* and the prymnesiophyte *Emiliania huxleyi*. Marine Ecology Progress Series 64 (1-2), 175–186.

Schudlich, R. R., Price, J. F., 1992. Diurnal cycles of current, temperature, and turbulent dissipation in a model of the equatorial upper ocean. Journal of Geophysical Research 97, 5409–5422.

Siegenthaler, U., Sarmiento, J. L., 1993. Atmospheric carbon dioxide and the ocean. Nature 365, 119–125.

Smith, R. C., Baker, K. S., 1981. Optical properties of the clearest natural waters (200-800 nm). Applied Optics 20 (20), 177–184.

Sprintall, J., McPhaden, M. J., 1994. Surface layer variations observed in multiyear time series measurements from the western equatorial Pacific. Journal of Geophysical Research 99, 963–979.

Steinberg, D. K., Carlson, C. A., Bates, N. R., Johnson, R. J., Michaels, A. F., Knap, A., 2001. Overview of the U.S. JGOFS Bermuda Atlantic time-series study (BATS): a decade-scale look at ocean biology and biogeochemistry. Deep-Sea Research II 48, 1405–1448.

Strutton, P. G., Chavez, F. P., 2000. Primary productivity in the equatorial Pacific during the 1997-98 El Niño. Journal of Geophysical Research 105, 26,089–26,101.

Strutton, P. G., Ryan, J. P., Chavez, F. P., 2001. Enhanced chlorophyll associated with tropical instability waves in the equatorial Pacific. Geophysical Research Letters 28, 2005–2008.

Sunda, W. G., Huntsman, S. A., 1995. Iron uptake and growth limitation in oceanic and coastal phytoplankton. Marine Chemistry 50, 189–206.

Sunda, W. G., Huntsman, S. A., 1997. Interrelated influence of iron, light and cell size on marine phytoplankton growth. Nature 390, 389–392.

Takeda, S., 1998. Influence of iron availability, on nutrient consumption ratio of diatoms in oceanic waters. Nature 393, 774–777.

Tomczak, M., Godfrey, J. S., 1994. Regional Oceanography: An introduction. Pergamon, New York.

Trenberth, K. E., Hoar, T. J., 1996. The 1990-1995 El Niño-Southern Oscillation event longest on record. Geophysical Research Letters 23, 57–60.

Van den Berg, C. M. G., 1995. Evidence for organic complexation of iron in seawater. Marine Chemistry 50, 139–157.

Vaulot, D., Marie, D., Olson, R. J., Chisholm, S. W., 1995. Growth of *Prochlorococcus*, a photosynthetic prokaryote, in the equatorial Pacific Ocean. Science 268 (5216), 1480–1482.

Verity, P. G., Stoecker, D. K., Sieracki, M. E., Nelson, J. R., 1996. Microzooplankton grazing of primary production at 140°W in the equatorial Pacific. Deep-Sea Research II 43 (4-6), 1227–1256.

Walsh, I. D., Chung, S. P., Richardson, M. J., Gardner, W. D., 1995. The diel cycle in the integrated particle load in the equatorial Pacific: A comparison with primary production. Deep-Sea Research II 42, 465–477.

Walsh, J. J., 1975. A spatial simulation model of the Peru upwelling ecosystem. Deep-Sea Research 22, 201–236.

Walsh, J. J., 1976. Herbivory as a factor in patterns of nutrient utilization in the sea. Limnology and Oceanography 21, 1–13.

Wells, M. L., Price, N. M., Bruland, K. W., 1995. Iron chemistry in seawater and its relationship to phytoplankton: A workshop report. Marine Chemistry 48, 157–182.

Wells, M. L., Vallis, G. K., Silver, E. A., 1999. Influence of tectonic processes in Papua New Guinea on past productivity in the eastern equatorial Pacific Ocean. Nature 398, 601–604.

Wheeler, P. A., 1983. Phytoplankton nitrogen metabolism. In: Carpenter, E. J., Carpone, D. G. (Eds.), Nitrogen in the marine environment. Academic Press, New York, pp. 309–346.

Wheeler, P. A., Kokkinakis, S. A., 1990. Ammonium recycling limits nitrate use in the oceanic subarctic pacific. Limnology and Oceanography 35, 1267–1278.

Wiebe, P. H., Madin, L. P., Haury, L. R., Harbison, G. R., Philbin, L. M., 1979. Diel vertical migration by *Salpa aspera* and its potential for large-scale particulate organic matter transport to the deep-sea. Marine Biology 53, 249–255.

Wroblewski, J. S., 1977. A model of phytoplankton plume formation during variable Oregon upwelling. Journal of Marine Research 35 (2), 357–394.

Wunsch, C., Gill, A. E., 1976. Observations of equatorially trapped waves in Pacific sea level variations. Deep-Sea Research 23 (5), 371–390.

Wyrtki, K., 1975. El Niño - the dynamic response of the equatorial Pacific Ocean to atmospheric forcing. Journal of Physical Oceanography 5, 572–584.

Wyrtki, K., 1985. Water displacements in the Pacific and the genesis of El Niño cycles. Journal of Geophysical Research 90, 7129–7132.

Yu, Z., McCreary, J. P. J., Proehl, J. A., 1995. Meridional asymmetry and energetics of tropical instability waves. Journal of Physical Oceanography 25 (12), 2997–3007.

Zhang, C., Zou, J., 1997. Nutrient uptake kinetics and growth under nutrient limitation of *Pseudonitzschia*. Oceanologia et Limnologia Sinica 28, 599–603.

Zhang, X., Dam, H. G., White, J. R., Roman, M. R., 1995. Latitudinal variations in mesozooplankton grazing and metabolism in the central tropical Pacific during the U.S. JGOFS EqPac study. Deep-Sea Research II 42 (2-3), 695–714.

VITA

Barış Salihoğlu

Department of Ocean, Earth and Atmospheric Sciences

Old Dominion University

Norfolk, VA 23529

Education

B.S., Natural Gas and Petroleum Engineering (1996) Middle East Technical University, Ankara, Turkey

M.Sc., Physical Oceanography (1998) Institute of Marine Sciences, Middle East Technical University, Icel, Turkey

Ph.D., Physical Oceanography (2005) Old Dominion University, Virginia, USA

Publications

Salihoglu, B., 1998. Three-layer model of plankton productivity in the Black Sea basin. M.Sc. Thesis. Institute of Marine Sciences, METU, Turkey, 92 pp.

Oguz, T., Salihoglu, B., 2000. Simulation of eddy-driven phytoplankton production in the Black Sea. Geophysical Research Letters, 27(14):2125-2128.

Salihoglu, B., Fraser, W.R., Hofmann, E.E., 2001. Factors affecting fledging weight of Adélie penguin (*Pygoscelis adeliae*) chicks: a modeling study. Polar Biology, 24:328-337.

Klinck, J.M., Hofmann, E.E., Beardsley, R.C., Salihoglu, B., Howard, S, 2004. Water mass properties and circulation on the west Antarctic Peninsula Continental Shelf in austral Fall and Winter 2001. Deep-Sea Research II, 52:1925-1946.

Hood, R.R., Laws, E.A., Moore, K.J., Armstrong, A.R., Bates, N.R., Carlson, C.A., Chai, F., Doney, S.C., Falkowski, P.G., Feely, R.A., Friedrichs, M.A.M., Landry, M.R., Nelson, D.M., Richardson, T.L., Salihoglu, B., Schartau, M., Toole, D.A., Wiggert, J.D. (in press). Functional group modeling: progress challenges and prospects. Deep-Sea Research II.

Typeset using LaTeX.